NANOSIZED ALKALINE EARTH METAL TITANATES: EFFECTS OF SIZE ON PHOTOCATALYTIC AND DIELECTRIC PROPERTIES

by

DMYTRO V. DEMYDOV

M.S., Ukrainian State University of Chemical Technology, Dnepropetrovsk, Ukraine, 1996
M.B.A., Ukrainian State University of Chemical Technology, Dnepropetrovsk, Ukraine, 1997
M.S., Pittsburg State University, Kansas, USA, 2002

AN ABSTRACT OF A DISSERTATION

submitted in partial fulfillment of the requirements for the degree

DOCTOR OF PHILOSOPHY

Department of Chemistry
College of Arts and Sciences

KANSAS STATE UNIVERSITY
Manhattan, Kansas

2006

ABSTRACT

A new approach to synthesize nanosized strontium titanate ($SrTiO_3$) and barium titanate ($BaTiO_3$) has been developed. Nanocrystals of mixed metal oxide were synthesized by a modified aerogel procedure from alkoxides.

The textural and surface characteristic properties were studied by nitrogen BET analysis, transmission electron microscopy, and powder XRD. The crystallite sizes of aerogel prepared powders can vary from 6 to 25 nm by the use of different solvents. A mixture of ethanol and toluene was found to be the best binary solvent for supercritical drying, which produced a $SrTiO_3$ sample with a surface area of 159 m^2/g and an average crystallite size of 8 nm, and a $BaTiO_3$ sample with a surface area of 175 m^2/g and an average crystallite size of 6 nm.

These titanates have been studied for photocatalytic oxidation of volatile organic compounds and acetaldehyde (CH_3CHO) in particular. The big band gaps of the bulk (3.2 eV for $SrTiO_3$ and 3.1 eV for $BaTiO_3$) limit their application to a UV light region only. The modification of titanates by doping with transition metal ions (partial substitution of Ti ions with metal ions) creates a valence band or electron donor level inside of the band gap, narrows it, and increases the visible light absorption.

The enhanced adsorption of visible light was achieved by the synthesis of nanosized $SrTiO_3$ and $BaTiO_3$ by incorporating Cr ions during the modified aerogel procedure. Gaseous acetaldehyde photooxidation has been studied on pure $SrTiO_3$ and $BaTiO_3$, and on chromium doped Cr-$SrTiO_3$ and Cr-$BaTiO_3$ under UV and visible light irradiation, and compared with the photoactivity of P25 TiO_2.

$SrTiO_3$ doped with antimony/chromium shows absorption in visible light and show photocatalytic activity for CH_3CHO oxidation. The reason for the codoping of $SrTiO_3$ with Sb/Cr was to maintain the charge balance and to suppress oxygen defects in the lattice. This photocatalyst shows high photoactivity under visible light irradiation even after several continuous runs. The photoactivity under visible and UV light irradiation was almost identical for the Sb/Cr-$SrTiO_3$ photocatalyst.

Dielectric properties of aerogel prepared barium titanate samples have being studied and the bulk resistance values of AP-$BaTiO_3$ were significantly lower than that of commercial $BaTiO_3$, by several orders of magnitude.

NANOSIZED ALKALINE EARTH METAL TITANATES: EFFECTS OF SIZE ON PHOTOCATALYTIC AND DIELECTRIC PROPERTIES

by

DMYTRO V. DEMYDOV

M.S., Ukrainian State University of Chemical Technology, Dnepropetrovsk, Ukraine, 1996
M.B.A., Ukrainian State University of Chemical Technology, Dnepropetrovsk, Ukraine, 1997
M.S., Pittsburg State University, Kansas, USA, 2002

A DISSERTATION

submitted in partial fulfillment of the requirements for the degree

DOCTOR OF PHILOSOPHY

Department of Chemistry
College of Arts and Sciences

KANSAS STATE UNIVERSITY
Manhattan, Kansas

2006

Approved by:

Major Professor

Kenneth J. Klabunde

ABSTRACT

A new approach to synthesize nanosized strontium titanate ($SrTiO_3$) and barium titanate ($BaTiO_3$) has been developed. Nanocrystals of mixed metal oxide were synthesized by a modified aerogel procedure from alkoxides.

The textural and surface characteristic properties were studied by nitrogen BET analysis, transmission electron microscopy, and powder XRD. The crystallite sizes of aerogel prepared powders can vary from 6 to 25 nm by the use of different solvents. A mixture of ethanol and toluene was found to be the best binary solvent for supercritical drying, which produced a $SrTiO_3$ sample with a surface area of 159 m^2/g and an average crystallite size of 8 nm, and a $BaTiO_3$ sample with a surface area of 175 m^2/g and an average crystallite size of 6 nm.

These titanates have been studied for photocatalytic oxidation of volatile organic compounds and acetaldehyde (CH_3CHO) in particular. The big band gaps of the bulk (3.2 eV for $SrTiO_3$ and 3.1 eV for $BaTiO_3$) limit their application to a UV light region only. The modification of titanates by doping with transition metal ions (partial substitution of Ti ions with metal ions) creates a valence band or electron donor level inside of the band gap, narrows it, and increases the visible light absorption.

The enhanced adsorption of visible light was achieved by the synthesis of nanosized $SrTiO_3$ and $BaTiO_3$ by incorporating Cr ions during the modified aerogel procedure. Gaseous acetaldehyde photooxidation has been studied on pure $SrTiO_3$ and $BaTiO_3$, and on chromium doped Cr-$SrTiO_3$ and Cr-$BaTiO_3$ under UV and visible light irradiation, and compared with the photoactivity of P25 TiO_2. $SrTiO_3$ doped with antimony/chromium shows absorption in visible light and show photocatalytic activity for CH_3CHO oxidation. The reason for the codoping of $SrTiO_3$ with Sb/Cr was to maintain the charge balance and to suppress oxygen defects in the lattice. This photocatalyst shows high photoactivity under visible light irradiation even after several continuous runs. The photoactivity under visible and UV light irradiation was almost identical for the Sb/Cr-$SrTiO_3$ photocatalyst.

Dielectric properties of aerogel prepared barium titanate samples have being studied and the bulk resistance values of AP-$BaTiO_3$ were significantly lower than that of commercial $BaTiO_3$, by several orders of magnitude.

TABLE OF CONTENTS

TABLE OF CONTENTS v
LIST OF FIGURES ix
LIST OF TABLES xiv
ACKNOWLEDGEMENTS xvi
DEDICATION xviii
PREFACE xix
Chapter 1 : Introduction 1
1.1 Literature review on titanates 3
1.2 Advantages of nanosized titanates 10
1.3 Possible applications 11
1.4 References 13
Chapter 2 : Synthesis of titanates 18
2.1 Introduction 18
2.2 Preparation of titanates 18
2.2.1 Solid-state reaction 19
2.2.2 Gas phase reaction 21
2.2.3 Sol-gel technique 29
2.2.4 Aerogel procedure 32
2.3 Temperature treatment 33
2.3.1 Heat treatment 35
2.3.2 Calcination 35
2.3.3 Drying 36
2.4 Conclusions 38
2.5 References 39
Chapter 3 : Characterization of titanates 41
3.1 Introduction 41
3.2 Synthesis of strontium and barium titanates 41
3.2.1 Solid–state reaction 42

3.2.2 Modified aerogel procedure 44
3.3 Structural studies 47
3.3.1 UV-visible spectroscopy 47
3.3.2 Braunauer-Emmer-Teller analysis (BET) 50
3.3.3 Powder X-ray diffraction 54
3.3.4 Transmission electron microscopy 65
3.3.5 Elemental analysis 71
3.3.6 Thermogravimetric analysis 71
3.4 Discussion 71
3.5 Conclusions 73
3.6 References 75
Chapter 4 : Photooxidation of acetaldehyde by titanates 76
4.1 Introduction 76
4.2 Photoactivity under light irradiation 77
4.2.1 Design of photocatalysts of high activity 82
4.2.2 UV light irradiation 84
4.2.3 Visible light irradiation 87
4.3 Acetaldehyde photodecomposition studies 88
4.3.1 Experimental setup for photodecomposition reactions 90
4.3.2 Photoactivity of commercially available and synthesized samples 96
4.4 Conclusions 102
4.5 References 103
Chapter 5 : Modification of titanates by doping 106
5.1 Introduction 106
5.2 Doping process 108
5.2.1 Doping with transition metals in solid-state reaction 112
5.2.2 Doping with transition metals in aerogels 112
5.3 Photoactivity of doped titanates 115
5.3.1 Cr doping and Sb/Cr codoping of aerogel prepared catalysts 115
5.3.2 Cr doping and Sb/Cr codoping of solid-state prepared samples 134
5.3.3 Cr doping of $SrTiO_3$ and $BaTiO_3$ catalysts 147

5.4 Discussion and conclusions 157
5.5 References 159
Chapter 6 : Surface studies of titanates by FTIR spectroscopy 160
6.1 Introduction 160
6.2 Acetaldehyde decomposition on the surface of aerogel prepared $SrTiO_3$ 163
6.2.1 Acetaldehyde adsorption over $SrTiO_3$ at 243 K: evidence of H-bonding 165
6.2.2 Warm up effect of adsorbed acetaldehyde: evidence of aldol condensation and formation of α, β-unsaturated aldehyde (crotonaldehyde, CH_3-CH=CH-CHO) 168
6.2.3 Dark oxidation: influence of dioxygen exposure over preadsorbed acetaldehyde at 243 K 170
6.2.4 Spectral development during photooxidation reaction: influence of dioxygen exposure over preadsorbed acetaldehyde at 243 K 173
6.3 Acetaldehyde decomposition on the 2% Cr doped and 2.5% Sb/2% Cr codoped AP-$SrTiO_3$ 176
6.3.1 Dehydroxylation on 2% Cr doped AP-$SrTiO_3$ 176
6.3.2 Dehydroxylation on 2.5% Sb/2% Cr doped AP-$SrTiO_3$ 177
6.3.3 Adsorption, evacuation, and warming prior to dark oxidation of acetaldehyde on 2% Cr doped AP-$SrTiO_3$ 177
6.3.4 Adsorption, evacuation, and warming prior to dark oxidation of acetaldehyde on 2.5% Sb/2% Cr codoped AP-$SrTiO_3$ 181
6.3.5 Attempted dark oxidation of acetaldehyde on 2% Cr-$SrTiO_3$ 181
6.3.6 Attempted dark oxidation of acetaldehyde on 2.5% Sb/2% Cr codoped AP-$SrTiO_3$ 184
6.3.7 Photooxidation of acetaldehyde on 2% Cr doped AP-$SrTiO_3$ 184
6.3.8 Photooxidation of acetaldehyde on 2.5% Sb/2% Cr doped AP-$SrTiO_3$ 187
6.4 Mass spectrometry studies on reaction products 187
6.5 Conclusions 191
6.6 References 192
Chapter 7 : Dielectric studies on titanates 193
7.1 Introduction 193
7.2 Dielectric properties of titanates 193
7.3 Aerogels for electrical applications 196

7.4 Synthesis of $Ba_{0.5}Sr_{0.5}TiO_3$ aerogel 197
7.5 Dielectric measurements 203
7.5.1 Impedance analysis 203
7.5.2 Raman spectroscopy 210
7.6 Conclusions 212
7.7 References 213
APPENDIX A: XRD analysis 215
APPENDIX B: Elemental analysis 217
APPENDIX C: TGA analysis 218
APPENDIX D: *in situ* FTIR 220
APPENDIX E: Dielectric measurements 223
APPENDIX F: Permission to reproduce materials 226

LIST OF FIGURES

Figure 1.1 Perovskite (ABO_3) Unit Cell 3
Figure 1.2 Perovskite Structure (BO_6 and A^{2+} Layers) 4
Figure 2.1 Unit Cell of $YBa_2Cu_3O_{7-x}$ Oxide 20
Figure 2.2 Principal Scheme for Chemical Transport (Adapted and Modified from Reference 5) 22
Figure 2.3 Principal Scheme of a CVD Reactor for Oxide Film Deposition (MFC – Mass Flow Controller) (Adapted and Modified from Reference 5) 25
Figure 2.4 Production Options for the Sol-gel Process (Adapted and Modified from Reference 5) 31
Figure 2.5 Sintering by diffusion (path 1 - surface diffusion, path 2 - volume diffusion) 34
Figure 2.6 Temperature-pressure Diagram for Supercritical Drying, where C - Critical Point, SCF – Super Critical Fluid, T_c – Critical Temperature, P_c – Critical Pressure (Adapted and Modified from Reference 5 and 13) 37
Figure 3.1 Solid-state Reactions for $SrTiO_3$ and $BaTiO_3$ Synthesis 43
Figure 3.2 Modified Aerogel Procedure (MAP) from Alkoxides for $SrTiO_3$ and $BaTiO_3$ Synthesis 46
Figure 3.3 UV-visible Spectra of TiO_2 P25 Degussa and Aerogel Prepared $SrTiO_3$ 48
Figure 3.4 UV-visible Spectra of Different $SrTiO_3$ Samples 49
Figure 3.5 Five Types of Adsorption Isotherms [2] 52
Figure 3.6 Powder XRD Patterns of Commercial and Synthesized $SrTiO_3$ with Different Alcohols Used in Synthesis (CM-$SrTiO_3$ – Commercial, NCM-$SrTiO_3$ – Commercial Nanosized, AP-$SrTiO_3$ – Aerogel Prepared Samples) 57
Figure 3.7 Powder XRD Patterns of Solid-state (SSR-$SrTiO_3$) and Aerogel Prepared (AP-$SrTiO_3$) Samples 58
Figure 3.8 Powder XRD Patterns of AP-$SrTiO_3$ (Ethanol) Calcined in Air at Different Temperatures 60
Figure 3.9 Powder XRD Patterns of Commercial and Synthesized $BaTiO_3$ with Different Alcohols Used in Synthesis (CM-$BaTiO_3$ – Commercial, NCM-$BaTiO_3$ – Commercial

Nanosized, AP-$BaTiO_3$ – Aerogel Prepared Samples). The XRD Studies of the Samples were Conducted using a Shimadzu XRD 6000 (NanoScale Materials, Inc.) 61
Figure 3.10 Powder XRD Patterns of AP-$BATiO_3$ (Ethanol) Calcined in Air at 500 °C with a $BaCO_3$ Phase vs. Freshly Prepared Sample of AP-$BaTiO_3$ (Ethanol) 63
Figure 3.11 Calcination of AP-$BaTiO_3$ (Ethanol) in Air and Oxygen at 500 °C.....64
Figure 3.12 Transmission Electron Micrographs of SSR-$SrTiO_3$ Prepared at 1100 °C.....67
Figure 3.13 Transmission Electron Micrographs of AP-$SrTiO_3$ after Synthesis (left) and after Calcination in Air at 500 °C (right) 68
Figure 3.14 Transmission Electron Micrographs of SSR-$BaTiO_3$ Prepared at 1100 °C.....69
Figure 3.15 Transmission Electron Micrographs of AP-$BaTiO_3$ (Isopropanol) Samples after Synthesis (left), Heat Treated in Vacuum at 500 °C (middle), and Calcined in Air at 500 °C (right) 70
Figure 4.1 Semiconductor Photocatalyst for Water Photolysis 78
Figure 4.2 Semiconductor Oxide Band Gaps and Potentials 80
Figure 4.3 Photocatalytic Reactions: Photoinduced Reaction (down hill) and Photon Energy Conversion Reaction (up hill) [17].....81
Figure 4.4 Photocatalytic Oxidation of Various Organic Compounds on TiO_2 Surface under UV Light Irradiation [33].....84
Figure 4.5 Oxidation of Acetic Acid on the TIO_2 under UV Irradiation and in Oxygen-free Environment [33] 86
Figure 4.6 UV-visible Absorbance of Titanium Based Semiconductor Oxides.....89
Figure 4.7 Experimental Setup for Photocatalysis Reactions.....92
Figure 4.8 Peak Areas versus Time for CH_3CHO Decomposition and CO_2 Evolution under UV Light for AP-$SrTiO_3$ 93
Figure 4.9 Concentration versus CH_3CHO Decomposition and CO_2 Evolution under UV Light for AP-$SrTiO_3$ 94
Figure 4.10 Photocatalytic Decomposition of Acetaldehyde under UV Light for P25 TiO_2.....95
Figure 4.11 CO_2 Evolution under UV Light Irradiation for Different Catalyst Samples 97
Figure 4.12 CH_3CHO Decomposition under UV Light Irradiation for Different Catalyst Samples 98
Figure 4.13 Defuse Reflectance Spectra of Different $SrTiO_3$ Samples 100

Figure 5.1 Transition Metal Doping of UV Photocatalysts 107
Figure 5.2 UV-Visible Absorption Spectra of a) Pure TiO_2 and b) –d) Cr Ion-implanted TiO_2 with Cr of 2.2, 6.6, and 13 $x10^{-7}$ mol/g [11] 109
Figure 5.3 Diffuse Reflectance Spectra of Doped $SrTiO_3$:M (0.5%) with a) Mn, b) Ru, c) Rh, d) Pd, e) Ir, f) Pt [12] 110
Figure 5.4 Metal Doping of $SrTiO_3$ Photocatalyst by Solid-State Reaction 113
Figure 5.5 Metal Doping of $SrTiO_3$ Photocatalyst by Modified Aerogel Procedure 114
Figure 5.6 Powder XRD Patterns of Aerogel Prepared Strontium Titanate Samples (AP-$SrTiO_3$ – Pure, AP-2%Cr-$SrTiO_3$ – 2% Chromium Ion Doped, AP-2.5%Sb/2%Cr-$SrTiO_3$ – 2.5% Antimony and 2% Chromium Ion Codoped) 117
Figure 5.7 Defuse Reflectance Spectra of Pure $SrTiO_3$, TiO_2 P25 Degussa, 2% Cr Doped and 2% Cr/2.5% Sb Codoped Aerogel Prepared Strontium Titanate Samples 119
Figure 5.8 Defuse Reflectance Spectra of 2% Cr Doped and 2% Cr/2.5% Sb Codoped Aerogel Prepared Strontium Titanate Samples Freshly Prepared and Calcined at 773 K 120
Figure 5.9 Transmission Electron Micrographs of 2% Cr Doped (left) and 2% Cr/2.5% Sb Codoped (right) Aerogel Prepared Strontium Titanate Samples 122
Figure 5.10 UV and Visible Photoactivity of Cr-$SrTiO_3$ Aerogel for CO_2 Production 125
Figure 5.11 UV and Visible Photoactivity of Sb/Cr-$SrTiO_3$ Aerogel for CO_2 Production 126
Figure 5.12 UV and Visible Photoactivity of Cr-$SrTiO_3$ Aerogel for CH_3CHO Degradation 127
Figure 5.13 UV and Visible Photoactivity of Sb/Cr-$SrTiO_3$ Aerogel for CH_3CHO Degradation 128
Figure 5.14 CO_2 Evolution for Aerogel Prepared Catalysts under UV Light 129
Figure 5.15 CO_2 Evolution for Aerogel Prepared Catalysts under Visible Light 130
Figure 5.16 CH_3CHO Degradation for Aerogel Prepared Catalysts under UV Light 131
Figure 5.17 CH_3CHO Degradation for Aerogel Prepared Catalysts under Visible Light 132
Figure 5.18 2.5% Sb/2% Cr Codoped $SrTiO_3$ Prepared by Solid-State Reaction and Aerogel Modified Procedure 135
Figure 5.19 Transmission Electron Micrographs of 2% Cr Doped (left) and 2% Cr/2.5% Sb Codoped (right) Solid-State Prepared Strontium Titanate Samples 138
Figure 5.20 Diffuse Reflectance Spectra of 2.5% Sb/2% Cr $SrTiO_3$ Prepared by Solid-State Reaction 139

Figure 5.21 Diffuse Reflectance Spectra of 2%Cr $SrTiO_3$ and 2.5% Sb/2% Cr $SrTiO_3$ Prepared by Solid-state Reaction and by Aerogel Modified Procedure 140
Figure 5.22 UV and Visible Photoactivity of Cr Doped SSR-$SrTiO_3$ for CO_2 Production 143
Figure 5.23 UV and Visible Photoactivity of Cr/Sb Codoped SSR-$SrTiO_3$ for CO_2 Production 144
Figure 5.24 UV and Visible Photoactivity of Cr Doped SSR-$SrTiO_3$ for CH_3CHO Decomposition 145
Figure 5.25 UV and Visible Photoactivity of Cr/Sb Codoped SSR-$SrTiO_3$ for CH_3CHO Decomposition 146
Figure 5.26 Diffuse Reflectance Spectra of Pure AP-$BaTiO_3$ and 2%Cr Doped AP-$SrTiO_3$ 148
Figure 5.27 CO_2 Evolution for Aerogel Prepared $SrTiO_3$ and $BaTiO_3$ Under UV Light Irradiation 151
Figure 5.28 CH_3CHO Degradation for Aerogel Prepared $SrTiO_3$ and $BaTiO_3$ Under UV Light Irradiation 152
Figure 5.29 CO_2 Evolution for Aerogel Prepared $SrTiO_3$ and $BaTiO_3$ Under Visible Light Irradiation 153
Figure 5.30 CH_3CHO Degradation for Aerogel Prepared $SrTiO_3$ and $BaTiO_3$ Under Visible Light Irradiation 154
Figure 5.31 CO_2 Evolution for Aerogel Prepared $SrTiO_3$ and $BaTiO_3$ Under Light Irradiation (UV or Visible Light) 155
Figure 5.32 CH_3CHO Degradation for Aerogel Prepared $SrTiO_3$ and $BaTiO_3$ Under Light Irradiation (UV or Visible Light) 156
Figure 6.1 Acetaldehyde Reaction on CeO_2 and M/CeO_2 (M is Po, Co and Po-Co) [3] 161
Figure 6.2 Acetaldehyde Adsorption on AP-$SrTiO_3$ and Sequential Change of Temperature 166
Figure 6.3 Dark Oxidation of Acetaldehyde on AP-$SrTiO_3$ Surface 171
Figure 6.4 Kinetics Study of Acetaldehyde Dark Oxidation Using Oxygen 172
Figure 6.5 Spectral Development during Photooxidation of Acetaldehyde on the AP-$SrTiO_3$ surface 174
Figure 6.6 Dehydroxylation as a Function of Temperature and Calcination on 2%Cr-$SrTiO_3$ Nanoparticles 178
Figure 6.7 Dehydroxylation as a Function of Temperature and Calcination on 2.5%Sb/2%Cr-$SrTiO_3$ Nanoparticles 179

Figure 6.8 Adsorption, Evacuation, and Warming prior to Dark Oxidation of Acetaldehyde on 2%Cr-$SrTiO_3$ Nanoparticles 180
Figure 6.9 Adsorption, Evacuation, and Warming prior to Dark Oxidation of Acetaldehyde on 2.5%Sb/2%Cr-$SrTiO_3$ Nanoparticles 182
Figure 6.10 Attempted Dark Oxidation of Acetaldehyde as a Function of Time at Constant Temperature on 2%Cr-$SrTiO_3$ Nanoparticles 183
Figure 6.11 Dark Oxidation of Acetaldehyde as a Function of Time at Constant Temperature on 2.5%Sb/2%Cr-$SrTiO_3$ Nanoparticles 185
Figure 6.12 Visible and UV-Visible Photooxidation of Acetaldehyde on 2%Cr-$SrTiO_3$ Nanoparticles 186
Figure 6.13 Visible and UV-Visible Photooxidation of Acetaldehyde as a Function of Time on 2.5%Sb/2%Cr-$SrTiO_3$ 189
Figure 6.14 Temperature Programmed Desorption/ Mass Spectroscopy after Photooxidation of Acetaldehyde on 2.5%Sb/2%Cr-$SrTiO_3$ 190
Figure 7.1 $BaTiO_3$ Structure 194
Figure 7.2 Modified Aerogel Procedure (MAP) from Alkoxides for $Ba_{0.5}Sr_{0.5}TiO_3$ Synthesis 199
Figure 7.3 Modified Aerogel Procedure (MAP) from Alkoxides for $Ba_{0.5}Sr_{0.5}TiO_3$ Synthesis 200
Figure 7.4 UV-visible Spectra of Different Aerogel Prepared Samples 201
Figure 7.5 Transmission Electron Micrographs of AP-$Ba_{0.5}Sr_{0.5}TiO_3$ Freshly Prepared (left and middle) and Calcined in Oxygen at 500°C (right) 202
Figure 7.6 Powder XRD of NCM-$BaTiO_3$ Powder and Powder of Crashed NCM-$BaTiO_3$ Pellet 205
Figure 7.7 Complex Impedance Spectrum of Aerogel Prepared AP-$Ba_{0.5}Sr_{0.5}TiO_3$ at Room Temperature 207
Figure 7.8 Resistance of Commercial $BaTiO_3$ and Aerogel Prepared $BaTiO_3$ and $Ba_{0.5}Sr_{0.5}TiO_3$ 208
Figure 7.9 Relative Permittivity of Commercial $BaTiO_3$ and Aerogel Prepared $BaTiO_3$ and $Ba_{0.5}Sr_{0.5}TiO_3$ 209
Figure 7.10 Raman Spectra of AP-$BaTiO_3$ and NCM-$BaTiO_3$ 211
Figure 7.11 Raman Spectra of $BaTiO_3$ and Extraction of Soft Mode Frequencies [31] 212

LIST OF TABLES

Table 1.1 Wet Chemical Methods for the Synthesis of Mixed-Metal Oxides 5
Table 2.1 CVD Related Methods [5] 26
Table 2.2 Oxide Powders Prepared by Aerosol Method [5] 27
Table 2.3 Critical Points of Some Solvents [13] 37
Table 3.1 Characteristic Properties of Different $SrTiO_3$ Samples 56
Table 3.2 Characteristic Properties of AP-$SrTiO_3$ (Ethanol) Calcined at Different Temperatures in Air 59
Table 3.3 Characteristic Properties of Different $BaTiO_3$ Samples 62
Table 3.4 Characteristic Properties of AP-$BaTiO_3$ (Ethanol) Calcined at Different Temperatures in Air 65
Table 4.1 Rate Constant (k) for the Reaction of $OH^{\bullet}$ Radical with Air Pollutants at 298 K [33] .85
Table 4.2 Initial Rates for CH_3CHO Decomposition and CO_2 Production under UV Light Irradiation for the Different Catalyst Samples 96
Table 4.3 Initial Rates for CH_3CHO Decomposition and CO_2 Production under Visible Light Irradiation for Different Catalyst Samples 101
Table 5.1 Textural Properties of Photocatalysts 121
Table 5.2 Initial Rates of Acetaldehyde Degradation and Carbon Dioxide Production 123
Table 5.3 Photocatalysts for Acetaldehyde Degradation and Carbon Dioxide Production 133
Table 5.4 Textural Properties of AP- and SSR-$SrTiO_3$ Samples.....136
Table 5.5 Photocatalytic Properties of AP- and SSR-$SrTiO_3$ Samples for Acetaldehyde Decomposition 142
Table 5.6 Photocatalytic Properties of Chromium Doped Aerogel Prepared and Solid-state Prepared Strontium Titanate and Barium Titanate Catalysts.....149
Table 6.1 Vibrational Frequencies & Assignments of Adsorbed Acetaldehyde and Related Surface Species 169
Table 6.2 Spectral Changes during the Photooxidation of Acetaldehyde.....175
Table 6.3 Desorbed Species Identified by Mass Spectroscopy from the $SrTiO_3$ Surface after Photooxidation of Acetaldehyde 188

Table 7.1 Dielectric Constants of Titanates [7] 195
Table 7.2 Textural properties of pelletized $BaTiO_3$ 204

ACKNOWLEDGEMENTS

First of all, I would like to express my deep appreciation to my high school teacher of chemistry, Lubov Shvedova. She opened my eyes to the beauty of chemistry and helped to choose a career of chemist. Secondly, I would like to express my deep gratitude to my undergraduate adviser at Ukrainian State University of Chemical Technology, Dr. Boris Melnikov who introduced me to the world of nanomaterials and broadened my research interests to include the synthesis of nanoparticles.

Thirdly and foremost, I would like to thank my doctorate advisor at Kansas State University, Dr. Kenneth J. Klabunde, for the privilege of working in his research group. In this group, I gained invaluable experience in the synthesis of different nanomaterials (metals, oxides, sulfides, and nitrides) and familiarized myself with the equipment, methods used for synthesis, and the characterization and applications of these materials. Under his guidance, I was given the freedom to pursue my research in my own way and I greatly appreciated that freedom.

My colleagues in our research group, Dr. Alexander Bedilo, Dr. Jeevanandam Pethaiyan, Dr. Uma Sitharaman, Dr. Ranjit Koodali, Dr. Shalini Rodriguez, Dr. Igor Martyanov, Dr Savka Stoeva, Dr. Peter Stoimenov, Dr. Gavin Medine, Dr. David Heroux, Dr. Aldo Ponce, Alexander Smetana, Johanna Haggstrom, Aaron Yang, Dambar Hamal, Luther Mahoney, Erin Beavers, Sreeram Cingarapu and Kevin Quinn, are gratefully acknowledged for helpful discussions, valuable suggestions, interesting collaborations, strong research group traditions, numerous travels for conferences, hard working and pleasant times. Thank you for memorable graduate school years.

I would also like to express extreme gratitude to Dr. Dilip K. Paul and students (Brian and Owen) in his research group at Pittsburg State University for the intense collaboration on the FTIR Surface studies.

The financial support provided by the Department of Defense through the MURI grant and National Science Foundation are gratefully acknowledged. I would also like to express my sincere appreciation to the Chemistry Department at KSU for their constant support and resources provided.

I would like to express my appreciation to the members of my Dissertation Committee, Dr. Kenneth J. Klabunde, Dr. Duy H. Hua, Dr. Stefan Bossmann, Dr. James H. Edgar, Dr. Daniel A. Higgins, and Dr. Kevin Lease. I whould like to thank them for their service, for useful suggestions and valuable discussions.

Last, but certainly not least, I would like to thank my family and friends for always supporting me. You do not know how much your support means to me and without you standing by me I would never have written this dissertation.

DEDICATION

To my beloved family and friends for always supporting, helping, and standing by me.

PREFACE

Minima maxima sunt.

The smallest things are most important.

Nanometer is 10^{-9} meter

Chapter 1 : Introduction

The new developments in modern industries have generated an increasing need for new types of materials. In this respect, the application of mixed metal oxides as catalytic, photocatalytic, photoelectric, and dielectric materials has shown tremendous promise [1-4]. Metal oxides exhibit very diverse properties, including optical, electrical, magnetic and etc. They have high hardness, high chemical resistance, and high thermal stability. These oxides have been widely used as ceramics, electronics, catalysts, and coatings. For example, silicon oxide (SiO_2) is a widely used oxide material. It has found numerous applications because of its use as an optical material, thermal and electrical insulator, and material with high hardness and chemical stability. Other oxides can be used as semiconductor (TiO_2) or superconductor ($YBa_2Cu_3O_7$) materials. Ferroelectric and dielectric oxides of perovskite structure ($BaTiO_3$, $PbTiO_3$) are widely used in electronics. The perovskite lead zirconate titanate ($PbZr_{1-x}Ti_xO_3$) is a ferroelectric and piezoelectric material. $SrTiO_3$ is used for high Curie temperature superconducting films.

Highly porous oxide materials like silica [5] and titania [6, 7] synthesized by sol gel processing have also received much attention recently because of their application in low-loss dielectrics, catalysis, filtering and photonics. High surface areas of the porous materials yield good candidates for catalysis. These materials have very low density and can be used for low-loss electronic devices due to a very low dielectric constant.

Semiconducting oxides have band gaps in the UV light spectrum. Titanium oxide (TiO_2) is one of the most promising wide-band-gap (3.2 eV for anatase phase and 3.0 eV for rutile phase) materials which has been used as a pigment because of its refractive index, absence of absorption of visible light, stability, and nontoxicity [8]. Titania did not find applications for structural ceramics due to its poor fracture toughness. However, it is widely used as the catalyst support for different oxides such as molybdena, tungsta, and vanadia [9]. This catalyst has been used for selective oxidation of hydrocarbons, decomposition of isopropanol, ammoxidation of aromatic hydrocarbons, and reduction of nitric acid [9, 10].

UV light illumination of the TiO_2 surfaces using light with higher energy than the TiO_2 band gap (shorter than 410 nm for rutile phase and shorter than 385 nm for the anatase phase) causes the photoexitation of electrons from the valence band (O^{2-} 2p-orbitals) to the unoccupied

conduction band (Ti^{4+} 3d-orbitals) [8]. Light irradiation causes a production of the highly active holes and increases the photocatalytic and photooxidative activity of titanium oxide.

Some mixed-metal oxides ($BaCeO_{3-\delta}$, $BaPb_{1-x}Bi_xO_{3-\delta}$, $CaTiO_3$)) can conduct ions and transport oxygen owing to oxide ion mobility [11, 12]. They conduct electrons and oxide ions and supply oxygen from the oxide to surface. This allows for oxidizing different hydrocarbons (oxidative coupling of methane) [13, 14]. Different methods can be used for the synthesis of metal oxides. The solid-state reaction or the ceramic method is the oldest and most commonly used process for the synthesis of bulk oxide material, but chemical vapor deposition can be applied for metal oxide film depositions on to different substrates. Finally, the aerosol process gives highly dispersed metal oxide (TiO_2, SiO_2, and ZrO_2) through controlled flame hydrolysis.

The conventional preparation of oxide powders is based on solid-state reactions and requires repeated cycles of milling and calcination at high temperature. However, the powders are agglomerated grains of different sizes and contaminated due to incomplete reactions. In contrast to a solid-state method, wet chemical syntheses provide nanosized oxides of high purity.

Sol-gel processing is the most widely used route and involves a colloidal sol that is converted into a gel through aging. The gel is subsequently calcined, giving rise to a crystalline product with a homogeneous composition and a large surface area.

An aerogel method can be successfully applied for the production of nanosized metal oxides of high purity [15]. This process involves the production of a gel of a three-dimensional polymeric network from alkoxides. Solvent removal by supercritical drying prevents the collapse of the network and preserves the unique properties of the product with a high porosity, small crystallite sizes, and a large surface area. Different mixed oxide aerogels (ZrO_2-MgO, Al_2O_3-MgO, TiO_2-MgO) have been synthesized [16].

Oxide nanomaterials have unique optical and electrical properties due to a very small size of the particles and the quantum confinement phenomenon. Oxide nanomaterials are good catalysts due to their high surface to volume ratio. Additionally, nanosized oxide powders are used for the production of novel ceramics and composites.

1.1 Literature review on titanates

Metal and mixed-metal oxides are of extreme interest because of their unique properties as well as already known industrial uses. They possess high mechanical, thermal, and chemical stability. Some of them prepared by aerosol or aerogel methods have low densities and are potential candidates for light-weight applications.

The application of mixed metal oxides as photoelectric, ferroelectric, piezoelectric, and dielectric materials is an area of tremendous promise in research currently. Many of these oxides have a perovskite structure and behave as semiconductors. Barium titanate ($BaTiO_3$), lead titanate ($PbTiO_3$), lead zirconate titanate ($PbZr_{1-x}Ti_xO_3$), and lead ferrate niobate ($PbFe_{1-x}Nb_xO_3$) are used in multilayer capacitors [17]. Strontium ($SrTiO_3$) is a well known photocatalyst for the decomposition of some organic compounds and production of hydrogen by water splitting under UV light irradiation [18, 19]. Some of them exhibit electro-optic or non-linear optical properties [20].

Perovskites are solid mixed metal oxides with a general formula of ABO_3 (Figure 1.1). In these compounds, the A^{2+} metal ions occupy the corners of the rock salt structure and B^{4+} metal ions form octahedral structure with oxygen anions (Figure 1.2).

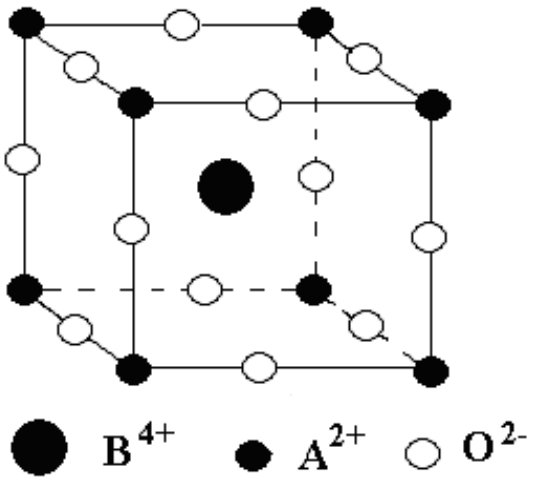

Figure 1.1 Perovskite (ABO_3) Unit Cell

High purity perovskite oxide powders, ABO_3 (where A is an alkaline-earth metal and B is a transition metal), are widely used for the preparation of dense ferroelectric, thin film electronic components and electro-optical materials. Perovskites are also known to be good catalysts in processes such as oxidation and hydrogenation [21, 22]. However, the small surface areas (≈ 1 m^2/g) and the lack of homogeneity of solids, owing to solid-state reactions and to incomplete reaction between the precursors, are not attractive for the preparation of catalysts.

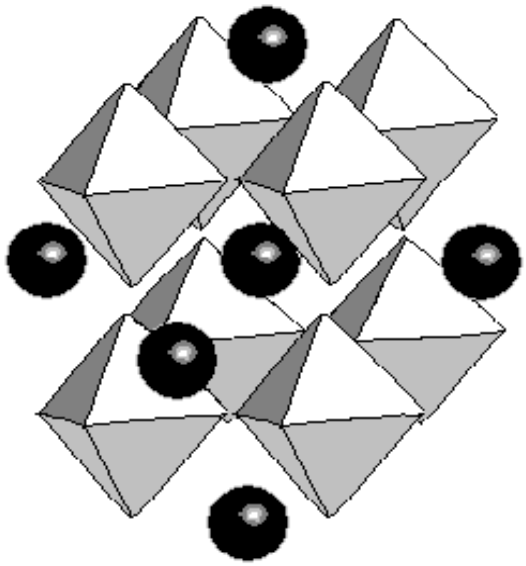

Figure 1.2 Perovskite Structure (BO_6 and A^{2+} Layers)

Many of the already mentioned perovskites belongs to the titanate compound family. The work described herein will emphasize the synthesis, characterization and applications of alkaline-earth metal titanates and in particular strontium titanate ($SrTiO_3$), barium titanate ($BaTiO_3$), and strontium barium titanate ($Sr_{1-x}Ba_xTiO_3$).

Traditional preparation of titanates ($MTiO_3$, where M is a bivalent metal) by solid-state synthesis includes repeated grinding and calcination above 1000ºC of metal carbonate and titanium oxide. Voorhoeve et al. synthesized a series of 20 perovskite oxides by solid-state reaction [23]. The synthesis of these oxides is inexpensive, simple and easy to perform. However, the prepared materials have very small surface areas of approximately 1 m^2/g and lack of homogeneity owing to incomplete reaction between solid precursors.

The preparation of barium titanate by solid-state reaction causes the formation of the pyrochlore phase and grinding contaminates the sample with the grinding medium. These impurities have a significant influence on the dielectric performance of this material [24]. High sintering temperatures are required for capacitor production. The examined literature on the topic shows that different research groups have attempted to synthesize titanate using other methods and techniques to obtain perovskite structure phase at lower temperature, with higher purity and smaller particle sizes. Some of those groups have used wet chemical methods for the synthesis of mixed-metal oxides (Table 1.1) [25]. Oxides prepared by these methods have several significant advantages over the traditionally solid-state prepared oxides. The wet chemically prepared oxides have higher homogeneity, higher surface area, and relatively higher reactivity.

Table 1.1 Wet Chemical Methods for the Synthesis of Mixed-Metal Oxides

Process	Method
Thermal Decomposition	1. Oxalate 2. Citrate 3. Peroxide 4. Acetate 5. Complex Cyanide
Evaporative Decomposition	1. Spray Pyrolysis 2. Liquid Mix
Sol-Gel Processing	1. Mixed Alkoxide 2. Carboxy-Alkoxide 3. Hydroxide-Alkoxide
Hydrothermal Synthesis	Hydroxides

The perovskite oxides prepared by coprecipitation methods have higher surface areas: up to 10 m^2/g irrespectively of the precipitating agent [26].

The sol-gel process is the most widely used technique where gel is produced by the aging of the colloidal sol. Mixed-metal oxides can be synthesized by the sol-gel technique using a mixture of two metal alkoxides, a mixture of metal salt and metal alkoxide, or a mixture of metal hydroxide and metal alkoxide. The final crystalline products are obtained by calcination of the dried gels. These materials have homogeneous composition and high surface areas. These mixed-metal oxides can segregate during calcination to produce a mixture of two separate phases (V_2O_5-TiO_2, SiO_2-TiO_2, and Nb_2O_5-TiO_2) or form one chemical phase ($MgTiO_3$, $CaTiO_3$, $SrTiO_3$, and $BaTiO_3$). The alkaline-earth metal titanates do not segregate and consist of one perovskite phase during synthesis or calcination.

Vanadia-titania mixed oxides were synthesized by the aerogel process with a nominal loading of V_2O_5 up to 30 wt% and surface areas up to 200 m^2/g [27]. The vanadium phase was uniformly distributed in the titania aerogel. The advantages of this aerogel catalyst included a higher possible loading of vanadia in comparison with traditional preparation methods and higher reaction rates per catalyst weight.

Silica-titania aerogels also suffered from phase segregation [28]. The pore structure consisted of mesopores and macropores with a pore size distribution up to 60 nm and specific pore volume of 3.6 cm^3/g. This oxide has interesting physical and chemical properties including acoustic impedance matching, transparency, thermal insulation and low coefficients of thermal expansion [29, 30].

Niobia-titania aerogel was synthesized by the hydrolysis of niobium (V) pentaethoxide and titanium (IV) tetrabutoxide in methanol [31]. The prepared samples with low concentration of titania were amorphous, while titania-rich samples segregated and contained poorly crystalline anatase.

Metal titanates of magnesium ($MgTiO_3$), calcium ($CaTiO_3$), strontium ($SrTiO_3$), and barium ($BaTiO_3$), were synthesized by the sol-gel technique by interaction of titanium (IV) n-butoxide ($Ti(OC_4H_9)_4$) with a nitrate salt of Mg, Ca, Sr, or Ba metal ($M(NO_3)_2$) in alcoholic solution at room temperature [32]. High-purity crystalline titanates were produced by calcination of the obtained amorphous gels at temperatures 700 – 900ºC.The surface area for $SrTiO_3$ was 40.8, $BaTiO_3$ – 7.3, $MgTiO_3$ – 2.2, and $CaTiO_3$ – 0.9 m^2/g respectively. Inhomogeneity in the

chemical composition of the titanates was caused by the difference in the precipitation speed of the precursor salt and alkoxide.

Magnesium titanate has many interesting properties and can be used for many applications. $MgTiO_3$ is widely used in low cost capacitors, high-frequency capacitors and temperature-compensating capacitors due to its dielectric properties [33]. Contrarily to other alkaline-earth metal titanates, conventionally prepared magnesium titanate has an ilmenite structure instead of the perovskite structure. Ilmenite can be transformed into the perovskite structure at very high pressure (40GPa) [34]. In ilmenite, the $MgTiO_3$ structure has octahedral coordination of magnesium and titanium with oxygen atoms and consists of alternative layers of magnesium and titanium octahedra. While in the perovskite structure, the structure consists of the TiO_6 octahedra layers and 12-fold coordinated Mg. The conventional magnesium titanate synthesis includes the solid-state reaction between MgO and TiO_2 at high temperature (1400ºC) [35]. The obtained product powders have relatively large particle sizes and high concentration of impurities contaminated by the grinding media and not-fully reacted precursors. Wet chemical methods allow synthesizing more pure $MgTiO_3$ powders at lower reaction temperatures. The coprecipitation of Mg/Ti from the sulfuric solution by the reaction with sodium hydroxide at room temperature and following calcination at 600ºC gave a pure $MgTiO_3$ product [36]. In addition, magnesium titanate powders were prepared by the peroxide method [37] and sol gel process [38, 39].

Calcium titanate, with its perovskite structure, has interesting refractory, chemical resistance and n-type semiconductor properties (band gap of 3.5 eV) [40, 41]. Traditionally, calcium titanate is prepared by the solid-state reaction of calcium carbonate ($CaCO_3$) and titanium oxide at a temperature above 1300ºC [42]. The calcination at high temperature caused a significant porosity decrease due to sintering.

Several wet chemical methods for the synthesis of $CaTiO_3$ with lower temperatures are known. Precipitated calcium titanyl oxalate was thermally degraded at 600ºC to produce calcium titanate [43]. An aqueous slurry of calcium oxide and hydrated titanium gel was prepared at 150-200ºC in an autoclave to produce fine particles of $CaTiO_3$ consisting of 0.1-0.5 μm size crystallites by the hydrothermal method [44]. High-purity $CaTiO_3$ was synthesized using the peroxide method [45, 46]. Calcium chloride ($CaCl_2$), titanium chloride ($TiCl_4$), hydrogen peroxide (H_2O_2) and ammonia (NH_4OH) were mixed together to prepare the $CaTiO_2(O_2)\cdot 3H_2O$

precursor which gave $CaTiO_3$ powder during calcination at 800ºC. It was possible to use titanium tetraisopropoxide instead of $TiCl_4$ [47]. Similar peroxide methods were used to synthesize $BaTiO_3$ and $SrTiO_3$ powders [48, 49].

Mixed calcium strontium titanate ($Ca_{1-x}Sr_xTiO_3$) was prepared by the Pechini method using calcium and strontium carbonates, tetraisopropyl orthotitanate, ethylene glycol, and citric acid [50]. The solvent was evaporated first, and the sample was calcined at 850ºC.

$CaTiO_3$-based oxides ($Ca_{1-x}Sr_xTi_{1-y}MyO_{3-\delta}$, M=Fe, Co, Cr or Ni, x = 0-1, y = 0-0.6) were synthesized by a modified sol-gel method using citrate [51]. Substitution with 10% Sr for Ca-sites in calcium titanate and substitution of Ti-sites with lower valent metal ions of iron, cobalt, chromium, or nickel, were performed to increase the electrical and ionic conductivity. This method still requires high temperature of 900ºC and gives a powder with small surface area of 20 m^2/g and big crystallite sizes.

Calcium titanate powder was studied and found active for the decomposition of water into hydrogen and oxygen under UV light irradiation [52]. This powder was prepared by the hydrothermal method. Particles were in the range of 0.1 - 0.4 μm and surface area was 11 m^2/g. Besides, powder was impregnated with noble metal (Pt, Au, Ir, or Ru) co-catalyst to separate the holes and electrons and increase production of H_2 and O_2.

Strontium titanate is a perovskite with a cubic structure whose dielectric constant increases upon cooling [53]. Non-stoichiometric or doped n-type semiconducting $SrTiO_3$ is used as a dielectric and photoelectric material [54]. Conventionally, strontium titanate is synthesized by the solid-state reaction between strontium carbonate and titanium oxide at temperatures above 1000°C [55].

Wet chemical methods give pure strontium titanate phase at lower temperatures. $SrTiO_3$ was prepared by the thermal decomposition of $SrTiO(C_2O_4)_2{\cdot}4H_2O$ precursor [56] or controlled hydrolysis of strontium titanium carboxylates [57].

Application of the sol-gel process gives high-purity, homogeneous, stoichiometric and ultrafine strontium titanate [58]. Strontium acetate and titanium isopropoxide were hydrolyzed to form a gel which was dried at 110ºC first and then calcined at 900ºC. After calcination, particles sizes were up to 500 nm and surface area of 20 m^2/g.

Nanosized powders of $SrTiO_3$ with the size of crystallites in the range of 5 - 13 nm were synthesized by gel to crystallite conversion [59]. The prepared material was found photocatalytically active for the mineralization of phenol.

Barium titanate is a dielectric material with good dielectric properties such as high dielectric constant, small dielectric loss, low leakage current, and large dielectric breakdown strength. It is a ferroelectric perovskite with Curie temperature T_c at 123ºC [60]. In this material, the ferroelectric and dielectric properties critically depend on the particle sizes [61, 62]. Different methods have been used for the barium titanate synthesis including hydrothermal [63], microemulsion [64], hydrolytic decomposition [65], precipitation from solutions [66], gas-condensation process [67], and sol-gel methods [68].

Barium titanate particles in the range from 10 nm to 1.5 μm were prepared by thermal decomposition of polymeric barium titanate methacrylate [70]. The precursor was obtained from the reaction of metallic barium, titanium isopropoxide and methacrylic acid in boiling methanol. The $BaTiO_3$ product was obtained by the pyrolysis of the precursor at different temperatures and oxidative atmospheres. High temperature (1350ºC) and oxidative atmosphere (O_2) causes production of big particles, while at lower temperature (600ºC) and inert atmosphere (N_2) smaller particle sizes were obtained.

Mixed strontium barium titanate was synthesized using a spark plasma sintering technique from a mixture of barium and titanium titanates [71]. The $Ba_{0.6}Sr_{0.4}TiO_3$ structure consisted of grain size of 1-3 μm surrounded by submicron barium titanate and strontium titanate grains. This technique gives ceramics with reduced dielectric losses and a significant diffuse transition in permittivity. However, it gives inhomogeneous composition and requires high pressure (50 MPa) and temperature (1100°C).

Also, barium strontium titanate (BST) was synthesized by a sol-gel technique to give $Ba_xSr_{1-x}TiO_3$ in the range of x = 0 to 1.0 [72]. The synthesis includes drying of the mixture of the barium acetate, strontium acetate, and titanium isopropoxide in dehydrated acetic acid at 90°C. After that, the white solid was ground and calcined at 1000°C.

1.2 Advantages of nanosized titanates

The unique properties of nanosized materials are determined by surface structures and sizes. High surface areas and small sizes can lead to unexpectedly new or different properties of the material [72, 73]. Nanomaterials are defined as nanostructured or nanoparticulate materials with sizes up to 100 nm. These materials are intermediates between single atoms and crystalline solids, single elements and single crystalline structures.

Currently, researchers in chemistry, physics, biochemistry, and engineering are exploring a new class of nanosized materials for applications in electronics, optics, catalysis, and for solar light conversion [74]. Size effects and processes for the synthesis of solids with desired size, shape and surface structure are currently being examined. For now, a growing knowledge in nanocrystals research allows the production of different materials at the nanometer scale, a better understanding of their properties, and control of their synthesis.

The novel and unique properties of nanomaterials are a result of the finite-size effect when the electronic bands are converted into molecular orbitals with the decrease in particle sizes. In nanoparticles, a high number of particle atoms are located on the surface of the grains or interface boundaries, which is why the physical and chemical properties of nanomaterials are different from the isolated atoms or bulk materials.

One of the specific properties of nanomaterials is the surface-to-volume ratio. This size-dependent effect includes a high percentage of surface atoms. The high distribution of electrons confines the quantized energy levels. This quantum confinement is used in semiconductors and optoelectronics. A high percentage of surface atoms lead to an increase in surface activity. In addition, the highly exposed surface stimulates the chemical reactions and promotes the catalysis.

The semiconductor nanoparticles have interesting optical properties that are different from the bulk. With the decrease in sizes, the spacing between energy levels becomes larger and the absorption band progressively shows a blue shifting. In addition, these nanoparticles can exhibit non-linear optical properties caused by the dependence of material induced polarization on the intensity of the incident light.

The electric properties of the nanomaterials also change with size decreases [75]. The electrical conductivity within nanoparticles decreases with the transition from the electronic band

structure of the bulk into separate molecular orbitals. Small sizes of nanoparticles can affect the sintering or miscibility properties of the material. The sintering of nanomaterials or achieving homogeneity of the phase requires relatively lower temperatures.

The surface area increase and particle size decrease can influence chemical properties of nanoparticles. Catalysis, sensing, adsorption, and separation processes are size and surface dependant. In heterogeneous catalysis, chemical reactions have traditionally higher reaction rates with the smaller particle sizes.

Several special methods are known for the synthesis of nanomaterials [76]. Milling, using mechanical attrition, can produce small particles from the bulk material. The drawback of this method includes the non-uniform size and shapes of obtained particles and severe contamination with the milling media (hardening steel or tungsten carbide in ball mills).

Nanosized materials can be synthesized using gas-phase reactions such as aerosol, chemical vapor deposition (CVD), solvated metal atom dispersion method (SMAD) or others. The aerosol process gives solid nanoparticles by heat treatment of the dispersed droplets of precursor [77]. SMAD technique is mainly used to prepare wide array of metal nanoparticle (Au, Ag, Cu, Pd, and others) by the metal vaporization and trapping of metal particles in the frozen organic solvent matrix [78].

The most common synthesis approach for the synthesis of nanoparticles involves the wet chemical method such as microemulsions, sol-gel, aerogel and other techniques. In microemulsion, each droplet is a small nanosized reactor where small nanoparticles can be synthesized. In sol-gel technique, small sol particles are formed first and then aggregate to form gel network of particles with uniform size and shape. Supercritical drying of the solvent preserve the network structure from collapse and the bulk from the densification.

1.3 Possible applications

High purity perovskite oxide powders are widely used for the preparation of electronic components, electro-optical and photocatalytic materials.

Their possible photocatalytic applications include

1. Oxidation and hydrogenation [79-80],
2. Photocatalytic surfaces (films, coated metals, laminated composite materials),

3. Antifouling and antibacterial materials (fibers, sanitary clothes, uniforms, mops),
4. Photocatalytic decomposition of NO_x and SO_x for sound-absorbing walls on highways,
5. Odor elimination (air purifier fans, vacuum cleaners, dishwashers, garbage disposers),
6. Decomposition of water and dioxin [81],
7. Photocatalytic self-cleaning glass windows and plasma screens.

Their possible electronic applications include

1. Dielectric devices (flexible film capacitors, dielectric bolometers, IR focal plane arrays) [82-85],
2. High-permittivity thin films (DRAMs, pyroelectric sensors, gas detection sensors) [86],
3. Superconducting microwave tunable devices, tunable phase shifters, and ring resonators [87, 88],
4. Acoustic imaging arrays (real-time acoustic cameras for underwater divers, medical imaging, and acoustic microscopy) [89].

Titanate ceramics are used in capacitors, piezoelectric ceramics, and PTCR (positive temperature coefficient resistors). Barium titanate is the main dielectric material component of ceramic capacitors. $SrTiO_3$ has applications as a dielectric and photoelectric material. Owing to its high dielectric permittivity that increases on cooling and to its low microwave losses, $SrTiO_3$ is an attractive material for many high-frequency and MW applications, particularly at low temperatures. Strontium titanate photocatalyst has a possible application in water electrolysis, hydrogen production, toxic water remediation, and in organic synthesis [90, 91].

The excellent dielectric properties of $Ba_xSr_{1-x}TiO_3$ dielectric material make it useful for a wide range of applications, including phase shifters, phased array antennas, thermistors, and pyroelectric detectors [92].

To summarize, the variety of applications for alkaline-earth metal titanate perovskites makes them the subject of intense investigations. Different production methods of titanate are available and depend on the required textural and industrial characteristics. The solid-state method is widely used for the production of cheap bulk titanates. However, growing demands for high-pure, homogeneous and nanosized titanate move the research investigations toward wet chemical methods and synthesis of nanosized titanate powders by the sol-gel process and aerogel process.

1.4 References

[1] J. Parker, in: Nanoscale Materials in Chemistry, K. J. Klabunde (Ed.), Wiley Interscience, New York, 2001, pp. 279-285.

[2] H. Kato and A. Kudo, J. Phys. Chem., B 106 (2002) 5029.

[3] T. R. N. Kutty and M. Avudaithai, Catal. Rev.-Sci. Eng., 34 (1992) 373.

[4] J. M. Kesselman, A. Kumar, and N. S. Lewis, in: Photocatalytic Purification and Treatment of Water and Air, D. F. Ollis, H. Al-Ekabi (Eds.), Elsevier, Amsterdam, New York, 1993, pp. 19-37.

[5] O.D. Velev, T.A. Jede, R.F. Lobo, and A.M. Lenhoff, Nature, 1997, 389, 448.

[6] J.E.G.J. Winjnhoven and W.L. Vos, Science, 1998, 281, 802.

[7] B.T. Holland, C.F. Blanford, and A. Stein, Science, 1998, 281, 538.

[8] M. Schneider and A. Baiker, Catalysis Today, 35 (1997) 339-365.

[9] G.C. Bond and S.F. Fischer, Appl. Catal., 71 (1991) 1.

[10] H. Knözinger and E. Taglauer, Catalysis (London), 10 (1993) 1.

[11] H. Nagamoto, K. Amanuma, H. Nobutomo, and H. Inoue, Chem. Lett., (1988) 237.

[12] Y. Inoue, H. Sano, and K. Sato, J. Mater. Sci. Lett., 8 (1989) 17.

[13] R.J.H. Voorhoeve, J.P. Remeika, P.E. Freeland, and B.T. Matthias, Science, 277 (1972) 352.

[14] H.M. Zhang, Y. Shimizu, Y. Teraoka, N. Miura, and N. Yamazoe, J. Catal., 121 (1990) 432.

[15] D. Demydov and K.J. Klabunde, Journal of Non-Crystalline Solids, 350 (2004) 165 -172.

[16] S. Teichner, G.A. Nicolaon, M.A. Vicarini, and G.E.E. Gardes, Advances in Colloid and Interface Science, 5 (1976), 245-273.

[17] J. Ravez, L'Actualité Chimique 11 (1986) 164.

[18] D.V. Demydov and K.J. Klabunde, in Nanostructured and Advanced Materials, Vaseashta, A.; Dimova-Malinovska, D.; Marshall, J.M. (Eds.), Proceedings of the NATO Advanced Study Institute, held in Sozopol, Bulgaria, 6-17 September 2004, Series: NATO Science Series II: Mathematics, Physics and Chemistry, Vol. 204.

[19] H. Kato and A. Kudo, J. Phys. Chem. B, 106 (2002) 5029-5034.

[20] D.R. Uhlman, J.M. Boulton, G. Teowee, L. Weisenbach, and B.J.J. Zelinski, Sol-Gel Optics I, Proc. SPIE, Vol. 1328, (1990) p. 270.

[21] R.J.H. Voorhoeve, Advanced Materials in Catalysis, Academic Press, New York, 1977.

[22] H. Arai, T. Yamada, K. Eguchi, and T. Seiyama, Appl. Catal., 36 (1986) 265.

[23] R.J. Voorhoeve, J.P. Remeika, and L.E. Trimble, Ann. N.Y. Acad. Sci., 272 (1976) 3.

[24] T.R. Shrout and A. Halliyal, Am. Ceram. Soc. Bull., 66 (1987) 704.

[25] P. Padmini and T.R.N. Kutty, "Wet Chemical Syntheses of Ultrafine Multicomponent Ceramic Powders through Gel to Crystallite Concversion," J. Mater. Cem., 4 (1994) 12, 1875-1881.

[26] J.M.D. Tascón, S. Mendioroz, and L.G. Tejuca, Z. Phys. Chem., Wiesbaden, 124 (1981) 109.

[27] A. Baiker, B. Handy, J. Nickl, M. Schraml, and A. Wokaun, Catal. Lett., 14 (1992) 89.

[28] D.C.M. Dutoit, M. Schneider, and A. Baiker, J. Catal., 153 (1995) 165.

[29] G. Cogliati, M. Guglielmi, T.M. Che, and T.J. Clarc, Mater. Res. Soc. Symp. Proc., 180 (1990) 329.

[30] M. Beghi, P. Chiurlo, L. Costa, M. Palladino, and M.F. Pirini, J. Non-Cryst. Solids, 145 (1992) 175.

[31] S.M. Maurer, D. Ng, and E.I. Ko, Catal. Today, 16 (1993) 319.

[32] J. Moreno, J.M. Dominguez, A. Montoya, L. Vicente, and T. Viveros, J. Mater. Chem., 5 (3) 509-512.

[33] G. Pfaff, Ceramics International, 20 (1994) 11-116.

[34] B.B. Karki, W. Duan, C.R.S Da Silva, and R.M. Wentzcovitch, American Mineralogist, 85 (2000) 317-320.

[35] B. Wechsler and A. Navrotsky, J. Solid State Chem., 55 (1984) 165-80.

[36] M.P. Baura-Pena, M.J. Martinez-Lope, and M.E. Garcia-Clavel, J. Mater. Sci., 26 (1991) 4341-3.

[37] V. Parvanova and M. Maneva, Godishnik na Visshiya Khimikotekhnologicheski Institute, Sofia, 31 (1997) 4, 86-93.

[38] M.I. Yanovskaya, N.V. Golubko, and E.A. Nenasheva, Neorganicheskie Materialy, Moscow, 32 (1996) 2, 201-3.

[39] J.C. Bernier, S. Vilminot, J.L. Rehspringer, S. El Hadigui, and P. Poix, in High Tech. Ceramics (ed. P. Vincenzini), Elsevier Science Publishers, Amsterdam, 1987, 1443-50.

[40] G.A. Cox and E.V. Tredgold, "Brit. J. Appl. Phys., 18 (1967) 37-40.

[41] U. Balachandran, B. Odekirk, and N.G. Eror, J. Solid State Chem., 41 (1982) 185-94.

[42] L.I. Verba and E.V. Degtyareva, Izv. Akad. Nauk USSR-Neorg. Mater., 11 (1975) 1622-5.

[43] G. Pfaff, F. Schmidt, W. Ludwig, and A. Feltz, J. Thermal Anal., 33 (1988) 71-9.

[44] T.R.N. Kutty and R. Vivekanandam, Mater. Lett., 5 (1987) 79-83.

[45] M. Murata and A. Kitao, Preparation of titanates. US Patent Number 4 061 583, April 1976.

[46] G. Pfaff, Z. Chem., 29 (1989) 30-1.

[47] Z.Z. Yang, H. Yamada, and G.R. Miller, Am. Ceram. Soc. Bull., 64 (1985) 1550-4.

[48] G. Pfaff, Z. Chem., 28 (1988) 76-7.

[49] G. Pfaff, J. Eur. Ceram. Soc., 9 (1992) 4, 293-9.

[50] A.G. Andersen, T. Hayakawa, T. Tsunoda, H. Orita, M. Shimizu, and K. Takehira, Catalysis Letters, 18 (1993) 37-48.

[51] K.A. Muller and H. Burkard, Phys. Rev. B, 19 (1979) 3593.

[52] H. Mizoguchi, K. Ueda, M. Orita, S.–C. Moon, K. Kajihara, M. Hirano, and H. Hosono, Mater. Res. Bull., 37 (20002) 2401-2406.

[53] H.P. Roaksby and H.D. Megaw, Nature (London), 155 (1945) 484.

[54] I. Burn and S. Neirmann, J. Mater. Sci., 17 (19820 3510.

[55] H. Tagawa, K. Kimura, T. Fujino, K. Ouchi, and Denki Kaguku, J. Electrochem. Soc. Jpn., 52 (1984) 154.

[56] P.K. Gallagher, F. Schrey, and F.V. DiMarcello, J. Am. Ceram. Soc., 46 (1963) 359.

[57] R.E. Riman, R.R. Landham, and H.K. Bowen, J. Am. Ceram. Soc., 72 (1989) 821.

[58] G. Pfaff, J. Mater. Chem., 3 (1993) 7, 721-724.

[59] S. Ahuja and T.R.N. Kutty, J. Photochemistry and Photobiology, A: Chemistry, 97 (1996) 1-2, 99-107.

[60] W.L. Zhong, Y.G. Wang, P.L. Zhang, and B.D. Qu, Phys. Rev. B, 50 (1994) 698.

[61] S. Wada, T. Suzuki, and T. Noma, Jpn. J. Appl. Phys., 34 (1995) 5368.

[62] T.R.N. Kutty and R. Vivekanadan, Materials Chemistry and Physics, 19 (1988) 533-546.

[63] H. Kumazawa, T. Kagimoto, and A. Kawabata, J. Mater. Sci., 31(1996) 2599.

[64] H. Herrig and R. Hempelmann, Ibid., 9 (1997) 241.

[65] S. Lu, H. Liu, Y. Han, L. Zhang, and X. Yao, Ferroelectrics, 197 (1997) 45.

[66] R.W. Schwartz, Chem. Mater, 9 (1997) 2325.

[67] S. Li, J.A. Eastman, L.J. Thompson, C. Bjormander, and C.M. Foster, Mater. Res. Soc. Symp. Proc., 457 (1997) 45.

[68] R.N. Viswanath and S. Ramasamy, Nanostruct. Mater., 8 (1997) 155.

[69] H.-J. Gläsel, E. Hartmann, D. Hirsch, R. Böttcher, C. Klimm, D. Michel, H.-C. Semmelhack, J. Hormes, and H. Rumpf, Journal of Material Science, 34 (1999) 10, 2319-2323.

[70] B. Su, J.Y. He, B.L. Cheng, T.W. Button, J. Liu, Z. Shen, and M. Nygren, Integrated Ferroelectrics, 61 (2004) 117-122.

[71] S.-Y. Kuo, W.-Y. Liao, and W.-F. Hsieh, Physical Review B, Volume 64, 224103.

[72] R. Rosseti, S. Nakahara, and L.E. Brus, J. Chem. Phys., 1983, 79 (2), 1086.

[73] L.E. Brus, J. Chem. Phys., 1984, 80 (9), 4403.

[74] A. Zunger, S. Wagner, and P.M. Petroff, J. Electronc. Mater., 1993, 22(1), 3.

[75] L.E. Brus, J. Chem. Phys. 1984, 80 (9), 4403.

[76] A.S. Edelstein and R. C. Cammarata (Eds.), Nanomaterials: Synthesis, Properties and Applications, Institute of Physics Publisher, Bristol, 1996.

[77] A. Gurav, T. Kodas, T. Pluym, and Y. Xiong, Aerosol. Sci. Technol., 19 (1993) 411-452.

[78] K.J. Klabunde and C. Mohs, in Chemistry of Advanced Materials, Wiley-VCH, New York, 1998, pp.271-328.

[79] R.J.H. Voorhoeve, Advanced Materials in Catalysis, Academic Press, New York, 1977.

[80] L.G. Tejuca, J.L.G. Fierro, and J.M.D. Tascón, Adv. Catal., 36 (1989) 237.

[81] H. Arai, T. Yamada, K. Eguchi, and T. Seiyama, Appl. Cat., 36 (1986) 265.

[82] K. Ravindranathan Thampi, M. Subba Rao, W. Schwartz, M. Grätzel, and J. Kiwi, J. Chem. Soc., Faraday Trans., 1 (1988) 84, 1703.

[83] T. Horikawa, N. Mikami, H. Ito, Y. Ohno, T. Makita, and K. Sato, IEICE Trans. Electron., E77 (1994) 385.

[84] A.T. Findikoglu, Q.X. Jia, D.W. Reagor, and X.D. Wu, Microwave Opt. Technol. Lett., 9 (1995) 306.

[85] A. I. Kingon, S.K. Striffer, C. Basceri, and S.R. Summerfelt, Mater. Res. Bull., 21 (1996) 7, 46.

[86] L.C. Segnupta, E. Ngo, J. Synowezynski, and S. Sengupta, Proceedings of the 10th IEEE International Symposium on Applied Ferroelectrics (IEEE, New York, 1996), p. 845.

[87] C. Hanson and H. Bertran, Proceedings of the 9th IEEE International Symposium on Applied Ferroelectrics (IEEE, New York, 1995), p. 657.

[88] B. Su and T.W. Button, J. Euro. Ceram. Soc., 21 (2001) 2641-2644.

[89] A. Amin, J. Electroceramics, 8 (2002) 99-106.

[90] D.F. Ollis, E. Pelizzetti, N. Serpone, in Photocatalysis: Fundamentals and Applications, N. Serpone and E. Pelizzeti (eds.), John Wiley & Sons, New York, 1989, 603.

[91] F. Williams and A.J. Nozik, Nature, 271 (1978) 137.

[92] R. Naik, J.J. Nazarko, C.S. Flattery, U.D. Venkateswaran, V.M. Naik, M.S. Mohammed, Physical Review B, 61 (2000) 17, 11367.

Chapter 2 : Synthesis of titanates

2.1 Introduction

There are three main steps in the development of new titanate materials: synthesis of titanates, their property characterization, and application. This chapter offers the discussion of the available methods for the synthesis of titanates. The synthesis and characterization of titanates will be presented and discussed in Chapter 3. Property studies applications of synthesized titanates will be investigated and discussed in Chapters 4, 5, 6, and 7.

For a long time, solid materials were produced with traditional techniques that did not allow synthesis control and desirable textural properties. The novel techniques presented in this dissertation allow the production of solids with controllable size and shape. These materials can be produced with well-defined structure and morphology.

2.2 Preparation of titanates

To design a new method for the synthesis of new materials in oxide chemistry, we explored the traditional synthetic methods in this field. The majority of oxide ceramics and powders have been synthesized by high temperature solid state reactions, and oxide films and coatings have been made by deposition from gas phase reactions. With such techniques as solid state reaction or chemical vapor deposition, researchers may have difficulties controlling particle size, shape, and size distribution. In these methods, the process requires high temperatures for the reaction of the precursors as solids or in gas phase.

In comparison with traditional methods, wet chemical techniques such as sol-gel, colloidal or cluster solutions, the synthesis of particles and the material structure can be controlled. Solvent plays an important role, while the process requires lower temperatures. Control of the synthesis can be achieved by mixing different precursors, choosing the right solvent, monitoring the nucleation, following stoichiometric ratio, and by using appropriate ligands.

2.2.1 Solid-state reaction

Different inorganic solids can be synthesized through the reaction of a solid with another solid ("solid/solid" reaction), a liquid (melt) or a gas ("solid/gas" reaction) at high temperature. Also, solids can turn into melt or gaseous intermediates through the ongoing reaction. Solid/solid reaction aka ceramic method has been widely applied for the production of oxides for a long time. The combination of solid and gaseous reactants gives a better contact between them in comparison to that between just two solids.

The ceramic method is the oldest method for the synthesis of solid-state materials [1]. High temperatures are required for solids to react with each other. The advantages of this method include low cost of production, available precursors, and simplicity of the processes. The shortcomings include formation of undesirable phases, nonhomogeneous distribution of dopants, and a difficulty in monitoring the reaction progress. High temperatures in this method require the application of chemically inert materials as containers (platinum, silica, stabilized zirconia, and alumina).

The reaction goes through the formation of product nuclei at the interface of the solids. The growth of the product layer slows down the counter diffusion of ions from the reacting solids to each other and decreases the rate of the reaction. Only very high temperatures provide enough energy for ions to diffuse through. To maximize the reaction rates, the starting precursors need to be well ground to increase surface areas and contact between particles.

The solid-state reaction depends on the reactivity of the starting precursors. The final oxide products can be produced by the oxidation of precursors by oxygen from the air or by the reaction during the decomposition of the precursor compounds. For example, the mixed-metal oxide of yttrium, barium, and cupper ($YBa_2Cu_3O_{7-x}$) can be prepared by the heating of a mixture of yttrium oxide (Y_2O_3), barium peroxide (BaO_2), and cupric oxide (CuO) and reacting with oxygen from the air. Moreover, $YBa_2Cu_3O_{7-x}$ (YBCO) can be synthesized using barium carbonate ($BaCO_3$) as the source of barium. In this case, barium carbonate decomposes at high temperature and gives highly reactive barium oxide (BaO). Other precursors that can decompose at a high temperature and can be used for solid-state reactions are oxy salts (citrates, acetates) or nitrates.

The $YBa_2Cu_3O_{7-x}$ oxide is a well known supercoductor (-181ºC) and has a structure similar to a perovskite structure. In YBCO, three perovskite (ABO_3) unit cells are stacked above each other. Barium ions in the II oxidation state and yttrium ions in the III oxidation state are sharing the B^{4+} sites (Figure 2.1). Copper ions are equally in the II and III oxidation states and occupy the A^{2+} sites in the unit cell. The oxygen deficiency in this material is derived from the presence of oxygen vacancies in the lattice to maintain the charge balance.

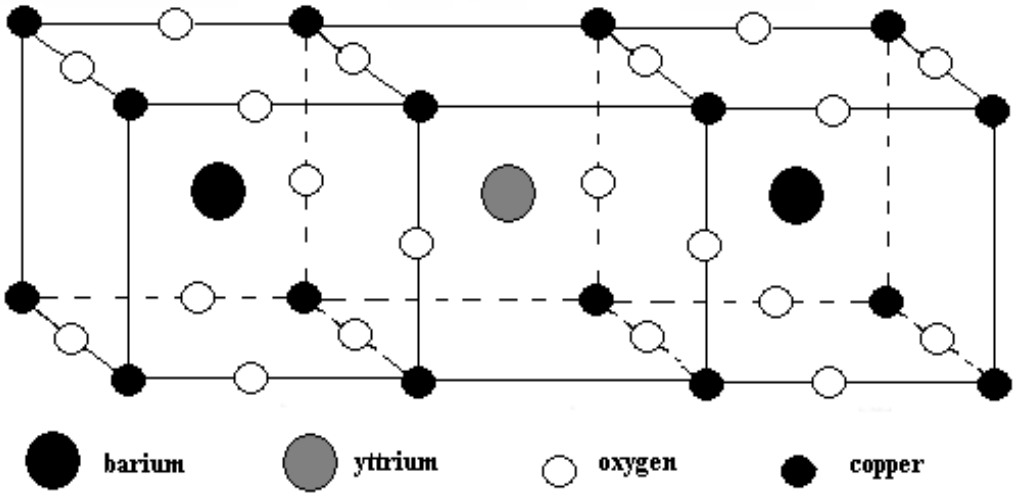

Figure 2.1 Unit Cell of $YBa_2Cu_3O_{7-x}$ Oxide

Barium titanate can be produced by the solid-state reaction of barium carbonate ($BaCO_3$) and titanium oxide (TiO_2). Barium carbonate decomposes into barium oxide (rock salt structure) that reacts with the titanium oxide (rutile structure). BaO reacts with titanium oxide to form an intermediate Ba-rich layer of the Ba_2TiO_4 phase. This phase allows the migration of Ba ions from the BaO phase into the TiO_2 phase to form the $BaTiO_3$. During synthesis of barium titanium, other undesirable phases can be produced such as $BaTi_2O_5$. The same approach can be used for the synthesis of other mixed metal oxides; however, the reactions between two solids may not occur due to unfavorable thermodynamic conditions (slow reaction rates, slow diffusion, or very high temperatures).

There are several other ways to synthesize mixed metal oxides through the heating and decomposition of the solid precursors that contain metal cations in an intimately mixed atomic dispersion. Different metal oxides can be synthesized by coprecipitation or precursor methods [2]. The cations are closer to each other so lower temperatures are required for the decomposition of precursors.

In the coprecipitation method, the precipitate of two salts of different metal cations from the solution is heat-treated to give the oxide products. Metal salts (carbonates, oxalates, formates, or citrates) are dissolved in water and coprecipated by the concentration of the solution.

Solid solutions of carbonates are coprecipated first and then heat treated to produce corresponding metal oxides:

$$(1\text{-}x)\ MCO_3 + x\ M'CO_3 \rightarrow M_{1-x}M'_x(CO_3) \rightarrow M_{1-x}M'_xO \qquad (2.1)$$

where M, M' are metals such as Mg, Ca, Sr, Ba, Zn, Cd and some others.

In the precursor method, the two different metal cations are incorporated in the same solid precursor. For example, barium titanate can be synthesized by slowly heating of the mixed-metal barium titania citrate $Ba[TiO(C_2O_4)_2]$ in air to burn off the organic matter. This method gives products with higher purity and more accurate stoichiometry in comparison with other ceramic methods. However, all oxide products synthesized by ceramic methods have a dense structure, big particle sizes, and small surface areas. The solid-state preparation of oxides requires repeated cycles of milling and calcination at high temperatures. The resulting powders from this preparation are agglomerated crystallites of different sizes and contain impure phases due to incomplete reactions [3, 4]. These disadvantages can be overcome by using other methods, as discussed below.

2.2.2 Gas phase reaction

It is also common to use gaseous precursors or intermediates for solid material production. Several techniques are used for synthesis of solid products from the gas phase, including chemical transport, chemical vapor deposition (CVD), and aerosol methods.

The chemical transport technique is mainly used for crystal growth and for the purification of solids. The purification is achieved by the reaction of a solid (A) with a gaseous agent (B), transportation of a gaseous product (AB), and following decomposition back to solid (A) and gaseous agent (B) (Figure 2.2).

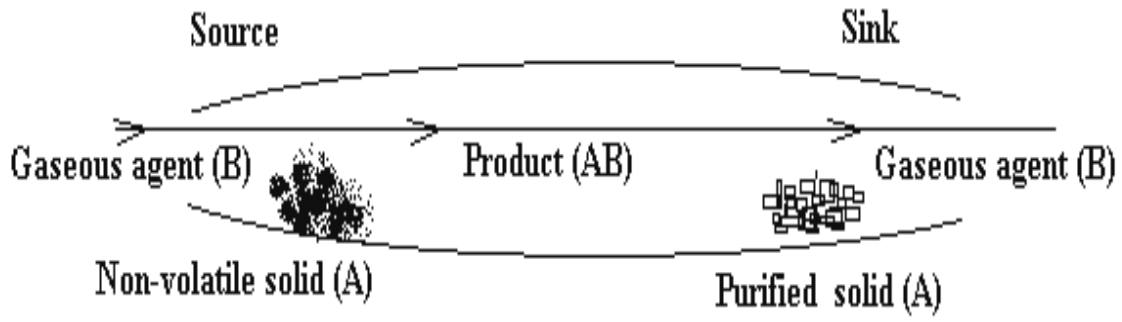

Figure 2.2 Principal Scheme for Chemical Transport (Adapted and Modified from Reference 5)

A non-volatile solid (A) reversibly reacts with a transport gaseous agent (B), and the equilibrium constant of this reaction is temperature dependent. Diffusion transportation from one site (the source) to another (the sink) is achieved by different temperatures by changing the temperature gradient for the AB product. The chemical equilibrium shifts from the product AB at the source site to A and B at the sink site.

Chemical transport can be applied for the synthesis of new compounds also if the transport reaction is followed by an additional reaction at the sink site. Transport of metal oxides (for example chromium oxide) is achieved by the use of a mixture of halides and water as transport agents.

Chemical Vapor Deposition (CVD) is a method for the preparation of thin films and coatings for a variety of inorganic materials. Solid thin films of different materials, including oxides, can be deposited on the substrate [5]. The formation of a material for the film occurs at significantly lower temperatures than its melting temperature, which is why this technique is intensively used on an industrial scale for hard coatings such as those on cutting tools or engine

parts [6]. CVD is also used to make three-dimensional microelectronic components, coatings on glass, and catalyst coatings on the support material, layers in solar cells.

In the CVD process, vapor phases of volatile precursors react on a heated substrate in the reaction chamber and the films of new materials are produced. Precursors go through adsorption onto the substrate surface, and the following chemical reaction leads to the deposition of a solid film. These films of metal oxides are mainly produced for dielectric and optical purposes. CVD is widely used for the deposition of oxide films (TiO_2, SnO_2, or SiO_2) on glasses. Besides, coatings and layers of oxides are used in solar cells, membranes and catalysts.

The most common precursors are metal hydrides (SiH_4), metal alkoxides ($Si(OEt)_4$), metal alkyls (Al^iBu_3, $GaEt_3$), and volatile metal halides ($TiCl_4$) in the presence of the oxygen source (O_2, N_2O, or water). The application of organometallic precursors is more preferable as they are more volatile than the inorganic ones. However, the organometallic precursors are less thermally stable; they can decompose and contaminate the product.

Several individual metal precursors can be decomposed together to produce mixed-metal oxide films. However, it is difficult to keep the stoichiometry in these films. In this system, precursors and intermediates have different volatilities and reactivity, and this causes the excess of one precursor and the deficiency of another on the surface of the substrate. For example, a lead deficient material is produced by CVD during the synthesis of lead titanate ($PbTiO_3$). The deficiency is caused by higher volatility of the lead oxide (PbO) and its higher desorption rate from the surface of the substrate.

The formation of the mixed metal oxide films can be achieved also by the use of a precursor which has all required elements for the product in the stoichiometric ratio. This is simplifying the delivery system of the precursor. However, in this case, precursors have higher molecular weights, and they are less volatile.

Silicon oxide (SiO_2) films produced by CVD are widely used in electronics for insulation and passivation layers. These layers separate and protect semiconductor layers in microcircuit electronic devices. The application of silicon alkoxides (tetraalkoxysilane, TEOS) as the precursor gives the SiO_2 growth without an external oxygen source by the decomposition of alkoxides:

$$Si(OEt)_4 \rightarrow SiO_2 + 2\ C_2H_4 + 2\ EtOH \qquad (2.2)$$

The formation of the Si-O-Si bond goes through the reaction of the silanol groups with TEOS and the release of ethanol:

$$(EtO)_3Si\text{-}OEt \rightarrow (EtO)_3Si\text{–}OH + C_2H_4 \quad (2.3)$$

$$(EtO)_3Si\text{-}OH + EtO\text{-}Si(OEt)_3 \rightarrow (EtO)_3Si\text{-}O\text{-}Si(OEt)_3 + 2\ EtOH \quad (2.4)$$

Decomposition of the alkoxides goes at 750ºC without the oxygen source. Adding oxygen from air does not have an influence on the decomposition temperature. However, oxygen removes carbon contamination in the films and improves the quality of the films. Contrary, the addition of ozone can decrease the decomposition temperature down to 300ºC and increase the quality of the film even further.

The typical CVD reactor consists of the precursor delivery system, reactor, and pumping system to remove by-products of the reaction (Figure 2.3). 200 - 800°C is the typical range of temperature in the reactor, and 0.1 mbar to 1 bar is the typical pressure.

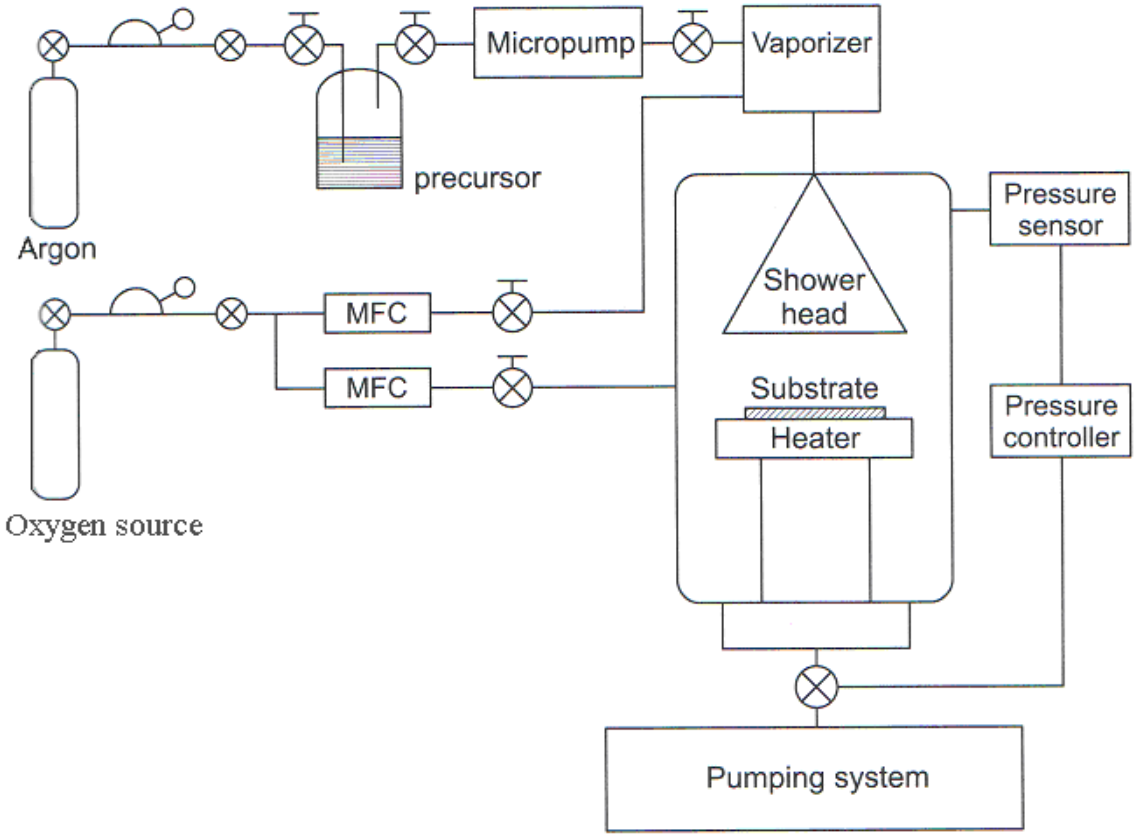

Figure 2.3 Principal Scheme of a CVD Reactor for Oxide Film Deposition (MFC – Mass Flow Controller) (Adapted and Modified from Reference 5)

Heating the precursor vessel can increase the volatility of the precursor. Several alternative methods of precursor delivery (aerosol, spray pyrolysis) can be used for precursors that are not sufficiently volatile or thermally unstable.

Many different techniques are based on the CVD process and the most frequently used and applied for oxide production are summarized in Table 2.1. The vapor phase epitaxy (VPE) technique is used to grow epitaxial crystalline films that have crystallographic orientation and lattice parameters similar to those of a single crystal. The OMCVD and OMVPE techniques use organometallic compound precursors with metal-carbon bonds. In contrast, the metal-organic precursors without any metal-carbon bonds (alkoxide, amines) are applied in the MOCVD and MOVPE techniques.

Table 2.1 CVD Related Methods [5]

Acronym	Full Name of the Techniques
CVD	**C**hemical **V**apor **D**eposition
VPE	**V**apor **P**hase **E**pitaxy
OMCVD	**O**rgano**m**etallic **C**hemical **V**apor **D**eposition
OMVPE	**O**rgano**m**etallic **V**apor **P**hase **E**pitaxy
MOCVD	**M**etal-**o**rganic **C**hemical **V**apor **D**eposition
MOVPE	**M**etal-**o**rganic **V**apor **P**hase **E**pitaxy
PACVD	**P**lasma-**a**ssisted **C**hemical **V**apor **D**eposition
LCVD	**L**aser-induced **C**hemical **V**apor **D**eposition

Other vapor deposition methods include Physical Vapor Deposition (PVD), Atomic-layer Epitaxy (ALE), Chemical-beam Epitaxy (CBE) and Metal-organic Molecular-beam Epitaxy (MOMBE).

The main disadvantages of the CVD method include the incorporation of carbon into films using organometallic precursors, the contamination with chlorine by using halide precursors, and contamination with unwanted by-products. The by-product must be removed from the deposition zone. The other problem is the non-uniform stoichiometry in the films due to different volatility and reactivity of precursors and intermediates.

The main difference between the chemical vapor deposition and aerosol methods is the place of the solid product formation. Gaseous precursors are adsorbed first on the substrate surface and then react to form the solid product in CVD, while by the aerosol method the solid particles are produced right in the gas phase. The products of CVD are films, while the products of the aerosol technique are fine powders.

In an aerosol, an atomized solution in the form of droplets or solid powders in a carrier gas in the form of suspension is passed through a heated region [7]. The product particles are obtained by the precursor pyrolysis or by the reaction with a gas. The solvent in the droplets evaporates, and solid particles form through the densification. However, if the solute precipitates at the supersaturated surface first, a crust forms, and this particle is hollow inside.

The aerosol process is widely used for the preparation of ultrafine particles (< 100 nm) of different oxides (Table 2.2). The process is performed in the presence of oxygen to favor the oxide production. Different oxide powders can be synthesized in thermal (combustion), laser (convection or radiation) or plasma (energy of highly ionized gases) reactors. In some cases, mixed-metal oxides can be prepared using a precursor mixture (for example $SiCl_4$ and $TiCl_4$). Aerosol powders are usually in the form of agglomerates of primary particles held together by weak van der Waals forces.

Table 2.2 Oxide Powders Prepared by Aerosol Method [5]

Oxides	Precursors
SiO_2	$SiCl_4$
TiO_2	$TiCl_4$
Al_2O_3	$AlCl_3$
Bi_2O_3	$BiCl_3$
Cr_2O_3	CrO_2Cl_2
Fe_2O_3	$FeCl_3$ or $Fe(CO)_5$
GeO_2	$GeCl_4$
NiO	$Ni(CO)_4$
MoO_2	$MoCl_5$
SnO_2	$SnCl_4$ or SMe_4
V_2O_5	$VOCl_3$
WO_3	$WOCl_4$
ZrO_2	$ZrCl_4$
$AlBO_3$	$AlCl_3$ and BCl_3
Al_2TiO_5	$AlCl_3$ and $TiCl_4$

The aerosol process can be also used for the synthesis of mixed metal oxides (spinels) by the spray pyrolysis method.

Typical examples of the aerosol process are the synthesis of highly dispersed silicon oxide (silica) and titanium oxide (titania). This Aerosil® process was developed by the German company Degussa, so the silica product has the name Aerosil A200 fumed silica, and the titania product has the name of titania P25 Degussa [8]. These oxides are produced by flame hydrolysis.

Titanium is produced by the reaction of titanium tetrachloride with water in the oxygen-hydrogen flame according to the following chemical reactions:

$$2\ H_2 + O_2 \rightarrow 2\ H_2O \qquad (2.5)$$

$$TiCl_4 + 2\ H_2O \rightarrow TiO_2 + 4\ HCl \qquad (2.6)$$

The overall reaction gives highly dispersed titanium oxide and hydrogen chloride as a byproduct:

$$TiCl_4 + 2\ H_2 + O_2 \rightarrow TiO_2 + 4\ HCl \qquad (2.7)$$

The produced titania is widely used as a pigment for paints. This material is a light powder consisted of agglomerated spherical particles of up to 40 nm diameter. It also has a high surface area of 50 m^2/g.

Fumed silica is produced by the similar flame hydrolysis reaction:

$$SiCl_4 + 2\ H_2 + O_2 \rightarrow SiO_2 + 4\ HCl \qquad (2.8)$$

Fumed silica and aerosol titania have found wide applications as the filler for rubber, additive for drilling fluids, plastics, paints, creams, tablets, cosmetic powders, toners, and toothpastes.

The high surface areas and low density of aerosol materials can be compared to the aerogel materials which will be discussed later in this chapter. However, the surface of aerosols originates only from the outer surface of particles, while the aerogels have traditionally higher surface areas originating not only from outer surfaces but also from the high porosity of aerogels.

In the aerosol process, products are produced at the expense of energy. Other disadvantages of the aerosol technique include the production of hollow particles, which can be explained by the differences in nucleation and growth rate of the precursors.

2.2.3 Sol-gel technique

The sol-gel technique is one of the most widely used soft chemical methods and mainly applied for the synthesis of metal and semimetal oxides. In this process, oxides are synthesized by the formation of an oxide network directly in solution by hydrolysis of alkoxides, followed by gelation and finally by removal of the solvent [9]. In contrast to the solid-state method, a wet chemical synthesis can provide homogenous nanosized oxides of high purity at lower reaction temperatures. Sol–gel and aerogel processes are the most widely used routes and involve a colloidal sol which is converted into a gel during aging [10, 11].

The main principle of the classical sol-gel process is the controlled hydrolysis of metallo-organic compounds (alkoxides) in an organic solvent. The sol-gel process involves olation (formation of hydroxyl bridges) and oxolation (formation of oxygen bridges) reactions during hydrolysis (reactions 2.9-2.11). The oxolation a.k.a. condensation reaction is responsible for the formation of colloidal agglomerates, and the oloation a.k.a. addition reaction is responsible for their aggregation into a polymeric gel.

$$\equiv M\text{-}OR + H_2O \rightarrow \equiv M\text{-}OH + HOR \qquad \text{(Hydrolysis)} \qquad (2.9)$$

$$\equiv M\text{-}OH + RO\text{-}M\equiv \rightarrow \equiv M\text{-}O\text{-}M\equiv + HOR \qquad \text{(Condensation)} \qquad (2.10)$$

$$2 \equiv M\text{-}OH \rightarrow \equiv M\text{-}O\text{-}M\equiv + H_2O \qquad \text{(Addition)} \qquad (2.11)$$

where R is alkyl group, and M is metal or semimetal (IV).

The gel formation depends on different parameters including the nature of starting material(s) (precursor[s]), kind of solvent, precursor concentration in the solvent, alkoxy to water ratio, temperature of the reaction, pH, kind of catalyst, stirring and aging time. Metal alkoxides

serve as starting materials and can be hydrolyzed by water. The alkoxides have been extensively used for the production of oxides and glasses. During hydrolysis, alkoxy groups are replaced by strong OH^- nucleophiles, and the following condensation and addition steps lead to the formation of oxide chains.

The sol-gel synthesis goes through the formation of a sol of colloidal particles or units in a solution, gelation of the sol by the agglomeration of these particles or sub-units into a big gel network structure, removing of the solvent, and heat treatment to transfer gel into solid. Depending on reaction conditions, the sol particles may grow further or form gel.

The sol-gel process can be used for the preparation of a variety of materials (Figure 2.4). The drying of the sol gives powders. The application of dip-coating or spin-coating leads to the preparation of the thin films.

The removal of the solvent by drying causes the shrinking of the gel and significant reduction in the volume due to increasing capillary forces. The high capillary pressure in the pores causes the collapse of the gel network structure and the production of less porous powder (xerogel). In contrast, the supercritical extraction when the solvent is removed above its critical temperature preserves the structure of the gel network and yields a highly porous material (aerogel). Dense ceramic material or glass can be produced by sintering the xerogel or aerogel.

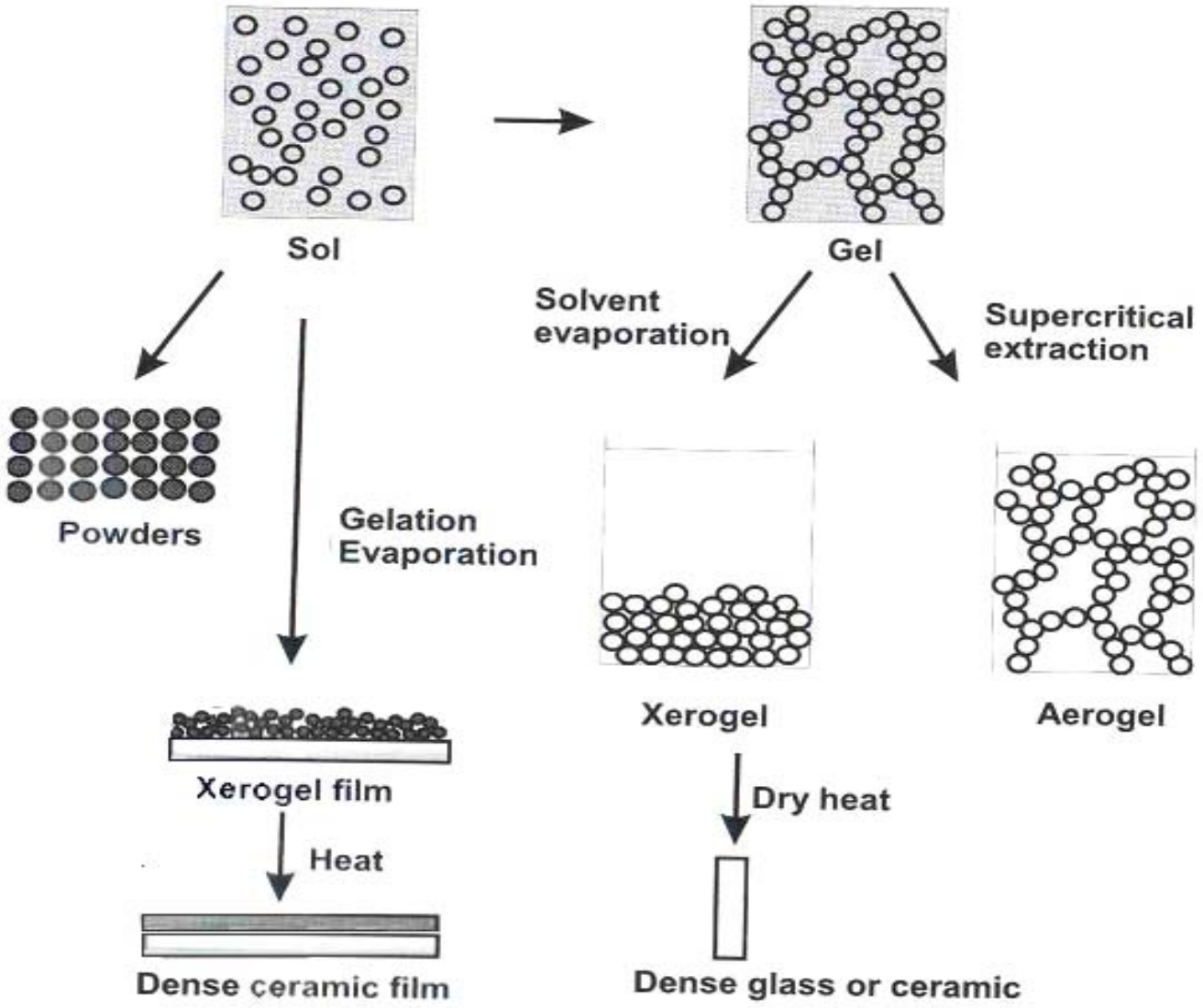

Figure 2.4 Production Options for the Sol-gel Process (Adapted and Modified from Reference 5)

2.2.4 Aerogel procedure

Samples prepared by the sol–gel method are porous and have a three-dimensional polymeric network. However, the liquid-vapor interfacial tension during conventional drying can cause destruction of this porous network, but the removal of the solvent by supercritical drying prevents the network from collapse [12-15]. Under the supercritical extraction of the solvent, the gel is processed with heat and pressure, giving rise to a nanocrystalline product with homogeneous composition, high porosity, and large surface area [16, 17].

The synthesis of mixed oxides by the sol–gel method can be achieved by cogelation of a metal precursor mixture (hydrolysis of metal alkoxides). The hydrolysis step (2.12) uses the metal alkoxide and releases the alcohol. The partially hydrolyzed intermediate undergoes a condensation reaction (2.13) forming a metal-oxygen-metal bridge (M-O-M) by either the removal of water (X is H) or alcohol (X is R).

$$M(OR)_n + m\,H_2O \rightarrow M(OR)_{n-m}(OH)_n + m\,ROH \qquad (2.12)$$

$$MOH + MOX \rightarrow MOM + XOH \qquad (2.13)$$

When synthesizing mixed-metal aerogels, the combination can yield condensation sites of MOM, MOM', and M'OM' (where M and M' are different metals). The final products are three dimensional crosslinked networks with oxo-bridged metals. In mixed-metal aerogels, each metal site has several possible combinations of bridged neighbors.

Often, mixed metal oxides can consist of two separate oxide phases (oxide segregation), or of one phase with cationic substitution in the lattice, depending on the solubility of the metal oxides in each other [18].

The aim of the research described herein was to substitute titanium for strontium or barium in a 1:1 stoichiometric ratio, and to synthesize single-phase nanosized strontium titanate and barium titanate powders ($SrTiO_3$ and $BaTiO_3$).

Commonly, metal alkoxides in different alcohols are used for the aerogel synthesis. For mixed metal oxide systems, the traditional way is the acid–alkoxide route through the mixing of

one metal (A) alkoxide with the salt (nitrate, acetate, acetylacetonate, citrate, or carbonate) of the second metal (B) or the hydroxide–alkoxide route through the mixing of metal (A) alkoxide with metal (B) hydroxide in alcohol followed by hydrolysis (gelation). The presence of acid anions from the salt or hydroxide supports faster gelation, but also causes impurities in the samples that must be removed by calcination [10, 18, 19]. In our research, the mixed alkoxide route through the mixing of two metal (A and B) alkoxides was used to achieve a better gelation and prevent the formation of impurities. Since strontium and barium oxides tend to produce a carbonate phase, conditions to prevent reaction with CO_2 during hydrolysis, supercritical drying, and calcination must be provided for. To accomplish this, supercritical solvent extraction was executed in a N_2 atmosphere.

The influence of solvent on the aerogel properties has been widely studied in our research group [20, 21]. It was found that a solvent mixture of alcohol and toluene affected the hydrolysis of the aerogel, and resulted in higher surface areas of aerogels compared to pure alcohol solvents. The presence of the hydrophobic solvent may reduce surface tension in gel pores and thereby prevent sintering [20].

The presence of toluene in the solvent also accelerated the hydrolysis and gelation processes; it also yielded more porous and, therefore, less dense wet gels with a lower mass fractal dimension [21]. Finally, the excess of toluene in solvent and nitrogen gas during hypercritical drying in the autoclave prevented the gel from stress and shrinkage, which results in products with higher surface areas.

2.3 Temperature treatment

Drying and/or heat treatment processes are important final steps for the preparation of the oxide products. The drying of the wet samples causes the collapse of the network structure and shrinkage to produce materials with smaller surface areas. Heating the powders at high temperatures causes the particles of the powders to fuse together, as well as decreasing the pore sizes and voids between particles. Further heat treatment leads to the production of dense solid material in a process called sintering.

Sintering is an important process for producing different materials like ceramics and ironware. However in case of the nanoparticles, the sintering process is undesirable because it will cause the increase of the particle sizes and the decrease of surface areas.

Particles in the powder have an excess of surface free energy. During heating, they try to decrease this free surface energy by decreasing the total surface area. Particles join together and transport mass to decrease the surface of particles (Figure 2.5). Surfaces within particles have different chemical potentials based on the curvature. The convex surface has a positive surface energy, while the concave surface has a negative free energy. Mass transport goes through the diffusion process from the concave particle surface to the concave interparticle surface (necks or pores). The driving force of sintering is greater for smaller particles, and nanoparticles undergo significant increase in particle sizes and decrease of surface areas.

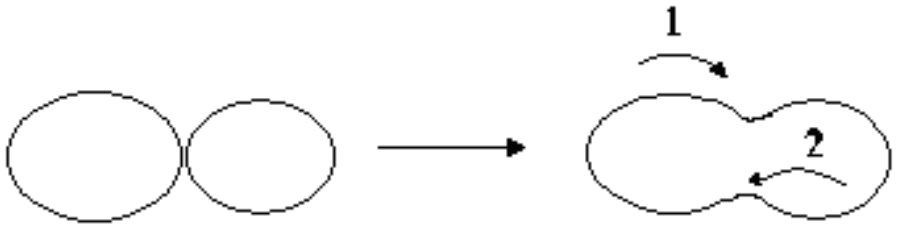

Figure 2.5 Sintering by diffusion (path 1 - surface diffusion, path 2 - volume diffusion)

The driving force for mass transport is the diffusion of mass flow depending on different vacancy concentrations. Diffusion goes through two main paths, which are surface diffusion and volume diffusion. In the surface diffusion, vacancies go from the neck surface to the convex surface, so the mass flow goes oppositely from the convex surface to the neck (Figure 2.1, path 1). In the volume diffusion, vacancies in the grain boundaries and/or dislocations in the grain matrix move in the volume to the surface while the mass flow tend to fill the place of moved vacancies (Figure 2.1, path 2).

2.3.1 Heat treatment

During the heat treatment of powders, the sintering of particles goes through three main steps. The first step includes the fusing of particles together and the mass transfer from the convex to concave surfaces. The total pore volume and distance between particles decreases insignificantly. During the second step, diffusion and mass transfer processes occur and cause an increase in density and growing of interparticle necks and decrease in pore diameters and distances between particle centers. Significant shrinkage and densification occurs also. In the final step, a dense material is produced, and all remaining pore are gradually eliminated.

Heat treatment has a significant influence on particle size, particle shape, and particle packing. For smaller particles, the mass transport goes faster and sintering starts at lower temperatures. High temperatures also cause an increase of the average size of particles and decrease of the particle size distribution. The coarsening process can be explained by larger particles growing at the expense of smaller particles. The sintering process goes faster for particles with a high surface area to volume ratio. In aggregates of particles, the high number of contacts between particles favors the sintering and densification of the material.

2.3.2 Calcination

Calcination is a heat treatment process where the decomposition of the precursor or the degradation of the impurities in the product occurs with the liberation of gases (H_2O and CO_2, or other gaseous products of degradation) in the oxidizing atmosphere (air, oxygen, nitrous oxide, or ozone). Metal oxides prepared by wet chemical methods are usually contaminated with organic residues from the organic components involved in the synthesis, such as physisorbed solvent, ligands, or modifiers. Studies on different aerogels showed that calcination at 300-500ºC is necessary to remove these organic residues, but it is still possible that a small amount is present in pores and on the surface of the aerogel [22]. Application of oxidative atmospheres such as air or oxygen helps to burn off the organic residuals and remove them in the form of CO_2 gas.

The oxide powder characteristics such as particle size, particle shape, surface area, crystallinity, phase purity are dependent on the conditions of calcination. The presence of

organic residuals on the surface can significantly influence the physical and chemical properties of an aerogel. They can cover active sites of the material and decrease the reactive and catalytic activity of the aerogel.

2.3.3 Drying

The freshly prepared wet gels obtained by the sol-gel method can be dried by several techniques. Drying of the wet gel in air results in gel network collapse and strongly shrunken gel (xerogel). To preserve the inorganic network structure from shrinkage, high-temperature supercritical drying, low-temperature supercritical drying, and freeze-drying techniques have been developed [23].

In the supercritical drying process, the solvent in pores is transferred into a supercritical fluid (SCF). In this state, solvent is above its critical pressure and critical temperature, so it has properties of liquid and gas together, so there is no liquid-vapor interface and no capillary pressure.

For supercritical drying, a gel is placed into an autoclave and heated following the steps showed in Figure 2.6. The gel is heated in such way that the solvent does not cross the liquid – gas phase boundary. Over the critical point, solvent is vented out in the form of gas, so the gel structure is preserved from collapsing by capillary forces. After that the aerogel is cooled down to room temperature in an inert atmosphere (N_2).

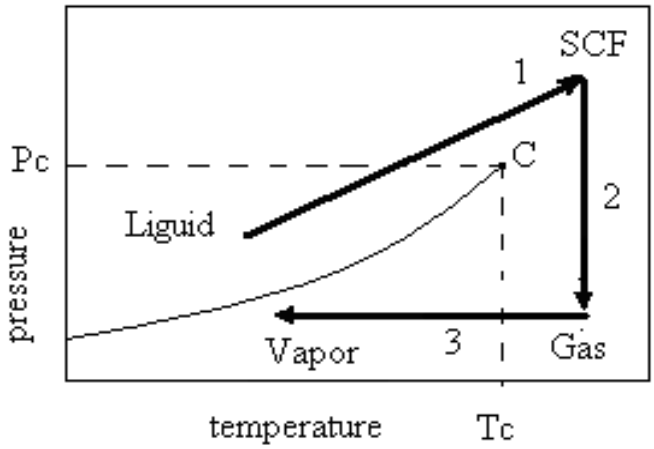

Figure 2.6 Temperature-pressure Diagram for Supercritical Drying, where C - Critical Point, SCF – Super Critical Fluid, T_c – Critical Temperature, P_c – Critical Pressure (Adapted and Modified from Reference 5 and 13)

Water can not be used as the solvent because many oxides dissolve in water at supercritical conditions and the oxide peptizes and causes production of a dense crystallized oxide bulk. Instead of water, alcohols are the most widely used solvents for the supercritical drying and preparation of the aerogels. However, high critical temperature and pressure of the alcohol solvents [Table 2.3] in combination with solvent flammability requires strong precautions.

Table 2.3 Critical Points of Some Solvents [13]

Solvent	Critical temperature T_c, °C	Critical pressure P_c, bar
H_2O	374	221
CO_2	31	74
Methanol	240	80
Ethanol	243	64
Isopropanol	235	47
1-Butanol	290	43

It was found that a mixture of alcohol and organic solvent such as benzene or toluene is essential for obtaining mixed metal oxides with high surface areas and small crystallite sizes [24]. Toluene in the mixture reduces the surface tension at the gas–liquid interface, resulting in the formation of more open porous network products with higher surface areas. Alcohol is important for the prevention of phase separation of the alkoxide precursors.

Carbon dioxide has a very low critical temperature of 31ºC, and it is non-flammable. These advantages can be used for low-temperature supercritical drying. This process is energy efficient and non-explosive. The solvent in gel is exchanged by liquid CO_2 before the drying step which gives dried aerogels (carbogels). This method can not be used for the preparation of some oxides, which react with carbon dioxide to form carbonates, such as alkaline-earth metal oxides.

In the freeze-drying method, gel is quickly frozen first to prevent the solvent from crystallization, and after that it slowly evaporates by sublimation under vacuum. The final product (cryogel) is a highly porous solid with a structure similar to an aerogel [25].

2.4 Conclusions

Many methods have been used for the synthesis of these materials, and new methods are been developed continually. Some of these methods allow synthesizing nanosized materials with unique characteristics and possible advantages over bulk materials.

The sol gel method in combination with supercritical drying is one of these methods that offer an improved way to prepare nanosized materials with unique properties. Aerogels are the lightest inorganic solid materials available today; they are of great value for thermal insulation, for catalysis and as electrode materials. Their unusual high surface areas make them attractive for different applications.

Oxide and mixed oxide aerogels are interesting for their textural, structural and chemical properties. They have morphological and structural properties that differ from the conventionally prepared by the solid-state technique.

Titania-based oxides synthesized buy the aerogel technique have high porosity, high surface areas, homogeneity, and thermal stability. In particular, nanosized alkaline-earth metal titanates offer new possibilities for different applications including catalysis, photocatalysis,

electronics, water electrolysis, organic synthesis and toxic waste remediation. Drawbacks of the aerogel technique include high cost of preparation, safety and technical risk due to high temperature, and high pressure.

2.5 References

[1] W. Lengauer, Surface and Interface Analysis, 15 (1990) 377.

[2] N.R. Rao, Mater. Sci. Eng., B18 (1993) 1-21.

[3] J. Petzelt, T. Ostapchuk, I. Gregora, I. Rychetsky, S. Hoffmann-Eifert, A. V. Pronin, Y. Yuzyuk, B. P. Gorshunov, S. Kamba, V. Bovtun, J. Pokorny, M. Savinov, V. Pokhonskyy, D. Rafaja, P. Vanek, A. Almeida, M. R. Chaves, A. A. Volkov, M. Dressel, and R. Waser, Phys. Rev. B, 64 (2001) 184111.

[4] J. Moreno, J. M. Dominguez, A. Montoya, L. Vicente, and T. Viveros J., Mater. Chem., 5 (1995) 509.

[5] U. Schubert and N. Hüsing, Synthesis of Inorganic Materials, Wiley-VCH, 2000, pp. 396.

[6] H. E. Hintermann, Thin Solid Films, 84 (1981) 215.

[7] M. Drygaś, C. Czosnek, R. T. Paine, and J. F. Janic, Materials Research Bulletin, 40 (2005) 1136.

[8] E. Wagner and H. Brünner, Angew. Chem., 72 (1960) 744-750.

[9] J. Gopalakrishnan, Chemistry of Materials, 7 (1995) 1265.

[10] L. G. Hubert-Pfalzgraf, S. Daniele, and J. M. Decams, J. Sol–Gel Sci. Technol., 8 (1997) 49.

[11] X. Wang, Z. Zhang, and S. Zhou, Mater. Sci. Eng. B: Solid-State Mater. Adv. Technol., B86 (2001) 29.

[12] S. S. Kistler, J. Phys. Chem., 36 (1932) 52.

[13] C. J. Brinker and G. W. Scherer, Sol–Gel Science: The Physics and Chemistry of Sol–Gel Processing, Academic Press, San Diego, 1990.

[14] L. C. Campbell, B. K. Na, and E. I. Ko, Chem. Mater., 4 (1992) 1329.

[15] C. L. Carnes, P. N. Kapoor, and K. J. Klabunde, Chem. Mater, 14 (2002) 2922.

[16] K. J. Klabunde, J. Stark, O. Koper, C. Mohs, D. G. Park, S. Decker, Y. Jiang, I. Ligadic, and D. Zhang, J. Phys. Chem., 100 (1996) 12142.

[17] T. Lopez, J. Hernandez, R. Gomez, X. Bokhimi, J. L. Boldu, E. Munoz, O. Novaro, and A. Garcia-Ruiz, Langmuir, 15 (1999) 5689.

[18] W.-S. Cho and E. Hamada, J. Alloys Compounds, 266 (1998) 118.

[19] S. Ahuja and T. R. N. Kutty, J. Photochem. Photobiol. A: Chem., 97 (1996) 99.

[20] S. Utamapanya, K. J. Klabunde, and J. R. Schlup, Chem. Mater, 3 (1991) 175.

[21] Y. Diao, W. P. Walawender, C. M. Sorensen, K. J. Klabunde, and T. Rieker, Chem. Mater., 14 (2002) 362.

[22] M. Scneider and A. Baiker, Catal. Rev.-Sci. Eng., 37 (1995) 515.

[23] P.H. Tewari, A.J. Hunt, and K.D. Lofftus, Mater. Lett., 3 (1985) (9-10) 363-367.

[24] Utamapanya, S., Klabunde, K.J., and Schlup, J.R., Chemistry of Materials, 3 (1991) 175-81.

[25] W. Mahler and U. Chowdhry, in Ultrastructure Processing of Ceramics, L.L. Hench and D.R. Ulrich (Editors), Glasses and Composites, Wiley, (1984) p. 207.

Chapter 3 : Characterization of titanates

3.1 Introduction

Synthesis of materials has been achieved by different chemical techniques. Characterization of the materials was conducted by using structural analysis and measurements of material properties. The structural analysis included the application of different instrumental techniques such as microscopy, spectroscopy, and X-ray diffraction. The properties measured for the large quantity of particles in powders are the average of all the individual particles.

These measurements were done using powder XRD, UV-visible spectroscopy, elemental analysis, and surface BET analysis. The property studies of individual particles are more complicated due to extremely small sizes of each of them and the lack of suitable techniques and handling procedures. The properties of the individual particles were studied mainly by transmission electron microscopy. Additionally, data on the properties of prepared materials characterized by Infrared spectroscopy can be found in Chapter 6 and by Raman spectroscopy in Chapter 7.

3.2 Synthesis of strontium and barium titanates

Strontium and barium titanate samples have been synthesized by using solid-state reaction and aerogel techniques. The textural and structural properties of these materials were characterized by different available techniques and compared with each other and with available commercial ($SrTiO_3$ and $BaTiO_3$ powder samples from Aldrich, and nanosized $SrTiO_3$ and $BaTiO_3$ powders from Aldrich). The comparison of novel, new samples with materials prepared by conventional methods allows one to observe the differences between them and possible advantages for future applications.

The available and prepared samples have the following abbreviations for future references:

CM – commercial samples purchased from a normal vendor or retailer,

NCM – commercial nanosized samples purchased from retailer,

AP – aerogel prepared samples synthesized by the Modified aerogel procedure,

XP – xerogel prepared samples synthesized by the Sol-gel process,

SSR or SCR – samples prepared by Solid-state chemical reaction.

Additionally, the prepared samples were compared with titanium oxide (P25, Degussa).

3.2.1 Solid–state reaction

Titanium (IV) oxide (Aldrich; 99.8% anatase), strontium carbonate (Aldrich; 98+%), and barium carbonate (Aldrich; 99.98%) were used as received. Commercially available oxides, CM-$SrTiO_3$ (99+%) from Alfa-Aesar, nanosized powder NCM-$SrTiO_3$ (99.5+%) from Aldrich, CM-$BaTiO_3$ (99%) from Aldrich, and nanosized powder NCM-$BaTiO_3$ (99+%) from Aldrich were also used as received.

Titanium oxide (TiO_2, anatase) and strontium carbonate ($SrCO_3$) powders were used for the preparation of the SSR-$SrTiO_3$, and titanium oxide (TiO_2, anatase) and barium carbonate ($BaCO_3$) powders were used for the preparation of the SSR-$BaTiO_3$.

The procedures for the synthesis of strontium titanate and barium titanate were identical (Figure 3.1). The starting materials were mixed in the molar stoichiometric ratio 1:1 of Sr/Ti or Ba/Ti according to the composition of $SrTiO_3$ or $BaTiO_3$. The powders were mixed together and calcined at 1100°C and 1200°C for 36 hours in air using alumina crucibles (99.7% purity). After 18 hours of calcination, each sample was cooled down, the sample ground and calcined again 18 hours. The resulting monoliths of fused particles were crushed, and the obtained powders were used for further analysis and characterization. The structure of the final titanate products was confirmed by X-ray diffraction.

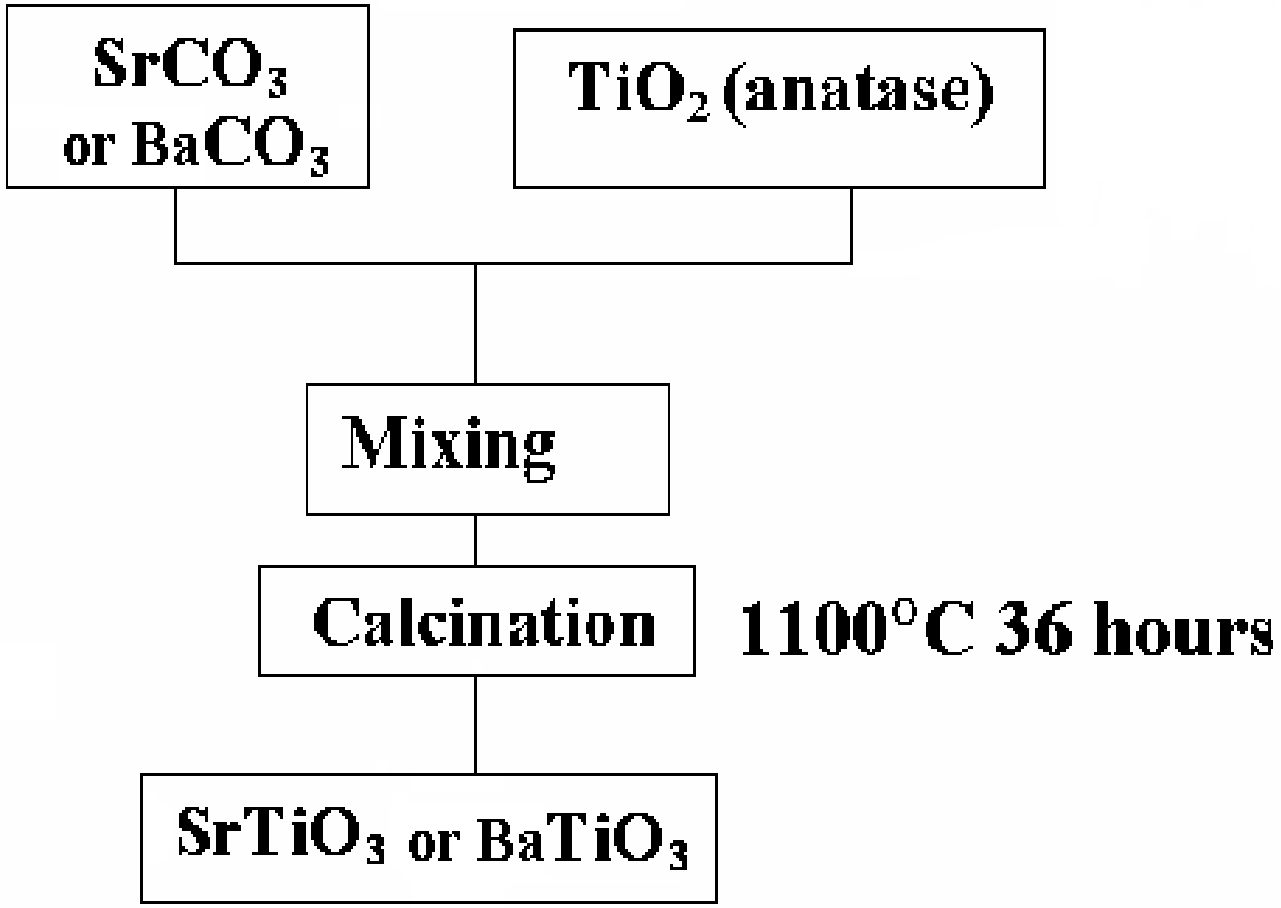

Figure 3.1 Solid-state Reactions for $SrTiO_3$ and $BaTiO_3$ Synthesis

3.2.2 Modified aerogel procedure

All manipulations during synthesis were performed under argon. Special consideration was given to the reactions of strontium and barium metals with alcohols: they are hazardous and must be conducted with precaution under an inert atmosphere only. All autoclave treatments for supercritical drying were performed on a Parr 4843.

Titanium (IV) isopropoxide (Aldrich; 97%), absolute ethanol (Aaper Alcohol and Chemical Co.; 200 proof), methanol (Fisher Scientific; certified ACS), 2-propanol (Fisher Scientific; certified ACS), toluene (Fisher Scientific; certified ACS), strontium metal (Aldrich; 99% dendritic pieces), and barium metal (Aldrich; 99% dendritic pieces) were used as received. Commercially available oxides, CM-$SrTiO_3$ (99+%) from Alfa-Aesar, nanosized powder NCM-$SrTiO_3$ (99.5+%) from Aldrich, CM-$BaTiO_3$ (99%) from Aldrich, and nanosized powder NCM-$BaTiO_3$ (99+%) from Aldrich were also used as received.

The Modified Aerogel Procedure (MAP) for mixed metal oxides employs the preparation of metal alkoxide mixtures in an alcohol–toluene solvent, hydrolysis, co-gelation of alkoxide mixture, and supercritical drying of the solvent. The final oxide products depend on the size and shape of the sol particles in the gel. The scheme for aerogel-prepared strontium and barium titanium oxides (AP-$SrTiO_3$ and AP-$BaTiO_3$) by a modified aerogel procedure are presented in Figure 3.2.

Different alcohols mixed with toluene were used as solvents for synthesis. Strontium titanate aerogels were prepared in either a methanol, ethanol, or isopropanol mixture with toluene in a toluene-to-alcohol volume-ratio of 1.5. Barium titanate aerogels were prepared in ethanol or isopropanol mixtures with toluene in the same ratio. All liquids were deaerated by bubbling with argon for 30 minutes.

The procedures for the synthesis of strontium titanate and barium titanate were identical. In a 250 ml flask, 0.02 mol of Sr (or Ba) metal was allowed to react with 40 ml of alcohol under a flow of argon and constant stirring. In a separate 250 ml flask, 0.02 mol of titanium isopropoxide was added to 40 ml of alcohol with similar stirring under Ar, allowing a 1:1 stoichiometric ratio between Sr (or Ba) and Ti.

After this, 60 ml of toluene was added into each flask forming clear solutions. The alkoxide solutions were mixed together and stirred, and then this mixture was hydrolyzed with a stoichiometric amount of doubly distilled water by slow, dropwise addition. The slow water hydrolysis transformed a solution of alkoxides into a slightly milky wet gel (gel in alcohol–toluene solution). The viscous solution was left for aging by vigorously stirring at room temperature for 1 hour.

The wet gel was transferred to a 600 ml glass liner and placed in an autoclave. The autoclave was flushed with nitrogen, and then pressurized to 100 psi (6.9 bar, 6.9×10^5 Pa). The reactor was slowly heated to 265 °C. The pressure increased from 100 to 1000 psi (68.9 bar, 68.9×10^5 Pa) upon heating. At 265 °C, the solvent vapors were removed by quick venting to the atmosphere, followed by flushing the reactor with nitrogen to remove any remaining solvent vapors. Finally the autoclave was cooled to room temperature.

The resulting slightly yellowish AP-$SrTiO_3$ and white AP-$BaTiO_3$ powders were dried in air at 120 °C. Aerogel products contained some residual solvent that was removed by heat treatment in vacuum and calcination in air or oxygen at different temperatures.

Sr or Ba metal

alcohol

Sr alkoxide
or Ba alkoxide

toluene

Ti alkoxide

alcohol
toluene

1:1

water

Co-Gellation

Supercritical
Drying

$SrTiO_3$
or $BaTiO_3$

4h under N_2,
≈1000psi, 265°C

Release of
pressure

Alcohols:
- Methanol
- Ethanol
- Isopropanol

Figure 3.2 Modified Aerogel Procedure (MAP) from Alkoxides for $SrTiO_3$ and $BaTiO_3$ Synthesis

3.3 Structural studies

3.3.1 UV-visible spectroscopy

Diffuse reflection spectra were obtained using a UV-visible-NIR spectrometer (Varian) and were converted from reflection to absorbance by the Kubelka-Munk method. The comparison of TiO_2 Degussa and aerogel prepared $SrTiO_3$ is presented in Figure 3.3. Both materials have a bright white color, absorb light in the ultra violet region, and reflect visible light. There are some insignificant differences in the line slopes in the spectra that are due to the different band gap of materials. The extrapolation of the titania slope gives an intersection with the x axis at 410 nm and the extrapolation of the strontium titanate slope gives intersection with the x axis at 380 nm. The conversion into energy of band gaps gives 3.0 eV for titanium oxide and a 3.2 eV for strontium titanate correspondently. This means that TiO_2 start to absorb light at higher wavelengths (from 410 nm and shorter) while $SrTiO_3$ absorbs at 380 nm and below.

Figure 3.4 shows the absorption spectra for several strontium titanate samples prepared by different methods. Comparison of aerogel prepared sample and solid-state prepared samples showed the same trend in the absorption of UV light (<380 nm). However, solid-state prepared samples are not pale white, but have a slightly pinkish gray color. The interesting color of these materials can be explained by the low purity of the $SrTiO_3$ product and by the presence of impurity phases produced by incomplete reaction of precursors (Sr_2TiO_4) and oxygen deficiency ($SrTiO_{2.7}$) (for more details see Section 3.3.3 and Appendix A). This causes the appearance of the small absorbance response in the visible light region.

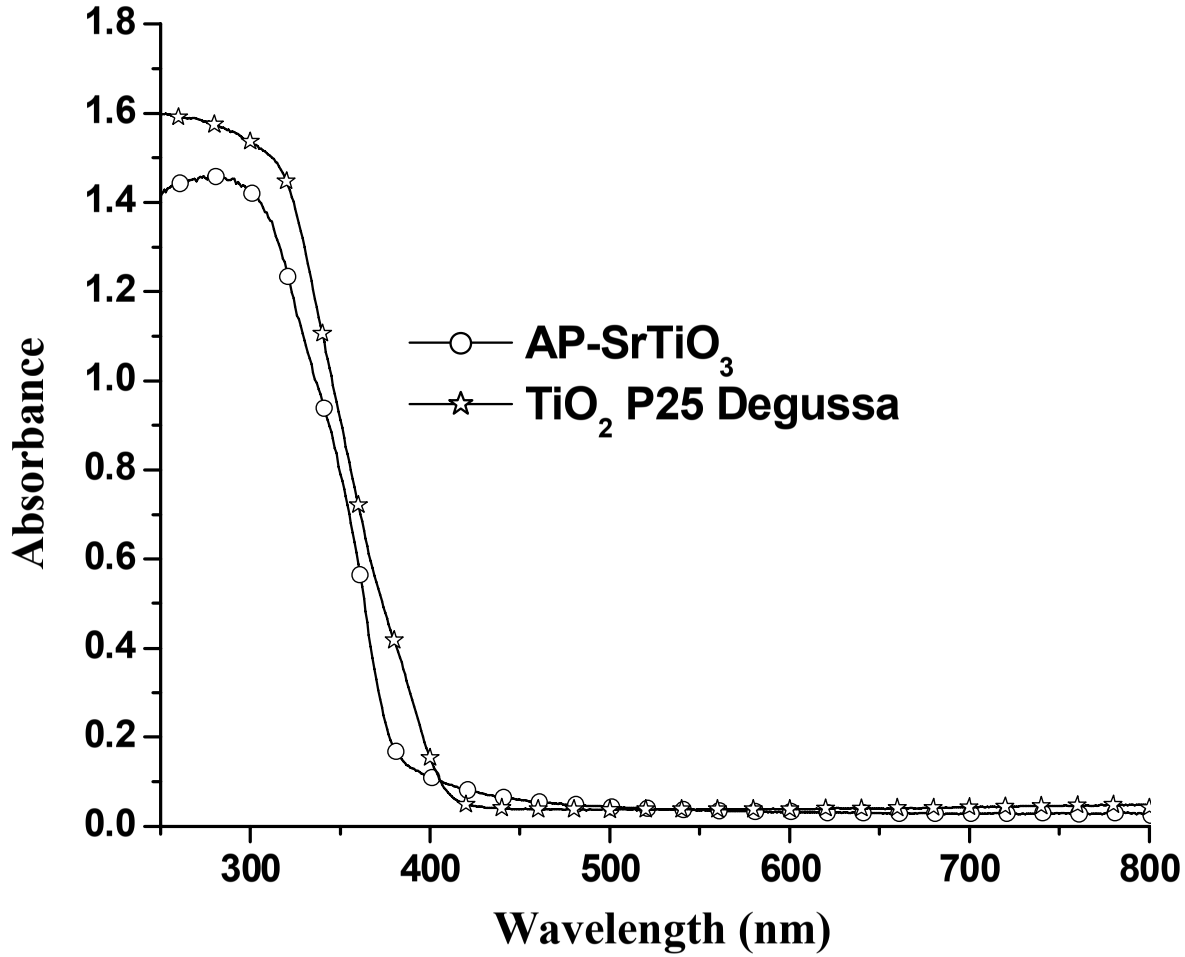

Figure 3.3 UV-visible Spectra of TiO_2 P25 Degussa and Aerogel Prepared $SrTiO_3$

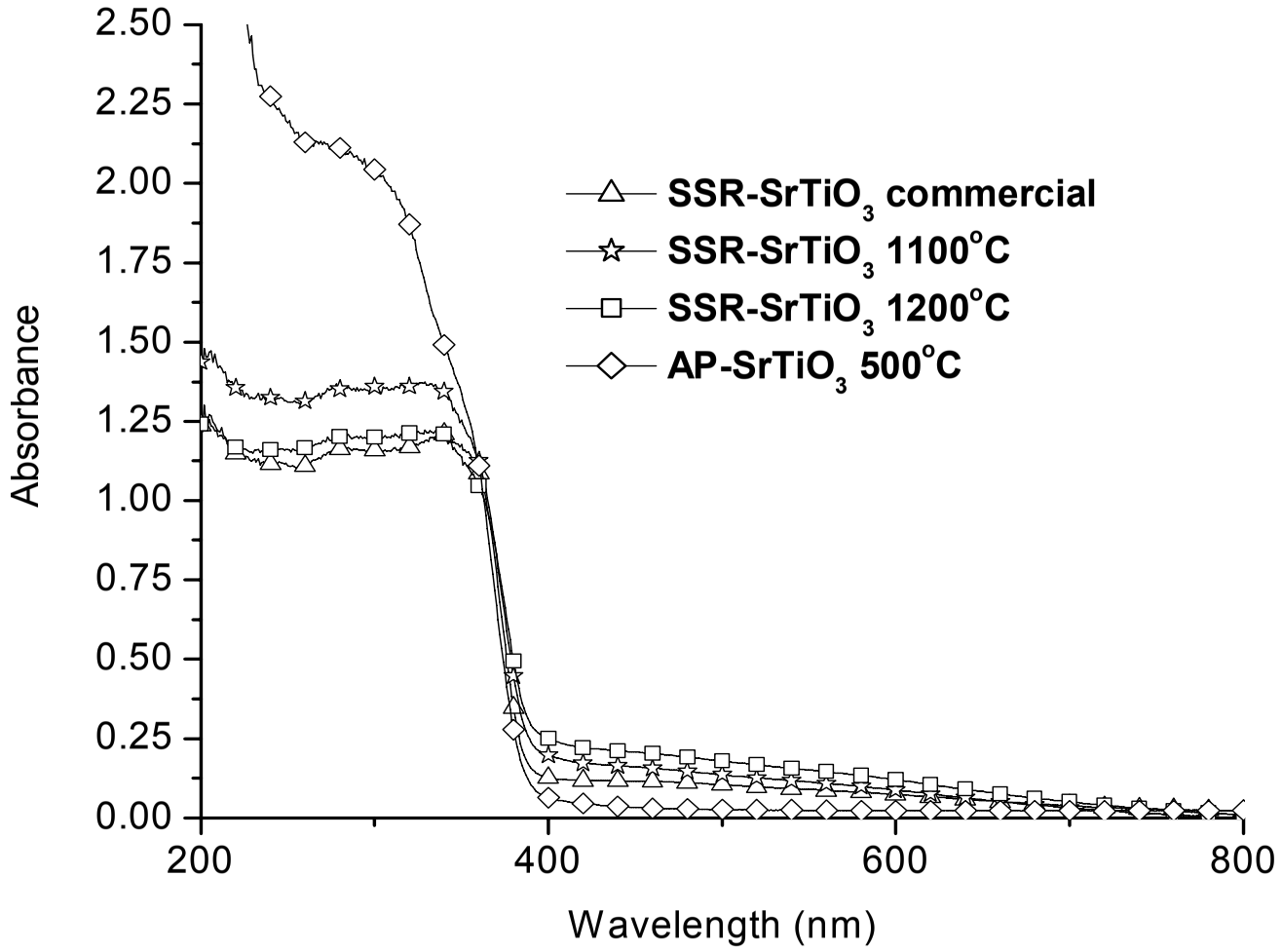

Figure 3.4 UV-visible Spectra of Different $SrTiO_3$ Samples

3.3.2 Braunauer-Emmer-Teller analysis (BET)

The textural properties of solid material can be characterized by porosity, surface area, pore volume, and pore size. Porous solids can have pores in the form of cavities, channels, or interstices. Some of these pores are closed, while open pores may have different shapes including cylindrical, blind with one open end, inkbottle or funnel shaped.

Porosity is the ratio of the total pore volume to the apparent volume of the particles in the powder. Pore volume is the volume of the pores in the investigated material. Pore size or pore diameter is the distance between two opposite walls of the pore.

Pore size is important for the application of materials. They are divided into three pore-size regions and characterized according to their sizes: microporous (diameter < 2 nm), mesoporous (2 nm < pore diameter < 50 nm), and macroporous (pore diameter >50 nm). Porosity of these solids can be characterized by gas adsorption studies.

The adsorption of gas over the surface of the material allows determination of the specific surface area, total pore volume, and pore size distribution of the sample. The free gas and absorbed gas are in dynamic equilibrium, and the surface coverage depends on the pressure of the gas. The fractional surface coverage measured at different pressures at a set temperature gives adsorption isotherms. The mathematical analysis of the adsorption isotherm gives necessary data for calculations of surface areas and porosity characteristics of the samples. Nitrogen is the gas traditionally used as the adsorbate since it exhibits intermediate values for the C constant (50-250) on solid surfaces and allows calculating the cross-sectional area of an adsorbate.

The Branauer-Emmet-Teller equation (3.1) is widely used for determining of the surface area of solid materials [1]

$$\frac{1}{W\left(\frac{P_0}{P}-1\right)} = \frac{1}{W_m C} + \frac{C-1}{W_m C}\left(\frac{P}{P_0}\right) \qquad (3.1)$$

in which W is the weight of the absorbed gas at relative pressure P/P_0, C is a constant related to the energy of adsorption in the first adsorbed layer, and W_m is the weight of a monolayer of adsorbate.

The total surface area of the sample can be calculated by

$$S_t = \frac{W_m N A_{cs}}{M} \tag{3.2}$$

where N is an Avogadro number (6.023×10^{23} molecules/mol) and M is a molecular weight of the adsorbate, and A_{cs} is a cross-sectional area (16.2 Å at 77 K).

The specific surface area can be calculated from the total surface area and the weight of the material sample:

$$S = \frac{S_t}{w} \tag{3.3}$$

The total pore volume can be calculated from the amount of vapor adsorbed at relative pressure close to unity. Besides, the pore size distribution can be calculated from the desorption branch of the isotherm.

Pore size is calculated using the Kelvin equation:

$$r_K = \frac{-2\gamma V_m}{RT \ln\left(\frac{P}{P_0}\right)} \tag{3.4}$$

where γ is a surface tension of nitrogen at its boiling point (8.85 ergs/cm^2 at 77 K), V_m is a molar volume of liquid nitrogen (34.6 cm^3/mol), R is a gas constant (8.314×10^7 ergs/deg mol), T is a boiling point of nitrogen (77 K), P/P_0 is a relative pressure of nitrogen, and R_K is a Kelvin radius of the pore.

The analysis of gas adsorption on the surface of the material can provide information on the surface area and porosity. The adsorption isotherm is obtained by introducing known volumes of nitrogen and measuring the equilibrium pressure. The desorption isotherm is obtained by measuring the quantities of released gas from the samples as the relative pressure is lowered.

All isotherms may be divided into five types according to the way the adsorption of nitrogen occurs.

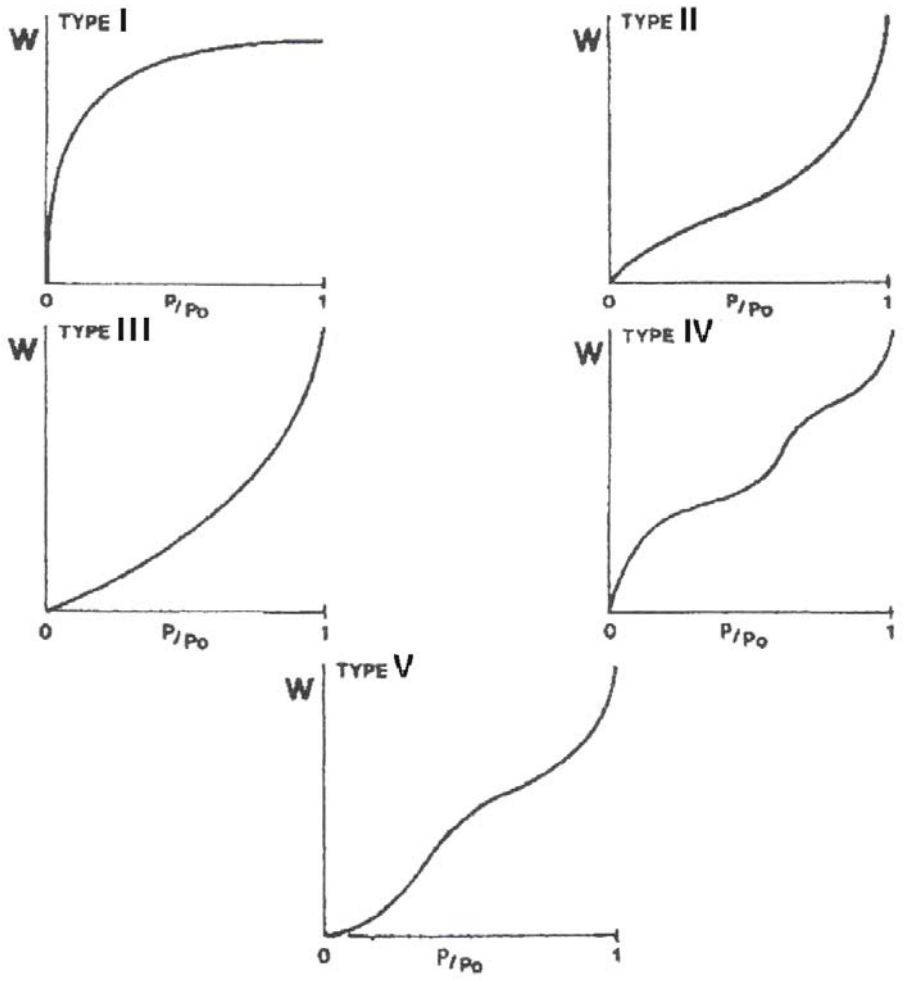

Figure 3.5 Five Types of Adsorption Isotherms [2]

Type I isotherm is associated with microporous materials where the adsorption of nitrogen is on the external surface area and is limited by the accessibility of the micropores. Type II isotherms represents nonporous and macroporous materials where unrestricted multilayers of nitrogen can be adsorbed. Type III isotherm is characterized by the heat of adsorption which is less than the heat of adsorbate liquefaction and there is an additional adsorption through the interaction with the adsorbed layer. Type IV isotherm represents mesoporous materials where the mesopores are filled at higher elevated pressures. Finally, Type V isotherm is similar to the Type III isotherm but this type is common for mesoporous materials.

The adsorption and desorption branches in Type I, Type II, and Type III isotherms are identical and hysteresis occurs very rarely. However, in Type IV and Type V isotherms there is a hysteresis effect between adsorption and desorption. The bottleneck shape of pores and differences in the meniscus of the condensing and evaporating nitrogen causes this effect [3, 4].

Isotherms from aerogels usually fall into the Type IV category for mesoporous solids. Aerogels are usually meso- to macroporous with little microporosity. These textural properties are catalytically favorable for easy accessibility to the internal surface and high availability of active sites.

Surface area studies were conducted using a Quantachrome NOVA 1200 instrument. Each sample was outgassed, and then the surface area, pore volume, and pore diameter data were measured by the BET method from the amount of N_2 absorbed at 77 K.

Traditionally, solid-state prepared materials at high temperatures can be characterized by absent or small porosity and high density, while aerogels are materials with extremely high porosity and low density. The pore structure of aerogels mainly corresponds to the mesoporous structure with interconnected pores in the range of 2 to 50 nm.

The surface areas of SSR-$SrTiO_3$ and SSR-$BaTiO_3$ have not exceeded over 1 m^2/g (Tables 3.1, 3.3). Compared to aerogel, solid-state prepared samples are not porous materials and contain significantly smaller pore volumes as is evident from the smaller amount of N_2 adsorption.

The surface area of AP-$SrTiO_3$ (ethanol) was $160 \pm 10\ m^2/g$ in comparison with 1 m^2/g of the commercial CM-$SrTiO_3$, and 17 m^2/g of nanosized commercial NCM-$SrTiO_3$ (Table 3.1). Calcination in air at 300 °C did not significantly affect the specific surface area. At higher temperatures (400 °C and 500 °C) the surface area decreased by one third and almost half

respectively (Table 3.2). The AP-$SrTiO_3$ (Methanol) and NCM-$SrTiO_3$ had similar crystallite sizes, but the surface area of the aerogel sample was five times higher due to much larger pore volume and pore accessibility.

The surface area of AP-$BaTiO_3$ (Ethanol) was 175 ± 15 m^2/g in comparison with 3 m^2/g of commercial CM-$BaTiO_3$, and 19 m^2/g of nanosized commercial NCM-$BaTiO_3$ (Table 3.3). During calcination in air, the surface area was dramatically reduced from 175 m^2/g to 89 m^2/g at 400 °C, and at 500 °C it decreased further to 45 m^2/g (Table 3.4). Sintering during heating caused an increase in crystallite size and average pore size, and decreased the total pore volume.

3.3.3 Powder X-ray diffraction

Powder X-ray diffraction (XRD) is a powerful technique for determining the structure of materials with long-range order [5]. However, for disordered and amorphous materials this technique finds only limited applications. The XRD pattern of each pure substance is unique, so for different substances there are no identical patterns. The availability of numerous standard patterns in data libraries allows identifying pure substance or crystalline phases in this substance by using simple search and matching procedures.

When an X-ray beam heats the atoms in the solid sample the electrons of these atoms start to oscillate and form constructive interference, which is characteristic of the arrangement of atoms in the crystal. The diffracted beam consists of in phase X-rays which mutually reinforce one another.

The diffraction can be explained by incident and reflected rays and theta angle (θ) between them. Using Bragg's Law, the unit cell dimensions (d) can be determined:

$$2d \sin\theta = n\lambda \qquad (3.5)$$

The average crystallite sizes of samples can be calculated from the XRD spectra using the Debye–Scherrer equation:

$$D = \frac{K\lambda}{B\cos\theta_B} \qquad (3.6)$$

where D is the thickness of the crystal (Å); K = 0.9 is a constant related to the crystallite shape; λ is the X-ray wavelength (1.54051 Å for CuKα); θ_B is the Bragg angle (between incident and diffracted beam); and B is the line broadening, measured from the peak width at half the peak height (radians).

Spectrometric studies were conducted using a Brucker D8 Advance and Scintag XDS 2000 (Chemistry Department, KSU), and a Shimadzu XRD 6000 (NanoScale Materials, Inc.; Manhattan, Kansas). Copper Kα was the radiation source used with an applied voltage of 40 kV and a current of 40 mA. The 2θ angles ranged from 20 to 85° with a scanning rate of 2°/min.

In comparison to commercial samples, synthesized $SrTiO_3$ aerogels have significantly broader peaks, corresponding to smaller crystallite sizes. The XRD patterns show the well-defined crystalline structure of the powders after supercritical drying (Figure 3.6). These samples do not require high-temperature treatments to initiate a phase change from an amorphous to crystalline state. The removal of a residual organic solvent can be achieved by heating procedures.

Solid-state prepared strontium titanate samples have narrow peaks of well-defined crystalline structure of the $SrTiO_3$ phase with crystallites of big sizes (Figure 3.7). The presence of additional peaks in the XRD patterns can be assigned to the impurity phases produced by incomplete reaction of precursors (Sr_2TiO_4) and oxygen deficiency ($SrTiO_{2.7}$) (Appendix A).

The crystallite sizes of different $SrTiO_3$ samples prepared by the aerogel procedure in different alcohol–toluene mixtures, prepared by the solid-state reaction, and available commercial $SrTiO_3$ samples are summarized in Table 3.1.

Ethanol mixed with toluene was the best solvent for AP-$SrTiO_3$, yielding products with the highest surface area and the smallest crystallite sizes in comparison with other alcohol–toluene mixtures.

Table 3.1 Characteristic Properties of Different $SrTiO_3$ Samples

$SrTiO_3$ sample (alcohol in solvent for aerogels)	Average crystallite sizes (nm)	Surface area (m^2/g)	Total pore volume (cm^3/g)	Average pore sizes (Å)
Commercial CM-$SrTiO_3$	145	1	0.003	93
Nanosized NCM-$SrTiO_3$	25	17	0.12	290
SSR-$SrTiO_3$	150	1	0.009	125
AP-$SrTiO_3$ (methanol)	25	82	0.58	280
AP-$SrTiO_3$ (ethanol)	8	159	0.62	160
AP-$SrTiO_3$ (isopropanol)	20	121	0.59	190

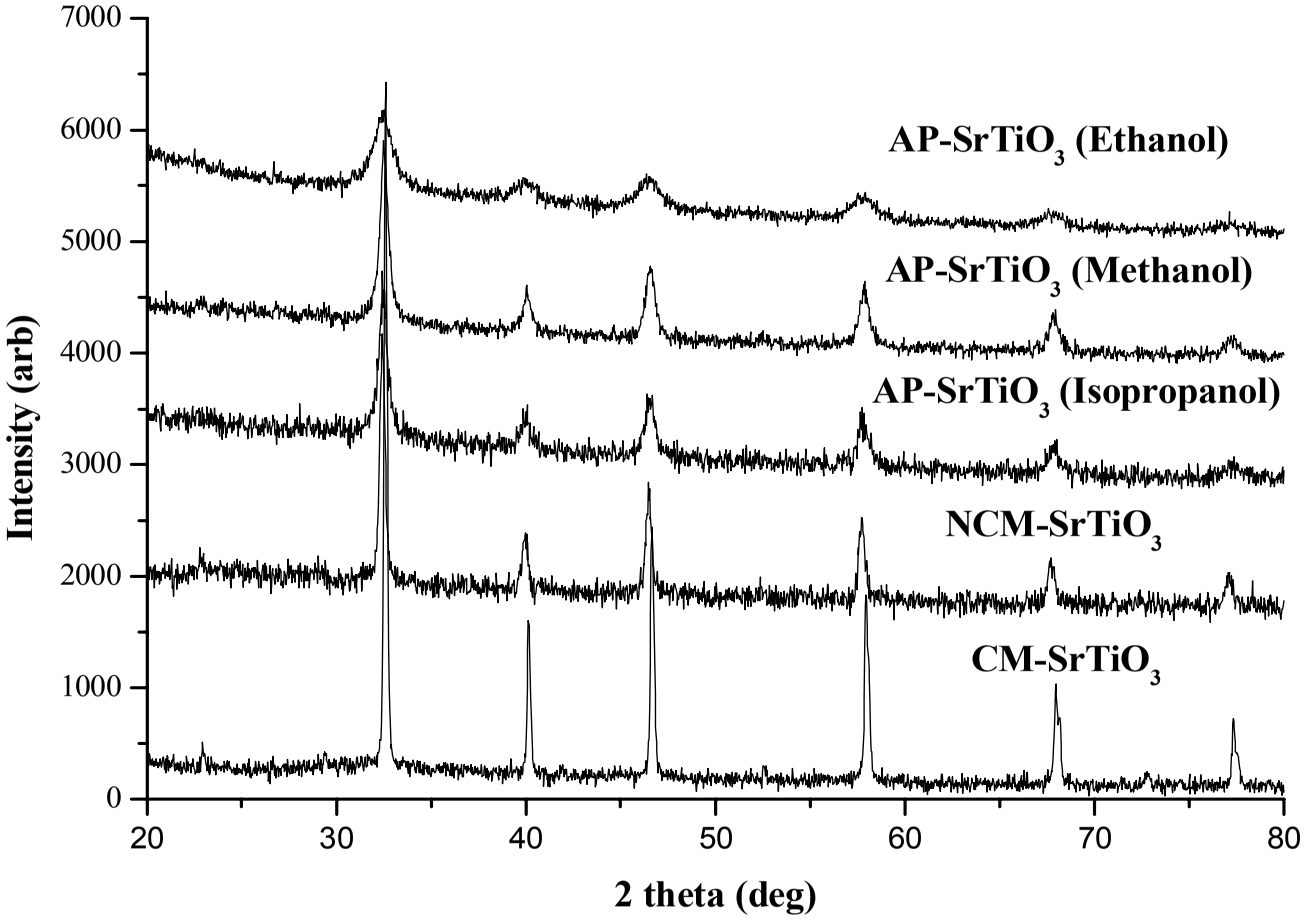

Figure 3.6 Powder XRD Patterns of Commercial and Synthesized $SrTiO_3$ with Different Alcohols Used in Synthesis (CM-$SrTiO_3$ – Commercial, NCM-$SrTiO_3$ – Commercial Nanosized, AP-$SrTiO_3$ – Aerogel Prepared Samples)

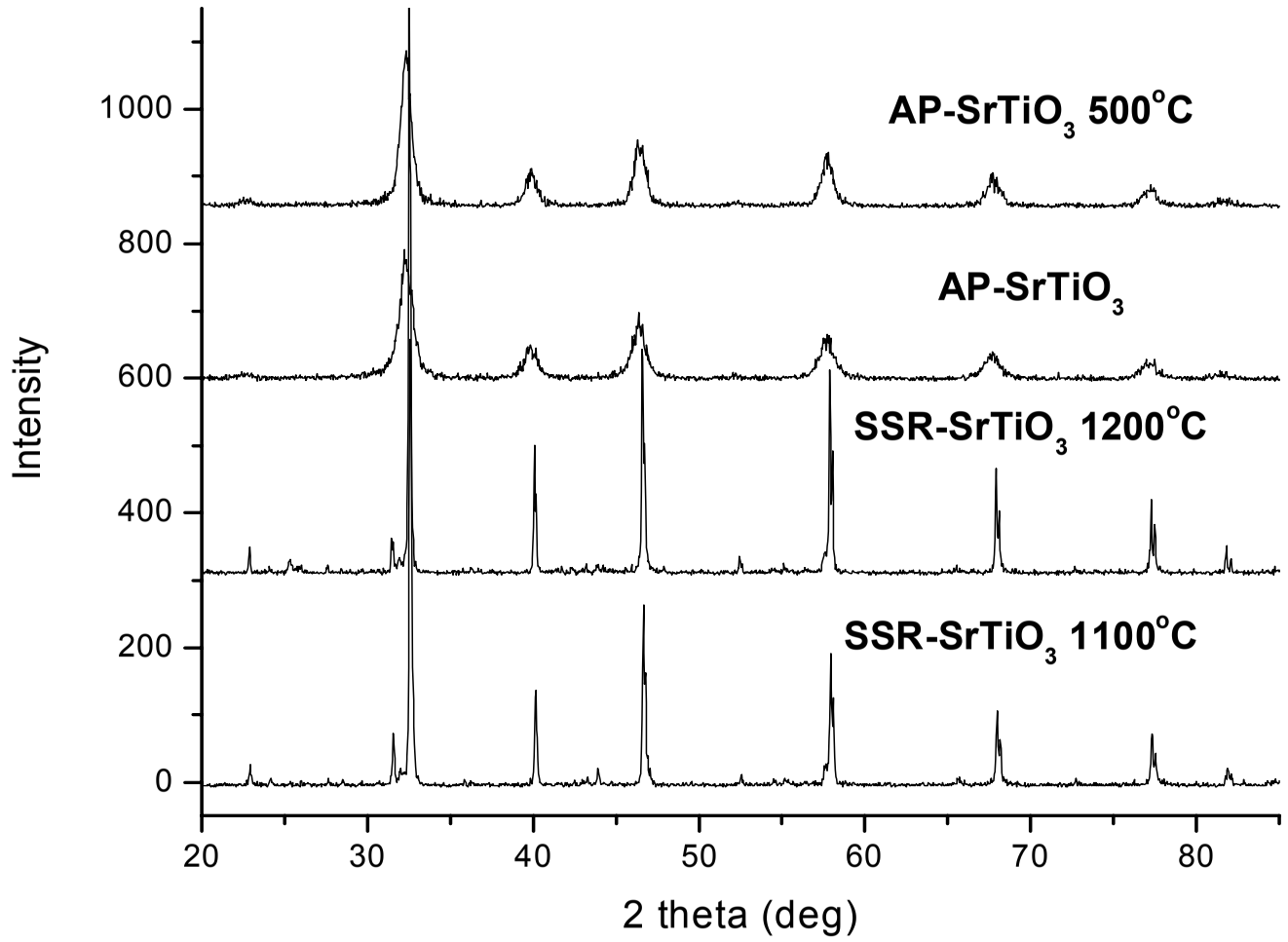

Figure 3.7 Powder XRD Patterns of Solid-state (SSR-$SrTiO_3$) and Aerogel Prepared (AP-$SrTiO_3$) Samples

The crystallite sizes of the SSR-$SrTiO_3$ sample have non-uniform shapes. Sizes and shapes of the particles for this sample are similar to commercially available CM-$SrTiO_3$. This sample has a small surface area of 1 m^2/g and the total pore volume of 0.009 cm^3/g.

The crystallite sizes of AP-$SrTiO_3$ synthesized in an ethanol/toluene solvent were an average of 8 ± 2 nm in diameter, and were three times smaller than commercial nanosized NCM-$SrTiO_3$ sample (25 nm), and almost twenty times smaller than commercial CM-$SrTiO_3$ (145 nm) (see Table 3.1). The information on sizes and shapes of AP-$SrTiO_3$ are also confirmed by transmission electron microscopy. The XRD showed no change in pattern for calcined $SrTiO_3$ aerogels although calcination caused narrowing of the peak width due to sintering and, therefore, to a slight increase in crystallite sizes (Figure 3.8 and Table 3.2).

Table 3.2 Characteristic Properties of AP-$SrTiO_3$ (Ethanol) Calcined at Different Temperatures in Air

Temperature of calcination (ºC)	Average crystallite size (nm)	Surface area (m^2/g)	Total pore volume (cm^3/g)	Average pore size (Å)
265	8	159	0.62	160
300	6	156	0.57	150
400	9	114	0.54	190
500	10	93	0.45	190

Identical to the synthesized $SrTiO_3$ aerogels, a well-defined crystalline structure of the powders was observed after supercritical drying for AP-$BaTiO_3$ (ethanol) and AP-$BaTiO_3$ (isopropanol) aerogels (Figure 3.9). The broad peaks in the spectra corresponded to smaller crystallite sizes in comparison with CM- and NCM-$BaTiO_3$ samples.

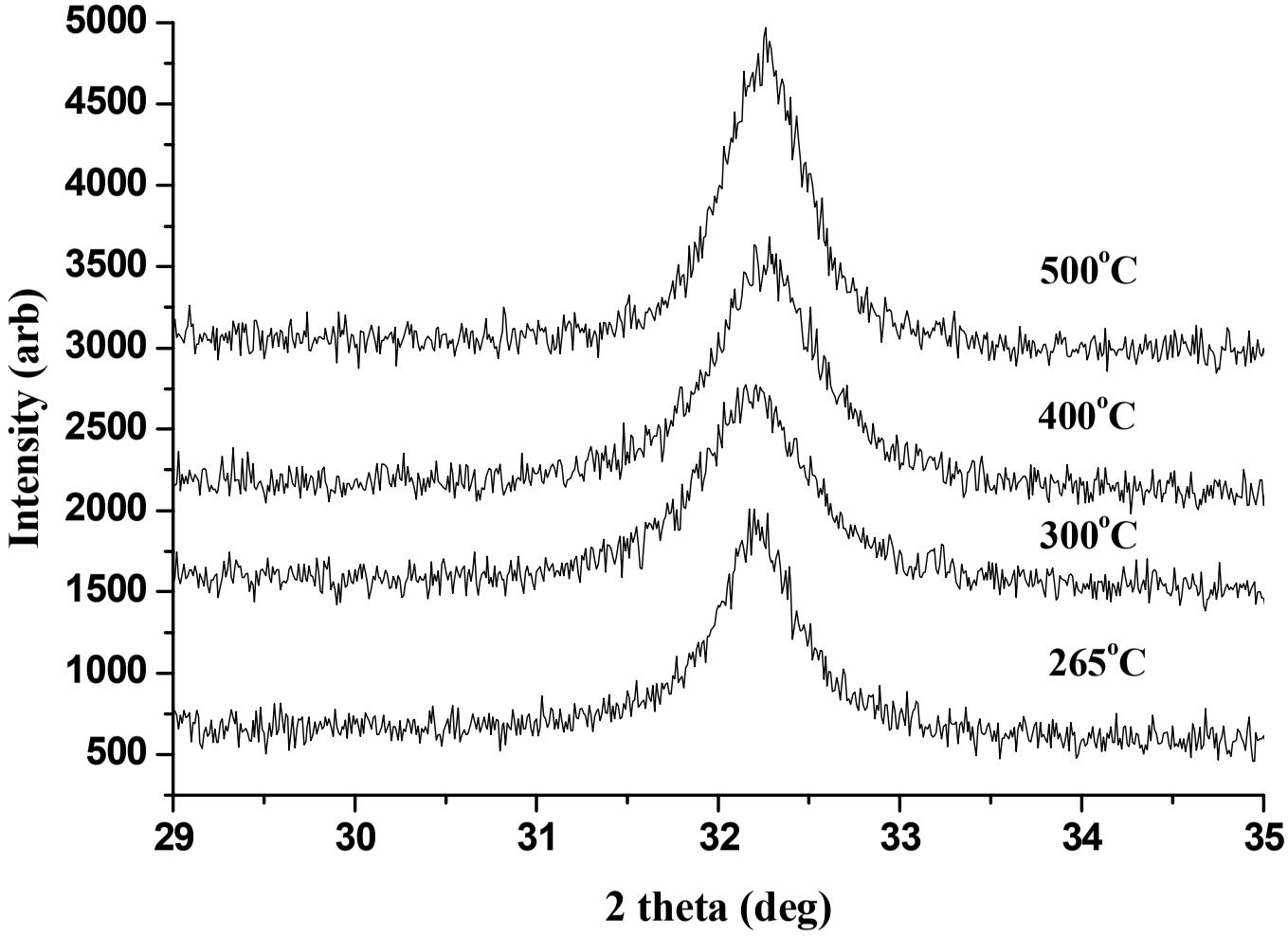

Figure 3.8 Powder XRD Patterns of AP-$SrTiO_3$ (Ethanol) Calcined in Air at Different Temperatures

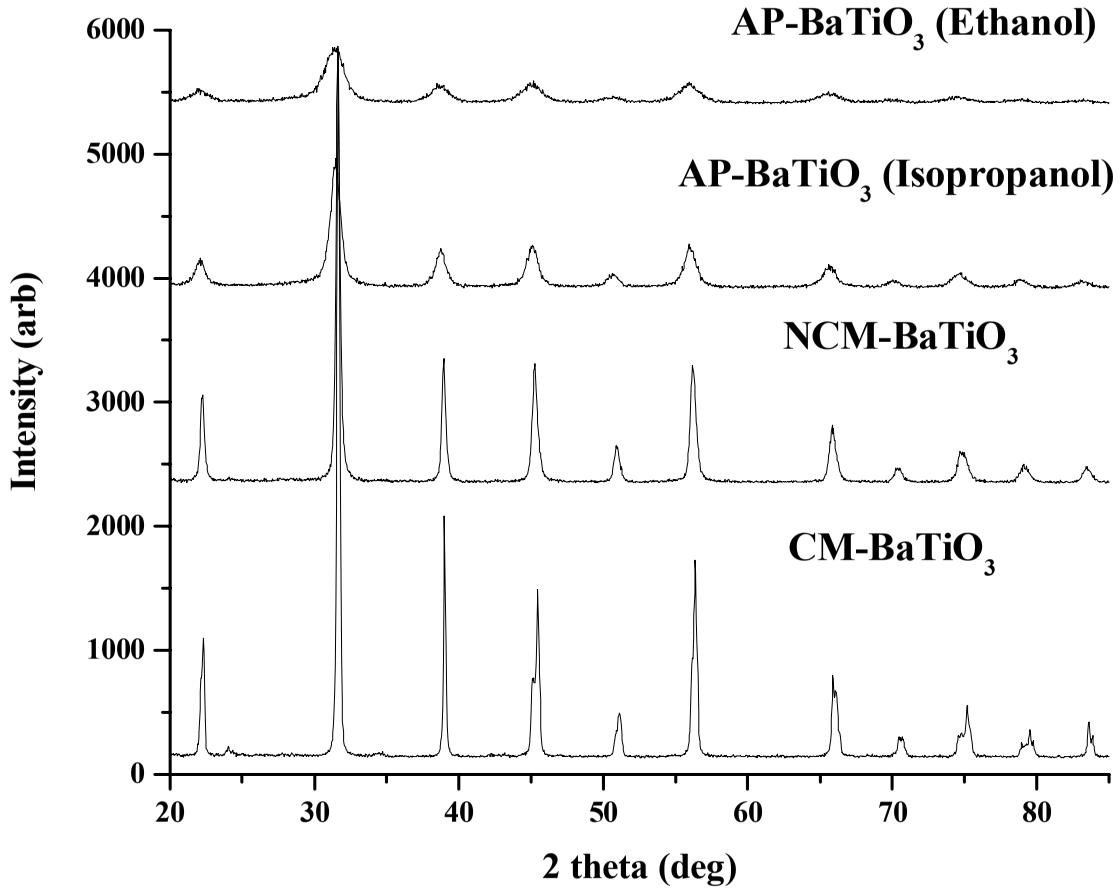

Figure 3.9 Powder XRD Patterns of Commercial and Synthesized $BaTiO_3$ with Different Alcohols Used in Synthesis (CM-$BaTiO_3$ – Commercial, NCM-$BaTiO_3$ – Commercial Nanosized, AP-$BaTiO_3$ – Aerogel Prepared Samples). The XRD Studies of the Samples were Conducted using a Shimadzu XRD 6000 (NanoScale Materials, Inc.)

Due to the high temperature synthetic method, the solid-state prepared barium titanate samples have similar textural properties to commercially available barium titanate. These samples have very small surface areas and total pore volumes.

For AP-$BaTiO_3$ samples, the use of ethanol/toluene solvent provided the smallest crystallites: an average of 6 ± 2 nm, compared to commercial CM-$BaTiO_3$ (76 nm) and commercial nanosized NCM-$BaTiO_3$ (36 nm) (Table 3.3).

Table 3.3 Characteristic Properties of Different $BaTiO_3$ Samples

$BaTiO_3$ Sample (alcohol in solvent)	Average crystallite sizes (nm)	Surface area (m^2/g)	Total pore volume (cm^3/g)	Average pore sizes (Å)
Commercial CM-$BaTiO_3$	76	3	0.009	110
Nanosized NCM-$BaTiO_3$	36	19	0.16	330
SSR-$BaTiO_3$	200	1	0.02	125
AP-$BaTiO_3$ (ethanol)	6	175	0.43	100
AP-$BaTiO_3$ (isopropanol)	12	101	0.23	92

In contrast to AP-$SrTiO_3$, the calcination of AP-$BaTiO_3$ in air caused the formation of a carbonate phase that can clearly be seen in the XRD pattern (Figure 3.10). The organic residues in the aerogel-prepared materials were removed by heat-treating the aerogels in vacuum, followed by calcination in air or oxygen (Figure 3.11). Calcination aerogels showed an increase in crystallite size (Table 3.4).

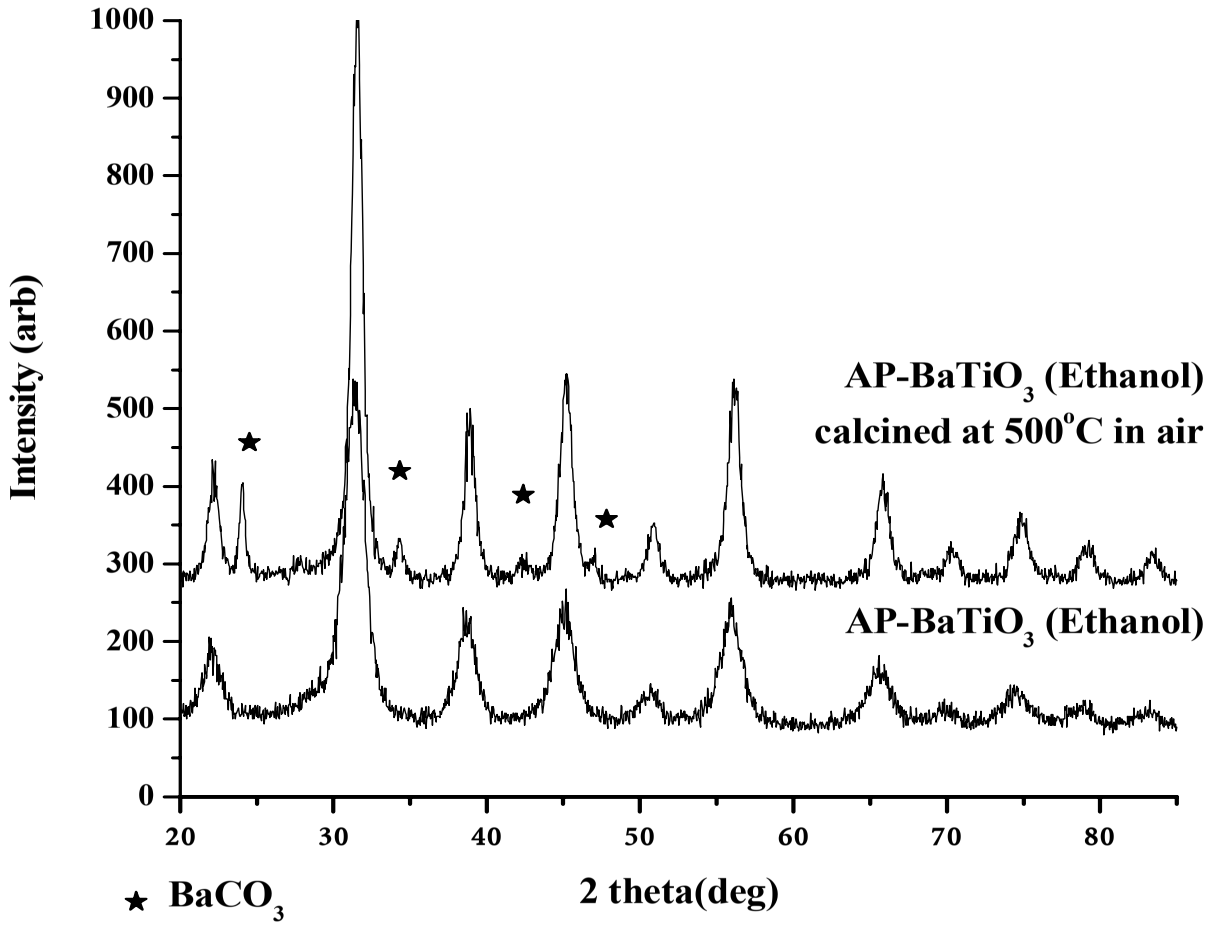

Figure 3.10 Powder XRD Patterns of AP-BATiO$_3$ (Ethanol) Calcined in Air at 500 °C with a BaCO$_3$ Phase vs. Freshly Prepared Sample of AP-BaTiO$_3$ (Ethanol)

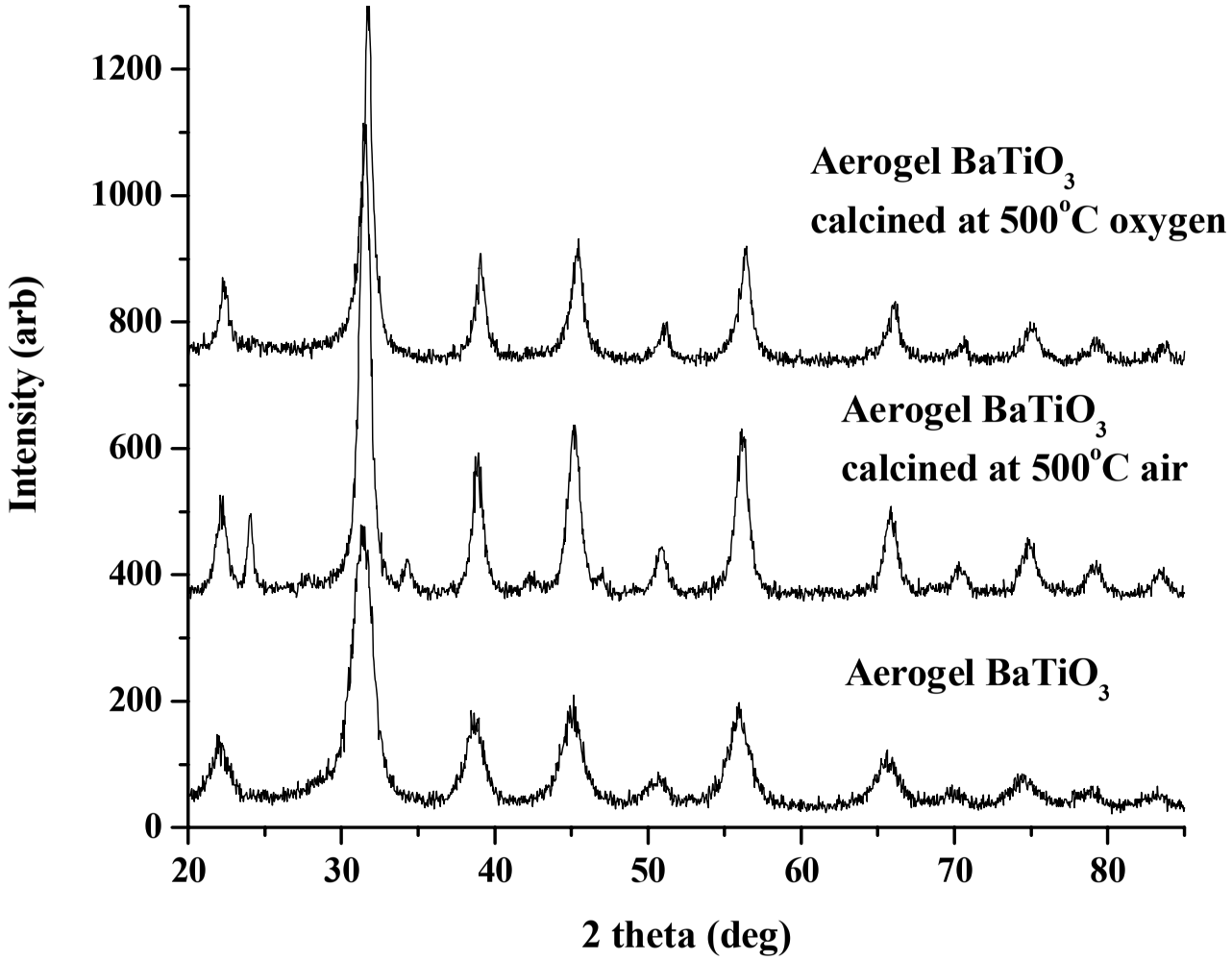

Figure 3.11 Calcination of AP-$BaTiO_3$ (Ethanol) in Air and Oxygen at 500 °C

Table 3.4 Characteristic Properties of AP-$BaTiO_3$ (Ethanol) Calcined at Different Temperatures in Air

Temperature of calcination (ºC)	Average crystallite size (nm)	Surface area (m^2/g)	Total pore volume (cm^2/g)	Average pore size (Å)
265	6	175	0.43	100
400	9	89	0.37	170
500	11	45	0.39	350

Significant crystallite size increase was observed for the aerogel prepared $BaTiO_3$ powders during calcination; the average crystallite sized increased almost double after calcination in air at 500°C.

3.3.4 Transmission electron microscopy

The characteristic property of powder materials is their particle sizes. Although the X-ray diffraction reveals the structure and the average size of the particles, it doesn't provide shape and size distribution of the crystallites. Fortunately, transmission electron microscopy (TEM) can give a real space image on the distribution of particles, their surface and shape [6]. With a finely focused electron probe, not only imaging of materials is possible, but also a single particle can be identified. Besides, electron microscopy shows the shape and state of agglomeration of particles.

Samples were placed onto a carbon-coated copper grid by physically interacting the grid and powders, and analyzed to see the particles that remained adhered to the grids. The TEM studies were performed using a Philips CM 100 (Biology Department, KSU).

The crystallite morphology of the solid-state and aerogel prepared strontium titanate samples was observed by TEM (Figures 3.12-3.15). The agglomeration of primary particles

(crystallites) is caused by van der Waals forces; and this tends to form secondary particles (agglomerates). In aerogel samples, crystallite sizes after calcination were slightly larger in comparison with crystallites of freshly prepared aerogels. All crystallites had uniform spherical shapes with a size distribution near 8 nm for synthesized AP-$SrTiO_3$ (ethanol) and near 10 nm for calcined AP-$SrTiO_3$ (ethanol) at 500 °C in air. The shapes of aerogel samples have a defined spherical form and sizes are relatively monodispersed, while solid-state prepared samples have non-uniform shapes and polydispersed sizes.

The crystallite morphology of AP-$BaTiO_3$ (isopropanol) after heat treatment in vacuum and calcination in air is presented in Figure 3.15. The heat treatment in vacuum did not cause significant changes in crystallite sizes; however, the calcination in air or oxygen increased the AP-$BaTiO_3$ crystallite size to almost double the original size.

Heat treatment in vacuum of AP-$BaTiO_3$ caused the formation of pure carbon (dark grey color). Calcination in air removed the coloring, but also formed the $BaCO_3$ phase. The formation of a carbonate phase was inhibited by calcination of AP-$BaTiO_3$ in oxygen. This procedure was done in a Schlenk tube under a flow of pure oxygen at 500°C for oxidation and removal of organic residuals. The XRD pattern confirmed the absence of a carbonate phase (Figure 3.11).

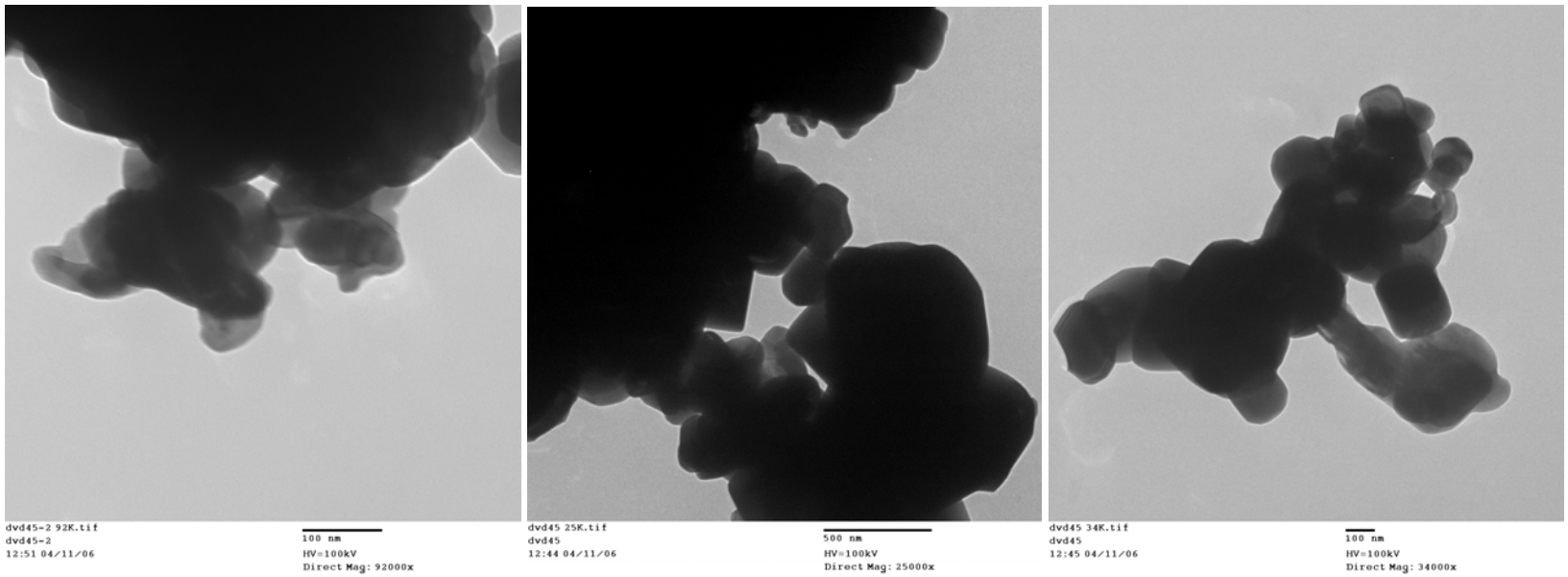

Figure 3.12 Transmission Electron Micrographs of SSR-$SrTiO_3$ Prepared at 1100 °C

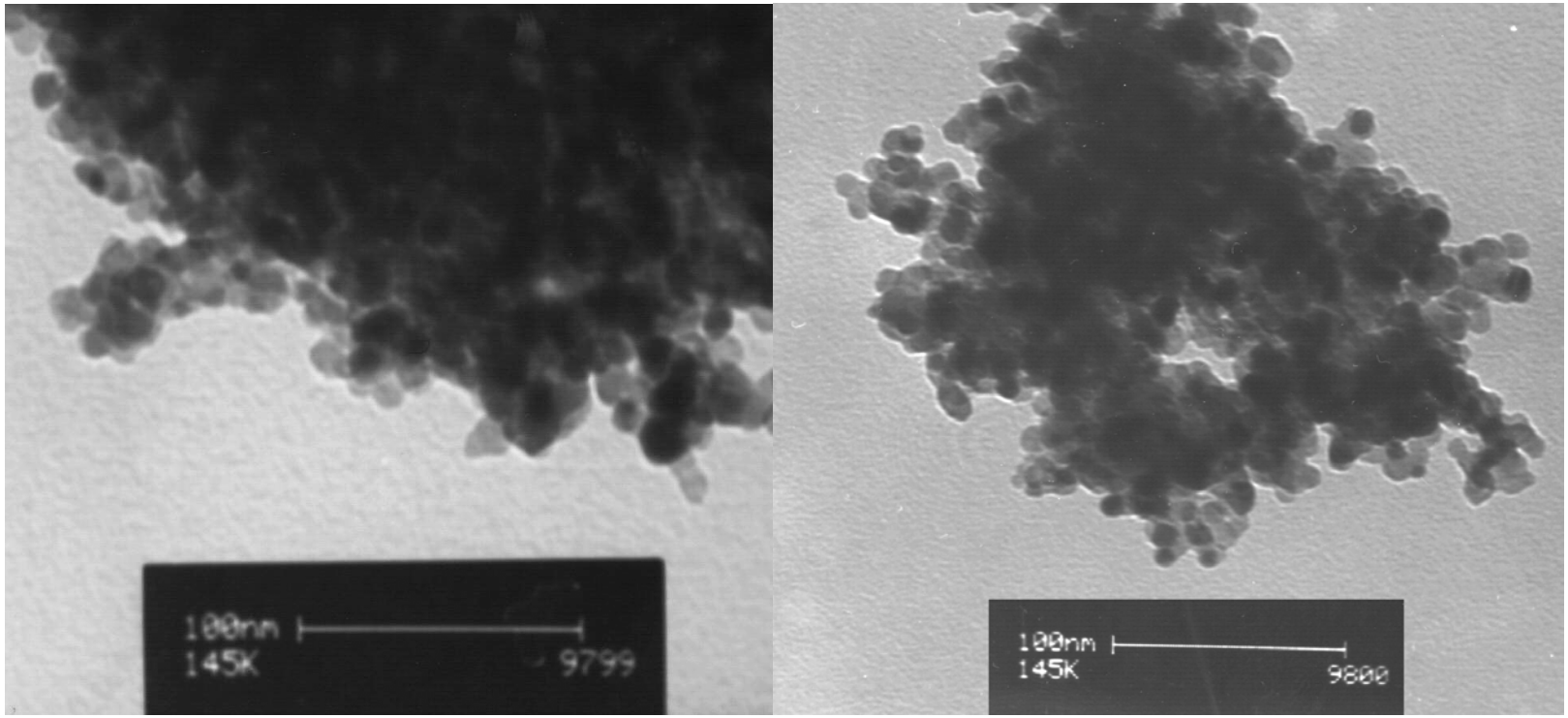

Figure 3.13 Transmission Electron Micrographs of AP-$SrTiO_3$ after Synthesis (left) and after Calcination in Air at 500 °C (right)

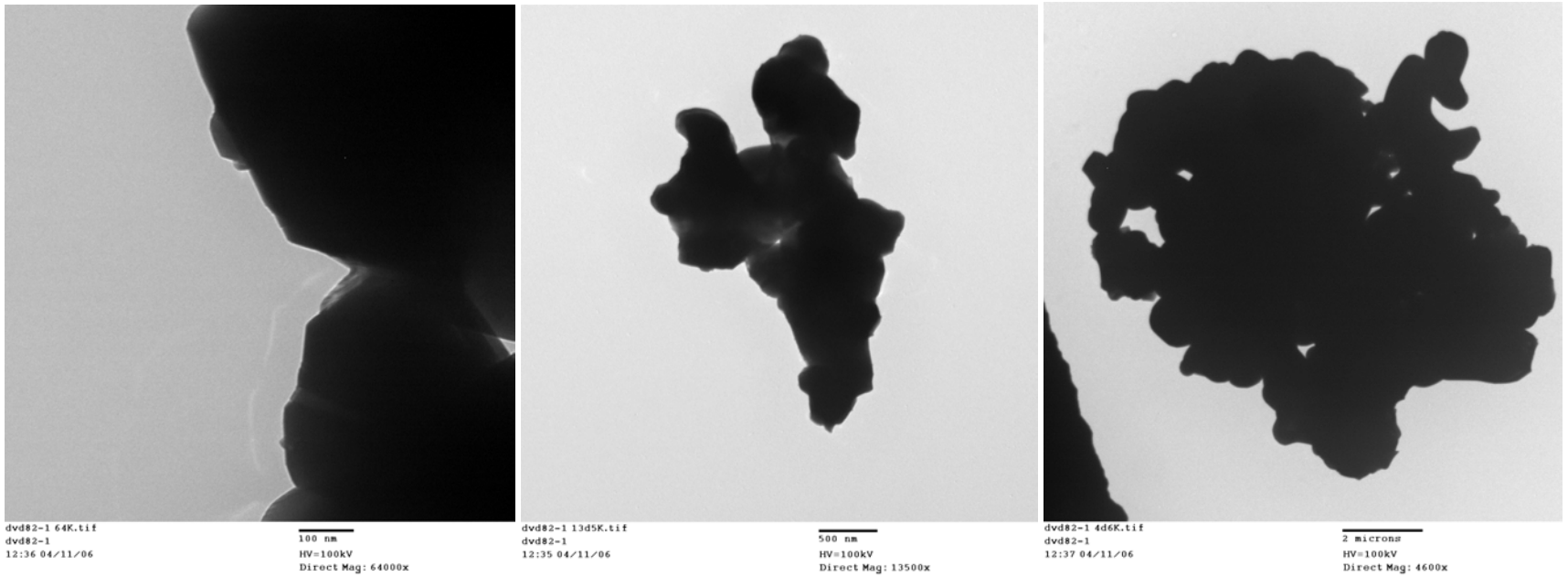

Figure 3.14 Transmission Electron Micrographs of SSR-$BaTiO_3$ Prepared at 1100 °C

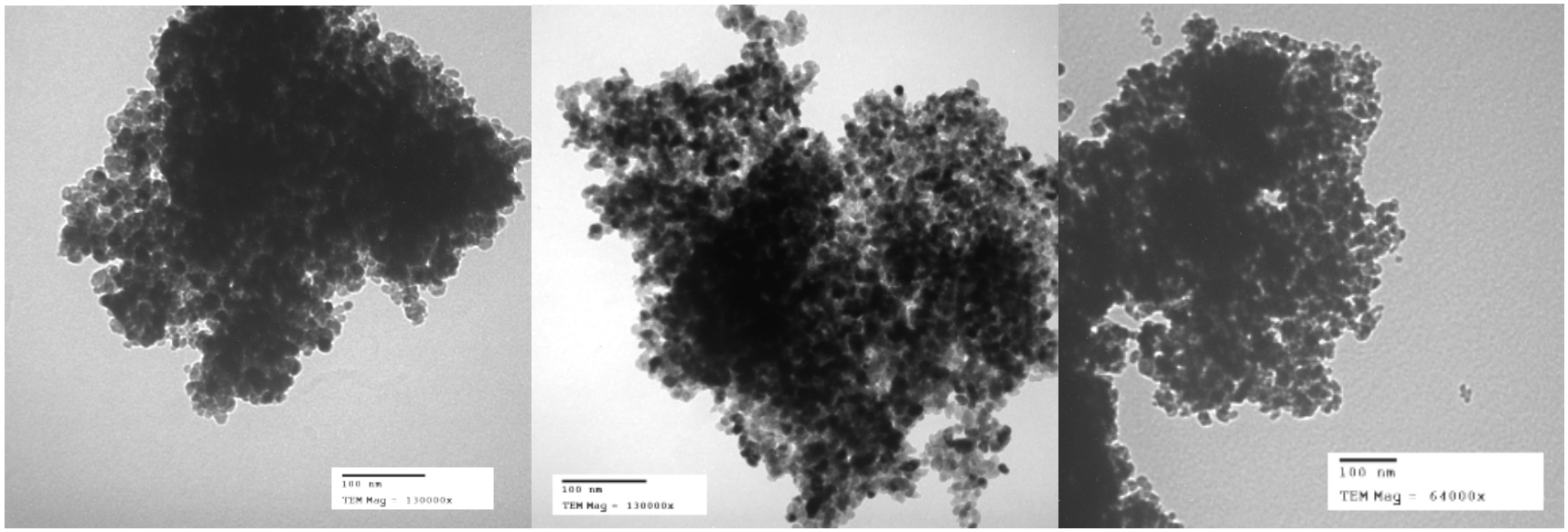

Figure 3.15 Transmission Electron Micrographs of AP-$BaTiO_3$ (Isopropanol) Samples after Synthesis (left), Heat Treated in Vacuum at 500 °C (middle), and Calcined in Air at 500 °C (right)

3.3.5 Elemental analysis

The content of organic residues in aerogel products, which arise from the organic components involved in the sol–gel process, was studied by CH analysis at Galbraith Laboratories, Inc. (Appendix B). Elemental analyses for carbon and hydrogen content were performed on freshly prepared and calcined aerogel samples.

The presence of organic residues after supercritical drying can significantly influence the physical and chemical properties of aerogel-prepared samples. In order to remove the organic residues, aerogel-prepared samples were heat treated in vacuum and/or calcined in air. After heat-treating AP-$SrTiO_3$ in vacuum, the sample color changed to dark grey, due to the pure carbon formed from the degradation of residual organics. Calcination in air allows nearly complete removal of residuals. The elemental carbon content in fresh AP-$SrTiO_3$ was 1.86 %, and the elemental H content was 0.70 %. The presence of carbon and hydrogen in a 500 °C-calcined sample significantly decreased to <0.5 % for both C and H.

3.3.6 Thermogravimetric analysis

Thermogravimetric studies (TGA-50, Shimadzu) shows that heating a freshly prepared aerogel sample in air causes the desorption of physically adsorbed solvent and water from the surface at 100-200ºC and decomposition of residual organic groups into carbon dioxide at 300-500ºC (Appendix C). This method was used to determine the weight loss of organic residuals during the heat treatment. Attention must be directed to the removal of organics to avoid undesirable blackening of the sample from the reduction of organic residuals into pure carbon.

Two major weight losses were observed. The first weight loss occurs during heating to 100°C and can be attributed to the remove of physisorbed water. The second weight loss occurs at 400°C which is due to the removal of chemisorbed water and organic residuals of solvent.

3.4 Discussion

The alcohol–toluene mixture was essential for obtaining mixed metal oxides with high surface areas and small crystallite sizes. The usefulness of a binary solvent (methanol–benzene)

was first noticed by Teichner and co-workers almost 30 years ago [7]. From long and continuous study of aerogel syntheses, we have found that a mixture of alcohol and hydrophobic solvent favors the production of high-quality aerogels. The use of alcohol without hydrophobic solvent yields an aerogel with significantly lower surface area [8]. Toluene in the binary solvent apparently serves to speed up gelation and perhaps to reduce surface tension at the gas–liquid–pore walls. This causes less dense and more porous wet gels to form of lower mass fractal dimension, leading to products with higher surface areas. Metal alkoxides are soluble in toluene and although alcohol is needed to aid hydrolysis, rates are faster in the presence of toluene. The role of alcohol is also important for the preparation of metal alkoxide, which is based on the zero-valent metal reacting directly with the alcohol.

Different alcohols in mixture with toluene lead to aerogels with different properties - crystallite size, surface area, pore-size distribution - thereby requiring studies of the alcohol effect on aerogel products. Ethanol in mixture with toluene was the best solvent choice to synthesize $SrTiO_3$ and $BaTiO_3$ aerogels with the highest surface areas and smallest crystallite sizes. The influence of this binary solvent on the aerogel process is not clear and requires further investigations. However, the gel stability was altered by the use of an organic solvent such as ethanol and powders prepared in ethanol exhibited a more uniform particle size distribution.

By the modified aerogel procedure, it is possible to produce pure powders of strontium and barium titanates with very small crystallite sizes and high surface areas. The morphology, as determined by powder XRD and TEM, indicates a crystalline nature with very small crystallites, and XRD and TEM results are in good agreement with respect to crystallite size. The high surface areas of aerogel-prepared samples correspond to their high total pore volume. The comparison of two samples (NCM-$SrTiO_3$ and AP-$SrTiO_3$ (methanol)) with similar crystallite sizes and pore sizes accentuates the big difference in total pore volume (Table 3.1).

Temperature treatment is a crucial step and must be done carefully in order to preserve the high surface area and total pore volume of the powders. Heat treatment in vacuum does not greatly influence crystallite size, while calcination in air increases the AP-$BaTiO_3$ crystallite size significantly. The surface area, however, is a parameter that is noticeably affected by heating. It decreases significantly due to a decrease in total pore volume. With calcination in air at 500 °C, the AP-$SrTiO_3$ surface area decreases by 40 % and the AP-$BaTiO_3$ surface area decreases to 25 % of the initial value (Tables 3.2 and 3.4). The formation of the $BaCO_3$ phase during

calcination in air is not desirable. Heat treatment in vacuum prevents formation of carbonate, but produces carbon impurities in the sample. Calcination in O_2 solves the carbonate formation problem although the surface area also decreases significantly.

3.5 Conclusions

Alkaline-earth metal titanates ($SrTiO_3$ and $BaTiO_3$) were synthesized by solid-state reaction through the reaction of alkaline-earth metal carbonate and titanium oxide, and by an aerogel procedure through the sol-gel process by hydrolysis of alkaline-earth metal alkoxide and titanium alkoxide with followed by supercritical drying.

The solid-state reaction produces materials with non-uniform shapes and polydispersed sizes. This morphology of crystallites arises from the high temperature calcination synthesis where the big particles grow by sintering and densification of small ones. The sol gel process is particularly attractive for the synthesis of multicomponent materials with binary or ternary metal composition using several metal alkoxides. Multicomponent gels can be thermochemically converted to form nanocomposite oxide powders.

The aerogel method for synthesis of nanosized $SrTiO_3$ and $BaTiO_3$ powders has been satisfactorily developed. This method permitted larger surface areas and smaller crystallite sizes to be obtained in comparison with the traditional solid-state reaction method. Another big advantage of the aerogel procedure is the significantly lower calcination temperature for the preparation of pure crystalline titanates.

Different alcohols mixed with toluene were used as solvents for synthesis. AP-$SrTiO_3$ and AP-$BaTiO_3$ were prepared in either an ethanol or isopropanol mixture with toluene in a toluene-to-alcohol volume-ratio of 1.5. The mixture of metal alkoxides and alcohol-toluene was hydrolyzed with water by a slow, dropwise addition, to transform it into a gel. Supercritical conditions were achieved by heating in an autoclave under a nitrogen atmosphere. The solvent vapors were removed by quick venting off, and the residual solvent in the prepared aerogel powders was removed by heat treatment (calcination in air for $SrTiO_3$, and calcination in oxygen for $BaTiO_3$).

A binary mixture of alcohol–hydrophobic solvent (ethanol–toluene) was the best solvent for obtaining high-surface-area $SrTiO_3$ and $BaTiO_3$ by the aerogel-modified procedure. The

presence of toluene in the mixed solvent changes gelation rates and lowered the surface tension in the gel pores, yielding more porous, less dense wet gels that were processed into aerogel-prepared products with a higher surface area and a higher pore volume. The presence of ethanol in the mixture solubilized the water added for hydrolysis in the homogeneous ethanol–toluene–metal alkoxides mixture.

Transmission electron micrographs confirmed the crystallite sizes of aerogel-prepared samples derived from XRD. Strontium titanate prepared by the above method has a surface area of 160± 1 0 m^2/g and a crystallite size of 8 ± 2 nm in comparison with 1 m^2/g and 145 nm of the commercial CM-$SrTiO_3$, and 17 m^2/g and 25 nm of nanosized commercial NCM-$SrTiO_3$. Barium titanate has 175 m^2/g of surface area and 6 nm crystallite size compared to commercial CM-$BaTiO_3$, which is 3 m^2/g and 76 nm, and 19 m^2/g and 36 nm for commercial nanosized NCM-$BaTiO_3$.

Aerogel products contain some residual solvents after synthesis, which can be removed by high-temperature oxidation. Heat treatment in vacuum of AP-$SrTiO_3$ and AP-$BaTiO_3$ caused the sample color to change to dark grey signaling the appearance of pure carbon from the degradation of the residual organics. Calcination in air almost fully removed residuals for AP-$SrTiO_3$ at 500 °C and caused a slight increase in crystallite sizes. Aerogel products contain some residual solvents after synthesis, which can be removed by simple calcination at 500 °C in air for AP-$SrTiO_3$. Calcination of AP-$BaTiO_3$ in air, however, generates the $BaCO_3$ phase; to prevent this, calcination in oxygen is necessary.

The high surface area in titanates tends to impart interesting properties as catalysts, sorbents, and electronic materials. Details concerning this surface chemistry will be reported later in the Chapter 6.

It should also be pointed out that the modified aerogel synthesis (MAP) can be used to prepare intimately mixed metal oxide nanomaterials of various compositions, including MgO–Al_2O_3, CaO–Al_2O_3, SrO–Al_2O_3, BaO–Al_2O_3, MgO–SrO, and others [9]. These materials invariably possess superior capacities and kinetics as sorbents for gases and toxic chemicals, and represent a new family of mesoporous inorganic mixed metal oxides [10].

3.6 References

[1] S. Braunauer, P. Emmet, and E. Teller, J. Am. Chem. Soc., 60 (1938) 309.

[2] S. Braunauer, L.S. Deming, W.S. Deming, and E. Teller, J. Am. Chem. Soc., 62 (1940) 1723.

[3] J.W. Mc Bain, J. Am. Chem. Soc., 57 (1935) 699.

[4] L.H. Cohan, J. Am. Chem. Soc., 60 (1938) 433.

[5] B.D. Cullity, Elements of X-Ray Diffraction, Addison-Wesley Publishing Co. Inc., CNM book, 1978.

[6] P.B. Useck, J.M. Cowley and L. Eyring eds. High Resolution Transmission Electron Microscopy and Associated Techniques, New York, London, Amsterdam, Oxford University Press, 1988.

[7] S. J. Teichner, G. A. Nicolaon, M. A. Vicarini, and G. E. E. Gardes, Adv. Coll. Interface Sci., 5 (1976) 245.

[8] S. Utamapanya, K. J. Klabunde, and J. R. Schlup, Chem. Mater., 3 (1991) 175.

[9] C. L. Carnes, P. N. Kapoor, and K. J. Klabunde, Chem. Mater., 14 (2002) 2922.

[10] G.M. .Medine, V. Zaikovskii, and K. J. Klabunde, J. Mater. Chem., 14 (2004) 4, 757.

Chapter 4 : Photooxidation of acetaldehyde by titanates

4.1 Introduction

Aerogel materials are potential candidates for catalysis due to their unique morphological characteristics and chemical properties. A major advantage of them is their high surface area and high number of active sites per gram of aerogel material respectively. The porous structure of aerogel oxides gives good access for molecules and resistance to thermal coarsening.

The mixed metal oxide aerogels of $NiO\text{-}Al_2O_3$ and $NiO\text{-}SiO_2\text{-}Al_2O_3$ were studied for selective oxidation [1, 2], $NiO\text{-}Al_2O_3$ for nitroxidation [3], $Fe_2O_3\text{-}Cr_2O_3\text{-}Al_2O_3$ for selective reduction [4], $Fe_2O_3\text{-}SiO_2$ and $Fe_2O_3\text{-}Al_2O_3$ selective hydrogenation [5, 6]. For this organic synthesis, aerogel catalysts give high selectivity; however, the activity is not outstanding.

Aerogel materials can be used for the protection of the environment and solving environmental problems by the reduction or decomposition of hazardous wastes, toxic air contaminants, toxic chemicals (volatile organics, solvents, pesticides, chlorophenols, heavy metals etc.), decrease of pollutant emissions or exhaust gases from automobiles, and purification of contaminated groundwaters [7].

It is desirable to decompose these toxic compounds and pollutants so that only CO_2, H_2O, and N_2 are released in the atmosphere. Traditionally, to fully decompose these compounds the catalysis at a temperature from 200 to 1200°C is necessary. This catalytic process is energy intensive and not economically feasible for low pollutant concentrations. Besides, high temperature causes oxide sintering and decrease of the active catalytic surface. Thus, processes that can decompose low pollutant concentrations under ambient conditions are needed.

The photocatalytic process can be used for the detoxification of air pollutants at low concentration and achieve complete contaminant mineralization. Aerogel prepared semiconductor metal mixed oxides of strontium titanate with a surface area of 160 m^2/g and barium titanate with a surface area of 175 m^2/g may have advantages for the photocatalytic decomposition of volatile organic compounds or pollutants, so further investigations are necessary.

4.2 Photoactivity under light irradiation

The discovery of photoinduced water splitting on titanium dioxide electrodes by Fujishima et al. in 1972 opened new possibilities for the application of semiconductor solid materials for catalysis induced by light irradiation [8, 9]. The production of hydrogen from water was based on a photoelectrochemical cell (PEC) where TiO_2 single crystal was a photoanode and Pt metal was a cathode. The UV light irradiation of the titanium oxide surface causes the separation of holes and electrons by electron migration to the conduction band and hole production in the valence band (Figure 4.1). The generation of electrons and holes in the conduction and valence bands occurs only when light with energy larger than the band gap ($h\nu \geq E_g$) is incident on the catalyst and excites it. A wider bang gap requires shorter wavelengths.

The photogenerated electrons and holes act as reducers and oxidizers and split water by reduction of water molecules with electrons to form H_2 and by oxidation with holes to produce O_2:

$$TiO_2 + h\upsilon \rightarrow h^+_{vb} + e^-_{cb} \qquad (4.1)$$

Valence band holes (h^+_{vb}) are powerful oxidants (+1.0 to +3.5V versus Normal Hydrogen Electrode, NHE) and can split water forming oxygen gas molecules and/or hydroxyl radical species.

$$2\ h^+_{vb} + H_2O \rightarrow 2\ H^+ + \tfrac{1}{2}\ O_2 \qquad (4.2)$$

$$h^+_{vb} + H_2O \rightarrow H^+ + OH^{\bullet}(ads)\ \ (E = 2.85eV) \qquad (4.3)$$

For H_2 gas conduction band electrons are good reductants (+0.5 to –1.5V versus NHE) and can form a hydrogen gas molecule and/or superoxide species.

$$2\ e^-_{cb} + 2\ H^+ \rightarrow H_2 \qquad (4.4)$$

$$e^-_{cb} + O_2 \rightarrow O^{2-} \quad (E = -0.13eV) \qquad (4.5)$$

For H_2 gas evolution the conduction band potential of the semiconductor must be more negative than the H_2 evolution potential (- 0.4 V (Standard Hydrogen Electrode, SHE) in acid solution or – 1.2 V (SHE) in alkaline solution). Similar, for the O_2 gas evolution the valence band potential of the semiconductor must be more positive.

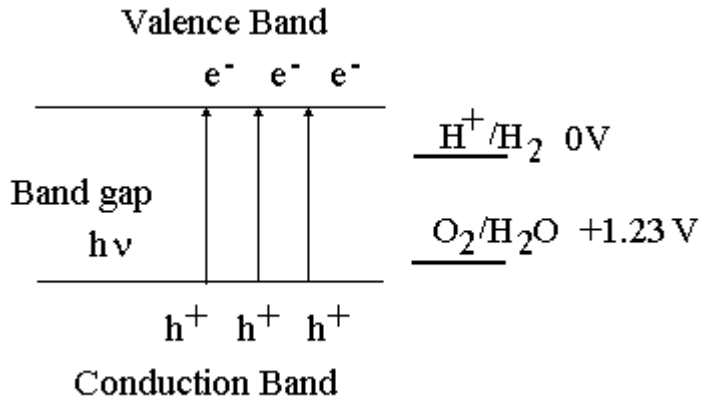

Figure 4.1 Semiconductor Photocatalyst for Water Photolysis

Holes and electrons tend to recombine, so to prevent recombination and a decrease in photoactivity, platinum metal cocatalyst was deposited on the titania. In this case, electrons were migrating to the metal and were trapped there, while holes were staying on the surface of titanium dioxide. Hydrogen gas was produced on the surface of Pt metal while oxygen bubbles were formed on the titania surface.

Four years later in 1976 it was found that strontium titanate ($SrTiO_3$) is also an efficient photocatalyst for the H_2 production from water and for the decomposition of organic compounds under the UV irradiation [10]. The $SrTiO_3$ sintered powder electrodes and the single crystal electrodes showed almost the same quantum efficiency, action spectra and potential of photocurrent. It was also found that $SrTiO_3$ had higher negative potential than that of TiO_2 and was more efficient for hydrogen production.

The desirable band gap of the semiconductor for optimum utilization of solar energy (visible light) for water splitting should be around 2 eV [11]. A non-oxide material such as

cadmium sulfide (CdS) has a matching band gap of 2.4 V and is a very good photocatalyst candidate for water photolysis and hydrogen production. However, this chalcogenide semiconductor undergoes easy photocorrosion, and rapidly loses photoactivity due to the surface covering with reduced sulfur. Oxide materials have higher stability during photocatalysis, but have wide band gaps and do not absorb visible light. Among conventional semiconductor oxides, only several show activity for water photolysis (Figure 4.2) and all of them requires UV light irradiation due to wide band gaps.

With time, the PEC cells were replaced by particulate systems [12-16]. The application of the monoccrystalline system (semiconductor single crystal) was very expensive, while the polycrystalline system (semiconductor powders in suspension) is simpler, requires low construction and maintenance cost and gives high light absorption efficiency.

The cocatalysts of noble metals deposited on the semiconductor oxide prevent the recombination of holes and electrons and increase the photoactivity toward water splitting. A Pt metallized powdered TiO_2 semiconductor (Pt/TiO_2) can work like a TiO_2-Pt photoelectrochemical cell (PEC). Pt/TiO_2 forms small amount of H_2 and no O_2 in pure water under UV irradiation in the absence of external bias. Pt/TiO_2 can not photodecompose gas-phase water in so called “dry state”; however, water was decomposed in a “wet state” when Pt/TiO_2 was moistened with a small amount of water.

$Pt/SrTiO_3$ decomposes gas-phase water into H_2 and O_2 when it is coated with basic material (NaOH). $Rh/SrTiO_3$ shows activity for water photolysis with 1.2 % maximum quantum yield.

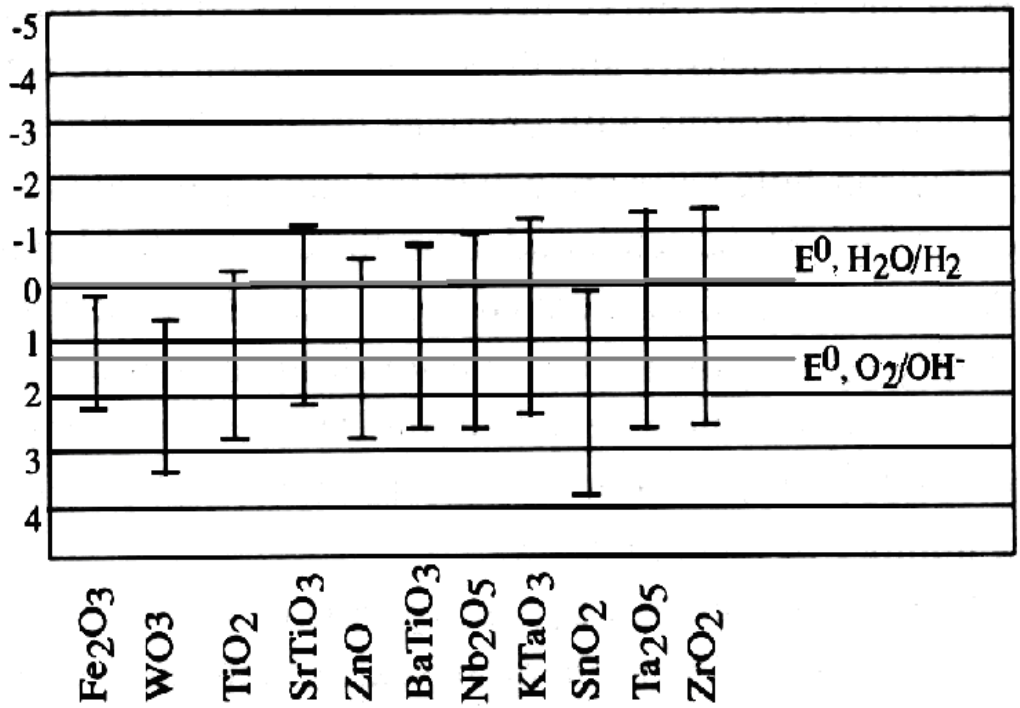

Figure 4.2 Semiconductor Oxide Band Gaps and Potentials

Photocatalytic reactions can be divided into two categories: down hill and up hill reactions. Water photolysis is an up hill reaction and has a high positive change in the Gibbs free energy (ΔG^0 = 237 kJ/mol) [17], while the photodegradation of organic compounds in the presence of oxygen is a down hill reaction (Figure 4.3). In down hill reactions, the catalyst produces active species of O_2^-, H^+, and $OH^\bullet$ (See reactions 4.3 and 4.5) for the oxidation of organic compounds. The studies of down hill reactions revealed that TiO_2 is an excellent catalyst for the photocatalytic degradation of organic compounds [18].

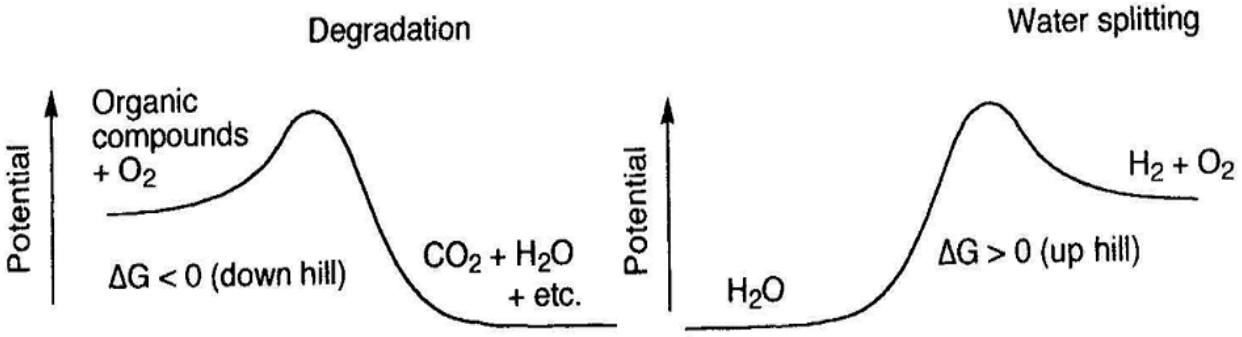

Figure 4.3 Photocatalytic Reactions: Photoinduced Reaction (down hill) and Photon Energy Conversion Reaction (up hill) [17]

TiO_2 was extensively studied for the photocatalytic degradation of volatile organic compounds (VOCs), such as aldehydes, aromatic compounds and chlorinated hydrocarbons [19-22]. The full photocatalytic degradation of these compounds gives simple CO_2 and H_2O (HCl for chlorine containing organic compounds) reaction products. The full degradation of acetaldehyde into CO_2 and H_2O was achieved in batch type reactors [23, 24]. The degradations of trichloroethylene (TCE) and benzene on TiO_2 under UV irradiation were also reported [22, 25, 26]. All reported investigations on the photodecomposition of organic compounds were mostly performed at elevated temperatures.

TiO_2 is not active for the oxidation of CO which was formed during the oxidation of benzene. The addition of Pt to TiO_2 by the photodeposition from $H_2PtCl_6/6H_2O$ enhances its reactivity for the CO oxidation under UV light irradiation. The difference in the reactivity of photocatalyst depends on the kind of an active oxygen species formed on the Pt/TiO_2 and reactants. It was also found that the addition of Pt enhances the stability of oxygen species (O^- and O_3^-) on the TiO_2 surface:

$$CO + O_3^- \rightarrow CO_2 + O_2^- \text{ (UV light and presence of } O_2) \qquad (4.6)$$

While extended investigations were performed on titanium oxide, some studies have been done on other oxide semiconductor powders. It was found that they also exhibit photoactivity in the oxidation of alcohols, hydrocarbons, and CO [27]. Nanosized $SrTiO_3$ powders (5-13 nm, 46.7

m^2/g) were used for the photodegradation of phenol in water [28]. The NiO supported $SrTiO_3$ was studied for the photocatalytic production of H_2 and acetone from mixture of H_2O and 2-propanol in a gas phase. The photooxidation of C_2H_6 in the presence of O_2 went through the production of alcohol and aldehyde intermediates to the final products of CO_2 and H_2O. $BaTiO_3$ photochemicaly reduced aqueous silver cations and oxidized thin films of steric acid converting it into CO_2 and H_2O [29].

From the comparison of catalytic activity of catalyst samples prepared by different methods, it was found that their photocatalytic activity strongly depends on the preparative source. The conventional solid-state reaction gives materials with small surface areas and large particle, while novel wet methods (sol-gel, aerogel) can offer catalyst materials with significantly higher surface areas which can benefit the photocatalysis. Besides, the xerogel or aerogel materials have higher purity and less crystal defects. The study of these novel materials for photocatalysis and comparison with already available samples prepared by conventional methods will bring more understanding of the complex process of catalysis induced by light irradiation on the surface of the semiconductor oxide.

4.2.1 Design of photocatalysts of high activity

Many factors influence the activity of a photocatalysts including the number of active sites in the catalyst, mobility and life time of electrons and holes, charge separation and recombination rate. These factors are strongly affected by bulk properties of material. The activity can be significantly influenced by the textural characteristics of the catalyst. The high specific surface area of the catalyst favors catalysis due to presence of more active reaction sites and higher rate of surface reaction of electrons or holes. However, the surface where the light irradiation does not reach does not contribute to the photoactivity.

Small particle size of catalyst is also in favor of higher photoactivity due to smaller distances for electrons and holes to migrate to the surface. It takes longer time for the photogenerated e^- and h^+ to reach the surface in larger size particles and recombination can occur more often. When the dimensions of semiconductor particles decrease, the energy levels shift according to the quantum size effect. The shift of the conduction band may accelerate the reduction, while that of the valence band may increase the oxidation reaction. However, when

the size of the particle decreases, the transfer efficiency of electron-hole separation decreases too.

Crystal structure of the catalyst material is an important factor and can influence catalytic activity by the rate of crystallinity and presence of crystal defects in the catalyst material. Higher crystallinity and less crystal defects allows a slower rate for the recombination of the holes and electrons. However, highly defective surface materials may also have high photocatalytic activity due to the electron or hole charge transfer between defects.

Good catalysts have high activity and selectivity toward promoting a desired reaction, high stability toward resistance to degradation, and they stay active over many catalytic cycles. Very often high activity and selectivity correlate with surface structure of the catalyst and the amount of active sites on this surface.

Textural properties can significantly influence the photocatalytic properties of a catalyst. Surface defects such as surface oxygen vacancies can act as photocatalytic sites and under UV irradiation [30]. O_2 can be absorbed by surface defects and form superoxide ions (O_2^-) by interaction with electrons [31, 32].

The uniqueness of high surface nanosized materials and possible advantages for the decomposition of organics under ambient conditions when illuminated with light attracts attention toward application of aerogel prepared samples for photocatalysis and investigation of their photoactivities. The designed photooxidation process includes the decomposition of volatile organic compounds on the surface of the catalyst in the presence of atmospheric oxygen at low temperature (room temperature, RT=25 °C) and under light irradiation (visible or UV). The oxidation of volatile organic compounds undergoes the following reactions:

$$\mathrm{VOC} + \mathrm{O_2} \xrightarrow[\text{catalyst}]{h\nu\ (\text{UV or visible})} \text{intermediates} \xrightarrow[\text{catalyst}]{h\nu\ (\text{UV or visible})} \mathrm{CO_2} + \mathrm{H_2O} \qquad (4.7)$$

The importance of these studies is based on possible numerous applications for water and air purification, self cleaning surfaces, and toxic chemical deactivation.

4.2.2 UV light irradiation

Titanium oxide has strong photooxidative ability and can be used for decomposition of volatile organics and air pollutants. The active oxygen species of hydroxyl radicals ($OH^{\bullet}$), oxide ions (O^-, O_2^-, O_3^-), and other active species produced from the reaction of holes and electrons with oxygen and water from air and OH^- groups and lattice oxygen of TiO_2, participate in the decomposition of organic compounds to form simple reaction products (Figure 4.4).

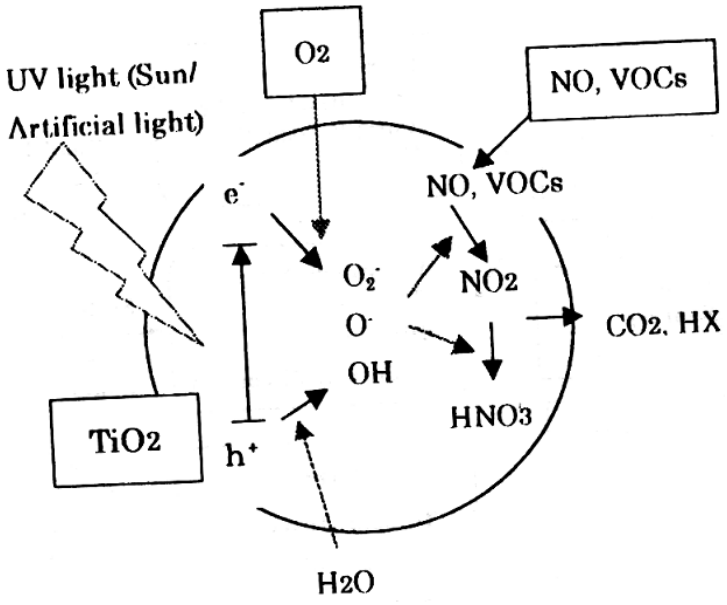

Figure 4.4 Photocatalytic Oxidation of Various Organic Compounds on TiO_2 Surface under UV Light Irradiation [33]

The active species on the surface of the catalyst can oxidize different air pollutants and volatile hydrocarbons, and halogenated hydrocarbons to form carbon dioxide, water and/or hydrogen halides. Besides, different sulfur oxides and nitrogen oxides can be oxidized to form sulfuric and nitric acids (H_2SO_4 and HNO_3).

The activity of $OH^{\bullet}$ radicals toward oxidation of different air pollutants is presented in Table 4.1. Common air pollutants like mercaptan (CH_3SH), hydrogen sulfide (H_2S), acetaldehyde (CH_3CHO) and formaldehyde (HCHO) can be easily decomposed. In addition, titanium oxide radicals have high activity toward the oxidation of some nitrogen and halogen

containing compounds (NO_2 and $CHCl=CCl_2$). In some cases however, titanium oxide was almost inactive for the oxidation of ammonium (NH_3), ethanol (C_2H_5OH), or trichloroethane (CH_3CCl_3).

Table 4.1 Rate Constant (k) for the Reaction of $OH^{\bullet}$ Radical with Air Pollutants at 298 K [33]

Pollutant	k	Pollutant	k	Pollutant	k
CO	1.3	CH_3OH	7.9	t-2-C_4H_8	700
NO_2	670	C_2H_5OH	1.6	CH_3CCl_3	0.1
NH_3	1.6	CH_3COOH	8.0	$CHCl=CCl_2$	21
SO_2	20	CH_4	0.06	$CCl_2=CCl_2$	1.7
CH_3SH	330	C_2H_6	2.5	C_6H_6	10
H_2S	48	C_3H_8	11	Toluene	61
HCHO	92	C_2H_4	90	m-Xylene	240
CH_3CHO	200	C_3H_6	300	C_6H_5Cl	6

Photooxidation of organic compounds is a complex process which undergoes several simultaneously running reactions with the production and consumption of different species on the surface, and this process is not fully understood. The adsorption and desorption steps when the reactants approach and adsorb on the surface and reaction products leave the surface can slow down the oxidation reaction and limit the whole process.

In aqueous suspensions of titanium oxide, the oxidation of organic compounds can go through direct and indirect oxidation. These two processes can go on simultaneously and the decomposition of acetic acid on titania particles under UV irradiation in deaerated environment is a good example (Figure 4.5). Indirect oxidation goes through the production of hydroxyl radicals ($OH^{\bullet}$) by the oxidation of water with holes. These radicals react with organics to form oxidized species or decomposed products. By direct oxidation, the organic compounds are oxidized on the surface by photogenerated holes.

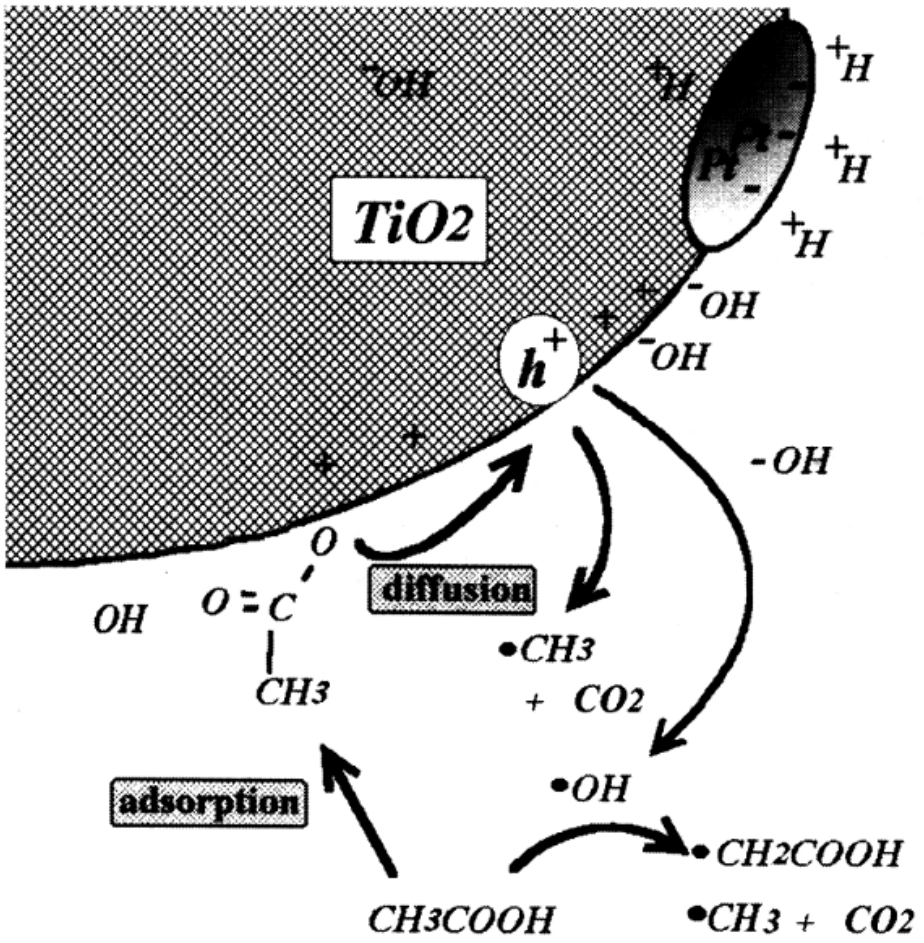

Figure 4.5 Oxidation of Acetic Acid on the TIO_2 under UV Irradiation and in Oxygen-free Environment [33]

It was found that strontium titanate ($SrTiO_3$) powders act similar to titanium oxide and is also photoactive for the oxidation of volatile organic compounds, alcohols, and hydrocarbons. A mixture of H_2O and 2-propanol were photocatalytically converted into H_2 and acetone on the $NiO/SrTiO_3$ surface. The photooxidation of C_2H_6 with O_2 over $SrTiO_3$ went via alcohol and aldehyde to final products of CO_2 and H_2O. $Pt\text{-}SrTiO_3$ cocatalyst assisted in the photoreduction of CO_2 with H_2 to CO in the presence and absence of water vapors, and side products such as methane, formaldehyde, and methanol (CH_4, CH_2O and CH_3OH) were also formed.

It is convincing that semiconductor oxide materials and aerogels in particular can demonstrate a wide range of applications for different catalytic reactions [34-36]:

1. Oxidation of air pollutants,
2. Photocatalytic reactions of volatile hydrocarbons (propylene, toluene, benzene),
3. Photocatalytic reactions of halogenated hydrocarbons (trichloroethylene, tetrachloroethylene, trichloroethane),
4. Oxidation of Nitrogen Oxides (NO_x).

4.2.3 Visible light irradiation

Unfortunately, all oxide semiconductors have wide band gaps and do not absorb visible light. In practice, they can not be used for the utilization of solar light energy. For efficient use of visible light from solar irradiation and to have high photoactivity, the doping of this oxide with metals (transition, noble) or nonmetals is required to create a bathochromic shift of the band gap energy. Another option is to induce external sensitization with dyes in order to harvest the visible light photons and transfer them to the catalyst.

The increase in photoactivity can be achieved by the application of organic photosensitizers ($Ru(bipy)_3^{2+}$) [37, 38] or by addition of platinum, palladium or nickel oxides [39, 40]. The distribution of a noble metal is very important and can be achieved by different deposition methods (co-precipitation, impregnation, photoplatinization) [41]. Doping with transition metal ions creates d donor and acceptor states in the forbidden area (between conduction and valence bands) of catalyst. This also improves trapping of the electrons and inhibits electron-hole recombination. Doped TiO_2 with Fe, Mo, V, Cr, transition metal ions are promising photocatalysts under visible light irradiation [42-44]. Nitrogen-doped TiO_2 catalysts showed photoactivity under visible light [45]. $TiO_{2-x}N_x$ was active for the acetaldehyde decomposition to CO_2 under visible light irradiation [46].

In this chapter, emphasis will be mainly put on the UV photoactivity of different catalysts. In the following chapter (Chapter 5), the doping of catalysts and their photoactivity properties under visible light irradiation will be studied more extensively. The results for visible light induced photoactivity for the degradation of acetaldehyde by different doped catalysts will also be discussed later.

4.3 Acetaldehyde photodecomposition studies

Acetaldehyde is a "probable human carcinogen" and hazardous air pollutant according to the EPA and is "ubiquitous" due in part to its appearance in vehicle exhaust, building materials (polyurethane foams, coatings), consumer products (adhesives, lubricants, inks, and nail polish) fruits, and etc. [47]. The U.S. Occupational Safety and Health Administration (OSHA) Permissible Exposure Limit (PEL) for acetaldehyde is 200 ppm.

The safe removal of or detoxification of these chemicals, possibly through decomposition on a catalytic nanoparticle surface, is therefore, a prime concern with regard to household safety. In addition, nanoparticles offer great opportunities for the development of reusable, solid catalysts in industries to replace the toxic liquid catalysts [48].

Titania based semiconductor oxides (TiO_2, $SrTiO_3$, and in limited cases $BaTiO_3$) are good UV photocatalysts that decompose volatile organic compounds and acetaldehyde in particular. The big band gap of this materials (3.2 eV for $SrTiO_3$, 3.1 eV for $BaTiO_3$, 3.0 eV for TiO_2 anatase) limits its application to a UV light region only ($\lambda < 400$ nm) (Figure 4.6). In this chapter, the results on acetaldehyde photooxidation in the gas phase over the solid-state and aerogel prepared strontium and barium titanate samples (SSR-$SrTiO_3$, SSR-$BaTiO_3$, AP-$SrTiO_3$, and AP-$BaTiO_3$) under UV light irradiation will be presented, discussed, and compared with the photoactivity of available samples of P25 Degussa (TiO_2), commercial and nanocommercial strontium and barium titanates (CM-$SrTiO_3$, CM-$BaTiO_3$, NCM-$SrTiO_3$, and NCM-$BaTiO_3$).

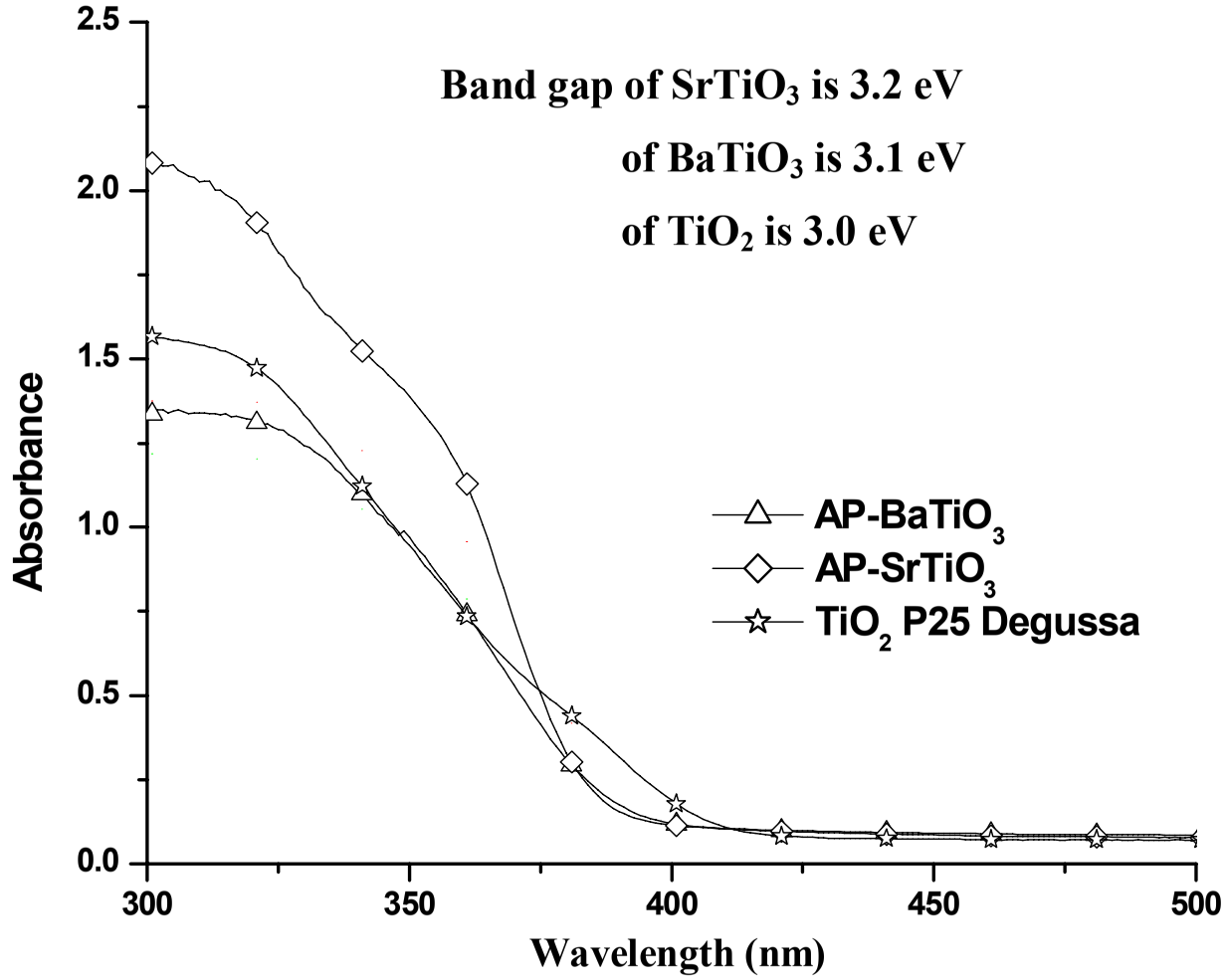

Figure 4.6 UV-visible Absorbance of Titanium Based Semiconductor Oxides

4.3.1 Experimental setup for photodecomposition reactions

The experimental setup included a light source, a static reactor and a circulating water thermostat (Figure 4.7). The light irradiation from the light of a 1000 W High pressure Hg lamp was employed to drive the photocatalytic oxidation of acetaldehyde over catalyst samples. Different filters (Oriel Spectra-Physics 57396, 59062, 57346, and 59680 filters) were used to pass UVA (320 nm < λ < 400 nm) or visible (420 nm < λ) light radiation. The IR irradiation was cut by passing it through the Newport 6123 liquid infrared filter. The light intensity for visible light was 7.6 mW/cm^2 (1.2 × 10^{16} photon/(s×cm^2)) and 8.4 mW/cm^2 for UV light, and it was measured with a Power Max 500D laser power meter from Molectron Detector, Inc.

The prepared photocatalysts were studied for visible and UV activity for gaseous acetaldehyde decomposition, which was carried out at room temperature. The powdered photocatalyst sample (100 mg) was placed into a circular glass dish to have a uniform surface and then mounted in an air filled cylindrical 305 mL glass reactor. The reactor was made of glass and had a quartz window for the passing of light irradiation. 100 μL of liquid acetaldehyde were introduced into the reactor. After that the reactor was closed and stirred continuously. All experiments were carried out at a constant temperature of 298 K by cooling with circulation water from a thermostat.

Before irradiation, the reaction was equilibrated for 30 minutes to allow the vaporization of the injected liquid acetaldehyde. The reactor is equipped with septum cups allowing multiple gaseous samples to be extracted. Gaseous samples (35 μL) were periodically (every 5-10 minutes) extracted from the reactor and injected into a GCMS to monitor the gaseous environment in the reactor.

A gas chromatograph with a mass-selective detector (GCMS-QP5000 from Shimadzu equipped with a phase XTI-5 capillary column, Restek Corp.) was used to follow the concentrations of acetaldehyde degradation and carbon dioxide evolution. The products were identified by following the characteristic masses and comparison of retention times of products with pure compounds. The separation of products and reagents was achieved in column, which was maintained at 313 K. The intensity of m/z = 44 peak was used to analyze the acetaldehyde and carbon dioxide. Concentrations of the two were calculated using calibration curves for the

pure compounds of known concentrations. The calibration curves are based on the known peak areas of known concentrations of carbon dioxide and acetaldehyde. Using this calibration, the peak areas for an unknown concentration can be recalculated into known concentrations (Figure 4.8). The concentrations of acetaldehyde decomposition and carbon dioxide evolution were plotted using Origin 6.1 software. The calibration parameters were incorporated into the Origin program data sheets to convert the peak areas into concentration of CO_2 and CH_3CHO (Figure 4.9).

The analysis in Figures 4.8 and 4.9 clearly shows the photoactivity towards the decomposition of acetaldehyde and carbon dioxide production under UV light irradiation. Without light, there was no activity toward CH_3CHO consumption or CO_2 production. Similarly, under visible light irradiation photoactivity was almost negligible, which can be explained by the inefficiency of the lower energy photons of visible light to excite electrons and holes within the wide band gap of $SrTiO_3$.

The linear fit for initial several experimental points can be used to calculate the slope which was later used for the initial reaction rate estimation. The comparison of the initial rates of different catalyst samples allows comparing their photoactivity. The slope from the linear equations for reaction curves are used to define the initial rates for the reaction. The standard deviation in parentheses shows how good the linear fit is (Figure 4.10).

Each catalyst sample has been studied for acetaldehyde photooxidation and the data from the GC experiment was plotted similar to Figure 4.9. For the sake of space, not all of them will be presented separately; for more clarity the results from these graphs will be combined in multicomponent graphs or summarized in tables.

The obtained photoactivity for different catalyst samples are compared with activity of P25 TiO_2 Degussa which is an unofficial standard catalyst for photoreactions under UV light (Figure 4.10). This comparison will allow seeing the efficiency and possible advantage over P25.

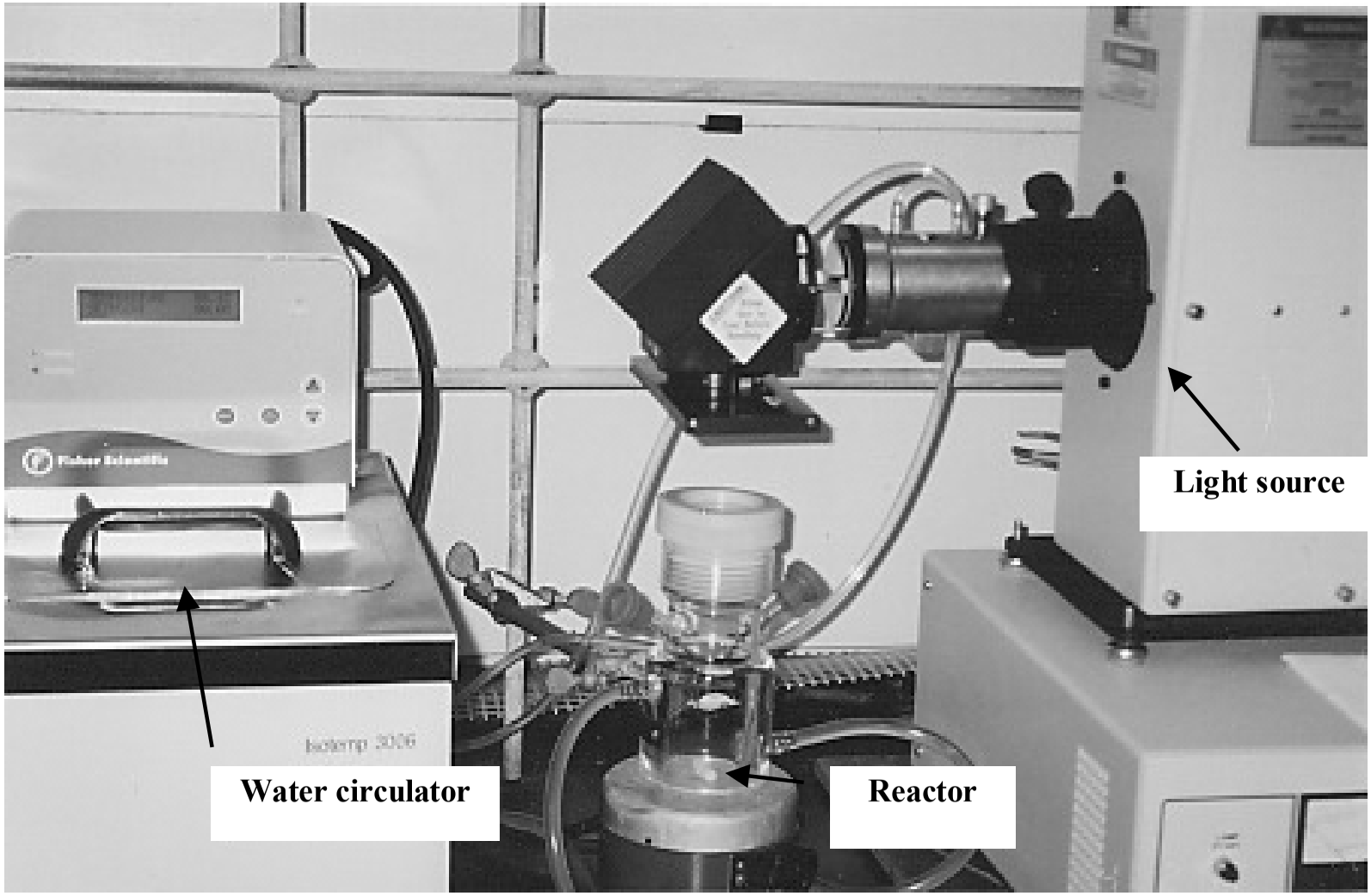

Figure 4.7 Experimental Setup for Photocatalysis Reactions

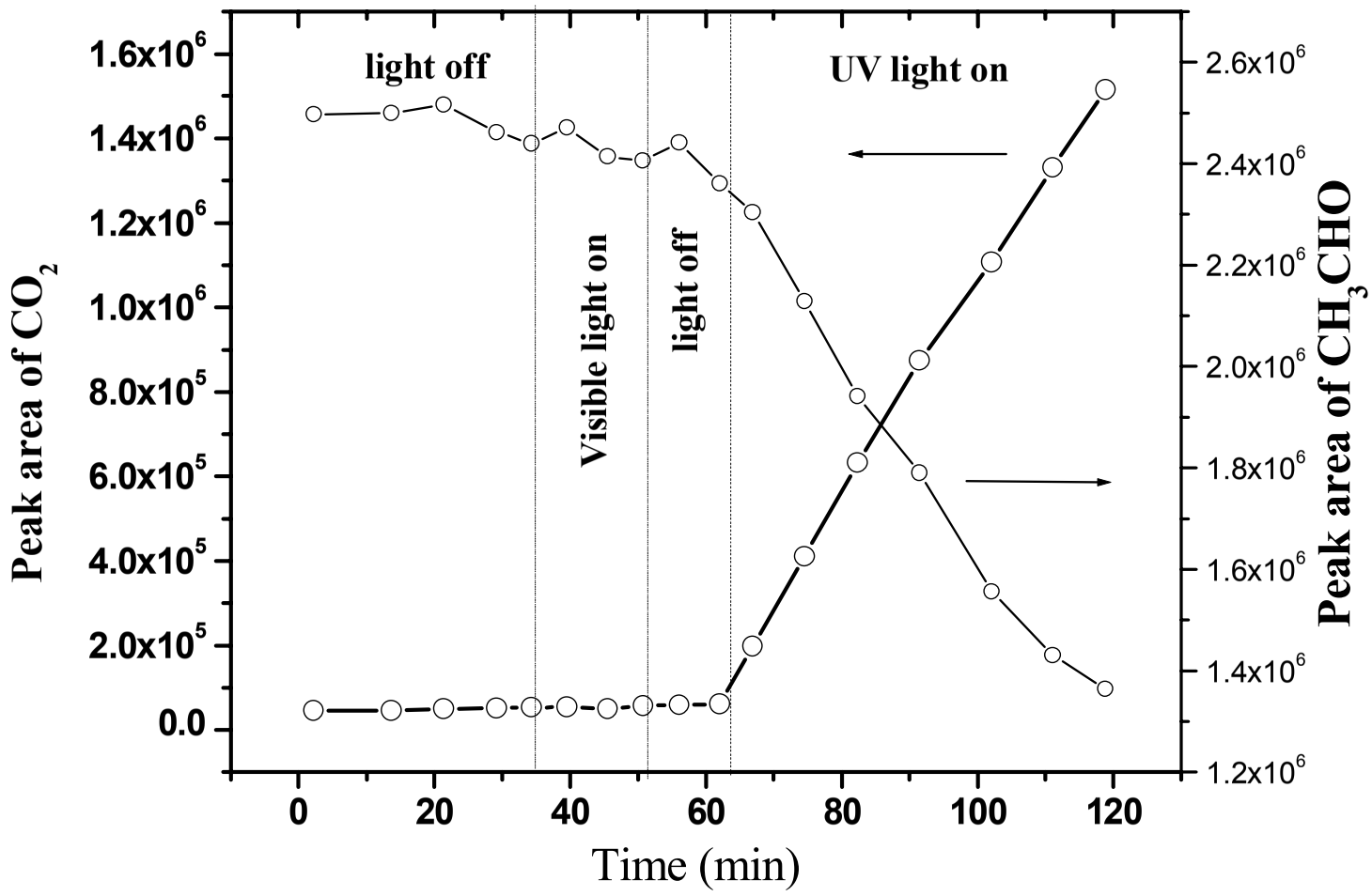

Figure 4.8 Peak Areas versus Time for CH_3CHO Decomposition and CO_2 Evolution under UV Light for AP-$SrTiO_3$

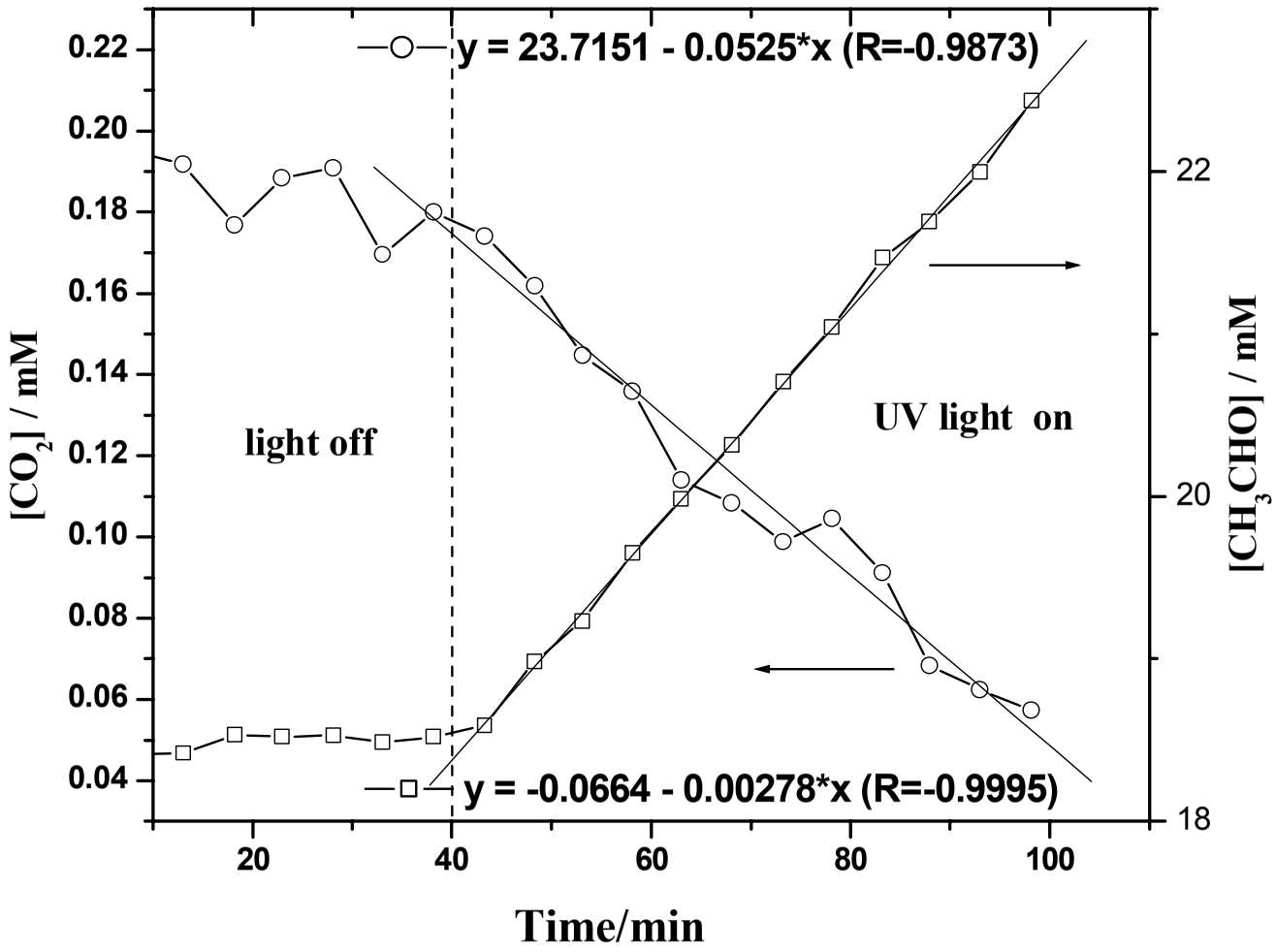

Figure 4.9 Concentration versus CH_3CHO Decomposition and CO_2 Evolution under UV Light for AP-$SrTiO_3$

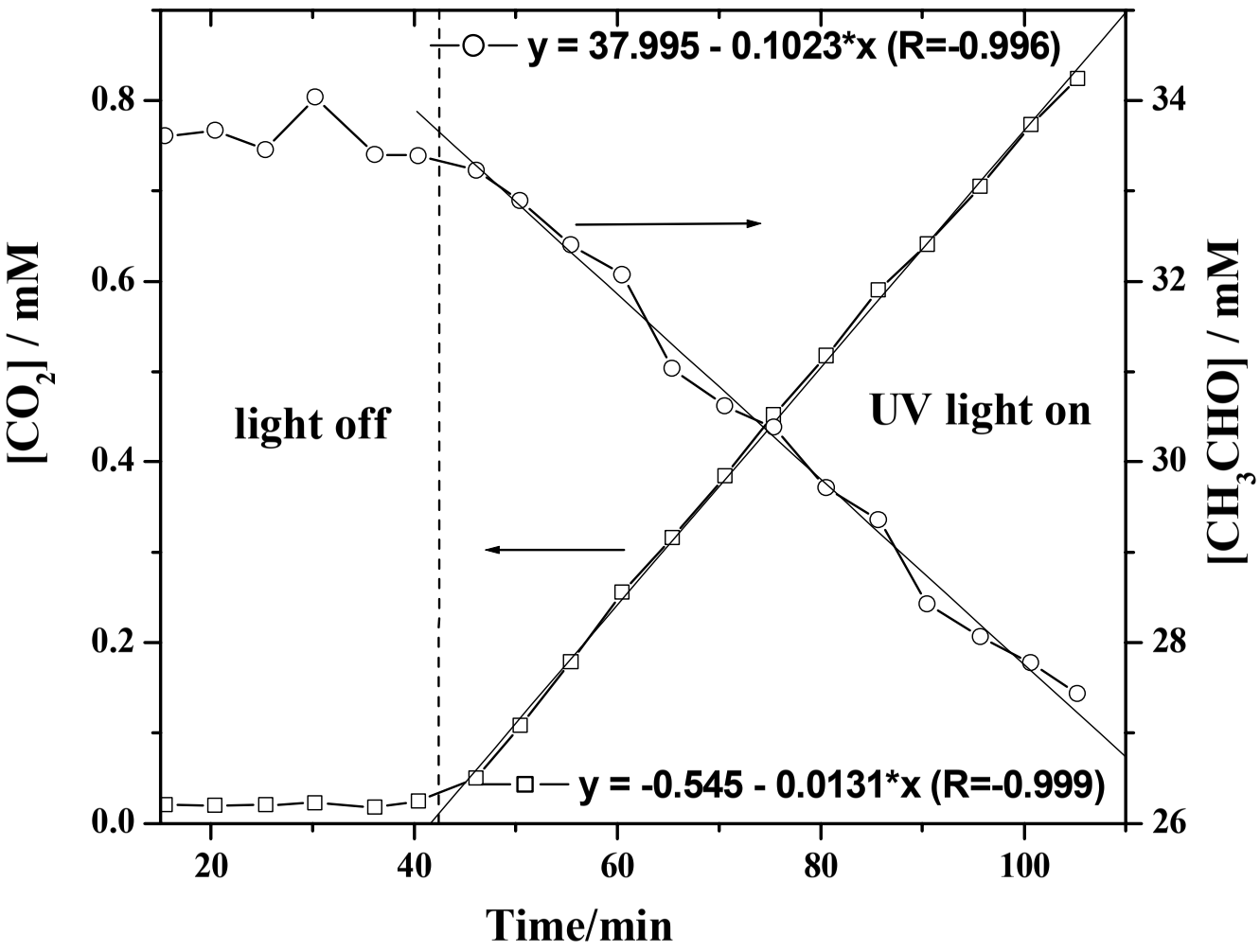

Figure 4.10 Photocatalytic Decomposition of Acetaldehyde under UV Light for P25 TiO_2

4.3.2 Photoactivity of commercially available and synthesized samples

Different catalyst samples including commercially available, solid-state prepared and aerogel prepared, were studied for the decomposition of acetaldehyde under light irradiation. The initial reaction rates for different catalyst samples were calculated and compared. Titania P25 shows very high activity toward the acetaldehyde decomposition and carbon dioxide production under UV light irradiation (Table 4.2). It has the highest initial reaction rates in comparison with all other studied catalyst samples (Figures 4.11 and 4.12).

Table 4.2 Initial Rates for CH_3CHO Decomposition and CO_2 Production under UV Light Irradiation for the Different Catalyst Samples

Catalyst Sample	r [CH_3CHO]	r [CO_2]
P25 TiO_2 Degussa	0.102	1.3×10^{-2}
AP-$SrTiO_3$	0.053	2.8×10^{-3}
AP-$BaTiO_3$	0.041	1.4×10^{-3}
SSR-$SrTiO_3$	0.116	1.1×10^{-3}
SSR-$BaTiO_3$	0.093	4.9×10^{-4}
CM-$SrTiO_3$	0.037	7.5×10^{-4}
NCM-$SrTiO_3$	0.034	6.6×10^{-4}

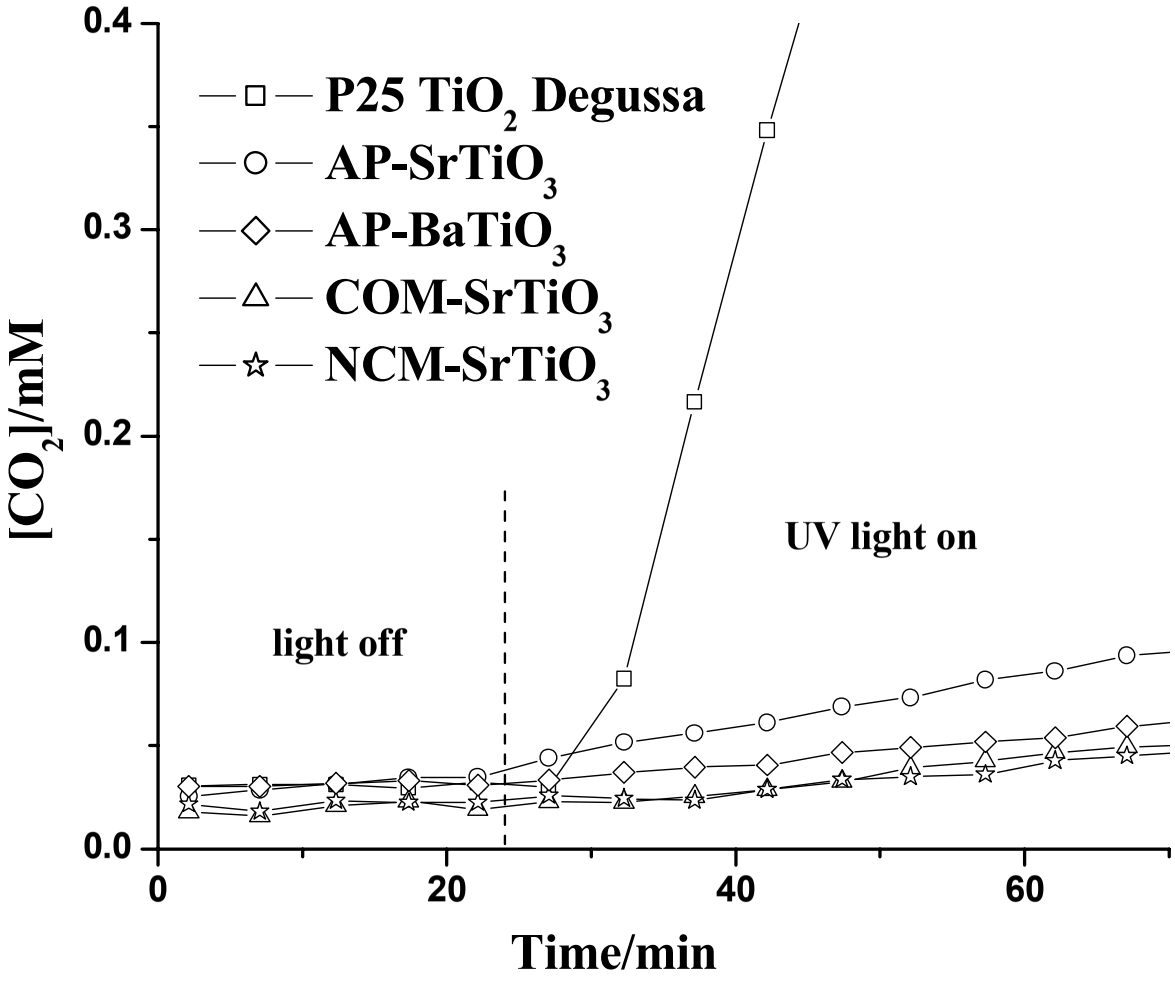

Figure 4.11 CO_2 Evolution under UV Light Irradiation for Different Catalyst Samples

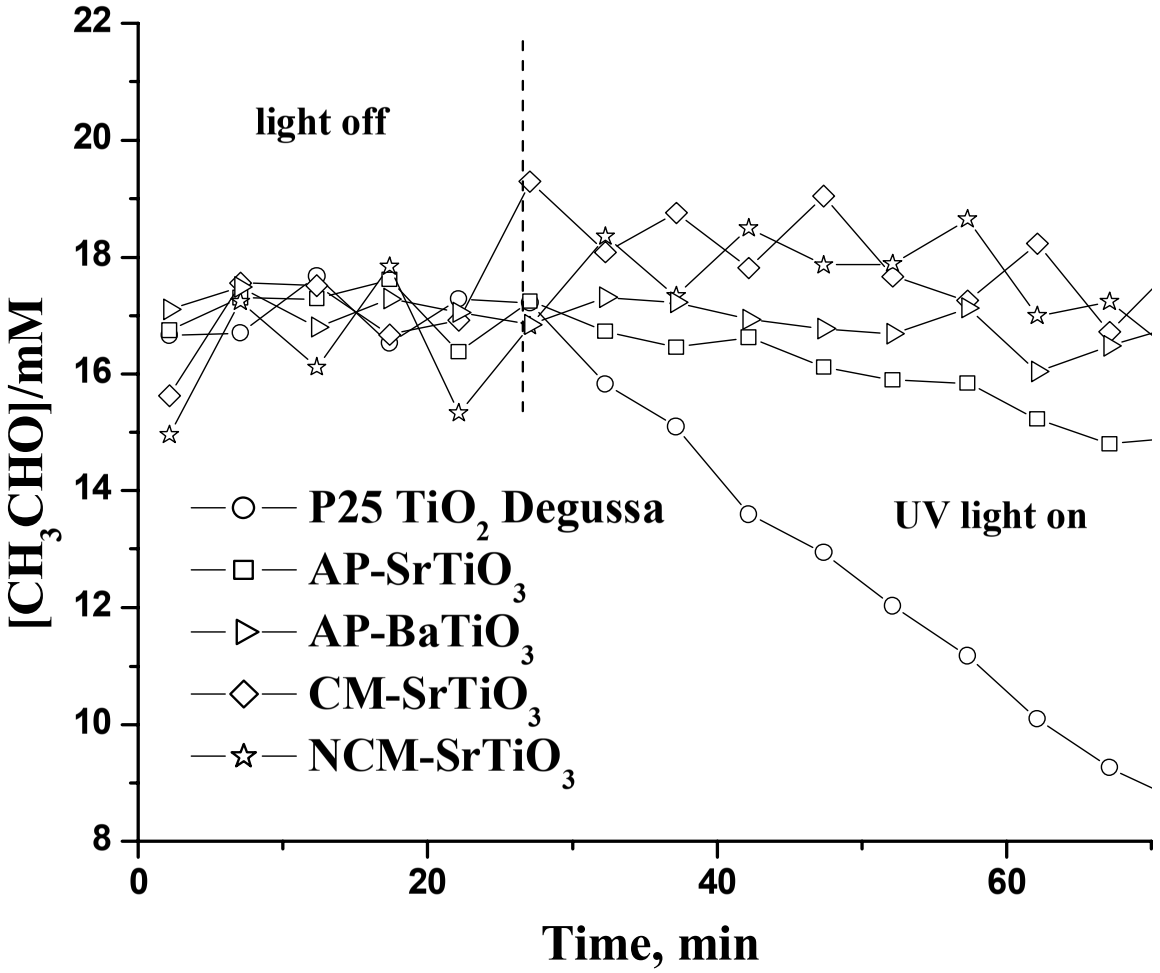

Figure 4.12 CH_3CHO Decomposition under UV Light Irradiation for Different Catalyst Samples

The initial rate for carbon dioxide production on titanium oxide P25 catalyst is significantly higher than that of other competitors (in the range of 4-25 times). The nearest competitor is an aerogel prepared strontium titanate which has activity for acetaldehyde decomposition two times lower and activity for carbon dioxide production four times less than P25. Aerogel prepared barium titanate is also photoactive for acetaldehyde decomposition, but less active than AP-$SrTiO_3$.

All synthesized samples including solid-state prepared and aerogel prepared were more active for acetaldehyde decomposition than those commercially available (commercial $SrTiO_3$ or nanosized commercial $SrTiO_3$).

Solid-state prepared samples of $SrTiO_3$ and $BaTiO_3$ have photoactivities similar to titania for acetaldehyde decomposition, but carbon dioxide production on these samples was significantly lower not only in comparison with P25 (10-25 less), but also in comparison with aerogel prepared $SrTiO_3$ and $BaTiO_3$ samples (3 times less).

The diffuse reflectance spectra of solid-state prepared, aerogel prepared, and commercial $SrTiO_3$ samples (Figure 4.13) show an interesting feature of a shallow shoulder adsorption in the 400-700 nm range for SSR-$SrTiO_3$ and CM-$SrTiO_3$. Besides, having similar textural characteristics (See Chapter 3, Table 3.1) these two samples also have a light purplish white color in comparison with the bright white color of AP-$SrTiO_3$. The similarity in properties and characteristics of them allows speculation that commercial $SrTiO_3$ was probably produced by a solid-state reaction. The absorbance of some visible light and color of these samples can be explained by the presence of impurity phases produced by the incomplete reaction of precursors (Sr_2TiO_4) and oxygen deficiency ($SrTiO_{2.7}$), and oxygen defects due to oxygen deficiency (See Appendix A).

The presence of oxygen defects can accelerate the adsorption of the acetaldehyde species on the surface of the catalyst giving a higher rate of acetaldehyde disappearance from the gaseous phase, or produce more superoxide species to decompose acetaldehyde and produce carbon dioxide. Since there is no significant increase in the carbon dioxide production in comparison with other samples, it is possible to postulate that the higher rate of decrease in the acetaldehyde concentration is due to the faster absorption of acetaldehyde molecules on the active sites of the catalyst. More surface studies are needed to prove this finding (FTIR studies on surface in Chapter 6).

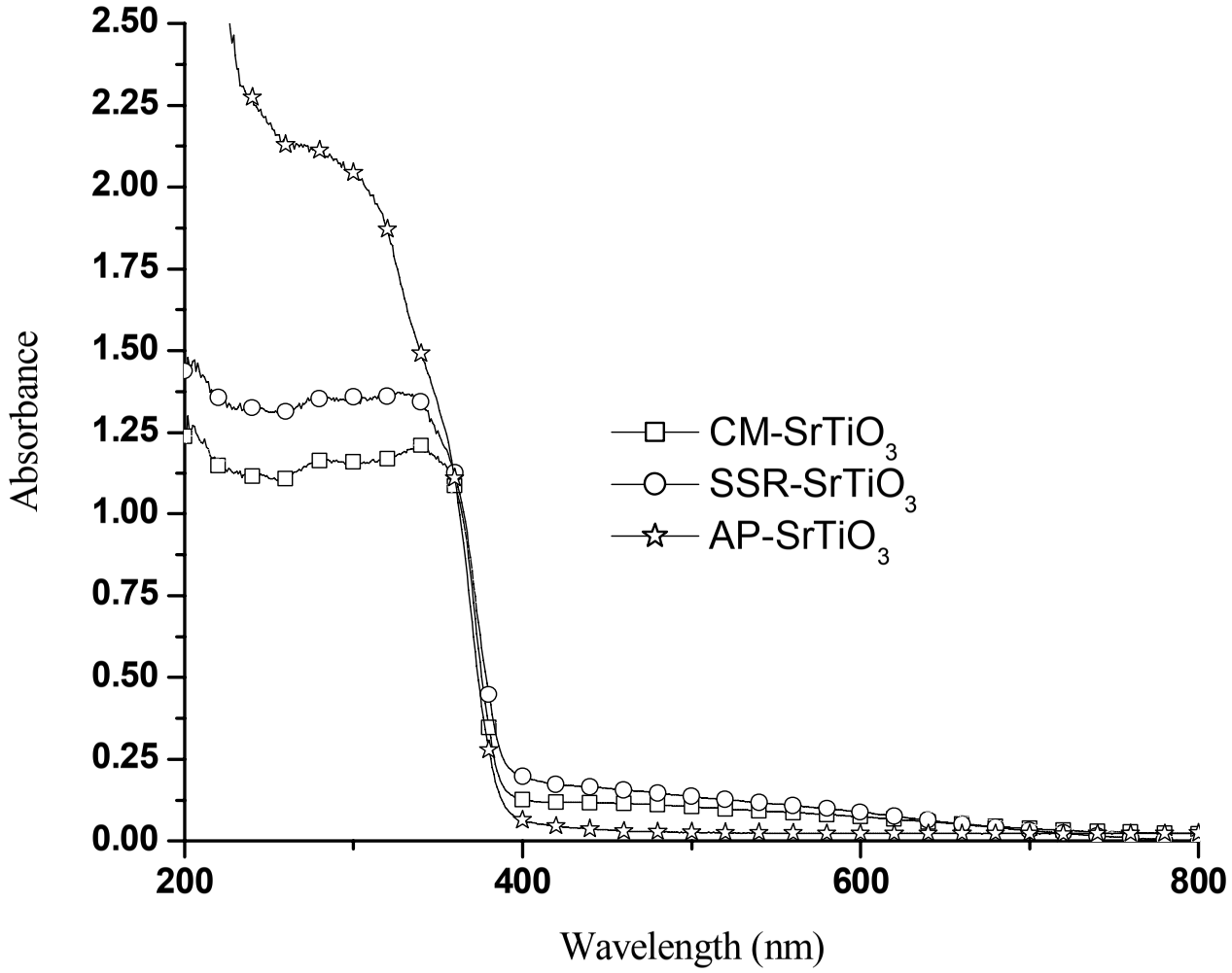

Figure 4.13 Defuse Reflectance Spectra of Different $SrTiO_3$ Samples

Aerogel prepared catalyst samples, despite their very high surface areas, in comparison with solid-state catalyst samples with lower surface areas, have not shown a significant increase in acetaldehyde decomposition. This proves one more time that photocatalysis is a complex process that depends on many different parameters. High surface area is important for heterogeneous catalysis but not a decisive factor.

Nevertheless, aerogel prepared samples are the most active samples for carbon dioxide production under UV light irradiation and AP-$SrTiO_3$ is second in photoactivity after P25 TiO_2.

The available samples were also tested for the photodecomposition of acetaldehyde under visible light irradiation (420 nm < λ). It is clear that under visible light all samples lose photoactivity toward the decomposition of acetaldehyde and carbon dioxide production (Table 4.3). The titania P25 photocatalyst is also inactive under visible light.

Table 4.3 Initial Rates for CH_3CHO Decomposition and CO_2 Production under Visible Light Irradiation for Different Catalyst Samples

Catalyst Sample	r [CH_3CHO]	r [CO_2]
P25 TiO_2 Degussa	0.015	1.6×10^{-4}
AP-$SrTiO_3$	0.008	2.1×10^{-4}
AP-$BaTiO_3$	0.005	1.4×10^{-4}
SSR-$SrTiO_3$	0.032	1.4×10^{-4}
SSR-$BaTiO_3$	0.017	2.0×10^{-5}

The level of produced carbon dioxide is similar for all catalyst samples. In case of solid-state prepared catalyst samples, the initial rates for acetaldehyde consumption were slightly higher in comparison with others, but again, there were no increases in carbon dioxide production.

A balance between the consumed acetaldehyde concentration and the amount of CO_2 produced is not achieved. While CO_2 is the main gaseous product, other non-volatile or less-volatile intermediates are probably formed and stay absorbed on the surface of the catalyst; that is why they were not detected in the gaseous phase by gas chromatography.

4.4 Conclusions

Volatile Organic Compounds and acetaldehyde in particular in the presence of photocatalyst can be decomposed from the gaseous phase into CO_2 and H_2O through different intermediates under light irradiation. Active oxygen species (O_2^-, $^{\cdot}OH$, O^-, O_3^-) are important species to promote the photoreaction. Surface holes and oxygen defect can also significantly influence the activity of catalyst.

Titanium based catalysts are known as materials that can be applied for the photooxidation of volatile organic compounds under light irradiation. Acetaldehyde photooxidation has been studied on aerogel prepared strontium and barium titanates (AP-$SrTiO_3$ and AP-$BaTiO_3$), solid-state prepared strontium and barium titanates (SSR-$SrTiO_3$ and SSR-$BaTiO_3$) under UV and visible light irradiation, and compared with the photoactivity of available commercial samples (CM-$SrTiO_3$ and NCM-$SrTiO_3$) and P25 TiO_2 (Degussa).

The degradation of CH_3CHO over AP-$SrTiO_3$ is lower than that of P25 under UV. Nevertheless, aerogel prepared titanates showed high activity for the acetaldehyde decomposition and carbon dioxide production in the UV region of irradiation compared to other available commercial and synthesized catalysts.

The comparison of aerogel prepared samples with differently prepared samples shows the influence of morphology and textural properties on photocatalytic activity of $SrTiO_3$ particles. The solid-state prepared samples with low surface areas showed reletively high initial rates for acetaldehyde consumption in comparison with aerogel prepared samples which have significantly higher surface areas. The higher consumption of acetaldehyde from the gaseous phase by the solid-state prepared samples can be explained by the higher rates of acetaldehyde adsorption on the surface of catalyst, but not by the higher rates of the acetaldehyde decomposition since the increase in carbon dioxide was not noticed. It seems that highly oxygen

defective surface of solid-state prepared samples, plays some role in this process, and the surface studies of catalyst during photooxidation would be useful.

TiO_2 and titanates are active only under UV light irradiation, and this limits their application. To make photocatalyst more efficient for solar light, it must work in the visible light region. The modification of photocatalysts by doping can solve this problem.

4.5 References

[1] M. Astier, A. Bertrand, D. Bianchi, A. Chenard, G.E.E. Gardes, G. Pajonk, M.B. Taghavi, S.J. Teichner, and B. Villemin, In Studies in Surface Science and Catalysis; B. Delmon, P.A. Jacobs, G. Poncelet, Eds.; Elsevier, Amsterdam, 1976; vol. 1, p. 315.

[2] G. Matis, F. Juillet, and S.J. Teichner, Bull. Soc. Chim. Fr., (1976) 1633.

[3] G.M. Pajonk, Appl. Catal., 72 (1991) 217.

[4] R.J. Willey, H. Lai, and J.B. Peri, J. Catal., 130 (1991) 319.

[5] F. Blanchard, B. Pommier, J.P. Reymond, and S.J. Teichner, J. Mol. Catal., 17 (1982) 171.

[6] F. Blanchard, B. Pommier, J.P. Reymond, and S.J. Teichner, Preparation of Catalysts III. In Studies in Surface Science and Catalysis; G. Poncelet, P. Grange, P.A. Jacobs, Eds.; Elsevier, Amsterdam, 1983; vol. 16, p. 395.

[7] M.R. Hoffmann, Chem.Rev., 95, (1995) 69.

[8] A. Fujishima and K. Honda, Bull. Chem. Soc. Japan, 44 (1971) 1148.

[9] A. Fujishima and K. Honda, Nature, 238 (1972) 37.

[10] J.G. Mavrodis and J.A. Kafalas, Appl. Phys. Lett., 28 (1976) 241.

[11] M. Butler and D.S. Ginley, J. Mater. Sci., 15 (1980) 1.

[12] A.J. Bard, J. Phys. Chem., 86 (1982) 172.

[13] J.F. Reber and M. Rusek, J. Phys. Chem., 90 (1986) 824.

[14] E. Borgarello, K. Kalayanasundaram, and M. Gratzel, E. Pelizetti, Helv. Chem. Acta, 65 (1982) 243.

[15] J.R. Harbour, R. Wolkow, and M.L. Hair, J. Phys. Chem., 85 (1981) 4026.

[16] J. Sabate, S. Cervera-March, R. Simarro, and J. Gimenez, Int. J. Hydrogen Energy, 15 (1990) 115.

[17] A. Kudo, Catalysis Surveys from Asia, 7 (2003) 1.

[18] A. Fujishima, T.N. Rao, and D.A. Tryk, J. Photochem. Photobiol. C, 1 (2000) 1.

[19] M.R. Hoffmann, S.T. Martin, W. Choi, and D.W. Banhemann, Chem. Rev., 95 (1995) 69.

[20] M.D. Driessen, A.L. Goodman, T.M. Miller, G.A. Zaharias, and V.H. Grassian, J. Phys. Chem. B, 102 (1998) 549.

[21] K.I. Zamaraev, M.I. Khramov, and V.N. Parmon, Catal. Rev., 35 (1994) 617.

[22] X. Fu, W.A. Zeltner, and M.A. Anderson, Appl. Catal. B, 6 (1995) 209.

[23] N. Negishi, T. Iyoda, K. Hashimoto, and A. Fujishima, Chem. Lett., (1995) 841.

[24] I. Sopyan, M. Watanabe, S. Murasawa, K. Hashimoto, and A. Fujishima, J. Photochem. Photobiol. A, 98 (1996) 79.

[25] M.A. Anderson, S.Y. Nishida, and S.C. March, in Photocatalytic Purification and Treatment of Water and Air, D.F. Ollis, (Ed.), Elsevier, Amsterdam, (1993), 405.

[26] P. Avila, A. Barhamonde, J. Blanco, B. Sanchez, A.I. Cardona, and M. Romero, Appl. Catal. B, 17 (1998) 75.

[27] T.R.N. Kutty and M. Avudaithai, Catal. Rev. – Sci. Eng., 3494 (1992) 389.

[28] S. Ahuja and T.R.N. Kutty, J. Photochem. Photobiol. A, 97 (1996) 99.

[29] J.L Giocondi and G.S. Rohrer, Mat. Res. Soc. Symp. Proc., 654 (2001) AA7.4.1-10.

[30] C.D. Jaeger and A.J. Bard, J. Phys. Chem., 83 (1979) 3146.

[31] J.R. Harbour and M.L. Hair, Adv. Colloid Interface Sci., 24 (1986) 103.

[32] R.F. Howe and M. Grätzel, J. Phys. Chem., 91 (1987) 3906.

[33] M. Schneider and A. Baiker, Aerogels in Catalysis, Catal. Rev. – Sci. Eng., 37 (1995) 4, 515-556.

[34] G.M. Pajonk, Catalysis Today, 35 (1997) 319-337.

[35] H. Hirashima, C. Kojima, K. Kohama, H. Imai, V. Balek, H. Hamada, and M. Inaba, Oxide aerogel catalysts, J. Non-Cryst. Solids, 225 (1998) 153-156.

[36] M. Kaneko and I. Okura, Photocatalysis: Science and Technology, Springer, 2002, 356.

[37] J. Desilvestro, M. Gratzel, M. Kavan, and J. Moser, J. Am. Chem. Soc., 107 (1985) 2988.

[38] R.M. Quint and N. Getoff, Int. J. Hydrogen Energy, 13 (1998) 269.

[39] J.-M. Herrmann, J. Disdier, and P. Pichat, J. Phys. Chem., 90 (1986) 6028.

[40] J.M. Lehn, J.P. Sauvage, and R. Zissel, Nouv. J. Chim., 4 (1980) 623.

[41] H. Nakamatsu, T. Kawai, A. Koreeda, and S. Kawai, J. Chem. Soc. Faraday Trans. I, 82 (1985) 527.

[42] W. Choi, A. Termin, and M.R. Hermann, J. Phys. Chem., 98 (1994) 13669-13679.

[43] G. Burgeth and H. Kisch, Coord. Chem. Rev, 230 (2002) 41-47.

[44] A. Fuerte, M.D. Hernandez-Alonzo, A.J. Maira, A. Matinez-Arias, M. Fernandez-Garcia, J.C. Conesa, and J. Soria, Chem. Commun., (2001) 2718-2719.

[45] R. Asahi, T. Morikawa, T. Ohwaki, K. Aoki, and Y. Taga, Science, 293 (2001) 269-271.

[46] Y. Sakatani and H. Koike, Japan Patent, P20001-72419A, 2001.

[47] Assessment and Standards Division Office of Transportation and Air Quality U. S. Environmental Protection Agency, "Draft Technical Support Document: Control of Emissions of Hazardous Air Pollutants from Motor Vehicles and Motor Vehicle Fuels," EPA420-D-00-003 July 2000.

[48] S.D. Jackson, Catalysis in Application, (2003) 129-135.

Chapter 5 : Modification of titanates by doping

5.1 Introduction

The search for new, inexpensive, environmentally friendly, and easy access energy sources is crucial in today's society. Doubtlessly, solar radiation is the most favorable candidate as an energy source for a variety of applications.

The annual consumption of energy on a world scale is 10^{17} kcal and this number constantly increases [1]. The annual incident solar energy on the Earth is 10^{21} kcal. 10^{16} kcal of solar energy is converted into chemical energy through photosynthesis in plants and microorganisms. Only a small part of solar energy is utilized by people through fuel and materials (10^{16} kcal), and food (10^{15} kcal).

The utilization of incident solar light can cover human needs for energy, which is why intensive efforts are going on for the discovery of materials which can convert the energy of light into other forms of energy like electricity (solar cells) and heat (solar collectors). Additionally, materials which can transfer it into chemical (photocatalysts) or mechanical (solar sails) work are also of high interest..

Photocatalytic processes can utilize light energy for water splitting, toxic waste mineralization, air and water purification [2, 3]. Different semiconductor titanium based oxide catalysts (TiO_2, and perovskites such as $CaTiO_3$, $SrTiO_3$, and $BaTiO_3$) were studied for the degradation of organic compounds and/or water splitting [4 - 6]. All these oxides were active only under UV irradiation and this is conditioned by large band gaps. Since UV light is only 3% of solar light, the semiconductor oxide materials with lower band gaps need to be developed to absorb visible light and to perform more effective catalysis.

Unlike titanium oxide, the combination of A and B cation sites can be varied and substituted with other metal cations in the perovskite structure of ABO_3. The substitution or doping with cations that are compatible with the lattice sizes of cations in perovskite ($A_xA'_{1-x}BO_3$ or $AB_xB'_{1-x}O_3$) can change its electronic properties [7]. Doping with different cations (A' or B') can also decrease the band gap size of the perovskites and thus will increase the

absorption of light in the visible light region and enhance photocatalytic properties of doped perovskites.

The modification of UV photocatalysts by doping (incorporation) with transition metal ions (partial substitution of Ti ions with metal ions) creates a valence band or electron donor level inside the band gap, narrows it, and increases the visible light absorption (>420 nm).

Recently, our group has developed a way to modify the UV photocatalytic materials so they will respond to visible irradiation [8-10]. These materials were doped with transition metals, which decreased the band gap and enhanced the absorption of visible light (Figure 5.1).

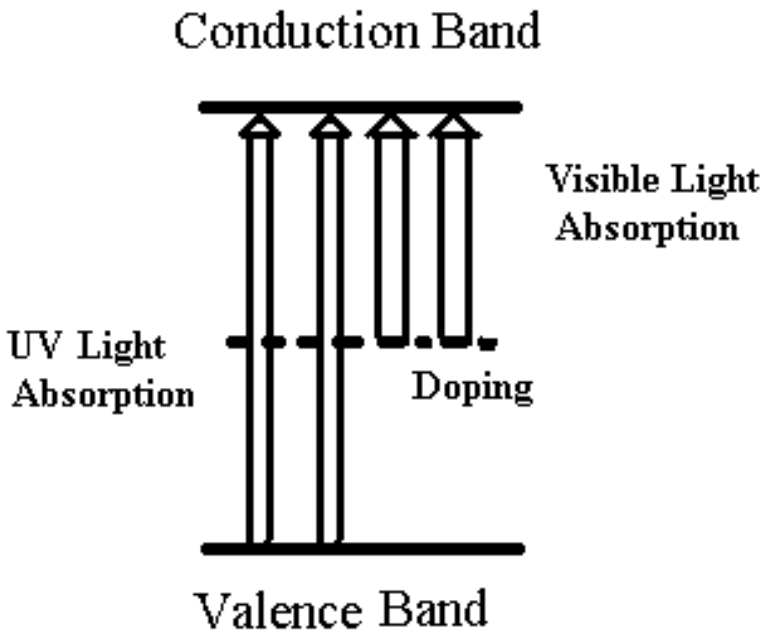

Figure 5.1 Transition Metal Doping of UV Photocatalysts

The enhanced absorption of visible light in titanate photocatalysts can be achieved by the synthesis of nanosized powders doped with metal ions. These novel nanosized catalysts may have higher photocatalytic activity in comparison with bulk catalyst powders. Nanoparticles offer advantages for catalysis by making available more surface area and active sites on the surface.

Therefore, the purpose of the research studies in this chapter are to answer the following questions:

a) Can the doping of perovskite affect the photocatalytic activity in visible light region?
b) Are the doped nanosized perovskite catalysts more efficient than other conventionally prepared doped perovskite catalysts?

5.2 Doping process

Modification of semiconductor photocatalysts to shift the light absorption into the visible light region can be achieved using several methods [11]:

1. Phosensitization by dyes (sensitizers) and transition metal complexes of the type [Ru (2,2'-bipiridyl)$_3$],
2. Ion-implantation by surface bombardment with V, Cr, Mn, Fe, or Ni ions,
3. Doping with V, Cr, Rh, Mn, Fe, Co, Ni, or Cu metals,
4. Doping with S, N, or F nonmetals,
5. Impregnation or incorporation with fullerenes (C_{60}).

Implantation is a very effective method and can significantly enhance the adsorption of visible light by the sample. Figure 5.2 shows that Cr implanted TiO_2 has an increase in absorption of visible light with increasing of the concentration of implanted chromium. The big disadvantage of this method is the high cost of catalyst production.

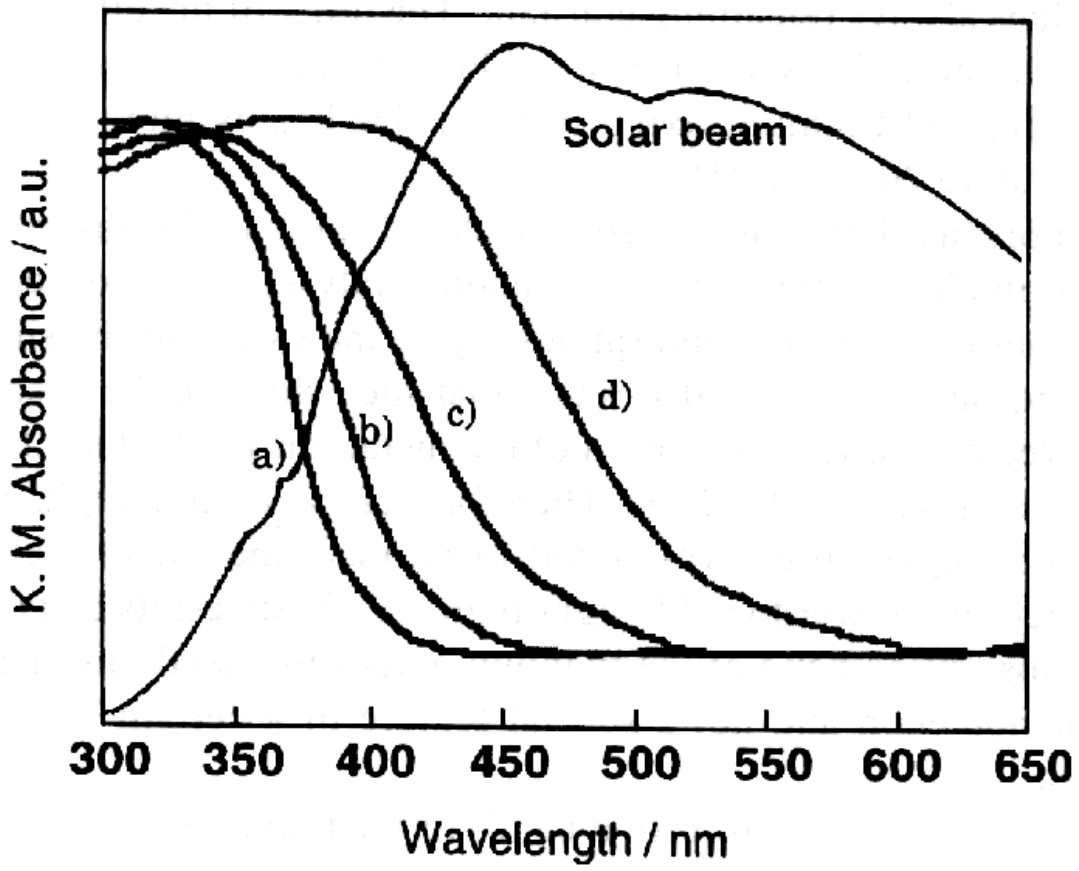

Figure 5.2 UV-Visible Absorption Spectra of a) Pure TiO_2 and b) –d) Cr Ion-implanted TiO_2 with Cr of 2.2, 6.6, and 13 $x10^{-7}$ mol/g [11]

Doping with transition metals is another effective method to increase the absorption of visible light by a semiconductor catalyst. Different transition and noble metals were used for doping of photocatalysts to enhance the visible light absorption (Figure 5.3). The visible light response of these catalysts can be explained by the creation of electron donor levels on bands formed by metal ions in the forbidden area and transition of electrons from them to the conduction band of Ti 3d orbitals.

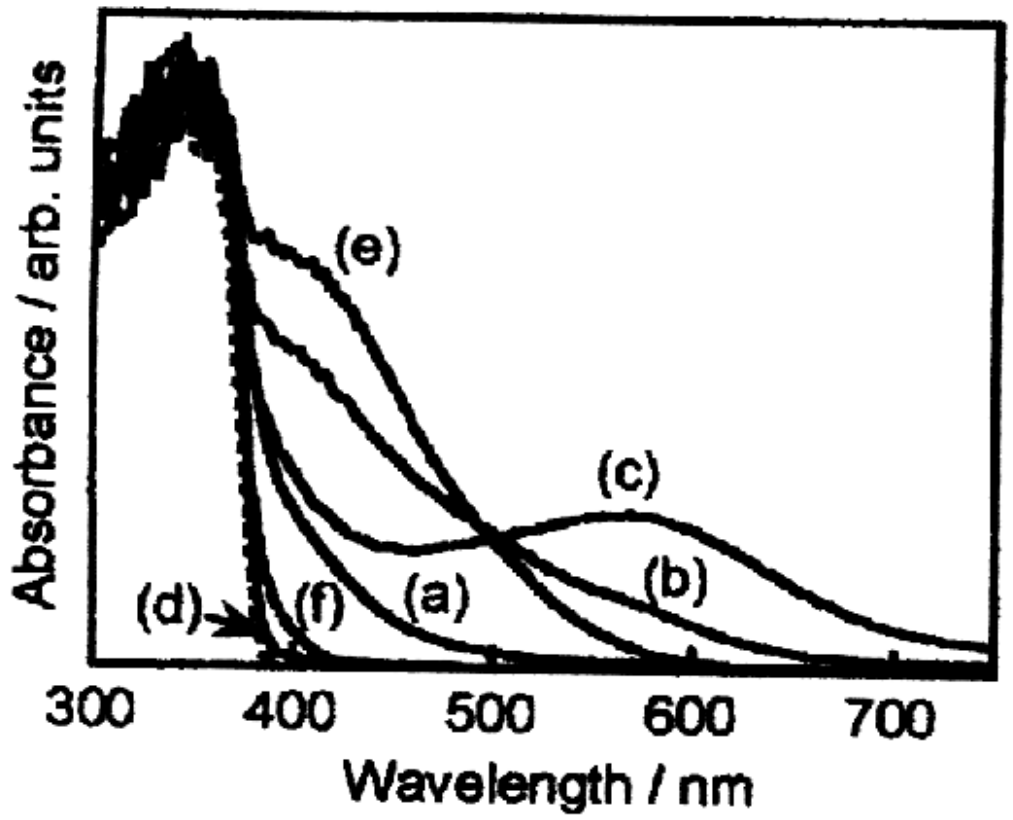

Figure 5.3 Diffuse Reflectance Spectra of Doped $SrTiO_3$:M (0.5%) with a) Mn, b) Ru, c) Rh, d) Pd, e) Ir, f) Pt [12]

All doped photocatalysts were mainly prepared to study water splitting under visible light, and information on application of them for organic compound photodecomposition is very limited. The main method to synthesize them is the solid-state reaction when all solid precursors are mixed together and calcined at very high temperatures (>1000°C). Not surprisingly, these materials are very dense powders with large particle sizes. In any case, they show good activities for H_2 or O_2 production during water photolysis process. Mn and Ru doped $SrTiO_3$ showed good photoactivity for O_2 production, while Ru, Rh, and Ir doped $SrTiO_3$ shows activity for H_2 production under visible light irradiation (λ >440 nm) [12].

The absorption of visible light does not mean that the doped material will be a good photocatalyst, but it indicates that harvested photons of visible light may be used for the photocatalytic process. For example, Cr^{3+} doped TiO_2 and $SrTiO_3$ absorb visible light; however, there is no increase in photoactivity and sometimes it even decreases [13-15]. The substitution of

Ti^{4+} with Cr^{3+} causes charge imbalance and formation of oxygen defects and/or Cr^{6+} ions to stabilize the charge balance. Oxygen defects and Cr^{6+} ions may act as recombination centers for holes and electrons and cause a decrease in photoactivity. In contrast, chromium and antimony codoped $SrTiO_3$ showed an increase in photoactivity for H_2 production in visible light range [16]. In this system two O^{2-} ions are replaced with one Cr^{3+} ion and one Sb^{5+} ion in such a way that charge balance is preserved and no defects were formed. In a similar manner, the Cr and Ta codoped, Cr and Nb codoped, Sb and Ni codoped $SrTiO_3$ catalysts were synthesized by the solid-state reaction method and showed an increase in photocatalytic activities [17].

Doping TiO_2 with Fe^{3+}, Mo^{5+}, Ru^{3+}, Os^{3+}, Re^{5+}, V^{4+} and Rh^{3+} showed a significant increase for photoactivity for carbon tetrachloride reduction and chloroform oxidation, while doping with Co^{3+} and Al^{3+} decreased the photoactivity [18].

In all previously mentioned cases, doping was done with cations. There are a few cases when the doping of titania with anions has been done, but has been achieved by the substitution of nonmetal ion for O^{2-} in the lattice of TiO_2 to form $TiO_{2-x}F_x$, $TiO_{2-x}N_x$, or $TiO_{2-x}S_x$ [19-21]. Doping can also be done with several nonmetals together. Doping of $SrTiO_3$ with nitrogen only where the O^{2-} is replaced with N^{3-} causes the formation of anion defects and forms charge imbalance. As already mentioned above the defects can act as electron-hole recombination centers. Charge balance can be preserved if two O^{2-} ions are replaced with one N^{3-} ion and one F^- ion simultaneously [22]. The photoactivity of N and F codoped $SrTiO_3$ increased significantly in comparison with N doped $SrTiO_3$ under visible light irradiation. It is necessary to mention that almost all doping with metal is done by solid-state reaction method or techniques similar to it.

Keeping in mind the work already done by other research groups, it would be interesting to prepare doped aerogel catalysts to study their photoactivity and compare with conventionally solid-state prepared samples. In this chapter doped aerogel catalyst will be investigated:

1) Cr doped AP-$SrTiO_3$ to increase photoactivity in a visible light region,
2) Cr doped AP-$BaTiO_3$ to increase photoactivity in a visible light region,
3) Sb/Cr codoped AP-$SrTiO_3$ to decrease the amount of recombination centers,
4) Cr doped SSR-$SrTiO_3$ to compare photoactivity with Cr doped AP-$SrTiO_3$,
5) Sb/Cr codoped SSR-$SrTiO_3$ to compare photoactivity with Cr and Sb codoped AP-$SrTiO_3$.

5.2.1 Doping with transition metals in solid-state reaction

The traditional way to prepare solid-state samples is to mix solid precursors in the necessary stoichiometric ratio and to calcine them at high temperatures. Solid-state prepared $SrTiO_3$ or $BaTiO_3$ doped with a transition metal are synthesized by mixing solid starting materials of titanium oxide, strontium or barium carbonate, and transition metal oxide according to the ratio $SrM_xTi_{1-x}O_3$ or $BaM_xTi_{1-x}O_3$ (where M is dopant metal) (Figure 5.4). The precursors are mixed and ground first, and these samples are packed in high purity alumina crucibles and calcined at 1100°C for 36 hours. After 18 hours, the samples are cooled down, ground, packed, and calcined for another 18 hours (More detailed information on the solid-state method operation procedure can be found in Chapter 3.2.1).

5.2.2 Doping with transition metals in aerogels

The sol-gel or aerogel methods for the synthesis of nanoparticles can also be used for doping of samples with transition metals (Figure 5.5). Titanium alkoxide with strontium or barium alkoxides ($Ti(OR)_4$ with $Sr(OR)_2$ or $Ba(OR)_2$) are mixed first, and solvent soluble salt of transition metal (nitrate or acetate) is added afterwards according to the ratio $SrM_xTi_{1-x}O_3$ or $BaM_xTi_{1-x}O_3$ (where M is dopant metal). The hydrolysis of this mixture gives the mixed metal oxides where some of the Ti ions in the lattice are substituted with transition metal ions (More detailed information on the aerogel method operation procedure can be found in Chapter 3.2.2).

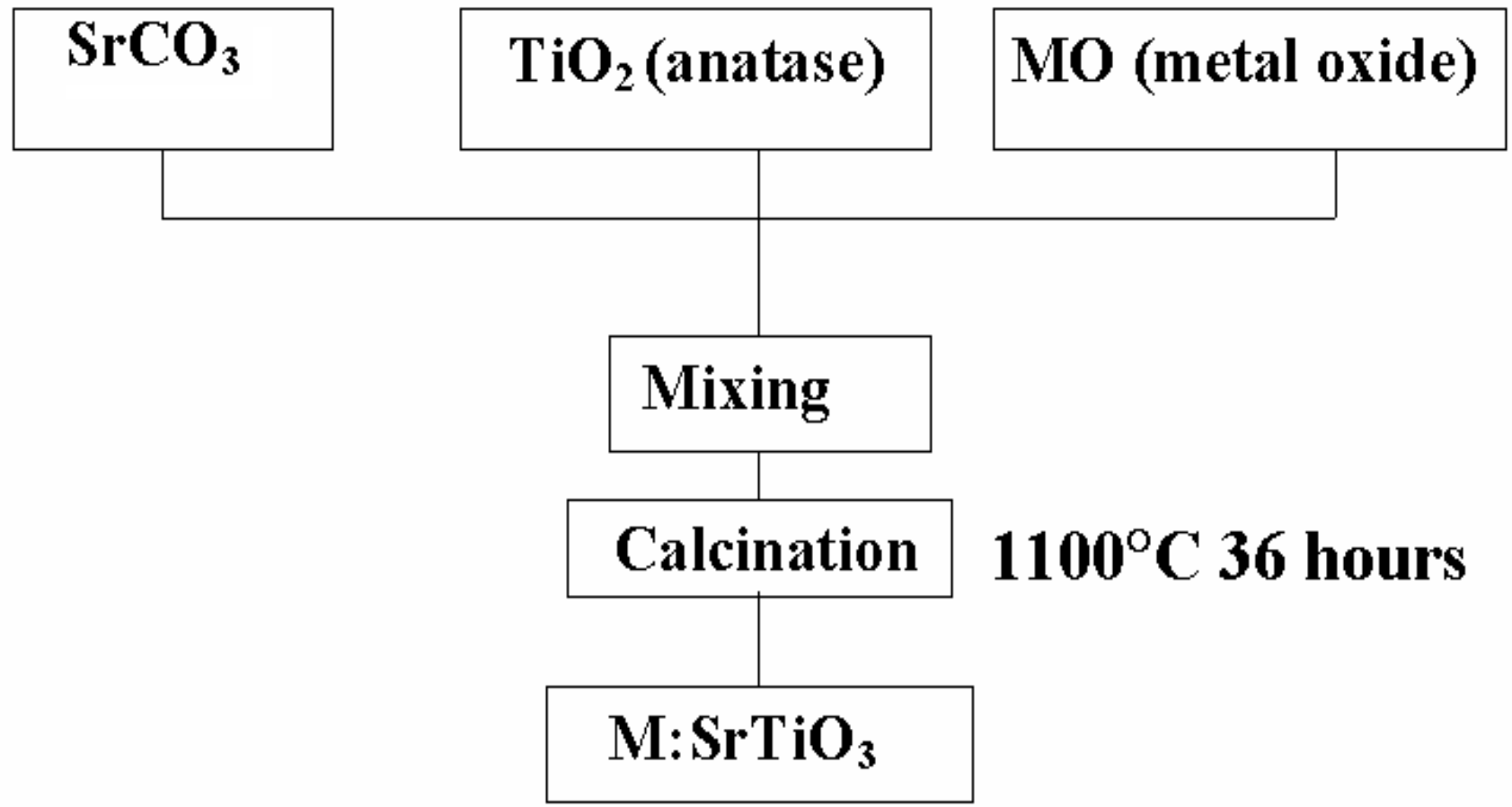

Figure 5.4 Metal Doping of $SrTiO_3$ Photocatalyst by Solid-State Reaction

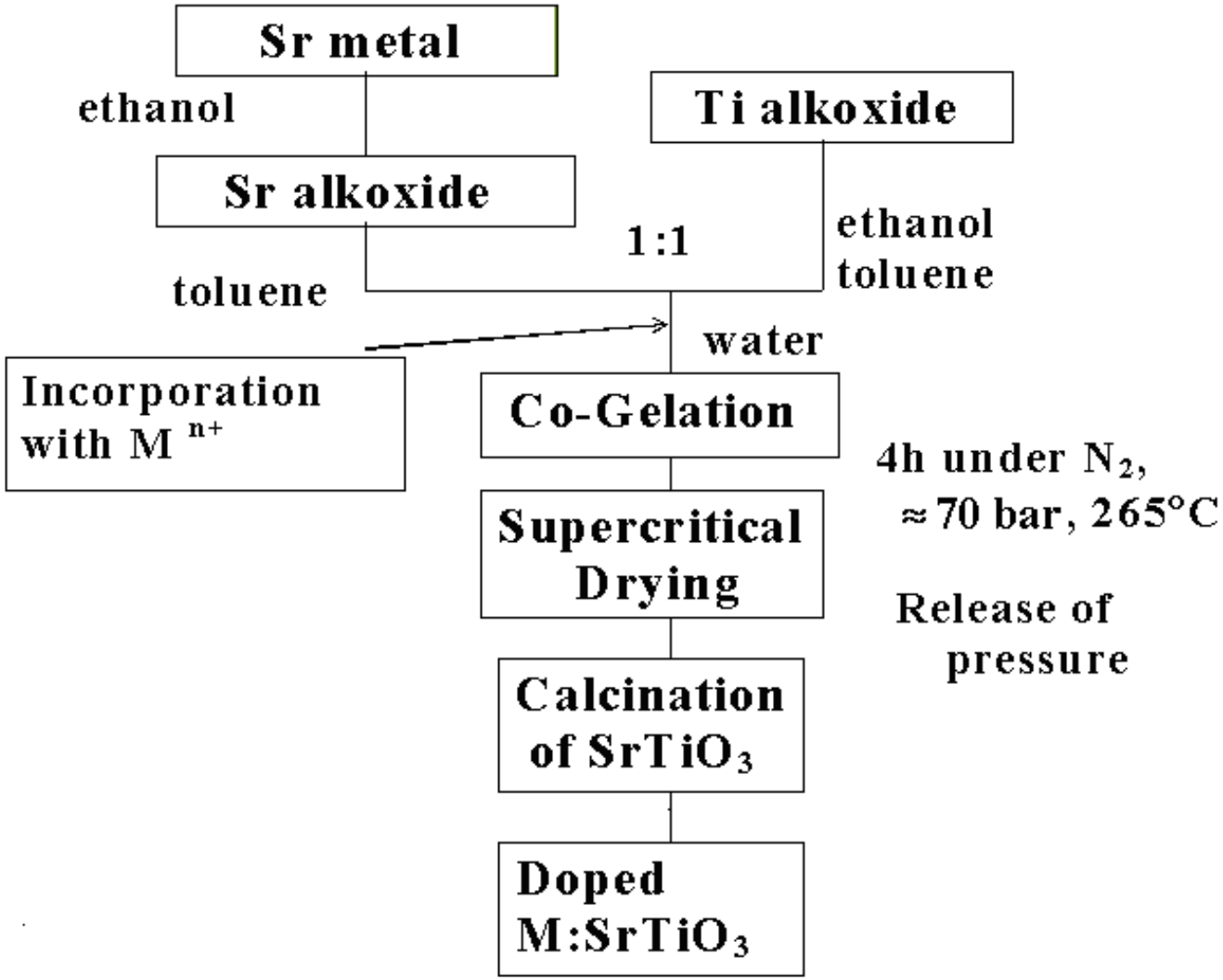

Figure 5.5 Metal Doping of $SrTiO_3$ Photocatalyst by Modified Aerogel Procedure

5.3 Photoactivity of doped titanates

The doped photocatalysts were studied for visible and UV activity for gaseous acetaldehyde decomposition at room temperature. Acetaldehyde photooxidation was performed on chromium ion-doped AP-$SrTiO_3$, chromium/antimony ion-codoped AP-$SrTiO_3$, chromium ion-doped SSR-$SrTiO_3$, chromium/antimony ion-codoped SSR-$SrTiO_3$, chromium ion-doped AP-$BaTiO_3$ under UV and visible light irradiation, and compared with the photoactivity of pure aerogel prepared strontium titanate and barium titanate (AP-$SrTiO_3$ and AP-$BaTiO_3$) and P25 TiO_2 (Degussa).

The experimental setup included a light source (1000W high pressure Hg lamp), a static reactor and a circulating water thermostat. Different filters (Oriel Spectra-Physics 57396, 59062, 57346, 59680 filters, Newport 6123 liquid infrared filter) were used to pass UV (320 nm < λ < 400 nm) or visible (420 nm< λ) light radiation.

The powdered photocatalyst sample (100 mg) was placed into a circular glass dish to have a uniform surface and then mounted in an air filled cylindrical 305 mL glass reactor. 100 μL of liquid acetaldehyde were introduced into the reactor. After that the reactor was closed and stirred continuously. All experiments were carried out at a constant temperature of 298 K. Before irradiation, the reaction was equilibrated for 30 minutes to allow the vaporization of the aldehyde. Gaseous samples (35 μL) were periodically extracted from the reactor and injected into a GCMS (gas chromatograph with a mass detector GCMS-QP5000 from Shimadzu equipped with a phase XTI-5 capillary column, Restek Corp.) to monitor the concentrations of acetaldehyde degradation and carbon dioxide evolution (More detailed information on operation procedures for photocatalytic study can be found in Chapter 4.3.1).

5.3.1 Cr doping and Sb/Cr codoping of aerogel prepared catalysts

Chromium and antimony/chromium doped strontium titanates aerogels were prepared with 2% Cr and 2% Cr/2.5% Sb loadings by molar weight. The addition of metal ions from salts (chromium (III) nitrate and/or antimony (III) acetate) was in such a way so that the molar ratio of

$SrTi_{0.98}Cr_{0.02}O_3$ and $SrTi_{0.954}Cr_{0.02}Sb_{0.025}O_3$ would be preserved. Metal salts were dissolved in alcohol and added under stirring to the Sr-Ti alkoxides mixture before hydrolysis.

Doping of $SrTiO_3$ with metal(s) is based on the substitution of Ti ions with metal ions. Substitution of Ti^{4+} with Cr^{3+} ions causes the formation of oxygen defects ($SrTi^{IV}_{1-2x}Cr^{III}_{2x}O_{3-x}$) and/or Cr^{6+} ions ($SrTi^{IV}_{1-3x}Cr^{III}_{2x}Cr^{VI}_{x}O_3$) to keep the charge balance. This increases the number of recombination centers where photogenerated electrons and holes can recombine. Contrarily, the charge balance can be preserved by the use of charge compensation. The application of charge compensators like antimony ($Sr\ Ti^{IV}_{1-2x}Cr^{III}_{x}Sb^{V}_{x}O_3$), tantalum ($Sr\ Ti^{IV}_{1-2x}Cr^{III}_{x}Ta^{V}_{x}O_3$), or niobium ($Sr\ Ti^{IV}_{1-2x}Cr^{III}_{x}Nb^{V}_{x}O_3$) has been studied for the Sb/Cr, Ta/Cr and Nb/Cr doped $SrTiO_3$ systems [16-17]. Until now, these materials were synthesized only by solid-state reactions and mainly studied as photocatalysts for the water splitting. To our knowledge, until the work described herein, such systems have not been synthesized by an aerogel method and studied as photocatalysts to destroy volatile organic compounds.

The textural properties of the aerogel prepared samples were studied by different available techniques (More detailed information on sample characterization operation procedures can be found in Chapter 3.3). Powder X-ray diffractions patterns were obtained on a Bruker D8 Advance spectrometer with a CuKα radiation source with an applied voltage of 40 kV and a current of 40mA. Scans were made in the 2θ range of 20-85º with a scanning rate of 2 º/min. The crystallite size was calculated from the XRD patterns using the Debye-Scherrer equation.

Peaks from the diffractograms patterns were assigned to the strontium titanate phase, and no additional peaks corresponding to the dopants were observed (Figure 5.6). The absence of the dopant peaks indicates the high dispersion and incorporation of the doped metal ions into the $SrTiO_3$ lattice. The average crystallite sizes of different AP-$SrTiO_3$ samples are summarized in Table 5.1.

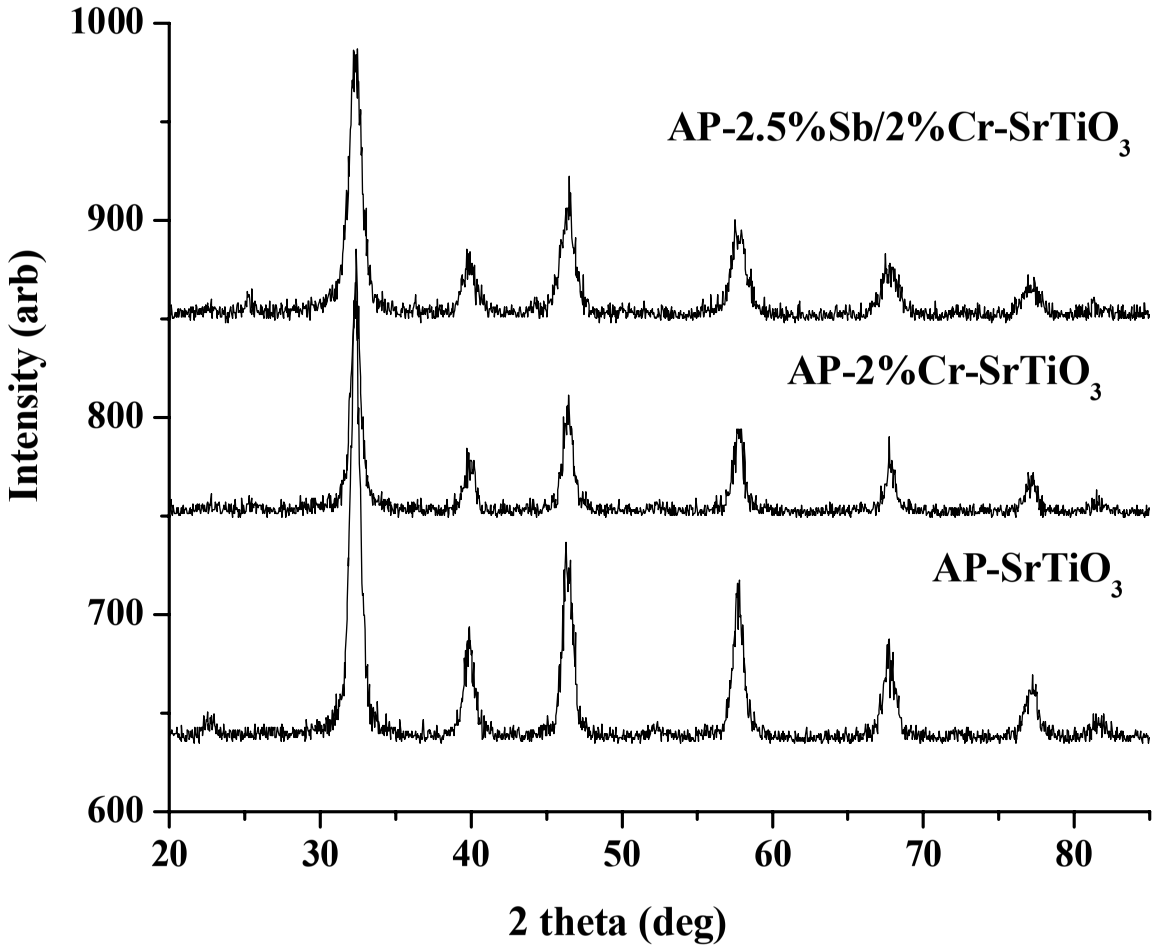

Figure 5.6 Powder XRD Patterns of Aerogel Prepared Strontium Titanate Samples (AP-$SrTiO_3$ – Pure, AP-2%Cr-$SrTiO_3$ – 2% Chromium Ion Doped, AP-2.5%Sb/2%Cr-$SrTiO_3$ – 2.5% Antimony and 2% Chromium Ion Codoped)

The surface areas, pore size distributions, and pore volumes of different samples were measured on a Nova 1200 gas sorption analyzer (Quantachrome Corp.) from the amount of N_2 absorbed at 77K and calculated according to the Brunauer-Emmett-Teller (BET) method. The samples were degassed at 423 K for 1 hour prior to the analysis.

Light absorption spectra of the samples were obtained on a Cary 500 Scan UV-Visible Spectrometer with an integrating sphere attachment for diffuse reflectance in the range 200-800 nm.

Transmission electron micrographs were obtained on a Philips CM 100. Samples were placed onto a carbon-coated copper grid by the physical interaction of the grid and powder in such a way that the particles remained adhered to the grids.

Pure strontium titanate ($SrTiO_3$) and titanium oxide (TiO_2 P25 Degussa) absorbed only UV light and did not absorb any visible light (Figure 5.7). Chromium doping has increased the absorbance in the visible light region compared with undoped samples. Cr and Cr/Sb doped strontium titanate samples had intense absorption in the 400-600 nm.

The freshly prepared Cr doped $SrTiO_3$ aerogels needed calcination in air at 773 K for five hours to remove the organic residuals of solvent in the pores and on the surface of the samples. The color of the samples changed from light green for freshly prepared chromium doped aerogels to light yellow for calcined Cr-$SrTiO_3$ aerogels.

The comparison between freshly prepared aerogel and calcined aerogel samples (Figure 5.8) showed the incorporation of the Cr^{3+} ions into the lattice of the $SrTiO_3$ samples (intense absorption band at 400-500 nm). Some of Cr^{3+} surface ions (absorption band at 610 nm) were oxidized into Cr^{6+} ions (absorption band at 380 nm) during calcination. The antimony/chromium doped exhibited more intense absorption compared with chromium doped strontium titanate.

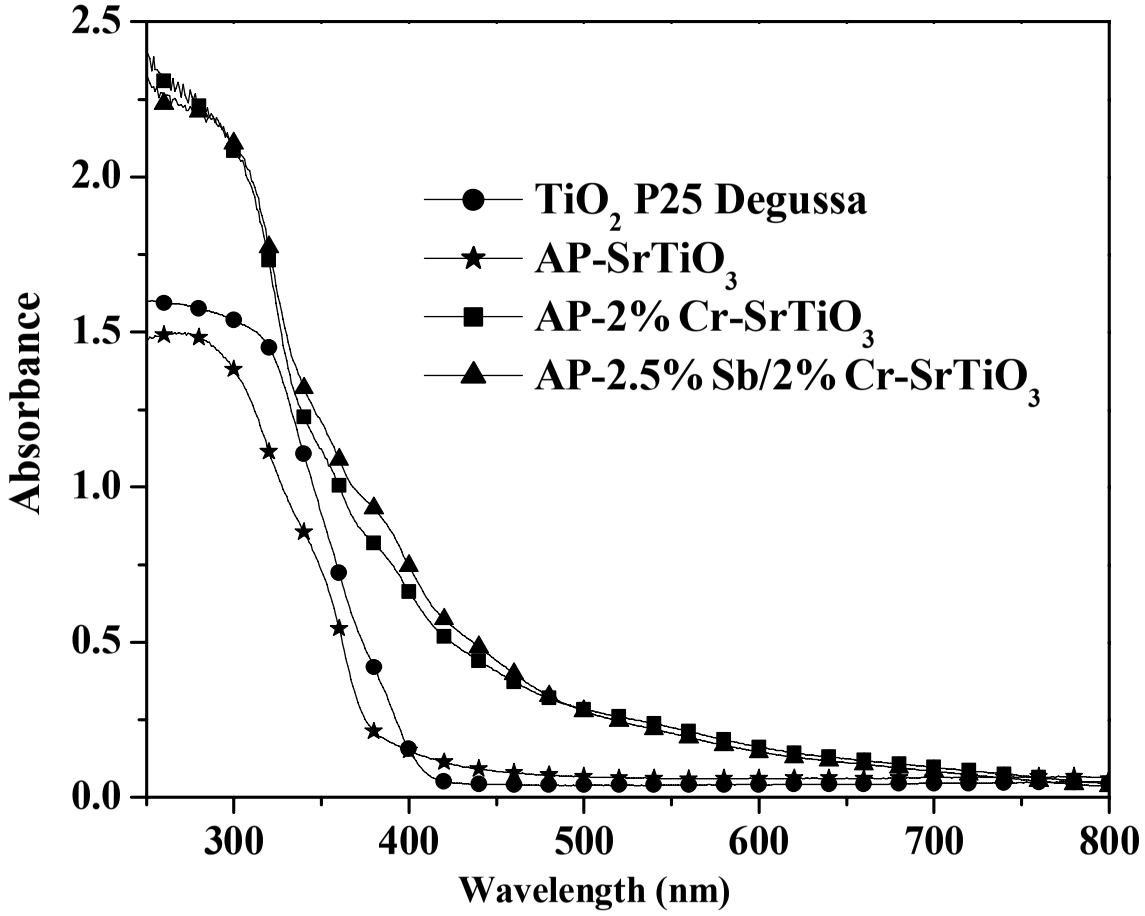

Figure 5.7 Defuse Reflectance Spectra of Pure $SrTiO_3$, TiO_2 P25 Degussa, 2% Cr Doped and 2% Cr/2.5% Sb Codoped Aerogel Prepared Strontium Titanate Samples

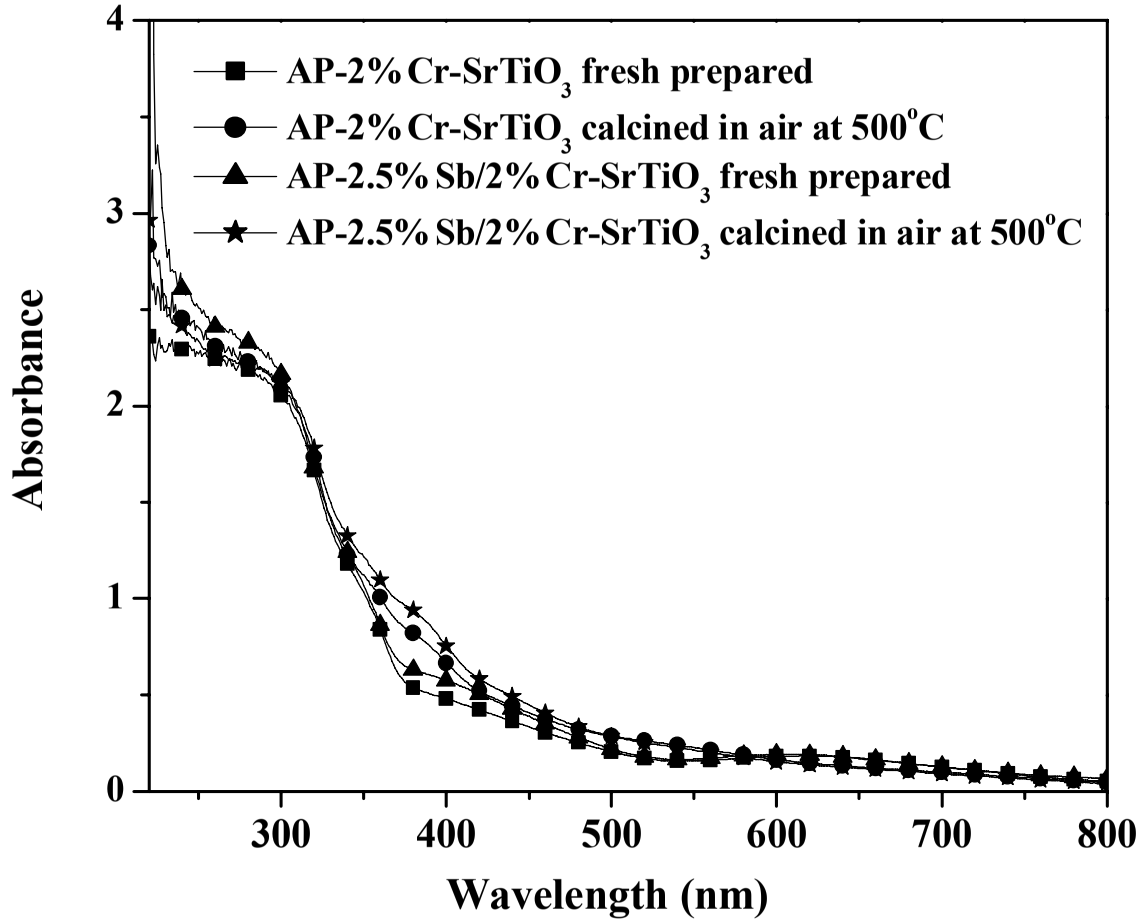

Figure 5.8 Defuse Reflectance Spectra of 2% Cr Doped and 2% Cr/2.5% Sb Codoped Aerogel Prepared Strontium Titanate Samples Freshly Prepared and Calcined at 773 K

The crystallite morphology of the synthesized chromium and chromium/antimony doped $SrTiO_3$ aerogels was analyzed by TEM (Figure 5.9). All crystallites had uniform spherical shapes with a size distribution near 12 nm for Cr-$SrTiO_3$ and near 10 nm for Sb/Cr-$SrTiO_3$ samples. The average crystallite sizes were calculated from XRD studies using the Debye-Scherrer equation. The nanosized crystalline primary particles tend to stay together and form aggregates of secondary particles.

The BET surface areas of the samples are shown in Table 5.1. The small loss in surface areas for doped samples could be due to sintering favored by the presence of dopants. Besides, the addition of the dopant (Cr or Cr/Sb) caused an increase in the total pore volume and average pore size. The average crystallite sizes of all prepared $SrTiO_3$ samples were around 10 nm in diameter.

Table 5.1 Textural Properties of Photocatalysts

Sample	Crystallite sizes, nm	Surface area, m^2/g	Total pore volume, cm^3/g	Average pore size, Å
TiO2 P25 Degussa	25	50.2	0.182	145
Pure Aerogel $SrTiO_3$	11	93.0	0.450	190
2%Cr doped $SrTiO_3$	12	81.9	0.488	236
2%Cr/2.5%Sb doped $SrTiO_3$	10	68.8	0.662	384

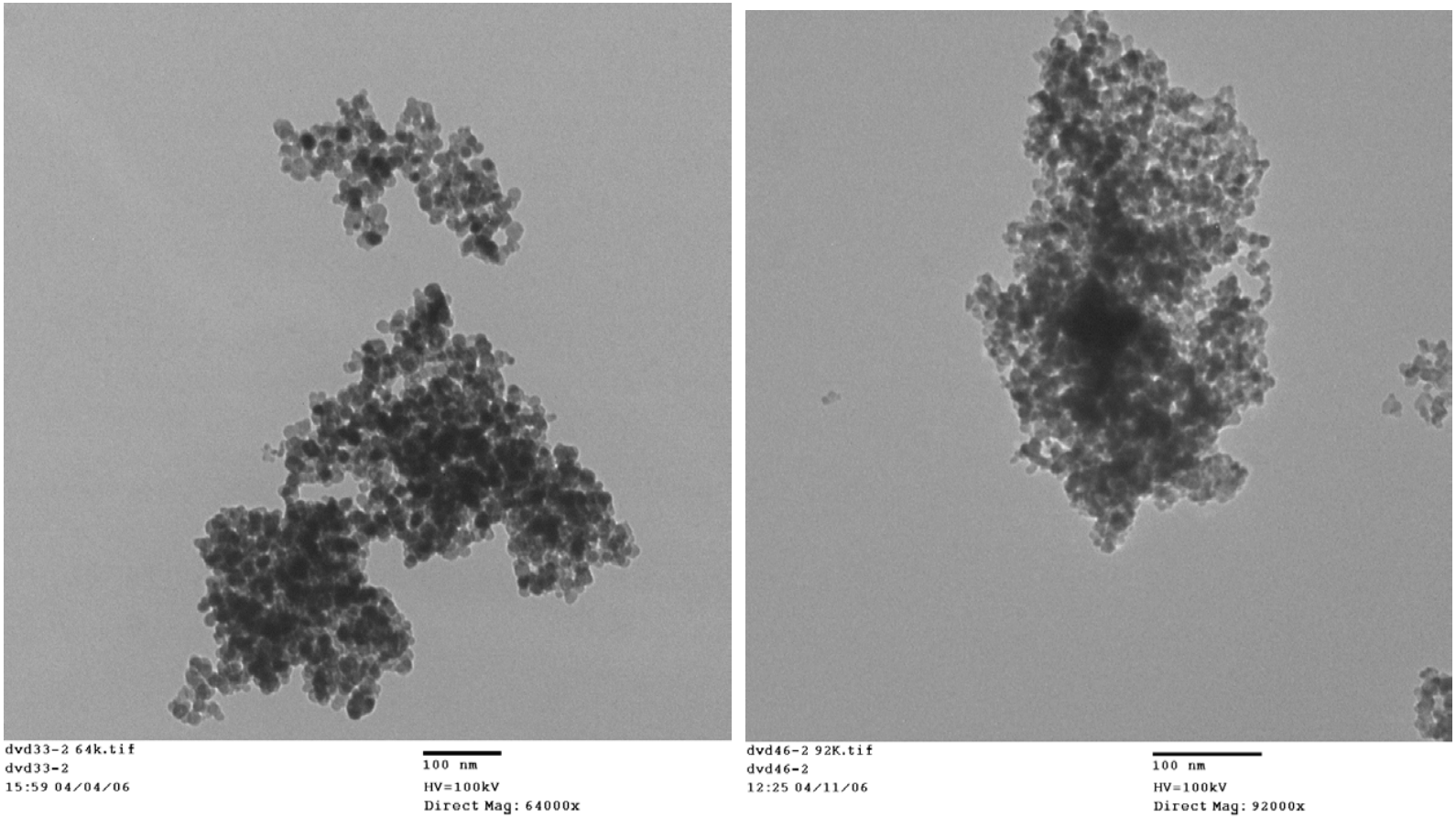

Figure 5.9 Transmission Electron Micrographs of 2% Cr Doped (left) and 2% Cr/2.5% Sb Codoped (right) Aerogel Prepared Strontium Titanate Samples

All doped aerogel samples were studied and compared with a typical photocatalyst standard, Degussa P25 TiO_2 particles. The undoped samples of titanium oxide (P25 TiO_2) and pure aerogel prepared strontium titanate (AP-$SrTiO_3$) showed significant activity for the degradation of acetaldehyde (CH_3CHO) and carbon dioxide (CO_2) production utilizing UV light (Table 5.2). When these samples were irradiated using visible light, the conversion of CH_3CHO into CO_2 was negligible. After doping with 2% chromium, the $SrTiO_3$ sample was active, not only under UV light irradiation, but also under visible light irradiation (Table 5.2). The introduction of Cr ions into the $SrTiO_3$ lattice caused an increase in the initial reaction rate for the acetaldehyde decomposition in the visible region and a slight decrease in this reaction rate under UV irradiation in comparison with undoped strontium titanate. The initial reaction rate for the carbon dioxide was significantly lower for the Cr doped AP-$SrTiO_3$ in the UV light region. This dramatic decrease in the rate can be explained by the stronger production of the not fully oxidized byproducts and less formation of the carbon dioxide final product. Nevertheless, Cr-doped AP-$SrTiO_3$ showed a higher activity in the visible region for carbon dioxide production and acetaldehyde decomposition compared to pure AP-$SrTiO_3$ and P25 TiO_2.

Table 5.2 Initial Rates of Acetaldehyde Degradation and Carbon Dioxide Production

Sample	Dopant	Light source	Initial rate r[CH_3CHO]	Initial rate r[CO_2]
TiO_2 Degussa	--	UV (320<λ<400 nm)	0.1023	0.01310
AP-$SrTiO_3$	--	UV (320<λ<400 nm)	0.0525	0.00280
AP-$SrTiO_3$	2% mol. Cr	UV (320<λ<400 nm)	0.0498	0.00084
TiO_2 Degussa	--	Visible (420 nm<λ)	0.0147	0.00016
AP-$SrTiO_3$	--	Visible (420 nm<λ)	0.0077	0.00021
AP-$SrTiO_3$	2% mol. Cr	Visible (420 nm<λ)	0.0350	0.00039

To study the photocatalytic properties and reproducibility of the Cr-$SrTiO_3$ and Sb/Cr-$SrTiO_3$ samples, three consecutive experiments of each sample for acetaldehyde decomposition were performed and compared. The photoactivity of 2.5%Sb/2%Cr codoped $SrTiO_3$ aerogel was significantly higher than that of the $SrTiO_3$ sample doped with only Cr. The

activity of antimony/chromium doped strontium titanate was almost twice as high for carbon dioxide production in UV and visible light regions (Figures 5.10, 5.11).

The photoactivity of 2.5%Sb/2%Cr codoped $SrTiO_3$ aerogel was relatively similar to the activity of chromium doped strontium titanate for acetaldehyde decomposition under UV and visible light irradiation (Figure 5.12, 5.13). There was an induction period for the Sb/Cr-$SrTiO_3$ sample during the first experiment. The lower activity could be assigned to the initial presence of the Cr^{6+} species. During the experiments, these species were reduced by organic material to Cr^{3+} ions, and this might be the reason for the increase in activity in visible and UV light regions. The Sb/Cr-$SrTiO_3$ aerogel also showed almost equal activity for acetaldehyde decomposition under UV and visible irradiation.

Strontium titanate aerogel was also doped with antimony to study the influence of Sb doping on the photoactivity of the catalyst. The addition of antimony did not have any effect on the photoactivity of the catalyst for carbon dioxide production under UV or visible irradiation (Figures 5.14, 5.15)

Also, the addition of antimony did not have a significant effect on the photoactivity of the catalyst for acetaldehyde decomposition under UV or visible irradiation (Figures 5.16, 5.17), and only a slight increase in initial reaction rates for acetaldehyde decomposition was noticed.

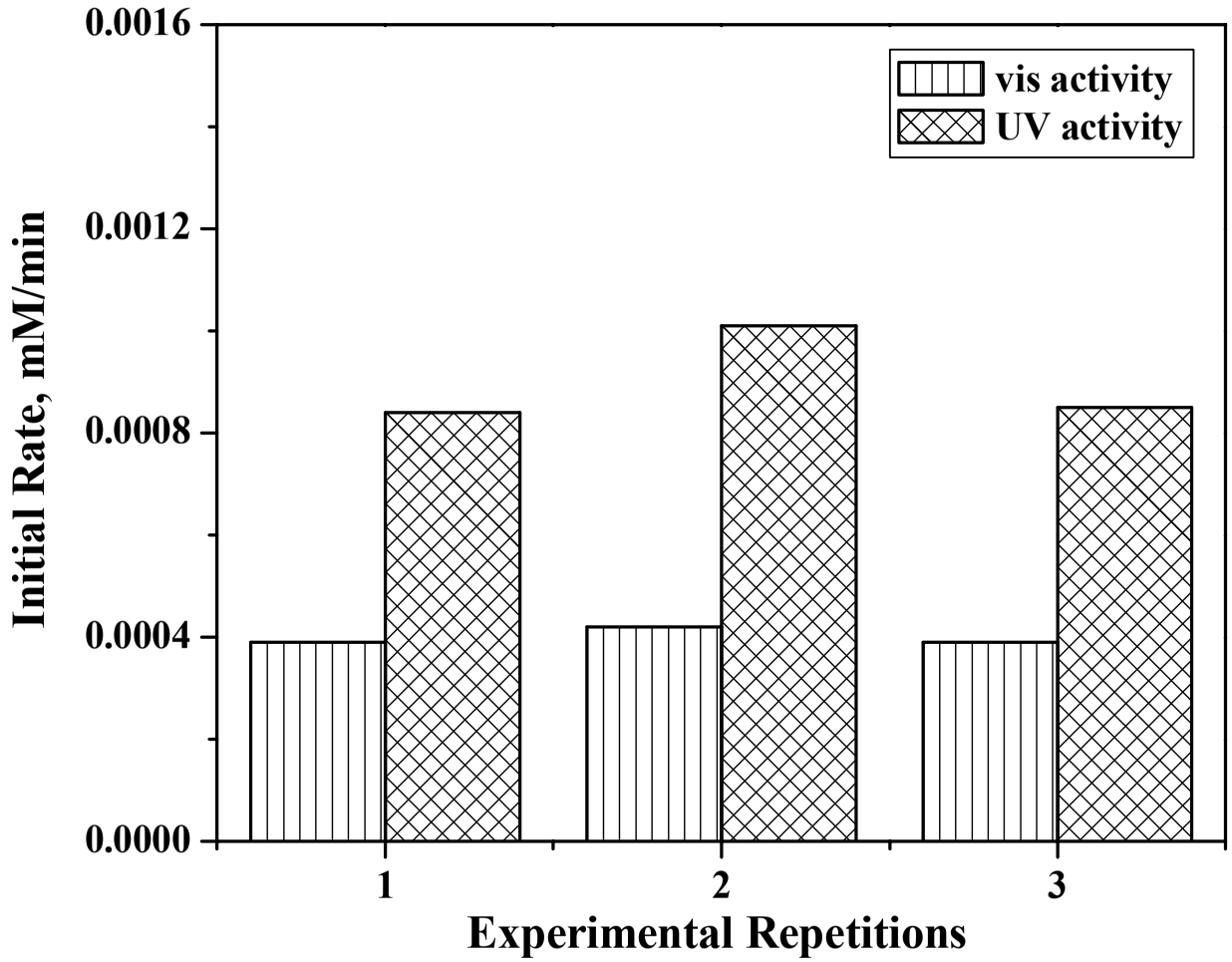

Figure 5.10 UV and Visible Photoactivity of Cr-$SrTiO_3$ Aerogel for CO_2 Production

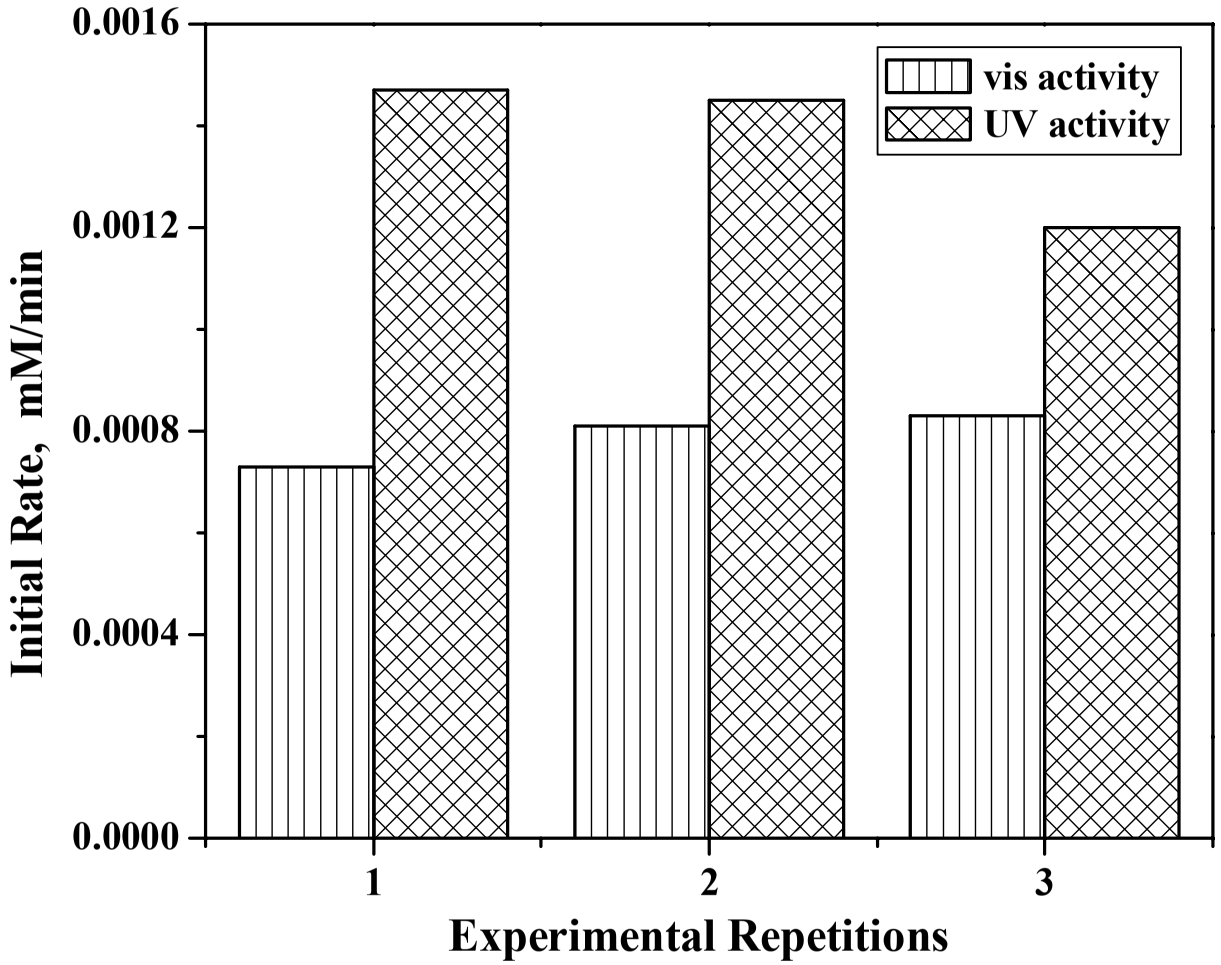

Figure 5.11 UV and Visible Photoactivity of Sb/Cr-$SrTiO_3$ Aerogel for CO_2 Production

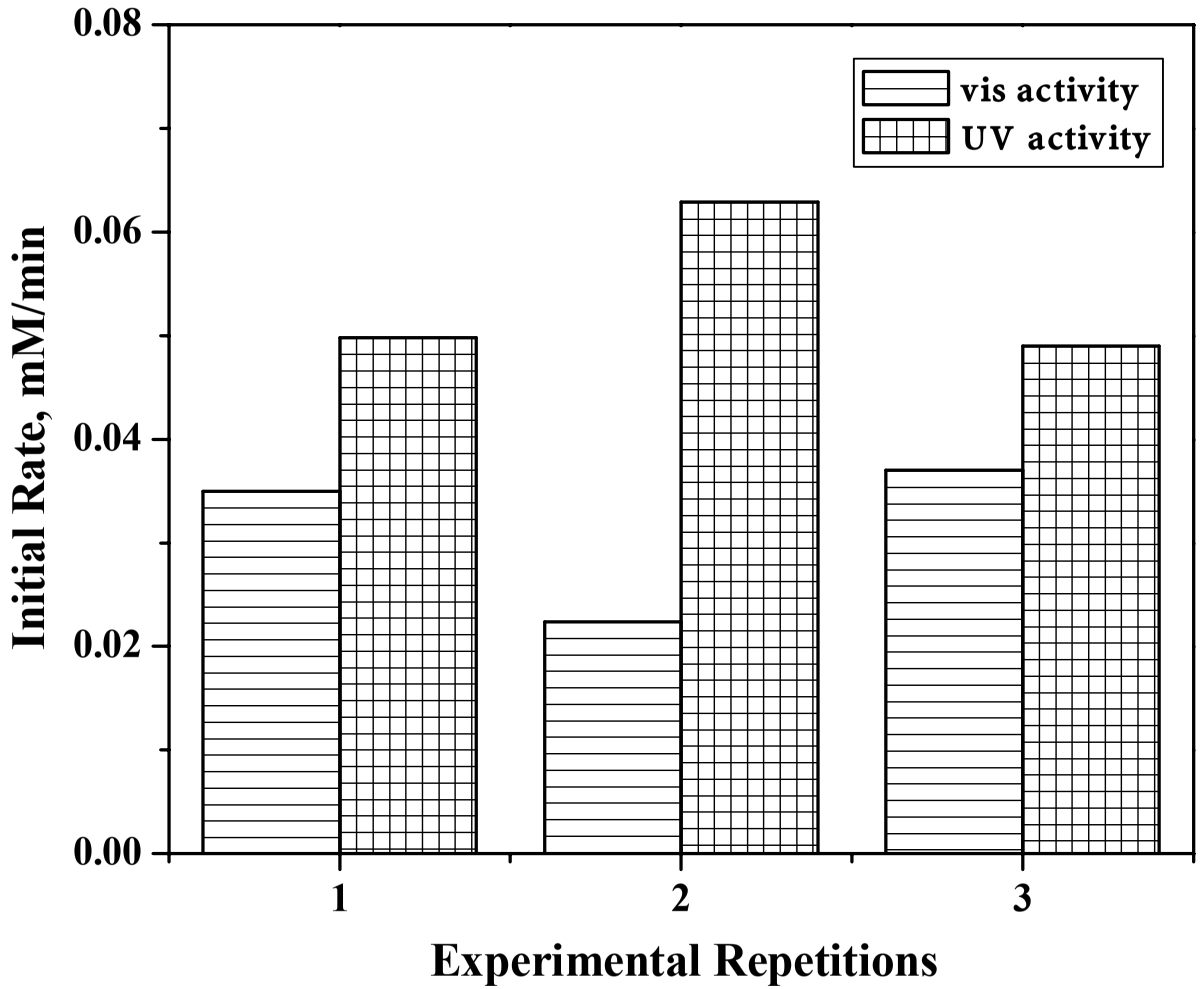

Figure 5.12 UV and Visible Photoactivity of Cr-$SrTiO_3$ Aerogel for CH_3CHO Degradation

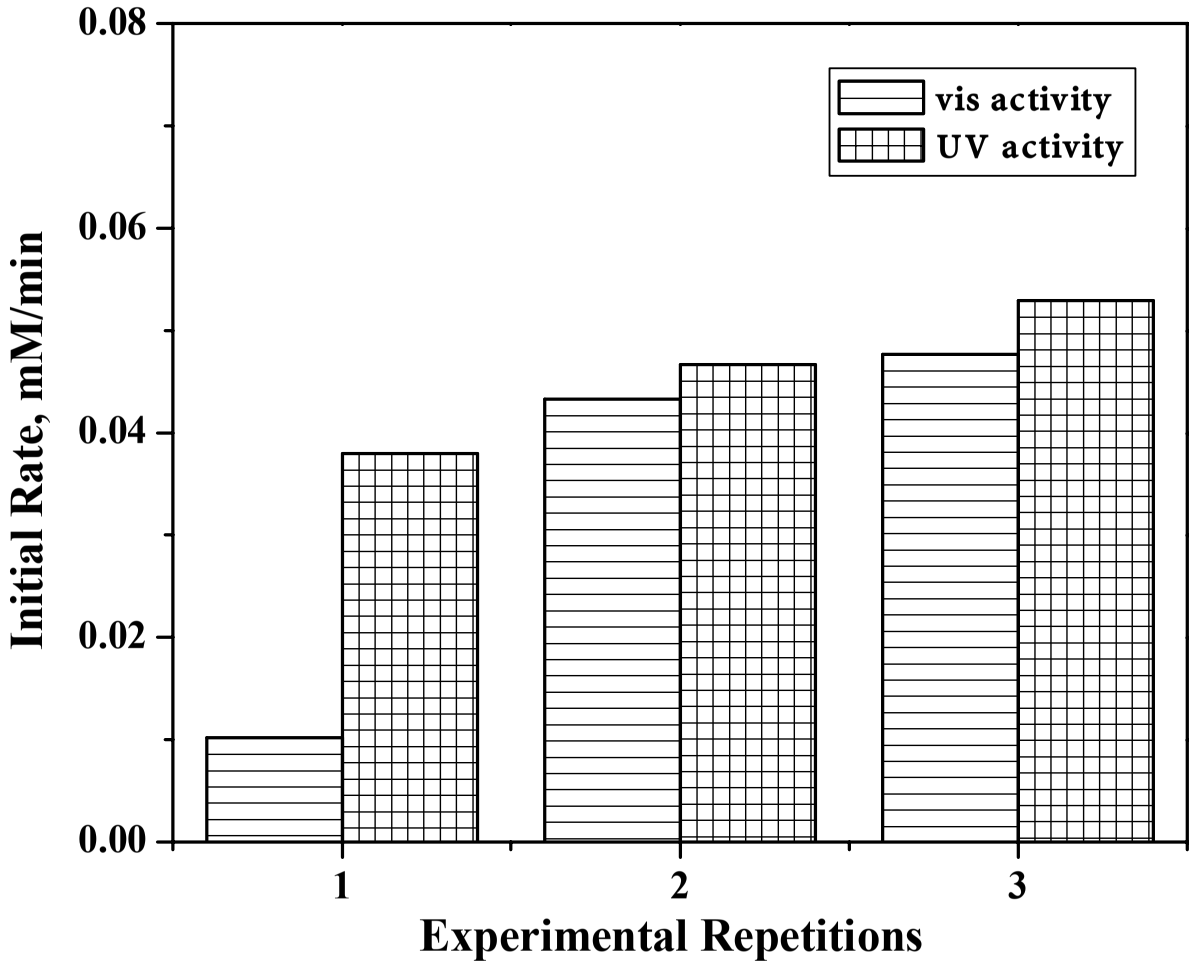

Figure 5.13 UV and Visible Photoactivity of Sb/Cr-$SrTiO_3$ Aerogel for CH_3CHO Degradation

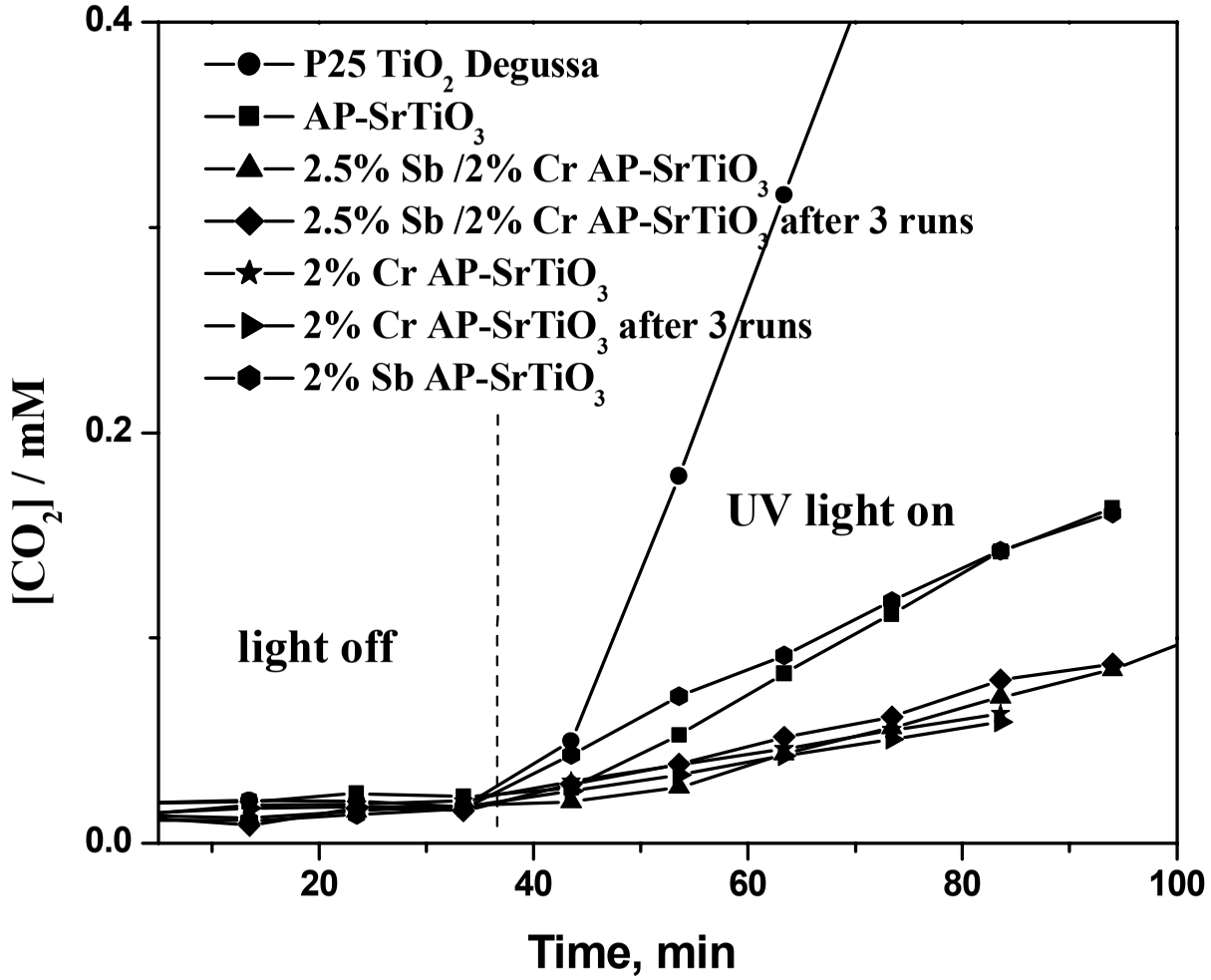

Figure 5.14 CO_2 Evolution for Aerogel Prepared Catalysts under UV Light

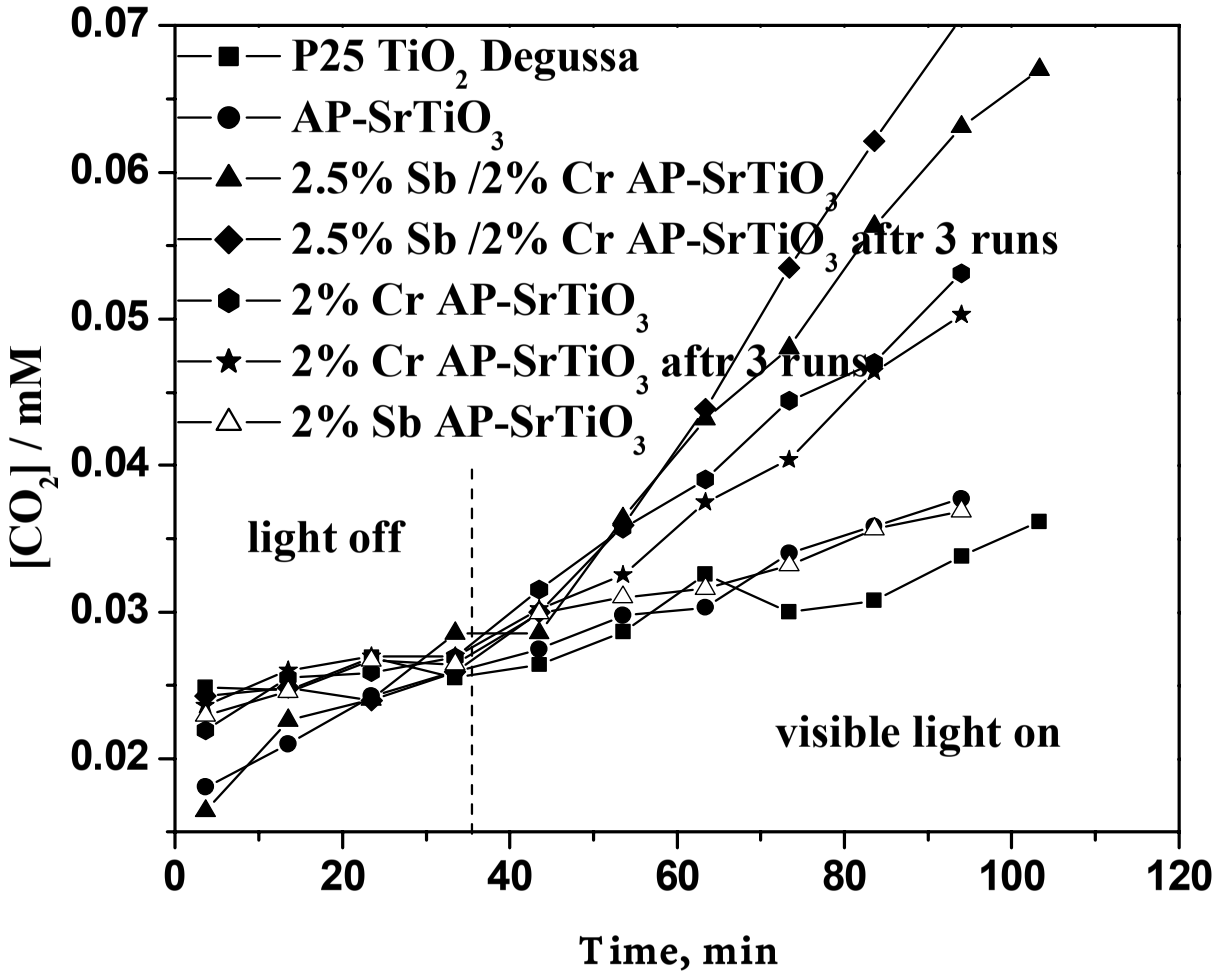

Figure 5.15 CO_2 Evolution for Aerogel Prepared Catalysts under Visible Light

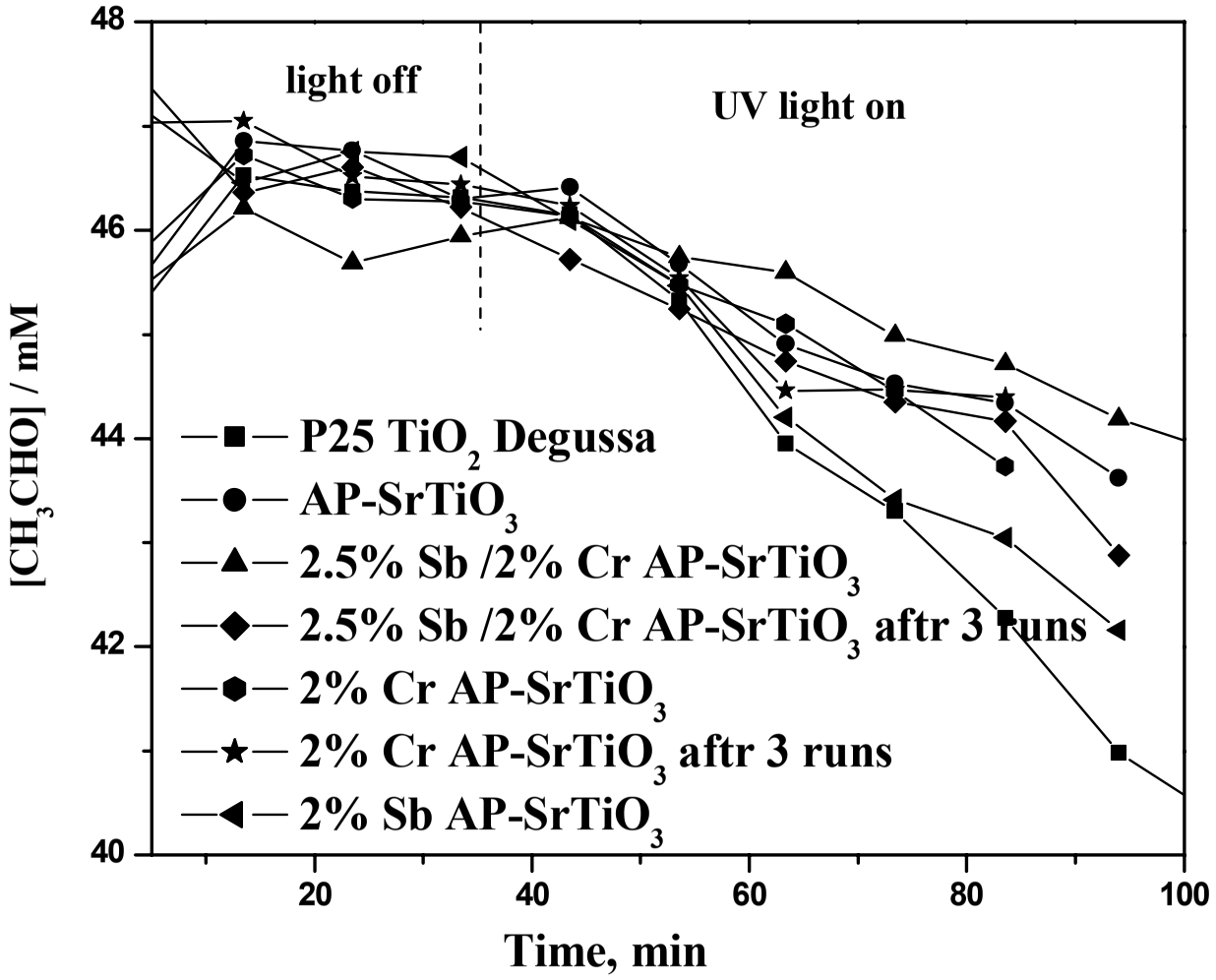

Figure 5.16 CH_3CHO Degradation for Aerogel Prepared Catalysts under UV Light

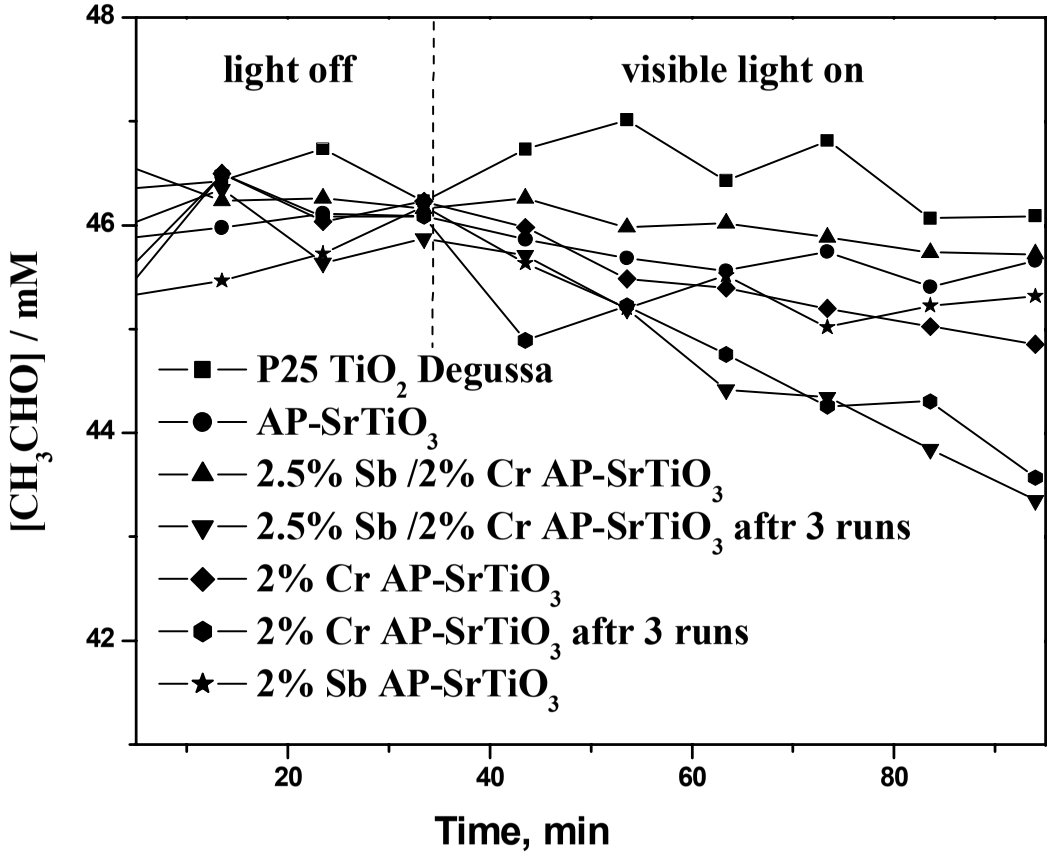

Figure 5.17 CH_3CHO Degradation for Aerogel Prepared Catalysts under Visible Light

The initial reaction rates for all samples used for acetaldehyde decomposition are summarized in Table 5.3. Undoubtedly, Cr doping and Sb/Cr codoping increased the photoactivity of $SrTiO_3$ aerogels towards the visible light region. The Sb/Cr-$SrTiO_3$ photocatalyst gave the highest activity for CO_2 production under visible light irradiation and is a promising candidate to be studied for other photocatalytic reactions.

Table 5.3 Photocatalysts for Acetaldehyde Degradation and Carbon Dioxide Production

Sample	Dopant	UV		Visible	
		Initial rate		Initial rate	
		r[CH_3CHO]	r[CO_2]	r[CH_3CHO]	r[CO_2]
P25 TiO_2 Degussa	no	0.1023	0.01310	0.0147	0.00016
AP-$SrTiO_3$ dopant free	no	0.0525	0.00280	0.0077	0.00021
AP-$SrTiO_3$ with 2%Cr	Cr^{6+}- Cr^{3+}	0.0498	0.00084	0.0350	0.00039
AP-$SrTiO_3$ with 2%Cr after 3 runs	Cr^{6+}- Cr^{3+}	0.0490	0.00085	0.0370	0.00039
AP-$SrTiO_3$ with 2.5%Sb/2%Cr	Cr^{3+}- Sb^{5+}	0.0380	0.00147	0.0102	0.00073
AP-$SrTiO_3$ with 2.5%Sb/ 2%Cr after 3 runs	Cr^{3+}- Sb^{5+}	0.0529	0.00120	0.0477	0.00083
AP-$SrTiO_3$ with 2%Sb	Sb^{3+} - Sb^{5+}	0.0775	0.00241	0.0181	0.00016

A balance between the amount of consumed acetaldehyde and the amount of formed carbon dioxide was not achieved since other less volatile byproducts besides carbon dioxide were also formed. To identify the nonvolatile byproducts, which were absorbed on the catalyst

surface and were not seen in the gas phase by gas chromatography, the FTIR studies were performed.

5.3.2 Cr doping and Sb/Cr codoping of solid-state prepared samples

To evaluate the photoactivity of chromium doped and chromium/antimony codoped aerogel prepared $SrTiO_3$ catalysts, the chromium doped and chromium/antimony codoped solid-state prepared $SrTiO_3$ were synthesized and activity of these catalysts was compared.

Chromium and antimony/chromium doped solid-state strontium titanates were prepared with 2% Cr and 2% Cr/2.5% Sb loadings by molar weight. The addition of metal ions from salts (chromium (III) nitrate and/or antimony (III) acetate) was in such a way that the molar ratio of $SrTi_{0.98}Cr_{0.02}O_3$ and $SrTi_{0.954}Cr_{0.02}Sb_{0.025}O_3$ would be preserved. The solid precursors of strontium carbonate ($SrCO_3$), titanium oxide (TiO_2), chromium oxide (Cr_2O_3) and additionally antimony oxide (Sb_2O_3) in case of Cr/Sb codoping) were mixed and calcined at 1100°C to synthesize Cr and Cr/Sb doped materials ($SrTi^{IV}_{1-2x}Cr^{III}_{2x}O_{3-x}$ and/or $SrTi^{IV}_{1-3x}Cr^{III}_{2x}Cr^{VI}_{x}O_3$, and $SrTi^{IV}_{1-2x}Cr^{III}_{x}Sb^{V}_{x}O_3$) according to method used in [16-17] and following the operational procedure for the preparation of solid state samples (Chapter 3.2.1). These materials have been already synthesized and extensively studied as photocatalysts for the water splitting[16, 17]. However, these catalysts have not been yet studied as photocatalysts to destroy volatile organic compounds.

The textural properties of the aerogel prepared samples were studied by different available techniques (More detailed information on sample characterization operation procedures can be found in Chapter 3.3). Powder X-ray diffractions patterns were obtained on a Bruker D8 Advance spectrometer with a CuKα radiation source with an applied voltage of 40 kV and a current of 40mA. Scans were made in the 2θ range of 20-85º with a scanning rate of 2 º/min. The crystallite size was calculated from the XRD patterns using the Debye-Scherrer equation. The comparison of powder diffractograms of chromium/antimony codoped solid-state and aerogel prepared strontium titanate is presented in Figure 5.18).

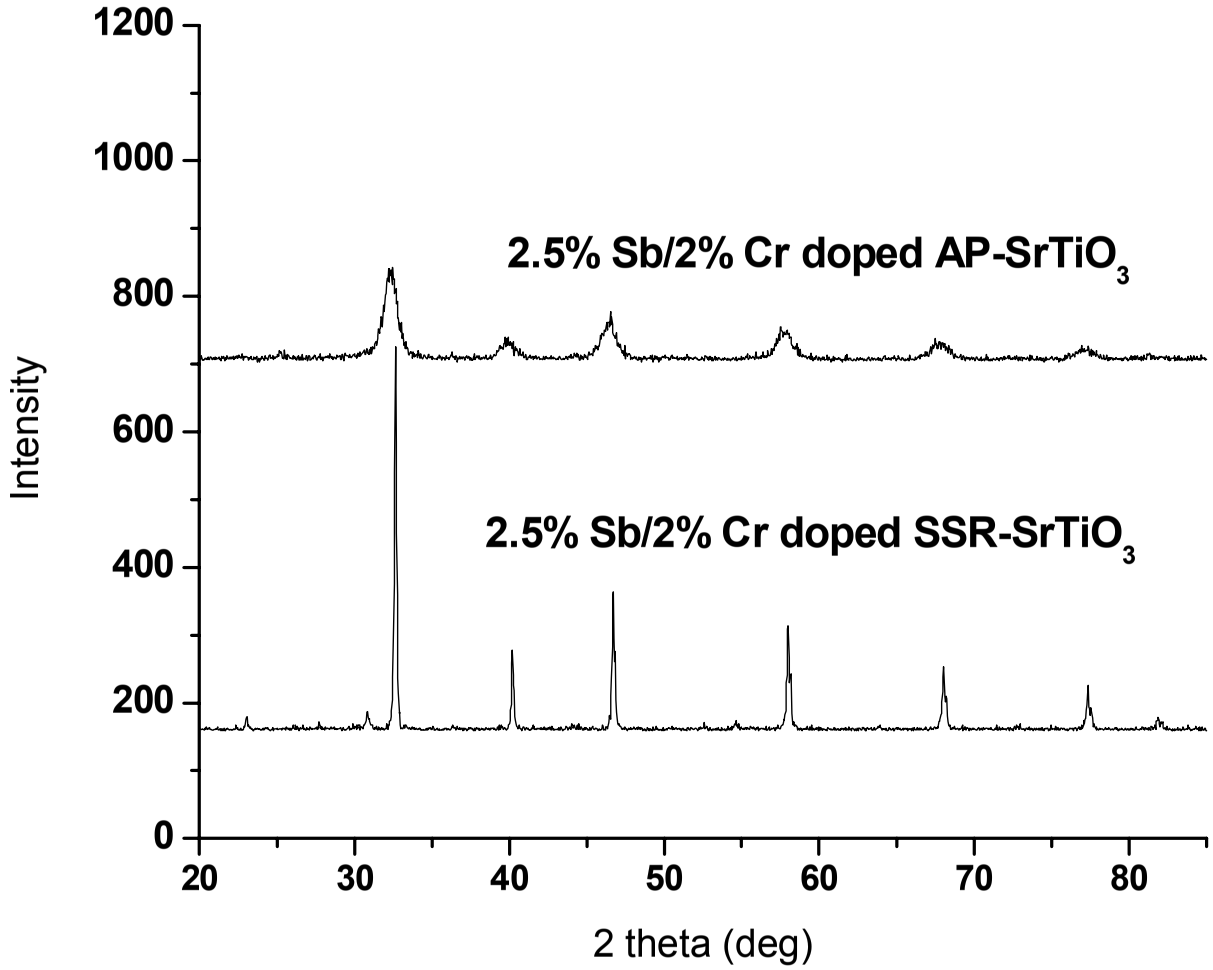

Figure 5.18 2.5% Sb/2% Cr Codoped $SrTiO_3$ Prepared by Solid-State Reaction and Aerogel Modified Procedure

The peaks of solid-state prepared samples are significantly narrow, which can be attributed to larger particle sizes. Besides, even after long calcination, the solid-state prepared sample is not pure and has some impurities caused by incomplete reaction of precursors and/or by oxygen deficiency. This problem is common for all samples prepared by the solid-state reaction method and has been already discussed in Chapter 3.3.3 (also see Appendix A). The absence of the dopant peaks indicates high dispersion and incorporation of the doped metal ions into the $SrTiO_3$ lattice. The application of the Debye–Scherrer equation for calculation of the average crystallite sizes of SSR-$SrTiO_3$ samples is limited by big particle sizes of these materials; the real sizes can be obtained from TEM graphs.

Surface areas, pore size distributions, and pore volumes of different samples were measured on a Nova 1200 gas sorption analyzer (Quantachrome Corp.) from the amount of N_2 absorbed at 77K and calculated according to the Brunauer-Emmett-Teller (BET) method. The samples were degassed at 423 K for one hour prior to analysis.The smaller surface areas of solid state prepared samples in comparison with aerogel samples can be explained by the preparation method. During the heating at high temperature, sintering causes the formation of nonporous or microporous dense material with large particle sizes and small surface area.

Table 5.4 Textural Properties of AP- and SSR-$SrTiO_3$ Samples

Sample	Surface area, m^2/g	Total pore volume, c^3/g	Average Pore Diameter, Å
AP-$SrTiO_3$	93	0.450	194
SSR-$SrTiO_3$	0.5	0.016	125
2% Cr doped AP-$SrTiO_3$	82	0.483	236
2% Cr doped SSR-$SrTiO_3$	1.1	0.009	229
2.5% Sb/2% Cr codoped AP-$SrTiO_3$	69	0.662	384
2.5% Sb/2% Cr codoped SSR-$SrTiO_3$	3	0.011	153

The addition of dopants (chromium oxide and antimony oxide) during solid-state reaction causes a slight increase in the porosity of the products and surface area. However, the total pore volume does not increase by doping; the higher surface area is caused by an increase in pore sizes.

Transmission electron micrographs were obtained on a Philips CM 100. Samples were placed onto a carbon-coated copper grid by the physical interaction of the grid and powder in such a way that the particles remained adhered to the grids. The solid-state prepared samples have polydispersed sizes up to 500 nm and nonuniform shapes due to grinding and sintering.

Light absorption spectra of the samples were obtained on a Cary 500 Scan UV-Visible Spectrometer with an integrating sphere attachment for diffuse reflectance in the range 200-800 nm. Chromium doping has increased the absorbance in the visible light region compared with the undoped solid state prepared sample (Figure 5.20). Solid-state prepared samples of Cr and Cr/Sb doped strontium titanate had intense absorption in 400-700 nm. The main differences between chromium doped and antimony/chromium codoped samples are the shapes of the adsorption peaks in the visible light region. The Cr doped SSR-$SrTiO_3$ has two combined peaks located at 400-500 nm and 500-600 nm regions, while Sb/Cr codoped SSR-$SrTiO_3$ has one steep peak at 400-500 nm. Besides, the colors of the samples are different, too. The color of Cr doped SSR-$SrTiO_3$ sample is dark purple, while the color of the Sb/Cr sample is beige.

Confirming findings of Kudo et al. [16], the Cr doped SSR-$SrTiO_3$ sample has incorporated Cr^{3+} ions (400 - 500 nm) and Cr^{6+} (500 - 600 nm), and the shallow shoulder (up to 700 nm) shows the presence of oxygen defects. Cr/Sb codoped SSR-$SrTiO_3$ has only incorporated Cr^{3+} at 400-500 nm. Antimony plays a role of a charge compensator and prevents it from the Cr^{6+} ions and oxygen defects production. The comparison of DRS between aerogel prepared and solid-state prepared doped samples (Figure 5.21) showed that aerogel prepared samples, besides having Cr^{3+} ions incorporated in the lattice of samples, also have some Cr^{6+} ions. The presence of Cr (VI) in both aerogel samples (Cr doped and Cr/Sb codoped) can be explained by the oxidation of some Cr (III) into Cr (VI) on the surface during the calcination of samples after aerogel preparation to remove the organic residuals.

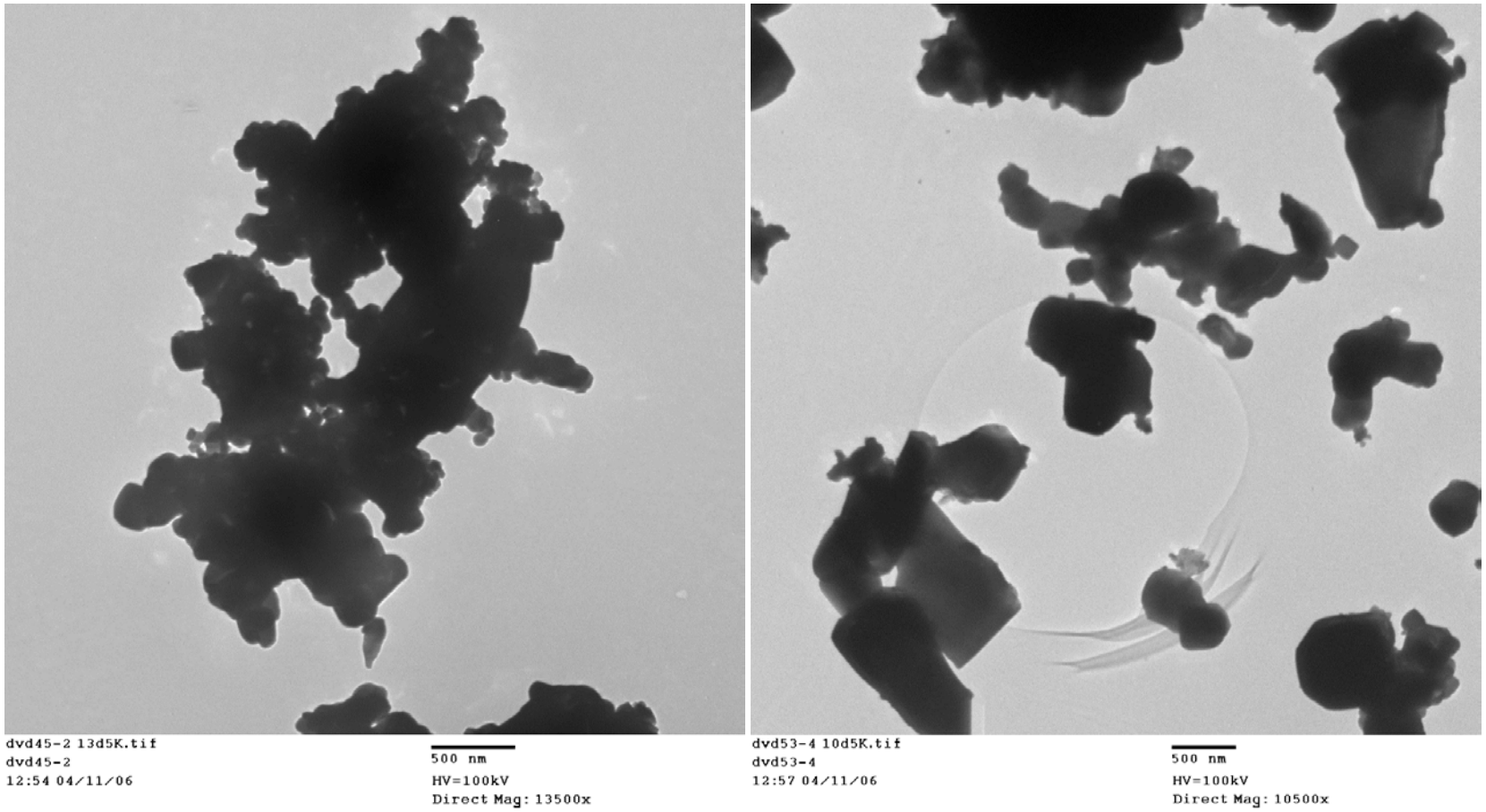

Figure 5.19 Transmission Electron Micrographs of 2% Cr Doped (left) and 2% Cr/2.5% Sb Codoped (right) Solid-State Prepared Strontium Titanate Samples

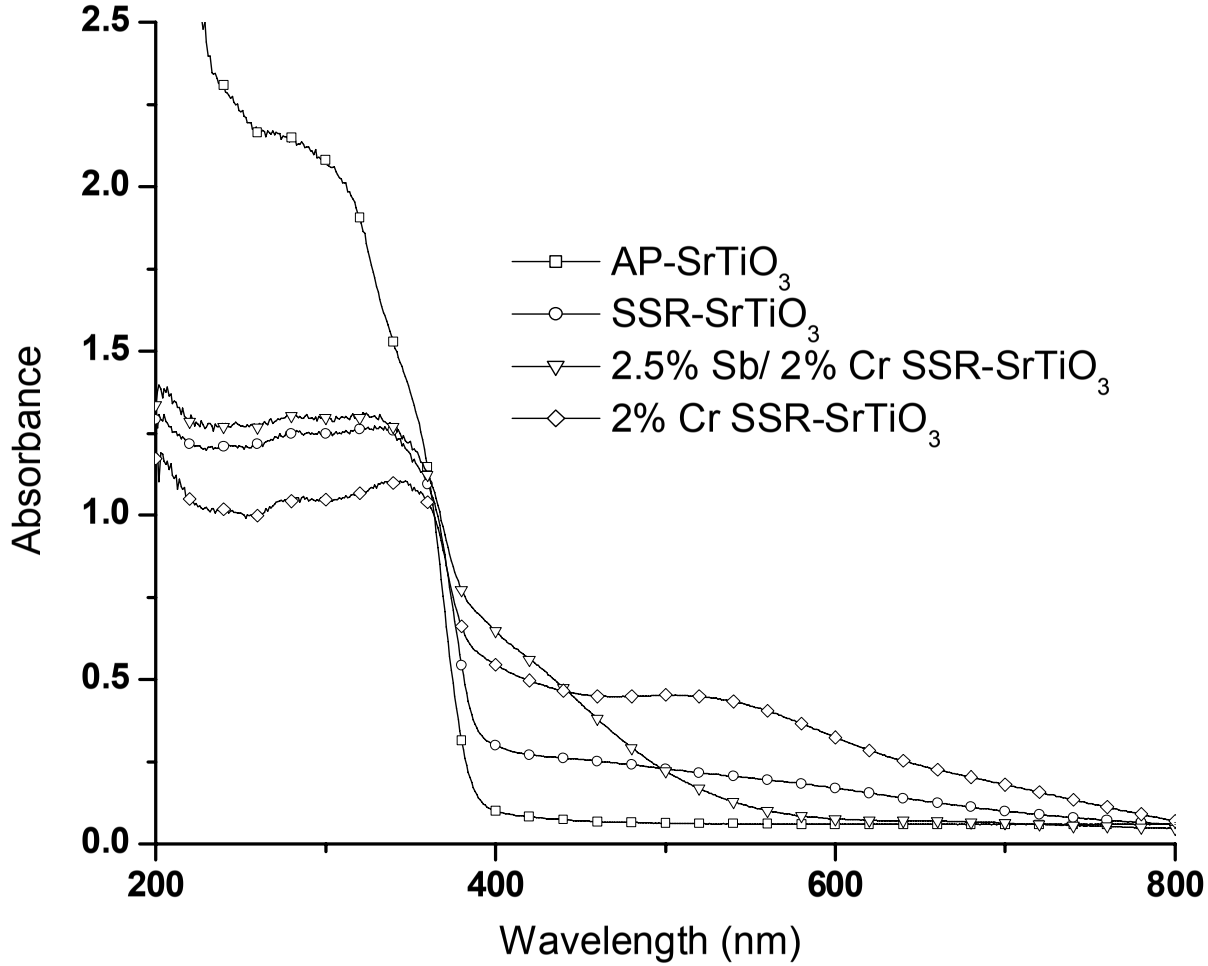

Figure 5.20 Diffuse Reflectance Spectra of 2.5% Sb/2% Cr $SrTiO_3$ Prepared by Solid-State Reaction

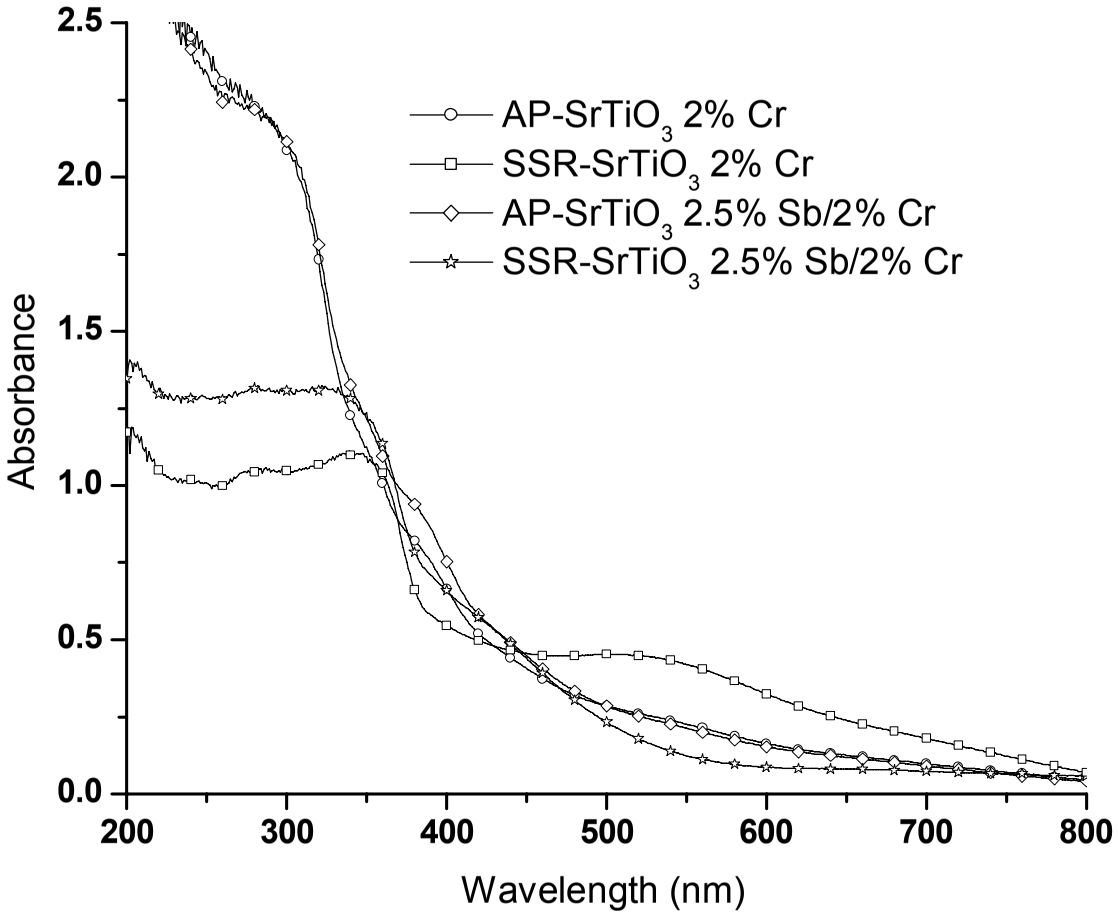

Figure 5.21 Diffuse Reflectance Spectra of 2%Cr $SrTiO_3$ and 2.5% Sb/2% Cr $SrTiO_3$ Prepared by Solid-state Reaction and by Aerogel Modified Procedure

To study the photocatalytic properties of solid-state prepared samples and reproducibility of them, three consecutive experiments of each sample were performed and compared with aerogel prepared catalysts, and standard catalyst (TiO_2 P25) for acetaldehyde decomposition under UV and visible light irradiation (Table 5.5).

All solid-state prepared samples including pure and doped catalysts show high activity for acetaldehyde decomposition under UV irradiation which is comparable with TiO_2 P25 and almost twice higher than the respective aerogel prepared catalysts. However, the production of the carbon dioxide under UV light for solid-state and aerogel prepared were on the same level. There is no direct dependence between the decomposition of acetaldehyde and the production of carbon dioxide due to the formation of intermediates and the adsorption of them on the surface. Nevertheless, if a catalyst decomposes twice more of the reagent, but forms twice less of the product, it means that additional reactions goes on the surface of the catalyst or a different mechanism of CH_3CHO decomposition takes place. From the analysis of the photoactivity data after several consecutive runs under UV irradiation, the first case is more likely. While the activity for acetaldehyde decreases significantly, the production of carbon dioxide stays on the same level (Figures 5.22-5.25). The comparison of Cr doped and Sb/Cr codoped solid-state prepared $SrTiO_3$ catalyst for carbon dioxide does not show any difference; however, for acetaldehyde decomposition, Cr doped SSR-$SrTiO_3$ sample losses activity twice faster than Cr/Sb codoped SSR-$SrTiO_3$ after three consecutive experimental runs (Figures 5.24, 5.25).

Similar in the visible region, the Cr doped SSR-$SrTiO_3$ sample loses activity for acetaldehyde decomposition twice faster than Cr/Sb codoped SSR-$SrTiO_3$ after three consecutive experimental runs. In contrast, aerogel prepared catalysts of Cr doped AP-$SrTiO_3$ and Cr/Sb codoped AP-$SrTiO_3$ after three consecutive experimental runs do not lose their activity.

The production of carbon dioxide on the surface of Cr doped and Cr/Sb codoped solid-state prepared catalysts is smaller than on the respective Cr doped and Cr/Sb codoped aerogel prepared samples.

Table 5.5 Photocatalytic Properties of AP- and SSR-$SrTiO_3$ Samples for Acetaldehyde Decomposition

Sample	UV light activity		Visible light activity	
	Initial rate r [CH_3CHO]	Initial rate r [CO_2]	Initial rate r [CH_3CHO]	Initial rate r [CO_2]
P25 TiO_2 Degussa	0.1023	0.01310	0.01470	0.00016
SSR-$SrTiO_3$	0.1160	0.00113	0.03230	0.00014
AP-$SrTiO_3$	0.0525	0.00280	0.00770	0.00021
2% Cr doped SSR-$SrTiO_3$	0.1027	0.00134	0.0489	0.00032
2% Cr doped SSR-$SrTiO_3$ 3runs	0.0526	0.00108	0.0297	0.00031
2% Cr doped AP-$SrTiO_3$	0.0498	0.00084	0.0350	0.00039
2% Cr doped AP-$SrTiO_3$ 3 runs	0.0490	0.00085	0.0370	0.00039
2.5% Sb/2% Cr codoped SSR-$SrTiO_3$	0.1080	0.00127	0.0376	0.00022
2.5% Sb/2% Cr codoped SSR-$SrTiO_3$ 3runs	0.0884	0.00102	0.0347	0.00034
2.5% Sb/2% Cr codoped AP-$SrTiO_3$	0.0380	0.00147	0.0102	0.00073
2.5% Sb/2% Cr codoped AP-$SrTiO_3$ 3 runs	0.0529	0.00120	0.0477	0.00083

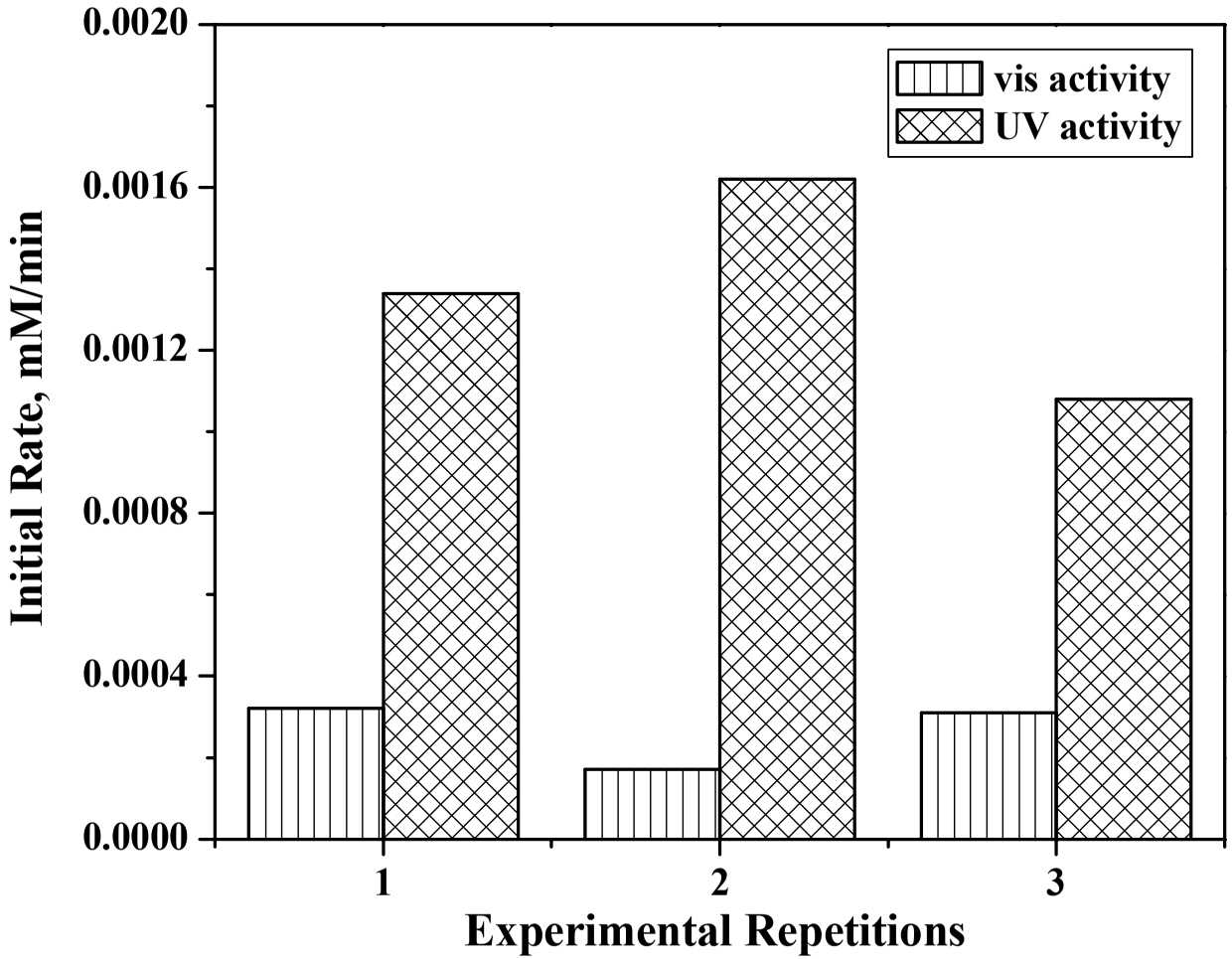

Figure 5.22 UV and Visible Photoactivity of Cr Doped SSR-$SrTiO_3$ for CO_2 Production

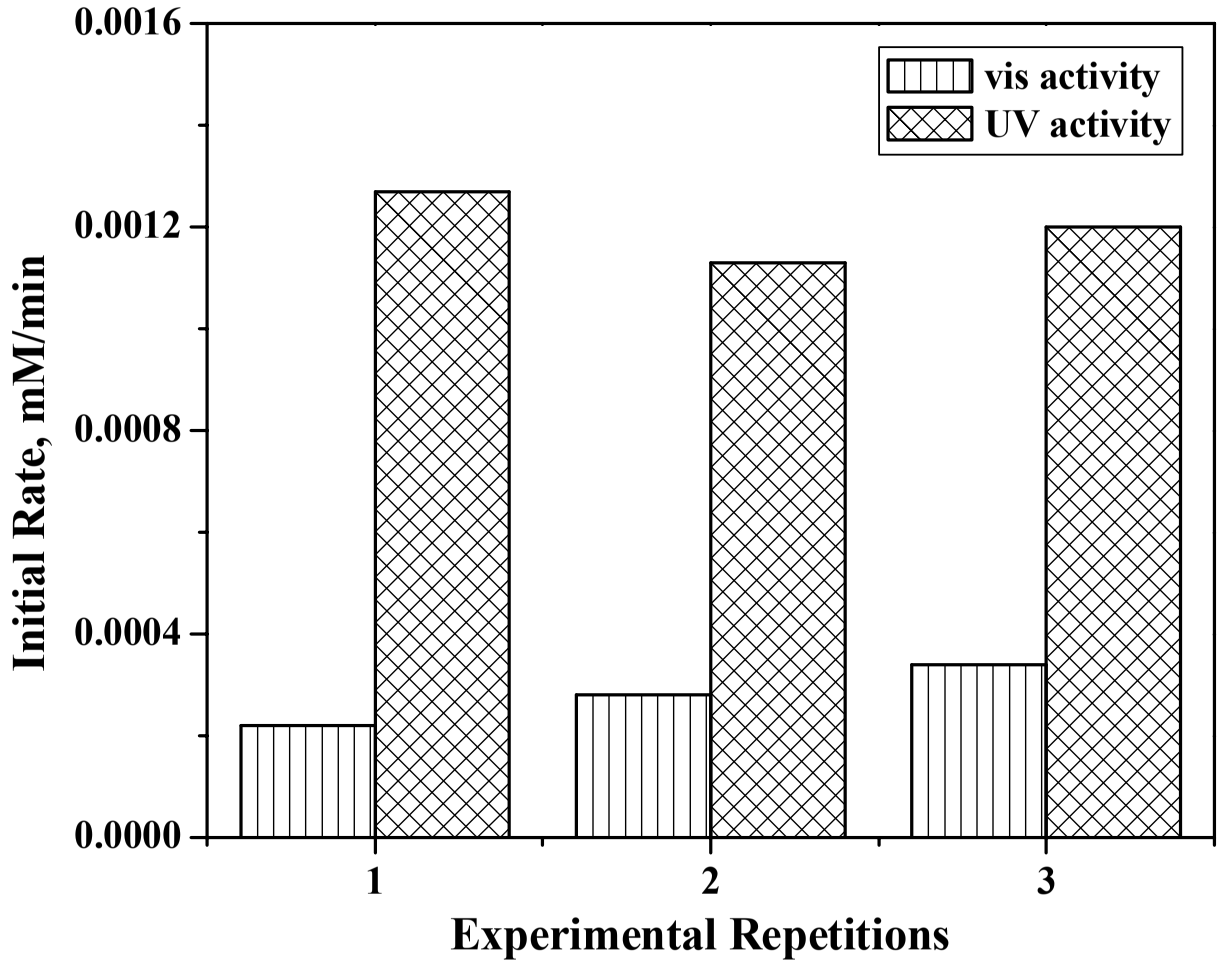

Figure 5.23 UV and Visible Photoactivity of Cr/Sb Codoped SSR-$SrTiO_3$ for CO_2 Production

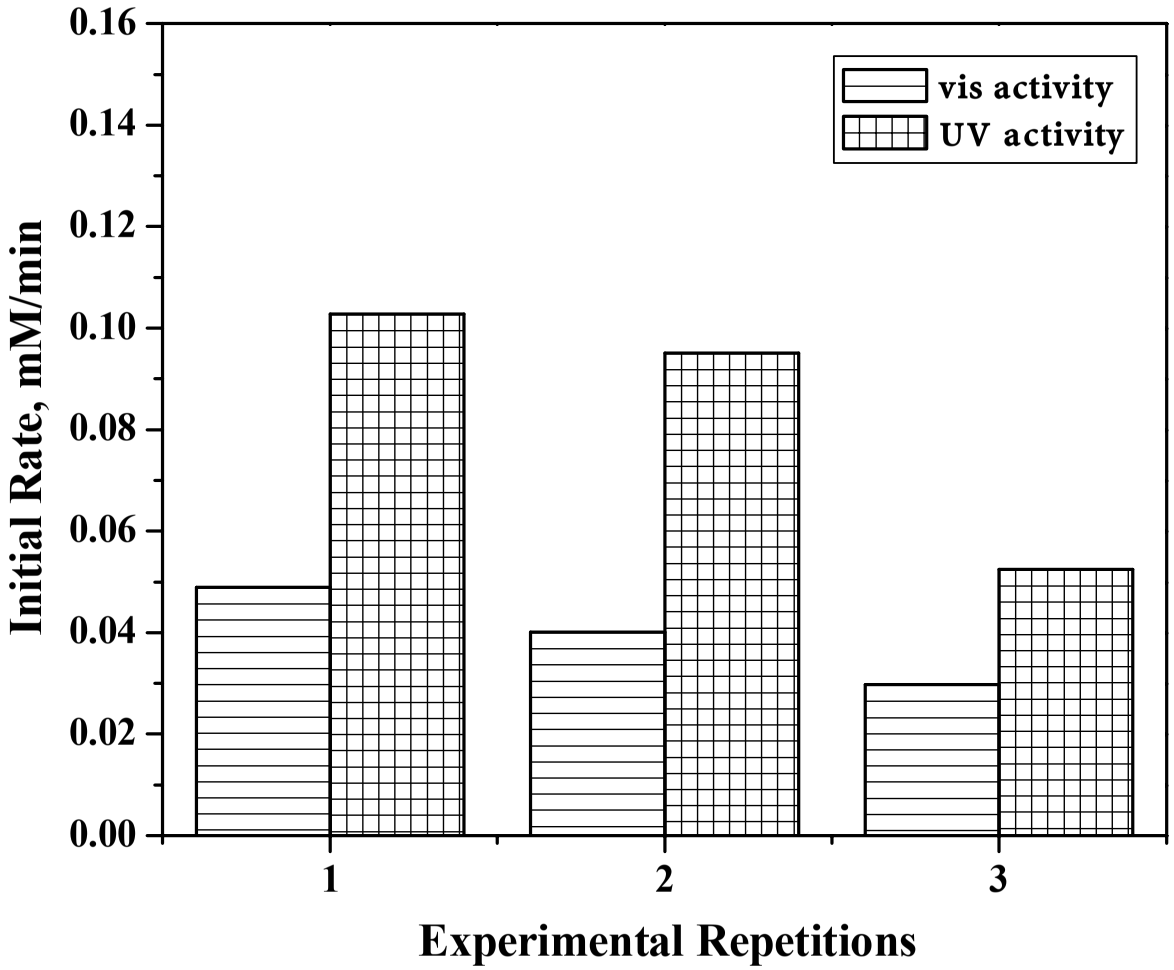

Figure 5.24 UV and Visible Photoactivity of Cr Doped SSR-$SrTiO_3$ for CH_3CHO Decomposition

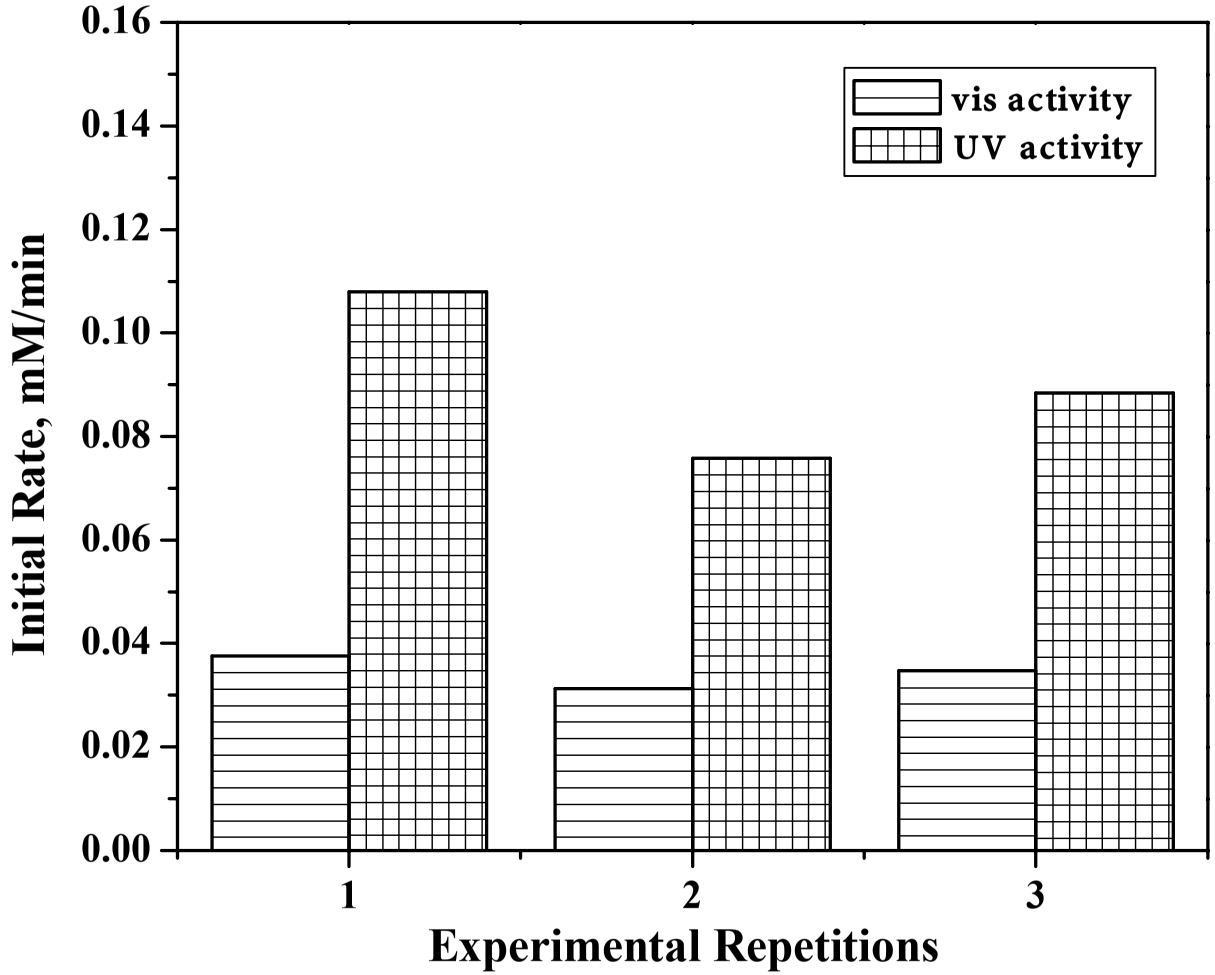

Figure 5.25 UV and Visible Photoactivity of Cr/Sb Codoped SSR-$SrTiO_3$ for CH_3CHO Decomposition

Finally, the activity of Cr/Sb codoped aerogel prepared AP-$SrTiO_3$ catalyst was highest among all synthesized and studied catalyst under UV or visible irradiation. This proves that novel nanosized Cr/Sb codoped AP-$SrTiO_3$ is a very effective catalyst for the decomposition of volatile organic compounds.

5.3.3 Cr doping of $SrTiO_3$ and $BaTiO_3$ catalysts

In the previous chapter, it was described that the nanosized barium titanate catalyst is also active for decomposition of acetaldehyde under UV light irradiation, which is similar to nanosized strontium titanate. While the activity of barium titanate is smaller than that of strontium titanate, it has the potential to be a good photocatalyst for visible light irradiation after doping with transition metals.

2% chromium doped barium titanate catalysts were prepared by solid-state reaction and aerogel procedure. The addition of chromium ion dopant (chromium (III) nitrate for aerogel, and chromium (III) oxide for solid-state prepared) was done in such a way that the molar ratio of $BaTi_{0.98}Cr_{0.02}O_3$ would be preserved.

Light absorption spectra of the samples were obtained on a Cary 500 Scan UV-Visible Spectrometer with an integrating sphere attachment for diffuse reflectance in the range 200-800 nm. Chromium doping of $BaTiO_3$ increased the absorbance in the visible light region compared with undoped solid state prepared sample (Figure 5.27). Solid-state and aerogel prepared samples of Cr doped barium titanate had intense absorption in the 400-500 nm due to incorporated Cr^{3+} ions. Besides, the aerogel prepared sample had an additional peack at 630 nm which can be assigned to surface chromium oxide (Cr_2O_3). Some of chromium did not incorporate into the lattice and stayed as a separate phase.

Surface areas of different samples were measured on a Nova 1200 gas sorption analyzer (Quantachrome Corp.) from the amount o N_2 absorbed at 77K and calculated according to the Brunauer-Emmett-Teller (BET) method. The samples were degassed at 423 K for one hour prior to analysis. The BET surface areas of the samples are shown in Table 5.6.

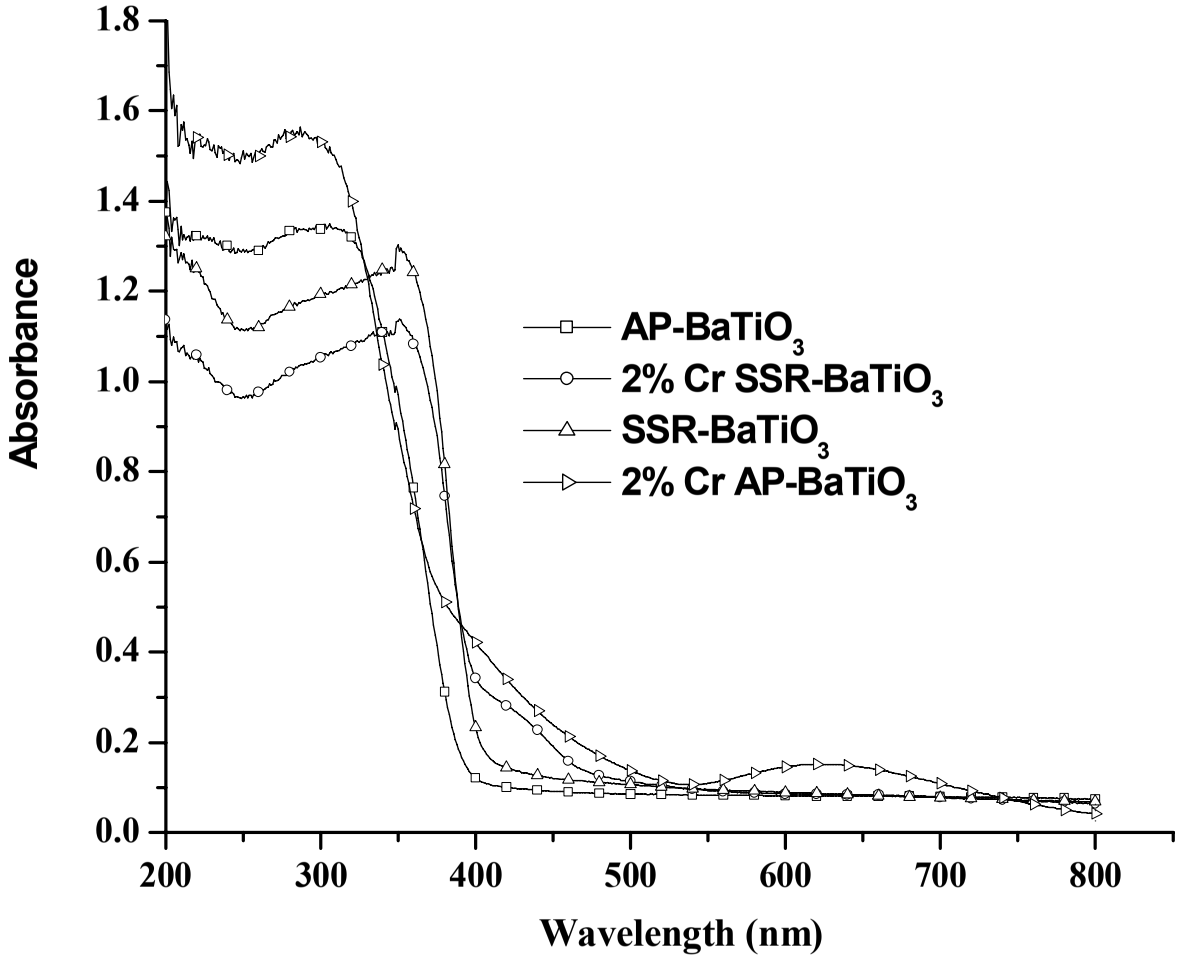

Figure 5.26 Diffuse Reflectance Spectra of Pure AP-$BaTiO_3$ and 2%Cr Doped AP-$SrTiO_3$

Table 5.6 Photocatalytic Properties of Chromium Doped Aerogel Prepared and Solid-state Prepared Strontium Titanate and Barium Titanate Catalysts

Sample		UV light activity		Visible light activity	
	Surface area, m^2/g	Initial rate r [CH_3CHO]	Initial rate r [CO_2]	Initial rate r [CH_3CHO]	Initial rate r [CO_2]
P25 TiO_2 Degussa	50.0	0.1023	0.01310	0.01470	0.00016
SSR-$SrTiO_3$	0.5	0.1160	0.00113	0.03230	0.00014
SSR-$BaTiO_3$	5.4	0.0930	0.00049	0.01680	0.00002
AP-$SrTiO_3$	93.0	0.0525	0.00280	0.00770	0.00021
AP-$BaTiO_3$	49.0	0.0415	0.00141	0.00492	0.00014
2% Cr doped SSR-$SrTiO_3$	1.1	0.1027	0.00134	0.03130	0.00028
2% Cr doped SSR-$BaTiO_3$	1.2	0.0930	0.00058	0.01670	0.00003
2% Cr doped AP-$SrTiO_3$	81.9	0.0498	0.00084	0.03500	0.00039
2% Cr doped AP-$BaTiO_3$	70.0	0.0348	0.00089	0.02660	0.00025

The difference in surface areas for aerogel prepared catalysts of barium titanate and strontium titanate can vary significantly, while for the solid-state prepared catalysts of $BaTiO_3$ and $SrTiO_3$, textural properties and surface areas are similar for both chemicals. The comparison of two different chemicals with similar surface areas helps to see more clearly the difference in their photoactivity.

Doping of strontium titanate or barium titanate with chromium causes the formation of impurity levels or bands in the forbidden area of the semiconductor band gap. While the purpose of this is to decrease the band gap and to achieve the absorption of visible light, the doping can influence the absorption of UV light also. It is common, when the doping causes a decrease in UV photoactivity, to explain this by more facile recombination of electrons and holes. This case is characteristic for the Cr doped AP-$SrTiO_3$ and AP-$BaTiO_3$ when under UV irradiation they have less activity for acetaldehyde decomposition and carbon dioxide production than that of pure aerogel prepared $SrTiO_3$ and $BaTiO_3$ (Figures 5.27, 5.28). The solid-state prepared samples of a doped catalyst have fewer tendencies for photoactivity decrease under UV irradiation (Table 5.6).

In the visible region, the photoactivity of doped catalysts is significantly higher in comparison with pure catalysts. The electrons and holes are excited by the visible light photons on the incorporated dopant bands, so electrons go to the conduction band and less recombination between holes and electrons is possible. This case can be seen in Figures 5.29 and 5.30 where Cr doped $SrTiO_3$ and Cr doped $BaTiO_3$ samples are more active for acetaldehyde decomposition and carbon dioxide production under visible light in comparison with undoped catalysts.

Finally, the complete comparison of photoactivity for different prepared samples of barium titanate or strontium titanate showed that the $SrTiO_3$ catalyst was more effective for acetaldehyde photodecomposition than the $BaTiO_3$ catalyst, and each $SrTiO_3$ sample was more photoactive than the corresponding $BaTiO_3$ sample (Figures 5.31 and 5.32, Table 5.6).

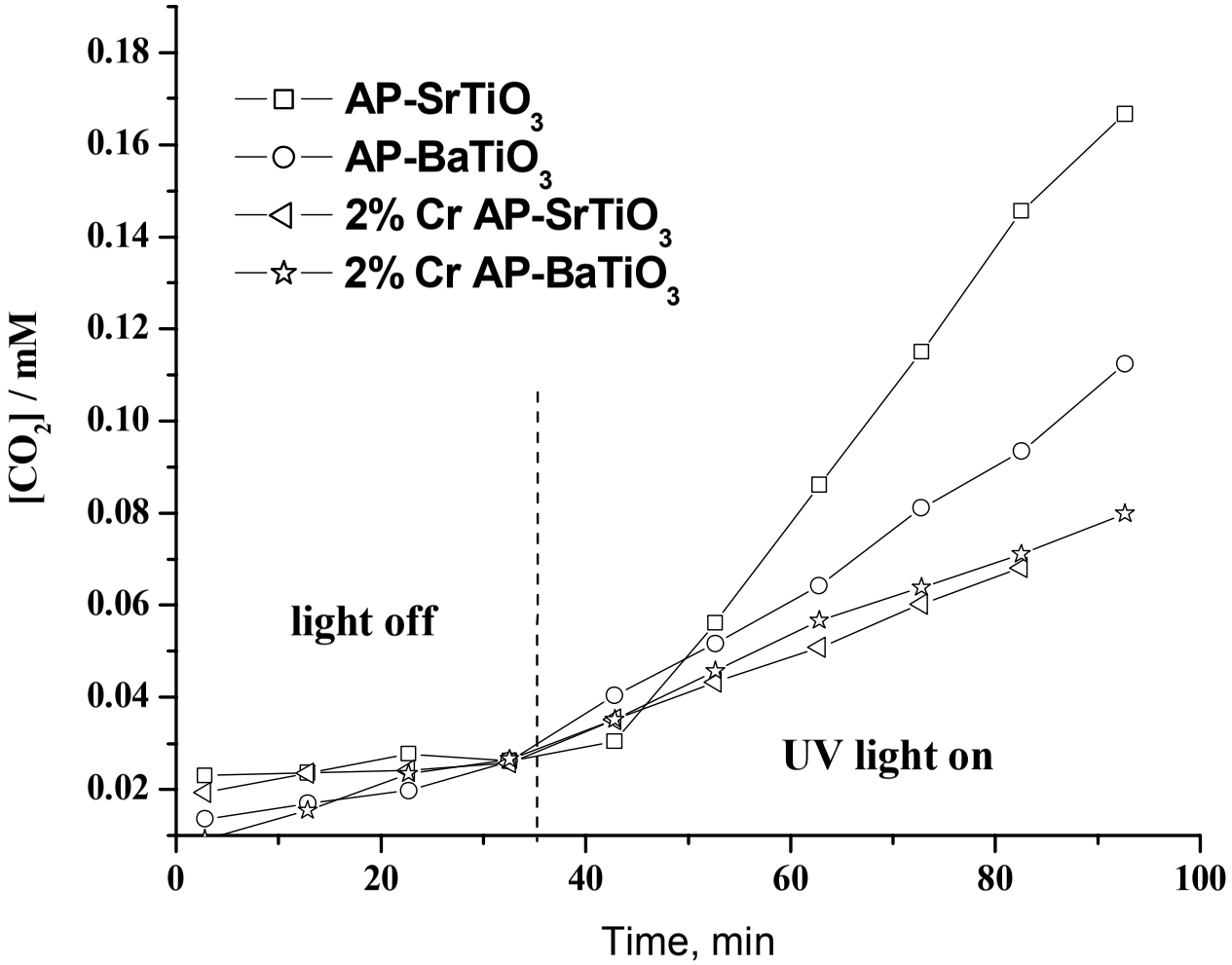

Figure 5.27 CO_2 Evolution for Aerogel Prepared $SrTiO_3$ and $BaTiO_3$ Under UV Light Irradiation

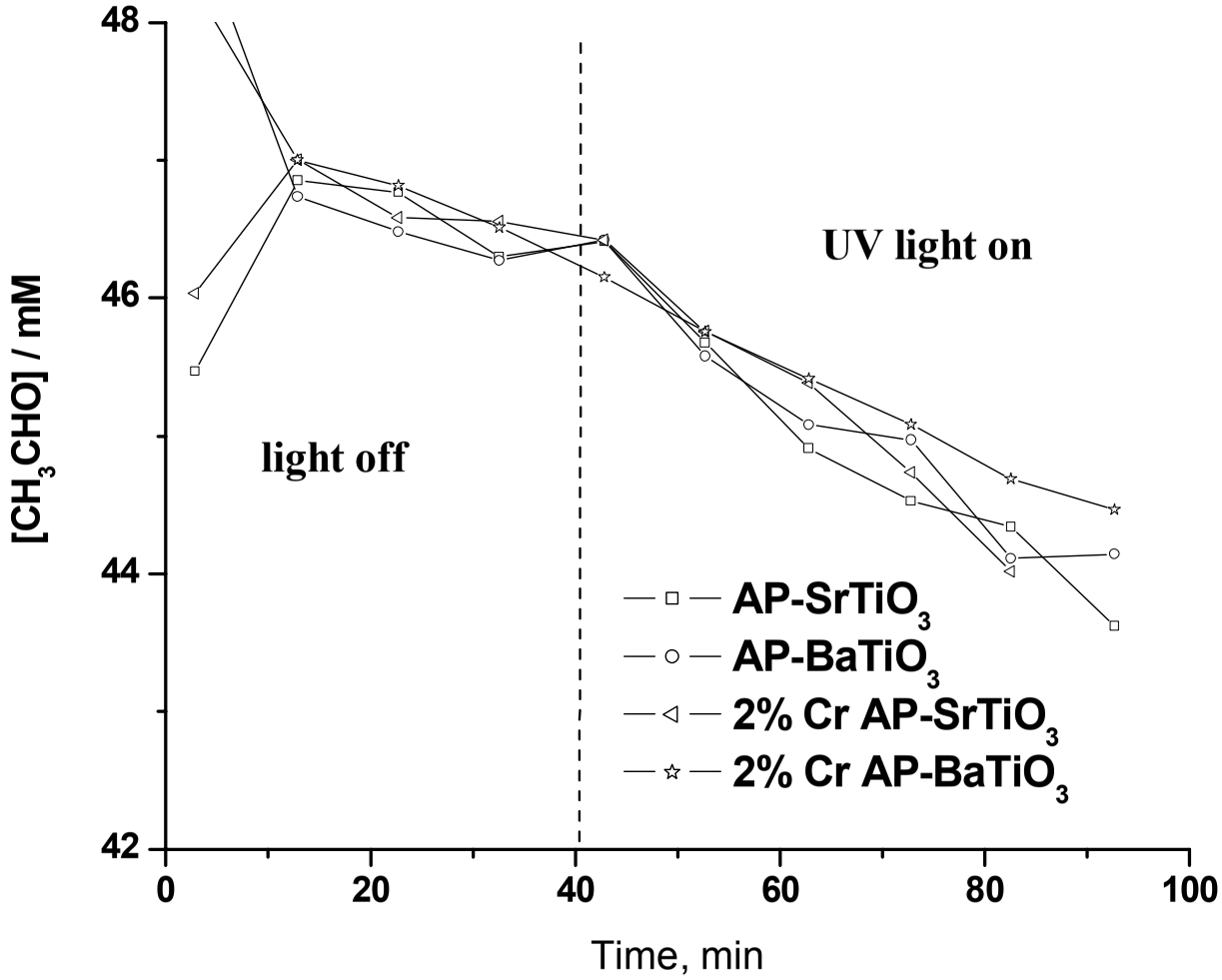

Figure 5.28 CH_3CHO Degradation for Aerogel Prepared $SrTiO_3$ and $BaTiO_3$ Under UV Light Irradiation

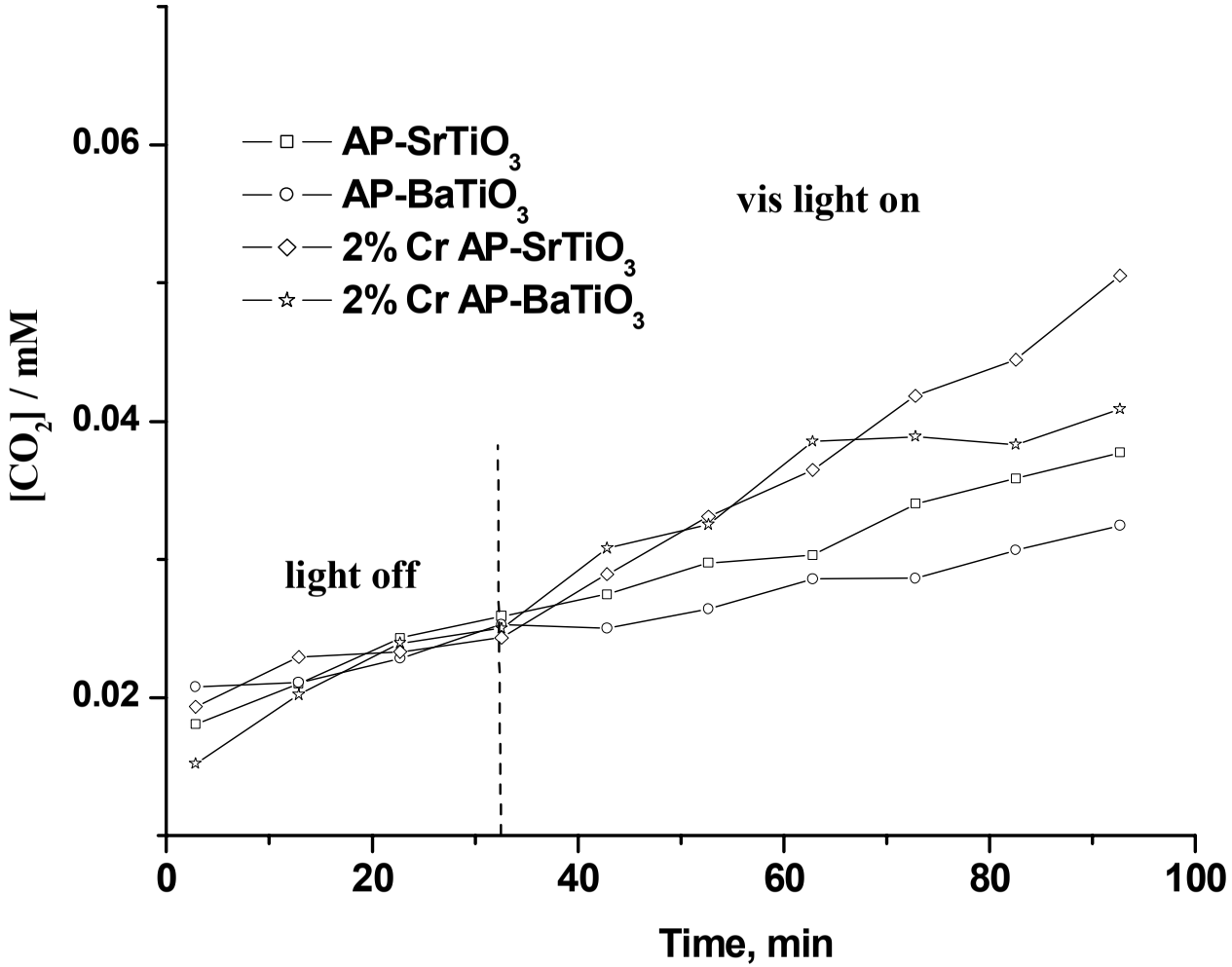

Figure 5.29 CO_2 Evolution for Aerogel Prepared $SrTiO_3$ and $BaTiO_3$ Under Visible Light Irradiation

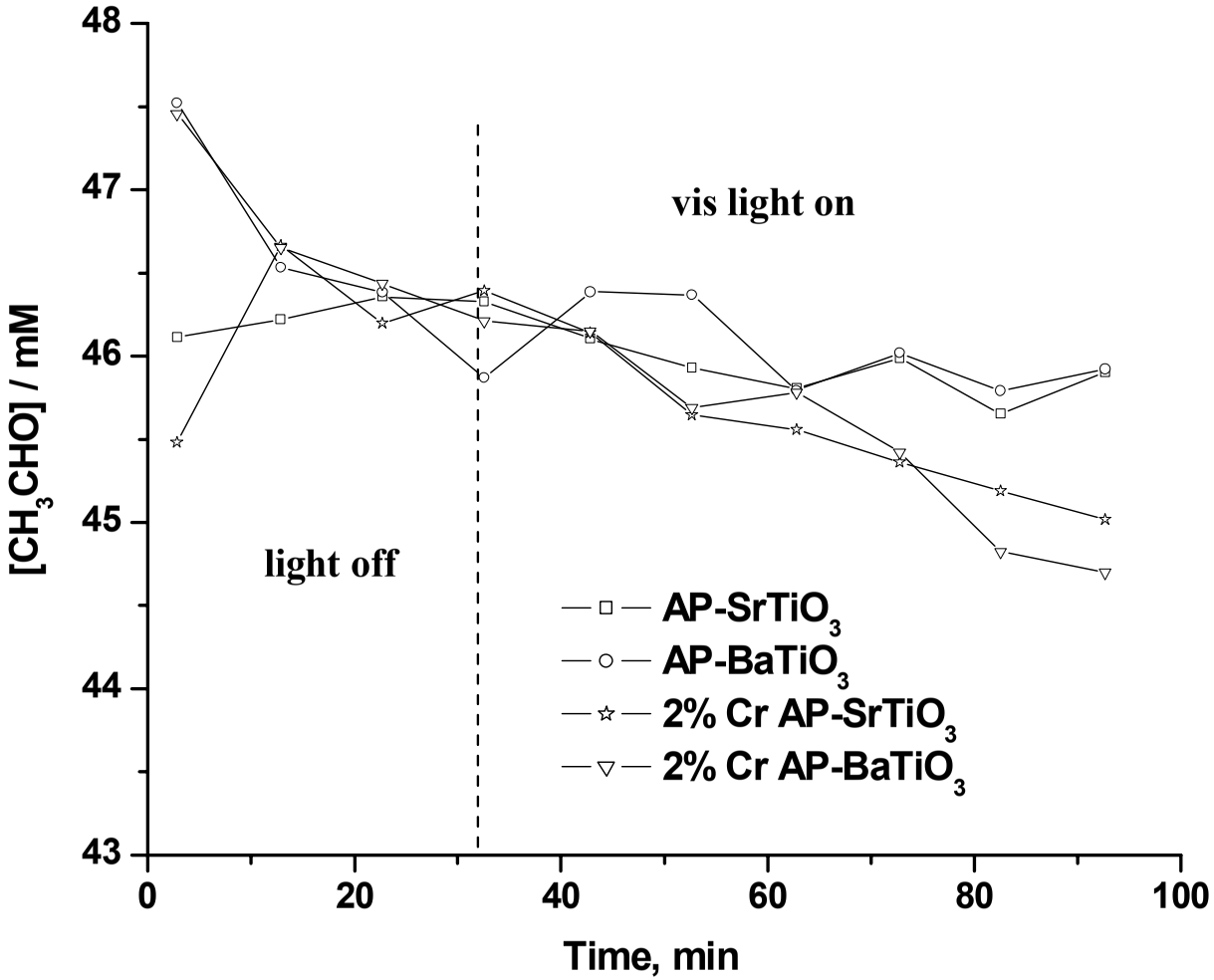

Figure 5.30 CH_3CHO Degradation for Aerogel Prepared $SrTiO_3$ and $BaTiO_3$ Under Visible Light Irradiation

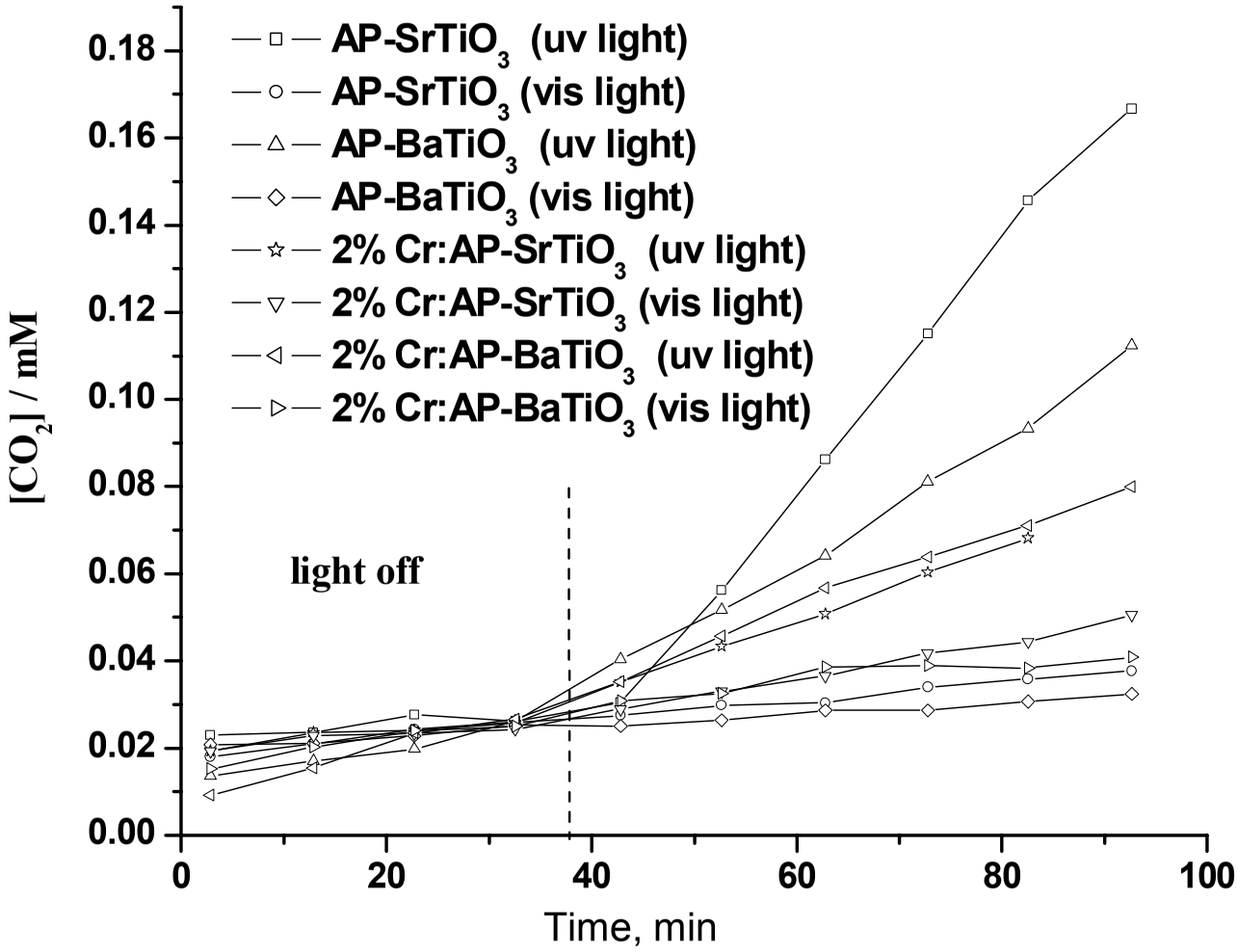

Figure 5.31 CO_2 Evolution for Aerogel Prepared $SrTiO_3$ and $BaTiO_3$ Under Light Irradiation (UV or Visible Light)

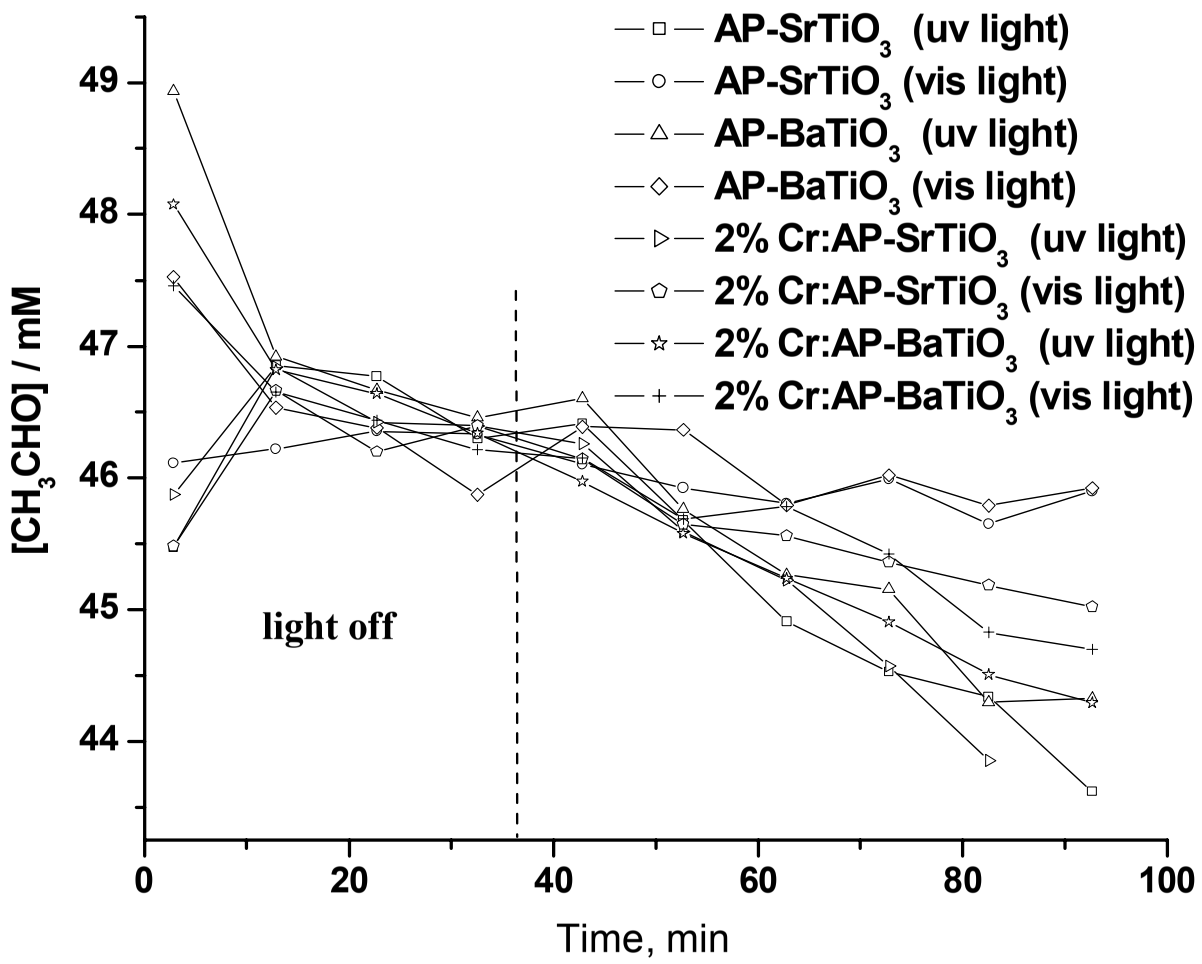

Figure 5.32 CH_3CHO Degradation for Aerogel Prepared $SrTiO_3$ and $BaTiO_3$ Under Light Irradiation (UV or Visible Light)

5.4 Discussion and conclusions

The goal of this research was to develop a photocatalyst (doped with transition metal), which would be active in the visible region for the decomposition of VOCs and acetaldehyde in particular. $SrTiO_3$ or $BaTiO_3$ doped with transition metals (Cr or Sb/Cr) showed absorption in visible light and photoactivity for CH_3CHO oxidation.

Doping with chromium decreased the band gap of the semiconductor by the incorporating of Cr donor bands or levels into the forbidden area of the band gap. The decrease in band gap allowed the excitement of electrons and holes by visible light photons. The visible light response was due to the transition from the electron donor level formed by Cr ions to the conduction band of $SrTiO_3$.The produced holes formed active species on the surface of the catalyst which participated in catalysis and decomposed organic compounds.

The introduction of Cr (III) ions in to the lattice to substitute Ti (IV) ions caused charge imbalance. The charge transfer between Cr and Ti ions induced by light allowed forming oxygen defects

$$Cr^{3+} + Ti^{4+} + h\nu \Rightarrow Cr^{4+} + Ti^{3+} \qquad (5.1)$$

The doping of $SrTiO_3$ with Sb/Cr was based on the ability to keep the charge balance and suppresses oxygen defects in the lattice. Codoping with Sb^{5+} ions suppressed the formation of Cr^{6+} ions and oxygen defects in the lattice.

Sb/Cr codoped samples had a wider absorption range in the visible region than that of Cr doped ones. Probably, the Sb/Cr codoped samples had more stabilized Cr^{3+} in the $SrTiO_3$ lattice in a comparison with Cr doped samples.

Novel aerogel prepared and conventional solid-state prepared $SrTiO_3$ and $BaTiO_3$ samples were used for photocatalytic studies. Codoping of $SrTiO_3$ with Sb/Cr was studied and compared with pure, Cr-, and Sb-doped $SrTiO_3$ samples and the standard catalyst of TiO_2 P25. The doped photocatalyst showed high photoactivity under visible light irradiation during several continuous experiments and photoactivities in visible and UV regions were similar. The photocatalytic

activity for CO_2 evolution of the antimony/chromium doped AP-$SrTiO_3$ was twice higher than that of doped with only chromium under UV or visible light irradiation.

Solid-state samples with a high amount of lattice defects gave a higher reaction rate of the acetaldehyde decomposition. However, there was no increase in the carbon dioxide production. After three consecutive experiments with the same catalyst, a decrease in acetaldehyde decomposition was noticed while the production of carbon dioxide stayed on the same level. It is possible to speculate that acetaldehyde decomposition went through several reactions on the surface of the catalyst. One of them was the photooxidation of acetaldehyde, while others are using the presence of high amount of lattice defects for the production of other products which were less photoactive and less volatile and stay absorbed on the surface. The case at hand, only carbon dioxide was monitored by gas chromatography and other intermediates and/or product are undetected because they are less volatile and stay absorbed on the surface. IR surface studies of the catalyst during photocatalysis would help to prove this hypothesis.

This hypothesis is more plausible considering the presence of a large amount of oxygen defects and Ti^{3+} ions (reaction 5.1) on the surface of solid-state prepared samples. They can absorb and hold more organic species on the small surface area in comparison with the large surface area of the catalysts which do not have surface defects.

Nevertheless, for a photocatalytic reaction of acetaldehyde decomposition on the $SrTiO_3$ catalyst under visible light irradiation, high activity can be achieved by the doping with Cr^{3+} and its charge compensation to prevent the formation of lattice defects.

The comparison of photoactivity for different barium or strontium titanate catalysts showed that $SrTiO_3$ catalysts are more effective for acetaldehyde photodecomposition than the $BaTiO_3$ catalysts.

The activity of Cr/Sb codoped aerogel prepared AP-$SrTiO_3$ catalyst is highest among all synthesized and studied catalysts under UV or visible irradiation for carbon dioxide production. The highest rate of mineralization of acetaldehyde proves that novel nanosized Cr/Sb codoped AP-$SrTiO_3$ is a very effective catalyst for decomposition of volatile organic compounds.

5.5 References

[1] K. Zamaraev and V. Parmon, Energy Resources through Photochemistry and Catalysis, Ed. M. Grätzel, Mir, Moscow, 1986.

[2] J.M. Herrmann, Catal. Today, 53 (1999) 115-129.

[3] N. Serpone and E. Pelizzetti, Photocatalysis. Fundamentals and Applications, John Wiley and Sons, New York, 1989, p. 650.

[4] H. Mizoguchi, K. Ueda, M. Orita, S.C. Moon, K. Kajihara, M. Hirano, and H. Hosono, Mater. Res., 37 (2002) 2401-2406.

[5] F.T. Wagner and G.A. Somorjai, Nature 285 (1980) 559-560.

[6] J.L Giocondi and G.S. Rohrer Mat. Res. Soc. Symp. Proc., 654 (2001) AA7.4.1-10.

[7] R.W. Schwartz, Chem. Mater., 9 (1997) 2325-2340.

[8] J. Wang, S. Uma, and K.J. Klabunde, Applied Catalysis, 48 (2004) 151-154.

[9] S. Uma, S. Rodrugues, I.N. Martyanov, and K.J. Klabunde, Microporous and Mesoporous Materials, 67 (2004) 181-187.

[10] I.N. Martyanov, S. Uma, S. Rodrigues, and K.J. Klabunde, Langmuir, 21 (2005) 2273-2280.

[11] M. Kaneko and I. Okura, Photocatalysis, Springer, 2002

[12] R. Konta, T. Ishii, H. Kato, and A. Kudo, J. Phys. Chem. B, 108 (2004) 8992-8995.

[13] J.-M. Herrmann, J. Disdier, and P. Pichat, Chem. Phys. Lett., 108 (1984) 618.

[14] G. Campet, M.P. Dare-Edwards, A. Hamnett, and J.B. Goodenough, Nouv. J. Chim., 4 (1980) 501.

[15] A. Mackor and G. Blasse, Chem. Phys. Lett., 77 (1981) 6.

[16] H. Kato and A. Kudo, J. Phys. Chem. B, 106 (2002) 19, 5029-5034.

[17] T. Ishii, H. Kato, and A. Kudo, J. Photochem. Photobiol. A, 163 (2004) 181.

[18] W. Choi, A. Termin, and M.R. Hoffmann, J. Phys. Chem., 98 (1994) 13669.

[19] R. Asahi, T. Morikawa, T. Okwaki, K. Aoki, and Y. Taga, Science, 293 (2001) 269.

[20] J.C. Yu, J. Yu, W. Ho, Z. Jiang, and L. Zhang, Chem. Mater., 14 (2002) 38008-3816.

[21] T. Umebayashi, T. Yamaki, S. Tanaka, and K. Asai, Chem. Lett., 4 (2003) 330-331.

[22] J. Wang, S. Yin, M. Komatsu, Q. Zhang, F. Saito, and T. Sato, Transaction of the Materials Research Society of Japan, 29 (2004) 6, 2693-2696.

Chapter 6 : Surface studies of titanates by FTIR spectroscopy

6.1 Introduction

The studies of oxygenated hydrocarbon reactions on metal oxide surfaces have a great deal of significance from both fundamental and practical perspectives. These reactions are rich and complex (oxidation, reduction, condensation, esterification etc.).

Aldehydes are a common representative of these oxygenated hydrocarbons and are the products of alcohol oxidation, carboxylic acid reduction, or can be found in automotive exhaust gases due to an incomplete combustion of fuel in the engine. The reactions of acetaldehydes have been extensively investigated on different oxide surfaces (TiO_2, CeO_2, Al_2O_3, and UO_3), although strontium titanate has not yet been examined. The results from these investigations can be useful as guidelines for the acetaldehyde reaction on the $SrTiO_3$ surface.

The studies on TiO_2 surfaces give the most important information due to similarity of the surface with strontium titanate and the presence of titanium-oxide layers in both materials. The studies dedicated to acetaldehyde reactions and photocatalysis on the TiO_2 P25 Degussa surface by Lue et al. showed the aldol condensation of acetaldehyde and production of the crotonaldehyde [1].

$$2\ CH_3CHO \rightarrow CH_3CH{=}CHCHO + H_2O \qquad (6.1)$$

Thermal programmable desorption for acetaldehyde on P25 surface gave crotonaldehyde, butane, butadiene, and acetone. It was found that after adsorption about, 90% of the CH_3CHO molecules were staying on the surface.

The acetaldehyde reaction on uranium oxide surfaces (UO_2, UO_3, and U_3O_8) was studied by H. Idriss et al. [2]. Different uranium oxides gave different product of the acetaldehyde reaction on the surface of the oxide in the presence of oxygen. Reductive coupling of two aldehydes to form $CH_3CH{=}CHCH_3$ was the dominant pathway for UO_2 oxide. The aldolization of two aldehydes gave crotonaldehyde on the surface of U_3O_8. Over UO_3, furan (C_4H_4O) was the

dominant reaction product at low surface coverage in the presence of oxygen. In the absence of oxygen, the reaction products were furan and crotonaldehyde and with time the production of furan decreased significantly. Also it was found that without oxygen the UO_3 transformed into U_3O_8 (mild reduction) and UO_2 (deep reduction). From IR analysis, acetaldehyde was absorbed only in η^1 (O) configuration over UO_3, while the η^2 (C,O) configuration was present over UO_2.

It is clear that the aldol condensation reaction is common on the surface of different oxides. It was found that silica supported alkali metal containing solid bases catalyzes the aldol condensation with 90% selectivity. Titanium oxide was found active for aldol condensation with 93% selectivity, and cerium oxide gave 48% selectivity [3]. The basicity of the oxidized CeO_2 favored aldolization reactions, while the reduced CeO_2 was more active for cross-reductive coupling between the absorbed aldehyde molecules (Figure 6.1).

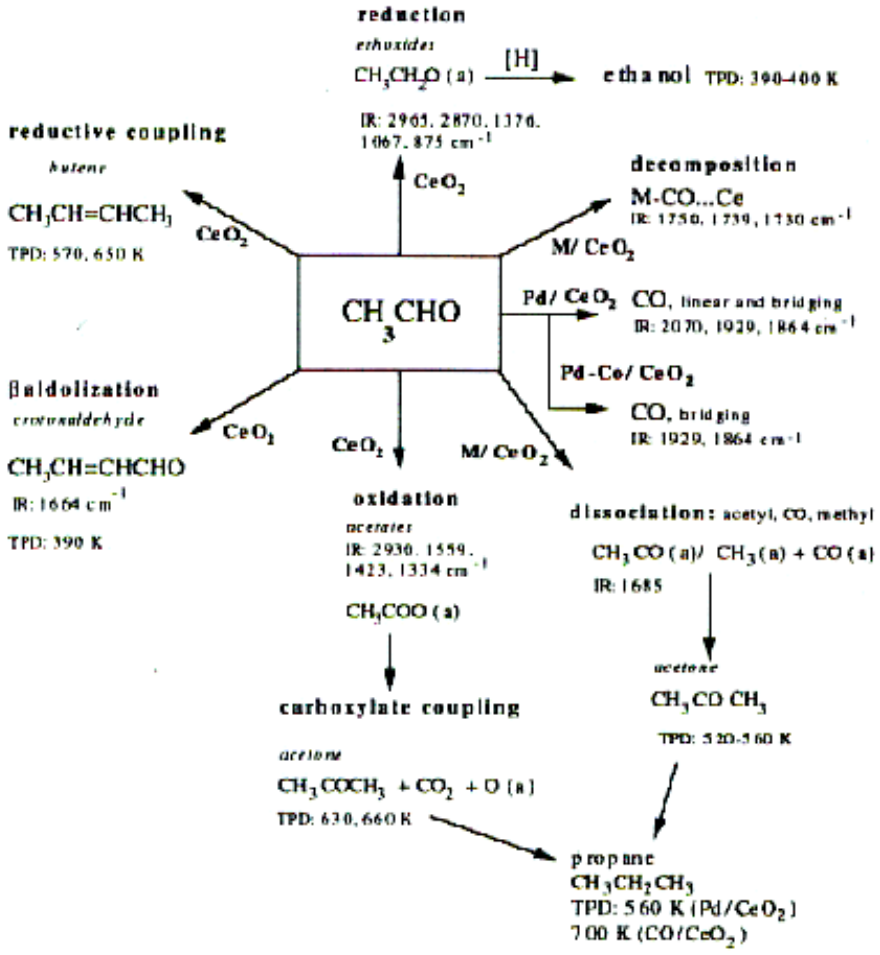

Figure 6.1 Acetaldehyde Reaction on CeO_2 and M/CeO_2 (M is Po, Co and Po-Co) [3]

The reduction of CH_3CHO to ethanol was observed on CeO_2 and Pd doped CeO_2, and the oxidation of acetaldehyde caused the production of acetates. The production of acetates was also observed on zinc oxide (ZnO) and titanium oxide (TiO_2). Adsorbed acetate species decompose to carbon dioxide (CO_2) and methane (CH_4), or can react by bimolecular ketonization to give CH_3COCH_3 and CO_2. Acetaldehyde can also decompose through the formation of carbon monoxide (CO). Linear and bridging modes of CO were observed on Pd-CeO_2 while only the bridging modes were observed on Co-CeO_2. Tungsten oxide on a silica support (WO_3/SiO_2) was also active for aldol condensation while molybdenum oxide on a silica support (MoO_3/SiO_2) was not active.

The acetaldehyde reaction on the surface of strontium titanate has not been studied intensely. Only in Wang et al. work, it was found that the surface of stoichiometric $SrTiO_3$ was not sufficiently active for aldol condensation [4]. However, the decomposition of acetaldehyde occurred in the presence of surface defects created by Ar^+ sputtering and gave H_2, C_2H_4, C_4H_6, and C_4H_8 products.

In situ FTIR studies in combination with photooxidation reactions of acetaldehyde on the surface of $SrTiO_3$ will bring more understanding to the process of photooxidation of CH_3CHO and help determine the products of reaction.

The following steps can be done to study acetaldehyde interaction with the surface of the strontium titanate

1. The activation of the $SrTiO_3$ sample (the removal of organic residuals from the surface in vacuum or oxygen),
2. IR studies of adsorbed acetaldehyde and evacuation of gas phase CH_3CHO,
3. IR studies on the dark oxidation of CH_3CHO in oxygen,
4. IR studies on the photooxidation of acetaldehyde in oxygen under UV light irradiation
5. IR studies on the photooxidation of acetaldehyde in oxygen under visible light irradiation
6. MS studies on reaction products.

The comparison of IR results for pure strontium titanate samples (AP-$SrTiO_3$) and chromium doped strontium titanate samples (Cr-AP-$SrTiO_3$ and Sb/Cr-AP-$SrTiO_3$) will help to

explain the advantages of doped samples for acetaldehyde decomposition under visible light irradiation.

6.2 Acetaldehyde decomposition on the surface of aerogel prepared $SrTiO_3$

For the *in situ* infrared studies, a Mattson Research Series RS_10000 FTIR with a liquid nitrogen cooled detector and manually translatable stage was used. WinFirst v.2.10 software was used to operate the spectrometer and for some data plotting purposes. Origin 6.1 was also used as a plotting application. Microsoft's Excel software was used for some data manipulation and calculations.

Reactions were carried out in a stainless steel reaction cell with KBr windows for the passage of the IR beam and a quartz window for the UV exposure (See Appendix D Figure D.1). The cell utilized differential pumping from a Pfeiffer-Balzers turbomolecular pump and a Duo Seal mechanical vacuum pump to reach pressures as low as 10 nanoTorr. Temperatures were monitored using an E-type thermocouple. Heating was done using electrical resistivity with a 50 amp power driver built by the University of Pittsburgh and Honeywell controller. Dosing of the gases and evacuation was controlled and directed using a bakeable, stainless-steel UHV manifold. Pressures were monitored via an ion gauge and dual, capacitance manometer gauges.

Samples were pressed onto 100 x 100, plain, 0.002 inch (0.0508 mm thick, with 0.22 mm^2 holes) tungsten mesh from the Unique Wire Weaving Company and held in the chamber with a nickel clamp. The powdered $SrTiO_3$ samples were hydraulically pressed at 12000 lbs/in^2 onto a tungsten mesh [5] as a circular spot 7 mm in diameter, typically weighing 1-1.5 mg (1.3-1.9 mg/cm^2) (See Appendix D Figure D.2). The transparency of the grid to the IR beam is about 80%, so that infrared radiation can pass through the sample efficiently. The grid is supported in the center of the stainless steel cell by nickel clamps along the grid edges. A chromel/costantan thermocouple spot-welded to the top center region of the grid is used for temperature control. Electrical heating and cooling with liquid nitrogen and a power supply/temperature programmer permit the temperature of the grid to be maintained to about ±2 K within the range 100-1500 K. The IR cell is connected through a gas port to a high vacuum system, equipped with a quadrupole mass spectrometer (See Appendix D Figure D.3). The base pressure of the system is kept below 10^{-8} Torr by a Pfeiffer Vacuum 60 1/s turbomolecular pump backed by an oil-free

diaphragm pump. The pressure was measured by a capacitance manometer (Baratron, 116A, MKS, range 10^{-3}-10^{3} Torr) or by the ion current drawn by the ion pump. The cell windows were KBr single crystals mounted on concentric Viton O-rings which are differentially pumped to prevent leaks.

The IR cell is mounted on a computer-controlled translation system (Newport Corporation), capable of moving the cell to ±1 μm accuracy in the horizontal and vertical directions. Thus, it is possible to study two samples, i.e. $SrTO_3$ and TiO_2 at the middle and the bottom positions on the same grid for comparison of their spectroscopic and adsorptive properties under identical conditions of temperature and gas exposure. The upper one third positions on the grid was empty and was used for the background absorbance measurements in the same experiments.

Light exposures were done with a water-cooled, PTI short arc xenon lamp passing through a Newport 6123 liquid infrared filter. The light source was a 100W Xenon Arc Lamp (Photon Technology International) which was focused onto the sample through a quartz window. The energy range for the radiation was 2.1-5 eV. In later trials, Oriel Spectra-Physics model 59044 and 59480 long pass filters were added to limit the light to the visual and the UV-visible ranges of 400 nm to 700 nm and 300 nm to 700 nm, respectively. A Cole-Parmer 8852 sonicator was used to clean the clamp and grid prior to sample mounting. Fisher-Scientific certified spectra-analyzed acetone was used in the sonications and for cleaning the probe on which the clamp is mounted in the cell. A MKS PPT Residual Gas Analyzer/quadrapole mass spectrometer was used for the mass spectral studies. Thermocouple wire leads, chromel and constantan, were welded to the mesh and thermocouple using a Rocky Mountain 506 Dial-a-Weld pulsation welding device. Dry ice and acetone were used as cryogenic agents for the cooling of the cell through thermal conduction. Compressed nitrogen was used when needed as a purging agent.

Infrared spectra were obtained with a dry CO_2-free air purged Mattson Research Series I FTIR spectrometer equipped with a narrow band HgCdTe detector operating at 77 K. The sample and background spectra shown here were recorded in the ratio mode with a resolution of 4 cm^{-1} using 300 scans.

Acetaldehyde (99%) and crotonaldehyde (99%) used for this work were obtained from Aldrich. These liquids were stored in glass bulbs and purified by five freeze-pump-thaw cycles

and attached to the ultra high vacuum system. The oxygen used is obtained from Matheson and was 99.999% pure.

The oxide samples were heated in vacuum at 473 K for ~10 h and then the temperature was raised gradually to 773 K for calcination with 20.0 Torr oxygen followed by evacuation. The evacuated sample was then heated at 873 K for 30 min before cooling. This procedure allows the removal of traces of residual organic species which could come from remnant alkoxy groups retained by the oxide nanoparticles after the preparation procedure. Before exposure to adsorbates the samples were cooled in vacuum to 233 K. The adsorption of acetaldehyde, crotonaldehyde, and FTIR measurements were carried out at different temperatures beginning 233 K.

6.2.1 Acetaldehyde adsorption over $SrTiO_3$ at 243 K: evidence of H-bonding

Figure 6.2 (A) shows the background spectrum of the $SrTiO_3$ sample at 233 K before exposure to acetaldehyde. The OH region shows an infrared feature at 3689 cm^{-1} which can be assigned to the ν(OH) mode for isolated hydroxyl groups bound to Ti atoms. However, in a recent TiO_2 study, Panayotov and Yates identified the small features at 3700 cm^{-1} as due to isolated Ti-OH groups [6]. This 11 cm^{-1} red-shift may be due to electron donating effect of the alkaline earth metal ion, Sr^{n+}. The low frequency band at 3403 cm^{-1} can be assigned to either Ti-OH perturbed by nearby Sr atom or to Sr-OH groups.

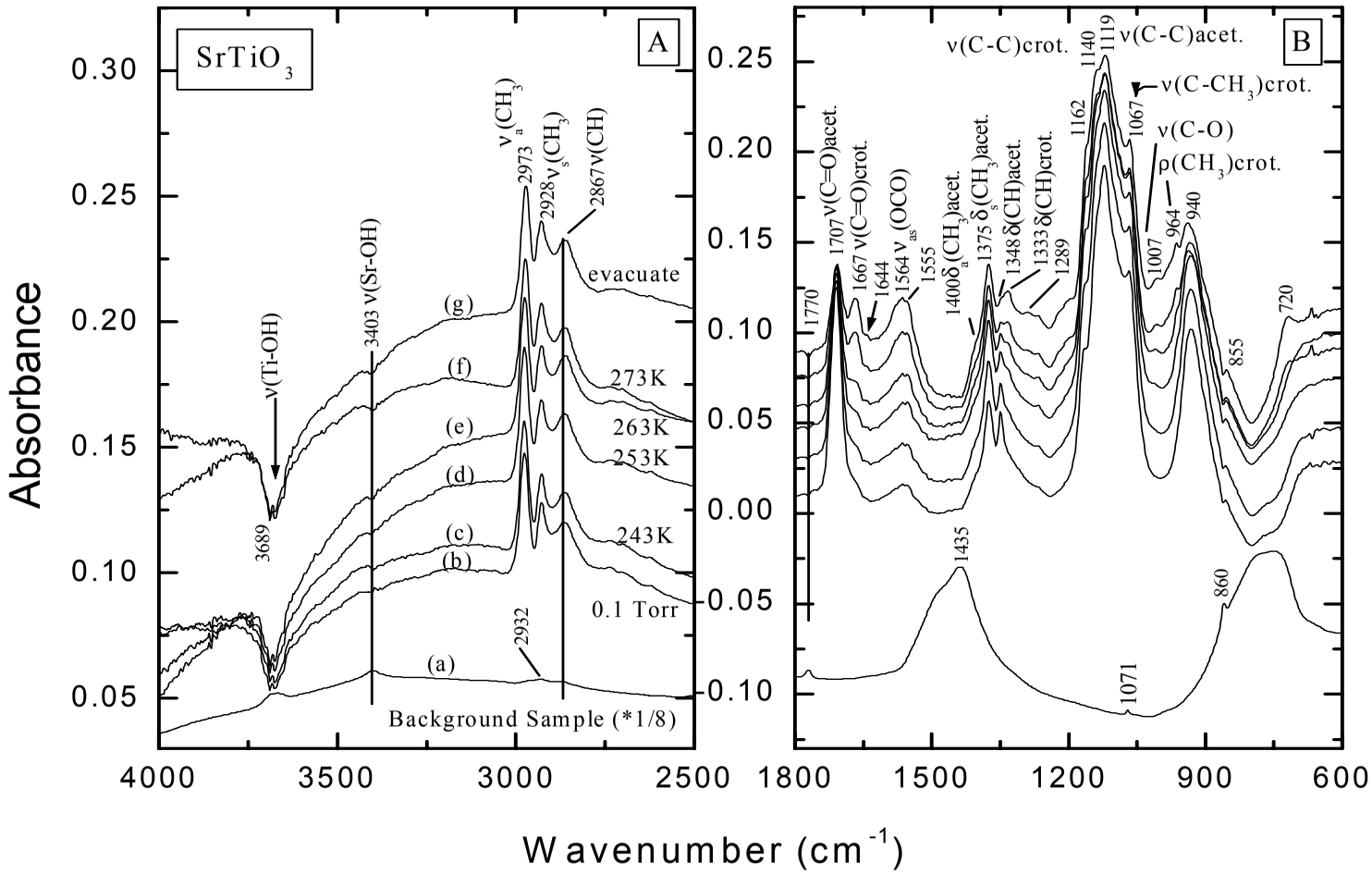

Figure 6.2 Acetaldehyde Adsorption on AP-$SrTiO_3$ and Sequential Change of Temperature

The strong broad feature at 1435 cm^{-1} can be assigned to $\nu_{asym}(OCO)$ groups for CO_3^{2-} groups formed during preparation of nanoparticles. All other spectra shown in Figure 6.2 were obtained by the subtraction of the background spectrum (A). Upon the exposure of 0.1 Torr acetaldehyde at 233 K, the evolution of ν(CH) and δ(CH) modes along with the concomitant depletion of ν(OH) absorbance are clearly observed as shown in spectrum (B).

The dominant spectral features in the ν(CH) region at 2973 and 2928 cm^{-1} can be assigned to $\nu_a(CH_3)$ and $\nu_s(CH_3)$ of acetaldehyde adsorbed onto the surface mainly through H-bonding, whereas the mode at 2867 cm^{-1} is due to the overtone for δ(CH) mode. The depletion of isolated Ti-OH intensity at 3689 cm^{-1} with an increase in intensity of the band in the low frequency side (3550-3350 cm^{-1}) indicates the formation of H-bond through the oxygen of the carbonyl group [$TiOH\cdots O=C(H)CH_3$]. Hydrogen bonding is generally characterized by (a) frequency shifts to lower frequency of the absorption bands due to ν(OH) stretching vibration and (b) broadening of the shifted OH band and the increase in the O-H absorbance. Upon evacuation for 15 minutes at $1x10^{-6}$ Torr, no apparent changes in spectral behavior were observed indicating the irreversibility of H-bonding. The configuration of irreversibly bound CH_3-CHO species is most likely those in which the partially negatively charged oxygen moiety of acetaldehyde interacts with positively charged hydrogen moiety of the surface hydroxyl groups, leaving the methyl moiety largely unperturbed relative to its behavior in the gas phase. This configuration is most probable since gas phase CH_3 CHO possesses a substantial dipole moment of 2.7 Debye. The relatively minor frequency and intensity changes in the observed $\nu(CH_3)$ and $\delta(CH_3)$ vibrational modes are a consequence of the local mode character of the CH_3 groups. A fraction of acetaldehyde may also be adsorbed through $>C=O \rightarrow Ti^{4+}$ and/ or Ti^{3+} ion, which forms by the thermal treatment of TiO_2 under evacuation. The fingerprint region shows a variety of deformation modes in addition to the strong ν(C=O) mode at 1707 cm^{-1} which are explained below. The infrared features at 1375 and 1348 cm^{-1} can be assigned to $\delta_a(CH_3)$ and $\delta_s(CH_3)$ respectively, whereas the strong signature at 1119 cm^{-1} indicate the ν (C-C) mode. The strong feature at 940 cm^{-1} may be assigned to $\rho(CH_3)$ consistent with other studies. The weak feature at 1564 cm^{-1} along with a shoulder at ~1420 cm^{-1} (on the high frequency side of 1375 cm^{-1}) is attributed to $\nu_{as}(OCO)$ and $\nu_s(OCO)$ respectively for the bidentate acetate species [$\nu_{as}(OCO)$ -

ν_s(OCO) =144 cm^{-1}]. The formation of acetate species from acetaldehyde molecules was previously observed on several oxide species including TiO_2, ZnO, and CeO_2.

6.2.2 Warm up effect of adsorbed acetaldehyde: evidence of aldol condensation and formation of α, β-unsaturated aldehyde (crotonaldehyde, CH_3-CH=CH-CHO)

As the temperature is raised at an interval of 10ºC (Figure 6.2 (B), b-e), the decrease in intensities of spectral bands of surface bound acetaldehyde at 1707-ν(C=O), 1348-δ(CH), 1119-ν(C-C) and 940 $-\gamma_r(CH_3)$ cm^{-1} can clearly be noticed. In addition, the new infrared spectral features appeared at 1667(s), 1644(shoulder), 1333, 1162, 1067, and 964 cm^{-1}. This observation is accompanied by a slight decrease in intensity of ν(O-H) mode at 3403 cm^{-1} feature along with an increase in intensity of an unresolved broad ν(O-H) feature ~3250 cm^{-1} indicating the probable formation of new aldol surface species formed by the condensation of two acetaldehyde molecules according to the reactions shown below having ν(C-O) mode at 1007 cm^{-1} and the unresolved ν(C-C) mode at 1140 cm^{-1}. In addition, $\delta(CH)_{ald}$ mode of acetaldehyde at 1348 cm^{-1} decreased in intensity forming a new band at 1307 cm^{-1} which can be assigned to $\delta(CH)_{ald}$ for aldol.

$$CH_3CHO + \text{-Ti-O-Ti-} \rightarrow CH_2\,CHO(a) + \text{-}Ti_2OH \qquad (6.1)$$

$$CH_2\,CHO(a) + CH_3CHO(a) + H_{(ad)} \rightarrow \underset{\beta\text{-hydroxy butanal (aldol)}}{CH_3\text{-}CH\,(OH)\,\text{–}CH_2\,CHO} \qquad (6.2)$$

$$CH_3\text{-}CH\,(OH)\,\text{–}CH_2\,CHO \rightarrow \underset{\text{2-butenal (crotonaldehyde)}}{CH_3CH{=}CH\text{-}CHO(a)} + H_2O_{(a)} \qquad (6.3)$$

The aldol ultimately dehydrates on the surface forming crotonaldehyde (an α,β-unsaturated aldehyde) surface species. The dehydration is clearly be evidenced by a gradual decrease in intensity of >C=O mode at 1707 cm^{-1} with the sequential growth of 1667 cm^{-1} feature accompanied by a weak ν (C=C) mode at 1644 cm^{-1}. Idriss and Barteau reported

acetaldehyde coupling over both oxidized and reduced TiO_2(001) forming self condensation products, crotonaldehyde and crotyl alcohol. The infrared frequencies and the vibrational assignments of surface species formed for acetaldehyde conversion during warm-up are given in Table 6.1.

Table 6.1 Vibrational Frequencies & Assignments of Adsorbed Acetaldehyde and Related Surface Species

Assignment	Gas Phase	Ar Matrix	TiO_2 Anatase	$SrTiO_3$	Crotonaldehyde /$SrTiO_3$
ν_{as} (CH_3)	3014	3022	2969	2973	2973
ν_s(CH_3)	2968	2921	2914/2846	2928/2867	2928/2867
ν(CH_{ald})	2716	2736	2759	2755	
ν(C=O)	1743	1729	1718	1707	1667
ν(C=C)					1644
δ_{as}(CH_3)	1433	1427		1400	1455
δ_s(CH_3)	1395	1399	1355	1375	1394/1371
δ(CH)	1352	1349		1348	1311
ν(C-C)	1114	1111		1119	1158
ν(C-CH_3)					1105
γ_r(CH_3)	920/867	873		940	968
γ(CH_3)	764				

6.2.3 Dark oxidation: influence of dioxygen exposure over preadsorbed acetaldehyde at 243 K

Figure 6.3 shows a series of subtracted (for clarity purposes) infrared spectra (for the duration of 85 minutes) obtained upon introduction of oxygen gas over preadsorbed acetaldehyde at 273 K. The reference spectrum used for subtraction purposes was Figure 6.2 (g), which has been evacuated before introduction of 14.0 Torr O_2 in order to observe the effect of oxygen exposure without the irradiation of UV light. It may be noted that at this temperature, below 1800 cm^{-1} region (Figure 6.3) (B) (a-g)), a number of bands (1668, ~1610, 1580, 1018, and 972 cm^{-1}) gained intensities as a function of time, while the other bands (1716, 1373, 1167, 1122, 1064, and 936 cm^{-1}) lost intensities within the same time period.

Here, the decrease in intensity of 1716 cm^{-1} feature along with simultaneous decrease in intensities of ν(C-C) mode at 1122 cm^{-1} and ν(C-CH_3) mode at 1064 cm^{-1} indicate that both preadsorbed acetaldehyde and crotonaldehyde (formed during warm-up) are continually being oxidized forming carboxylate surface species showing strong infrared feature ~1580 cm-^{1} and a medium intense peak at 1424 cm^{-1} for ν_a(OCO) and ν_s(OCO) surface species respectively.

However, there is no evidence confirming the formation of CO_2 for ν_a(OCO) in 2300-2400 cm^{-1} region. In addition there was no overall change in the integrated absorbance for both ν_a(OCO) and ν(CH) for the entire duration (85 minutes) of dark oxidation as observed by in the plot given in Figure 6.4. The decrease in the ν(CH) (at 2980 cm^{-1}) absorbance may be due to a slight shift in CH stretching mode due to the partial oxidation of adsorbed aldehyde forming acetate.

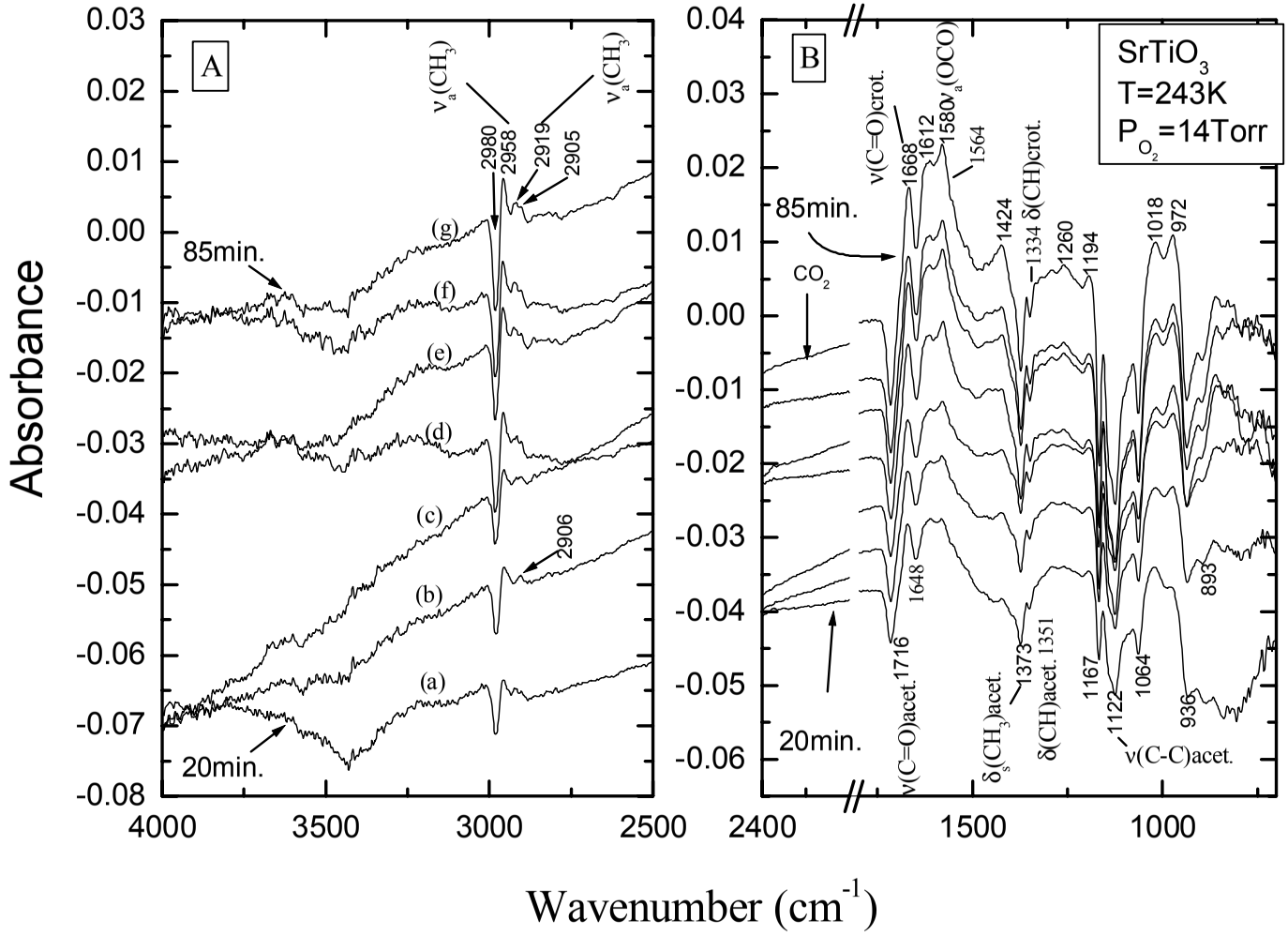

Figure 6.3 Dark Oxidation of Acetaldehyde on AP-$SrTiO_3$ Surface

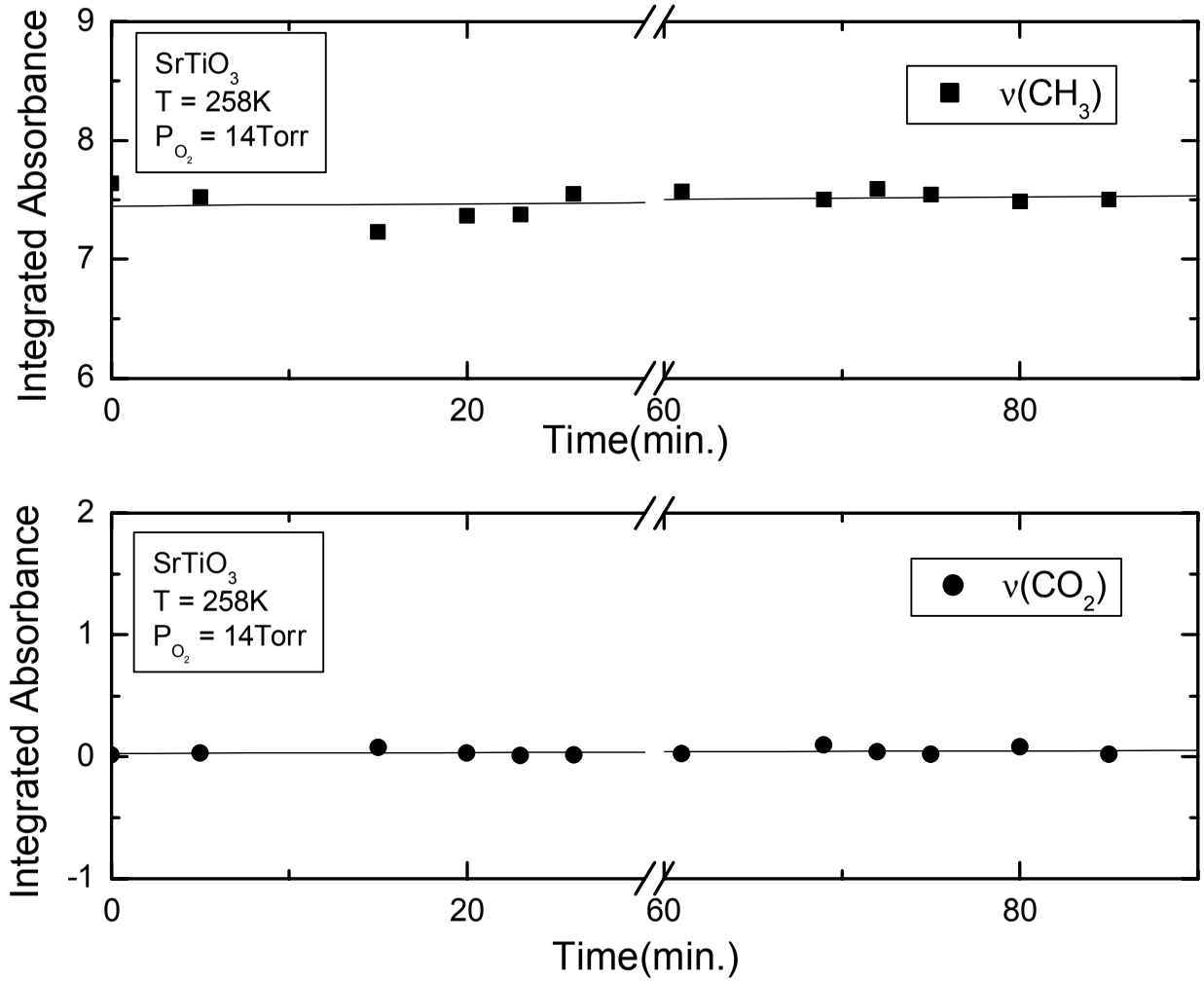

Figure 6.4 Kinetics Study of Acetaldehyde Dark Oxidation Using Oxygen

6.2.4 Spectral development during photooxidation reaction: influence of dioxygen exposure over preadsorbed acetaldehyde at 243 K

Figure 6.5 shows that the intensity of CH_3 vibrational modes (at 2964, 2919, and 2862 cm^{-1}) of adsorbed acetaldehyde is significantly attenuated during 149 minutes of photooxidation. The fact that new CH_x stretching modes in this spectral region are not clearly observed to be produced during photooxidation indicates that C-H bond oxidation is occurring extensively, and that any intermediate species containing CH_x bonds are of low surface coverage. Simultaneously various carbonyl stretching modes due to aldehyde, carboxylate, and formate are developed, as shown in Table 6.1.

The gradual production of gas phase CO_2 is observed for CH_3CHO photooxidation for a continuous period of 150 minutes at 273 K as shown in Figure 6.5 (A). The formation of CO_2 is the final oxidation product, often referred to as mineralization product because of the extreme level of oxidation which it represents. It represents the result of multiple elementary photooxidation steps and these aldehydes are destroyed by a sequence of intermediate oxidation products which ultimately reach CO_2. However, no CO formation is observed during photooxidation.

As photooxidation takes place over a period of 149 minutes, the intensity of the H-bonded Ti-OH mode at 3680 cm^{-1} decreases slightly as acetaldehyde/crotonaldehyde molecules are gradually destroyed. This suggests that the photooxidation products containing carbonyl or water are also H-bonded which caused the red shift of the Ti-OH mode ~200 cm^{-1}.

The spectral region below 2000 cm^{-1} contains a complex overlap of vibrational modes which undergo systematic changes in absorbance as photooxidation takes place. The observation of modes which increase or decrease in absorbance can be observed most conveniently by presenting the difference spectra obtained over the course of the photooxidation experiments, and this has been indicated in Figure 6.5 (B). Table 6.1 summarizes these results and presents a tentative assignment of each mode.

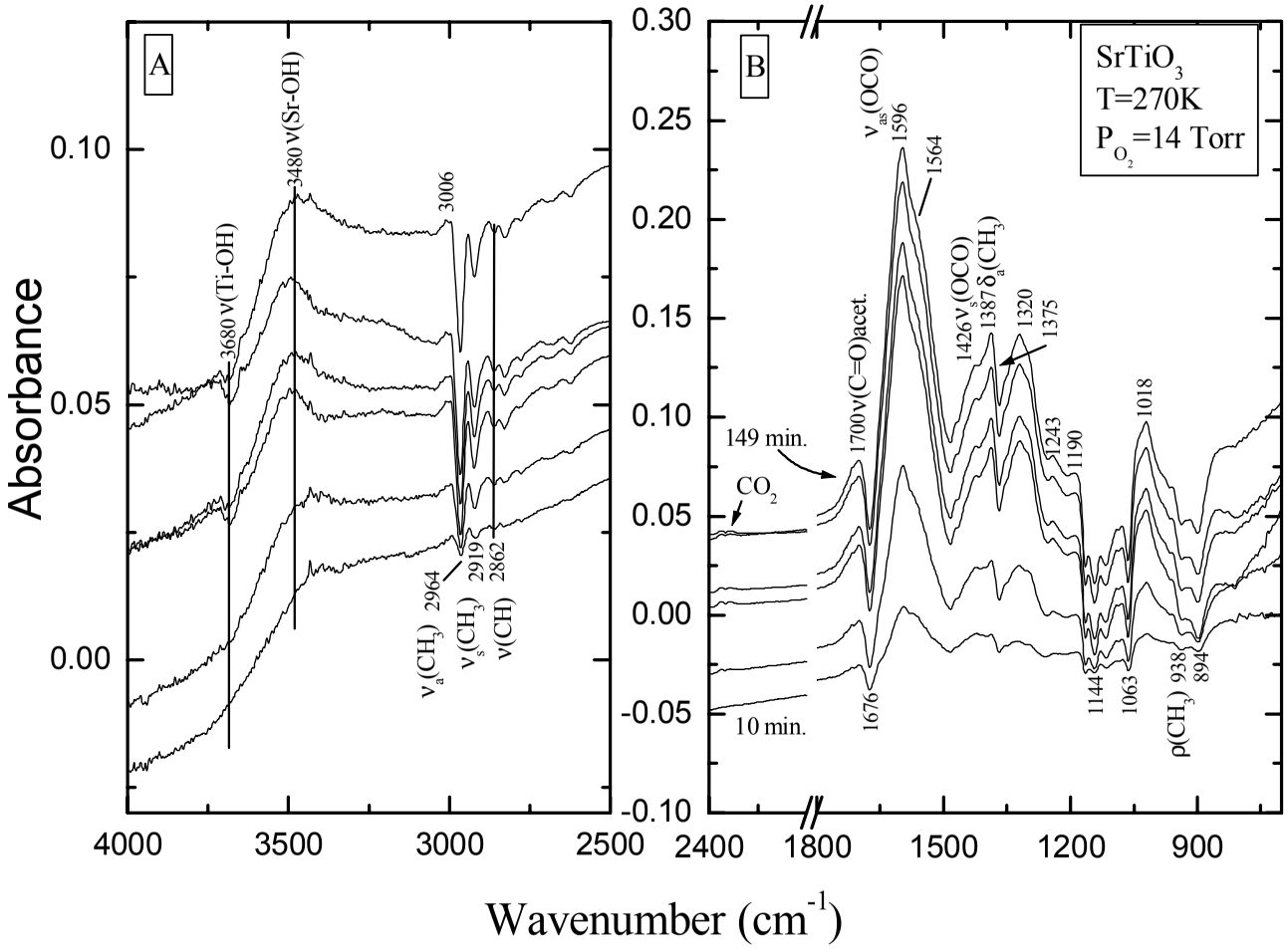

Figure 6.5 Spectral Development during Photooxidation of Acetaldehyde on the AP-$SrTiO_3$ surface

The simultaneous growth of bands, attributed to various carbonyl stretching modes due to aldehyde, carboxylate, formate, and carbonate are observed, as shown in Figure 6.5 and Table 6.2.

Table 6.2 Spectral Changes during the Photooxidation of Acetaldehyde

Frequency (cm^{-1})		Frequency (cm^{-1})	
(species formed during oxidation)		(spectral features depleted during oxidation)	
2353	CO_2	1676	Carbonyl $\nu(C=O)_{as}$
1700	Carbonyl $\nu(C=O)$	1144	$\nu(C-C)$
1596/1564	Carbonyl ν_{as} (OCO)	1063	$\nu(C-O)$
1424/1378	Carbonyl $\nu(OCO)_s$	938	$\gamma_r(CH_3)$
3680 decrease	Ti-OH···OCO	2964	ν_{as} (CH_3)
3480 increase		2919	$\nu_s(CH_3)$
		2862	$\nu(CH)$

Adsorption of acetic acid on this catalyst showed bands at 1560 cm^{-1} (ν_a OCO), 1458 cm^{-1}(δ_a CH_3), 1391 cm^{-1} (ν_s OCO), 1340 cm^{-1} (δ_a CH_3), and 1021 (ρ CH_3) (Spectrum not shown). The shape and location of these bands are similar to the spectra obtained during photooxidation experiments indicating that a large fraction of acetaldehyde formed acetate species including other minor products. These frequencies and assignment of carboxylate species are consistent with studies of acetic acid over different metal oxide surfaces such as CeO_2, TiO_2, Fe_2O_3, and UO_2. One of the products suspected to have formed during photochemical oxidation was CH_3CH_2OH; however, the key infrared features for ethoxide species on TiO_2 such as ν(C-O) band at 1119 and 1042 and $\omega(CH_2)$ at 1356 cm^{-1} are apparently missing.

6.3 Acetaldehyde decomposition on the 2% Cr doped and 2.5% Sb/2% Cr codoped AP-$SrTiO_3$

The samples were pressed onto a 1" x 1.125" section of tungsten mesh under 12,000 lbs of pressure between two stainless steel cubes and mounted into the reaction vessel [6]. The vessel was then attached to the UHV line and heated to 373 K internally and 323 K externally while under evacuation. After several hours at this temperature, the sample was taken to 473 K and left overnight. The next day the external heating was removed and the grid and sample spectra were taken at 473 K. The sample was then heated to 573, 673, and 773 K. Each temperature was held for approximately an hour and followed by a cooling to 473 K for the taking of an IR spectrum. At 773 K, 15-20 Torr of oxygen was dosed and left in the reaction vessel for 15 minutes. The gas was then evacuated and the sample heated another 50 to 100 K for a half hour. The sample was then cooled to 473 K for a final dehydroxylation spectrum and then to room temperature.

The cell was cooled to approximately 233 K and exposed to acetaldehyde or crotonaldehyde in a series of 3-5 dosings. IR spectra, 250-300 scans per, were taken one after another during the exposure period and for approximately 30 minutes after the final exposure. The gas phase aldehydes were then evacuated and the sample was warmed in 5 K increments to 273 K. 15-20 Torr of oxygen was then introduced to the cell and spectra were taken over the next hour or so. The arc lamp was then ignited and the sample exposed to it through the quartz window of the cell with spectra being continuously taken. The temperature of the cell was controlled as much as ambient conditions would allow. Temperatures were usually maintained within 5 K of 273 K. Ambient heat, the presence of gas in the reaction cell, imperfections in the thermocouple weld, and the heat of the lamp were the primary causes of this variation in temperature.

6.3.1 Dehydroxylation on 2% Cr doped AP-$SrTiO_3$

The dehydroxylation as a function of temperature and calcination on chromium incorporated $SrTiO_3$ can be seen in Figure 6.6. Decreasing negative peaks at 3667 cm^{-1} and 3391 cm^{-1} can be seen forming as the temperature was increased and calcination was undergone.

These correspond to the stretching modes of the titania hydroxyl groups and strontium/chromium perturbed titania hydroxyl groups, respectively.

6.3.2 Dehydroxylation on 2.5% Sb/2% Cr doped AP-$SrTiO_3$

When antimony is incorporated into the nanoparticle, three negative features develop with increasing temperature and calcination. The first is at 3659 cm^{-1} and represents the stretching mode of the titania hydroxyl groups. The peak at 3438 cm^{-1} represents the strontium and/or chromium perturbed titania hydroxyl groups, and the last peak at 3361 cm^{-1}, which is absent on the Cr-$SrTiO_3$, appears to be either an antimony perturbed titania hydroxyl group or a surface antimony hydroxyl group (Figure 6.7).

6.3.3 Adsorption, evacuation, and warming prior to dark oxidation of acetaldehyde on 2% Cr doped AP-$SrTiO_3$

As acetaldehyde was sequentially dosed onto the Cr-$SrTiO_3$ nanoparticle surface a number of distinct bands can be seen. There is a slight negative feature at 3403 cm^{-1}, which corresponds to the chromium/strontium perturbed titania hydroxyl groups. This indicates that they play some role, though apparently not a large one, in acetaldehyde adsorption. The peaks from 2975 cm^{-1} to 2702 cm^{-1} represent the stretching modes of the methyl groups and the C-H of the aldehyde. The carbonyl stretches of acetaldehyde and in the later spectra crotonaldehyde can be found at 1709 cm^{-1} and 1669 cm^{-1}, respectively. At 1645cm^{-1}, the C=C stretch of crotonaldehyde can be seen forming as a shoulder peak. Another shoulder peak at 1588 cm^{-1} is believed to be an adsorbed acetate species' O-C-O stretching mode. The bending/deformation modes of acetaldehyde's and crotonaldehyde's CH_3's and CH aldehydes appear between 1373 cm^{-1} and 1267 cm^{-1}. The carbon-carbon stretching modes of both acetaldehyde and crotonaldehyde occur in the 1161 cm^{-1} to 1066 cm^{-1} region and form a large peak complex. The final peak is the rocking deformation mode found at 966 cm^{-1} (Figure 6.8).

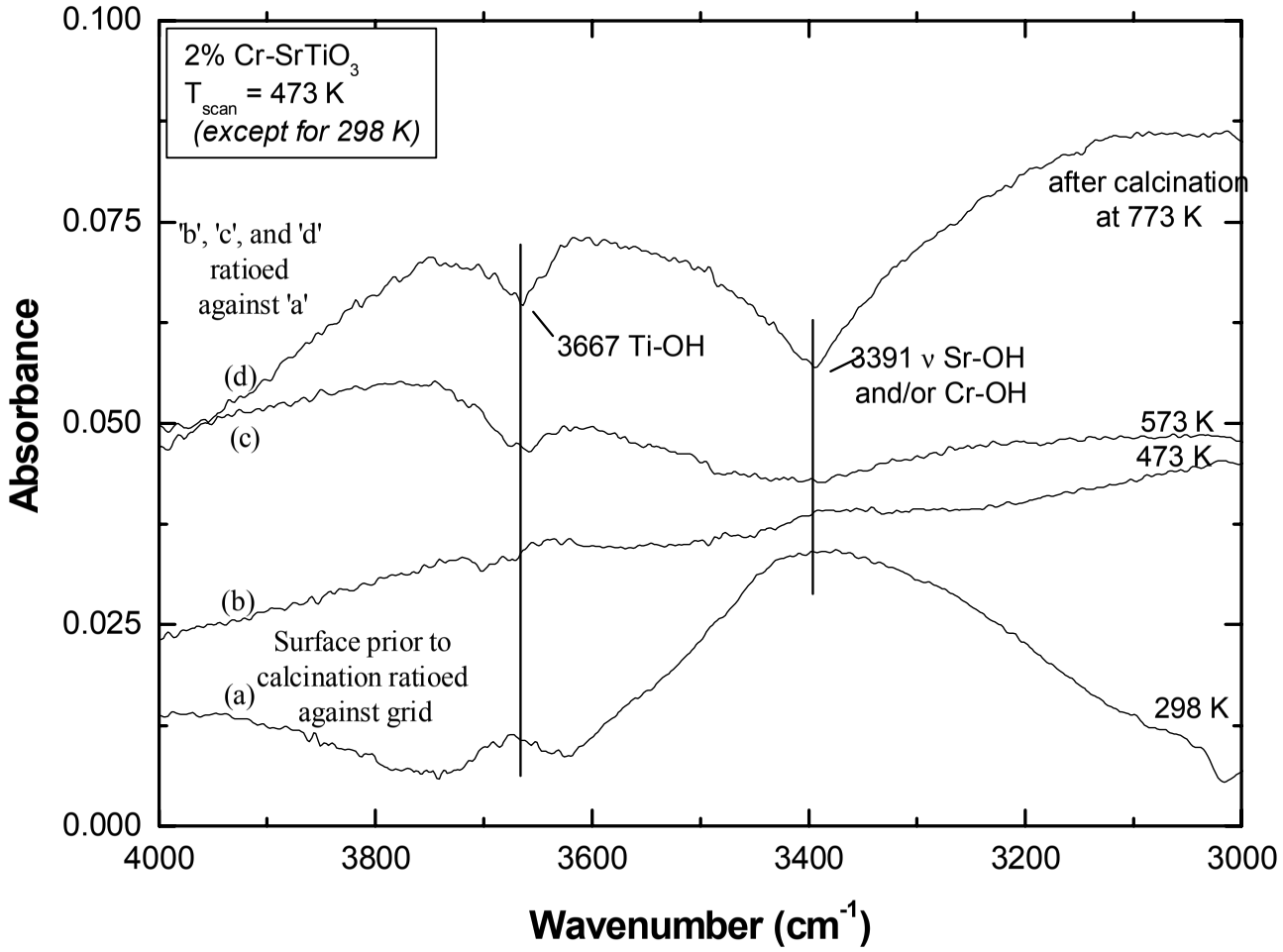

Figure 6.6 Dehydroxylation as a Function of Temperature and Calcination on 2%Cr-$SrTiO_3$ Nanoparticles

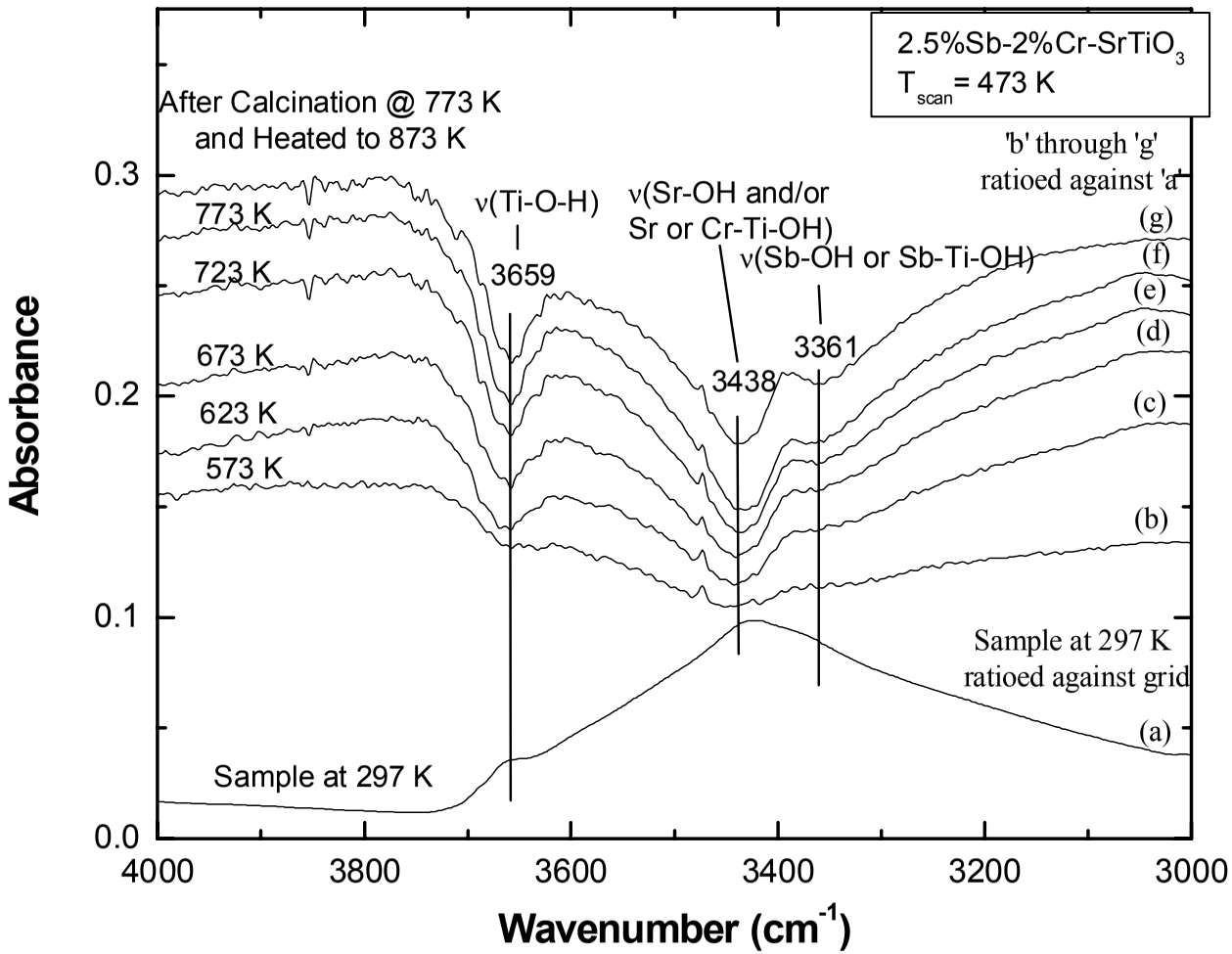

Figure 6.7 Dehydroxylation as a Function of Temperature and Calcination on 2.5%Sb/2%Cr-$SrTiO_3$ Nanoparticles

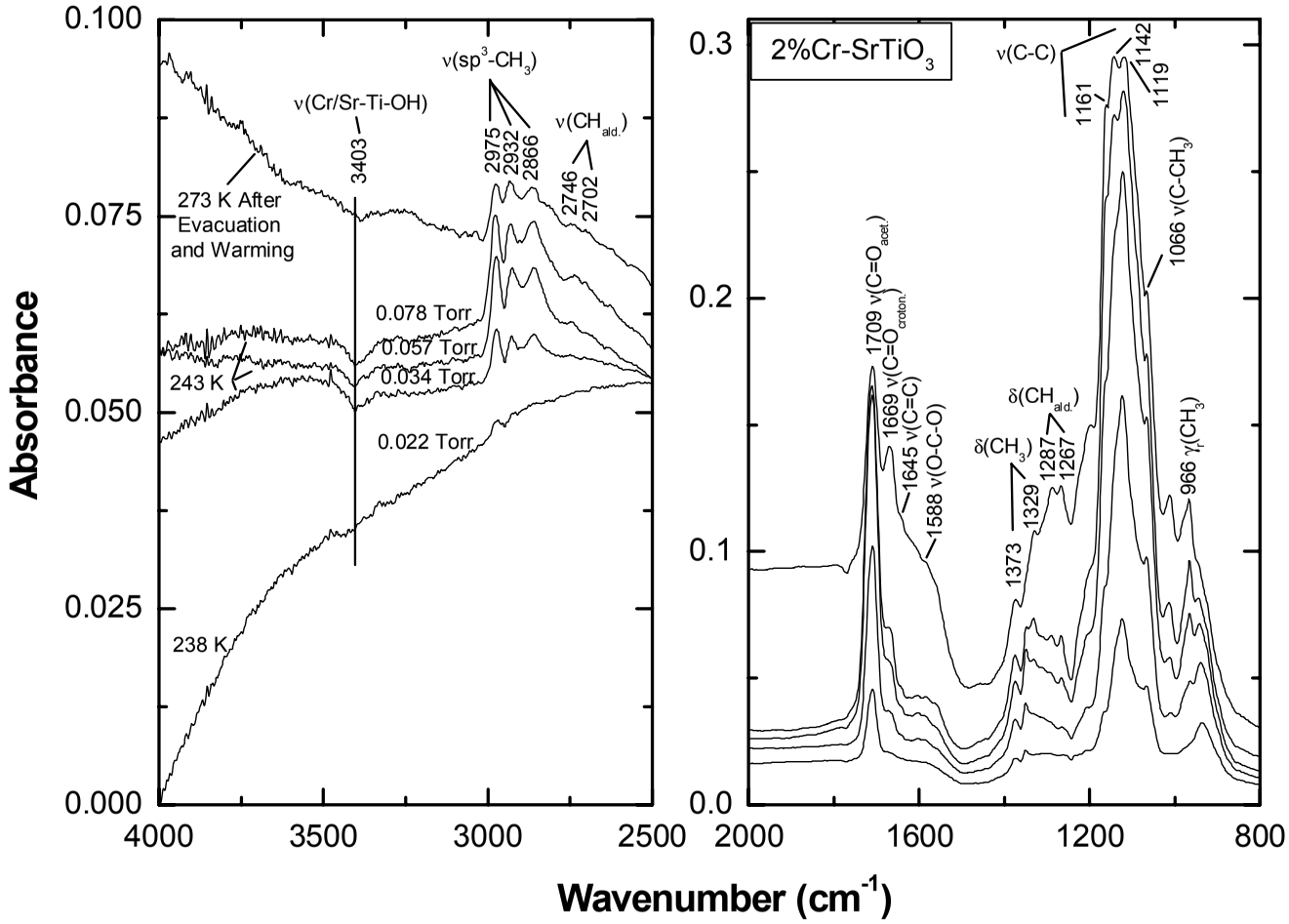

Figure 6.8 Adsorption, Evacuation, and Warming prior to Dark Oxidation of Acetaldehyde on 2%Cr-$SrTiO_3$ Nanoparticles

The fact that the 966 cm^{-1} peak does not depreciate significantly upon evacuation indicates that the species observed after evacuation are surface bound and that the adsorption is to an extent irreversible. No significant formation of crotonaldehyde was seen until the sample was warmed above ~252 K.

6.3.4 Adsorption, evacuation, and warming prior to dark oxidation of acetaldehyde on 2.5% Sb/2% Cr codoped AP-$SrTiO_3$

The analogous spectra for the Sb/Cr-$SrTiO_3$ sample can be found in Figure 6.9. Similar trends are seen here as were seen on Cr-$SrTiO_3$ with a few exceptions. There is a significant negative feature between the 1719 cm^{-1} ν(C=O) of acetaldehyde and 1667 cm^{-1} ν(C=O) of crotonaldehyde. This is a surface artifact, not shown, that was not removed by calcination. In addition, the hydroxyl features not only appear at 3666cm^{-1} and 3401 cm^{-1}, but are more significant than on the chromium incorporated sample. This is most likely a function of the amount of sample present on the grid and not a real difference between the adsorption of acetaldehyde on the two samples. The rest of the major groups that were present on the chromium-incorporated sample can be seen on the antimony/chromium sample as well. A significant difference between the two experiments was that the antimony/chromium sample was taken to room temperature, 298 K, prior to dark oxidation while the chromium only sample was stopped at 273 K.

6.3.5 Attempted dark oxidation of acetaldehyde on 2% Cr-$SrTiO_3$

The most noticeable aspect during the entire course of the dark oxidation in presence of oxygen was the lack of change in the spectrum. The 1669 cm^{-1} crotonaldehyde carbonyl stretch did become predominant over the 1705 cm^{-1} acetaldehyde carbonyl stretch, but this was mostly due to the temperature increase prior to the oxygen introduction and not to the oxidation itself. This indicates that the presence of an oxidative atmosphere is not enough to engage the catalytic properties of the nanoparticles (Figure 6.10), without the presence of light.

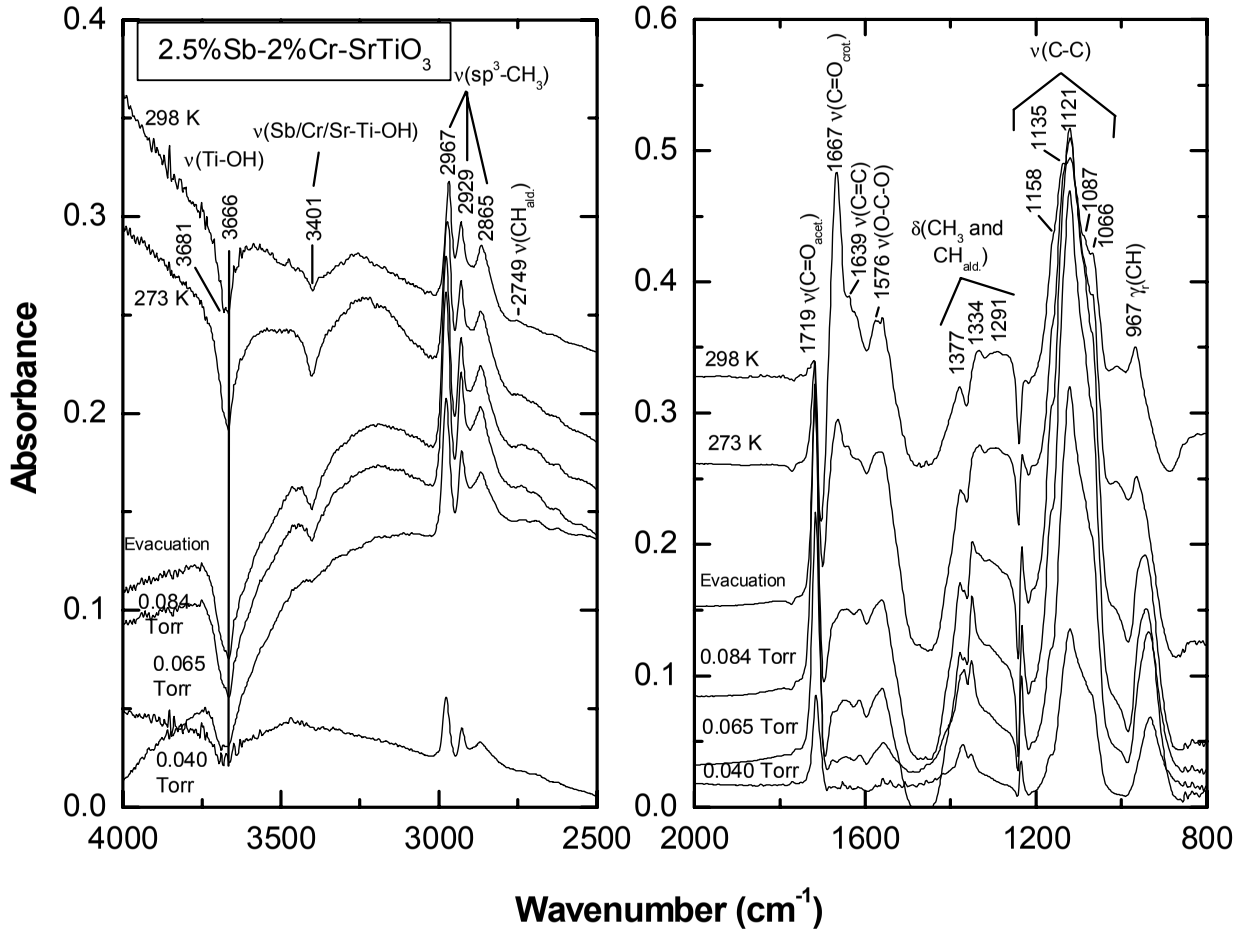

Figure 6.9 Adsorption, Evacuation, and Warming prior to Dark Oxidation of Acetaldehyde on 2.5%Sb/2%Cr-$SrTiO_3$ Nanoparticles

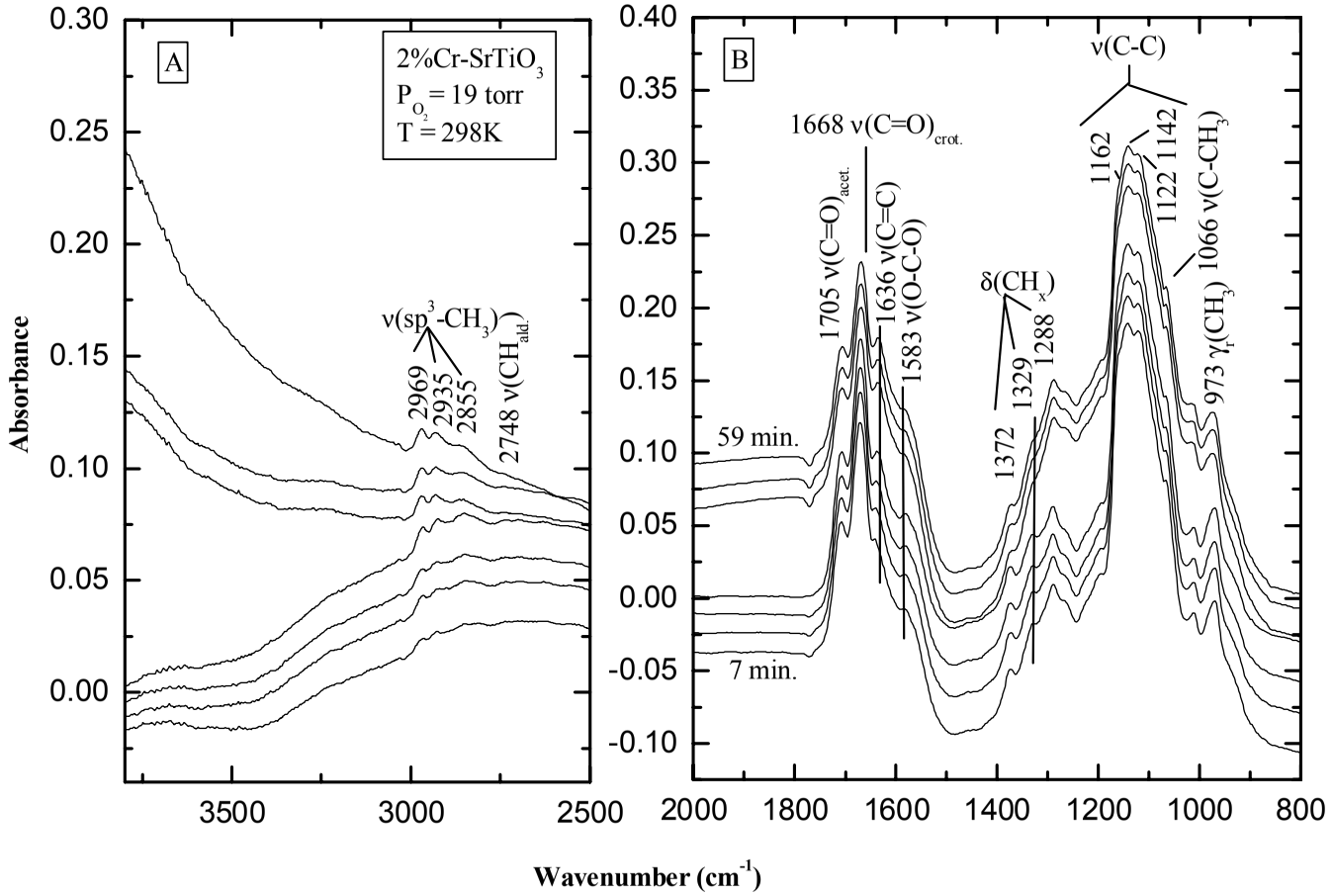

Figure 6.10 Attempted Dark Oxidation of Acetaldehyde as a Function of Time at Constant Temperature on 2%Cr-$SrTiO_3$ Nanoparticles

6.3.6 Attempted dark oxidation of acetaldehyde on 2.5% Sb/2% Cr codoped AP-$SrTiO_3$

The antimony/chromium sample also experienced no significant changes with the addition of oxygen (Figure 6.11). It should be noted that this section of the reaction was carried out on this sample at 298 K while the same section on the chromium only sample was done at 273 K.

6.3.7 Photooxidation of acetaldehyde on 2% Cr doped AP-$SrTiO_3$

There were two parts to the photooxidation. In the beginning, filters were used to restrict the spectrum of the incoming light from the lamp to between 400 nm and 700 nm, the visible range. After 2 hours, some of the filters were removed to open up the spectrum of incoming light to include all the way down to 300 nm, thus including a portion of the ultraviolet spectrum. As expected, with photooxidation there was evolution of carbon dioxide, but for reasons concerning space, that section of the spectra are not shown.

Once the light was turned on, a reaction can be seen taking place. The crotonaldehyde carbonyl stretch at 1671 cm^{-1} can be seen to decrease in relationship to an incoming peak at 1600 cm^{-1}. This peak is believed to be the O-C-O asymmetric stretch of an acetate species that is forming. A methyl group deformation mode for this species appears at 1313 cm^{-1} and its C-O stretching mode can be seen coming in at 1024 cm^{-1}. At 1723 cm^{-1}, an incoming feature was detected that can be attributed to a surface bound acetaldehyde species with the hydrogen abstracted from the aldehyde carbon, $CH_3C^{-}=O$. In Figure 6.12, the decrease in the crotonaldehyde carbonyl stretch is accompanied by decreases in all the acetaldehyde and crotonaldehyde carbon-carbon, single-bond stretches between 1162 cm^{-1} and 1066 cm^{-1} and the methyl deformation mode at 1377 cm^{-1}. Note that the spectra were cut off above 2000 cm^{-1} due to the lack of any changes in the features beyond the range shown.

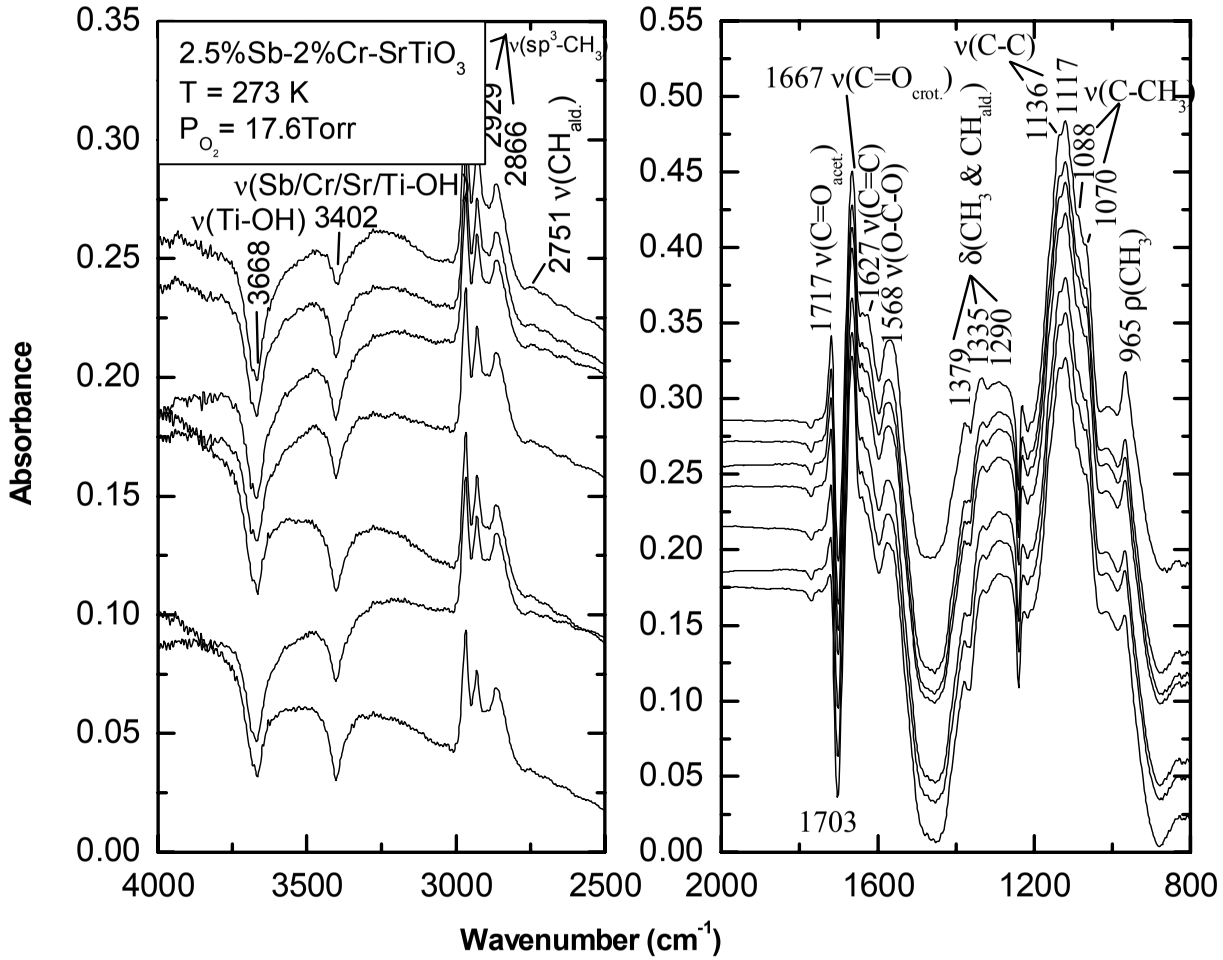

Figure 6.11 Dark Oxidation of Acetaldehyde as a Function of Time at Constant Temperature on 2.5%Sb/2%Cr-$SrTiO_3$ Nanoparticles

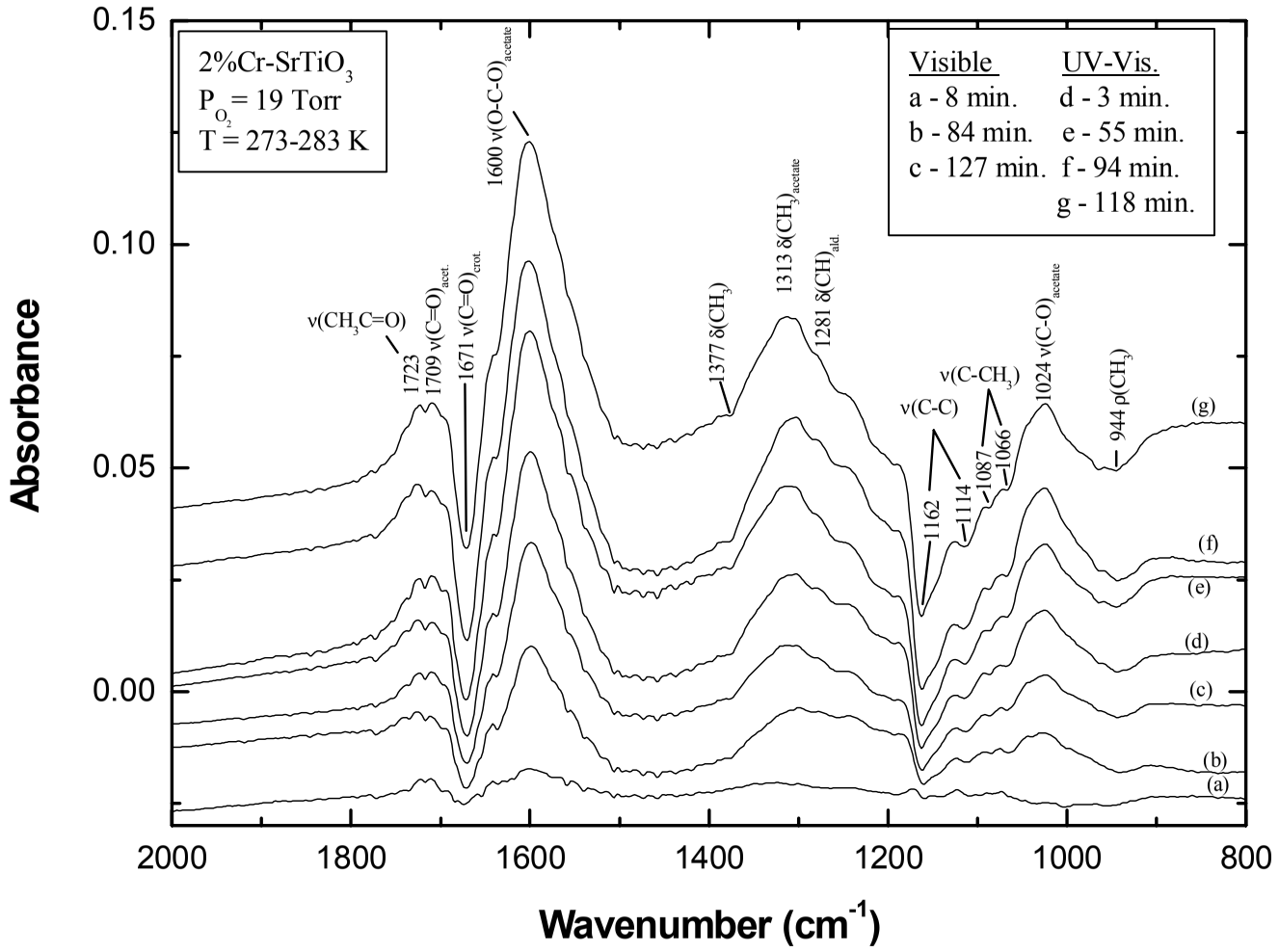

Figure 6.12 Visible and UV-Visible Photooxidation of Acetaldehyde on 2%Cr-$SrTiO_3$ Nanoparticles

6.3.8 Photooxidation of acetaldehyde on 2.5% Sb/2% Cr doped AP-$SrTiO_3$

A similar reaction to what occurred on the chromium only sample occurred on the antimony/chromium sample but with some significant differences. Negative features were seen for the sp^3-hybridized carbon-hydrogen stretches between 2969 cm^{-1} and 2868 cm^{-1} and for the carbonyl stretches of acetaldehyde and crotonaldehyde at 1708 cm^{-1} and 1669 cm^{-1}, respectively (Figure 6.13). This is an area of difference between the two samples. The chromium sample saw no decrease in the carbonyl stretch of acetaldehyde, but the sample with antimony and chromium experience a significant decrease in both acetaldehyde and crotonaldehyde carbonyls. Though the basic reaction taking place does not appear to change with the addition of the ultraviolet light, the fact that after the initial concentrations of reactants has decreased due to visible light photooxidation, the reaction did not slow down. On the contrary, it appears to have increased in rate and suggests that ultraviolet light is probably more effective than visible light only.

6.4 Mass spectrometry studies on reaction products

Thermal Programmed Desorption (TPD) has been used to identify the reaction product adsorbed on the surface of the $SrTiO_3$ samples. The samples after photooxidation have been heated up to 500ºC to achieve the desorption of the reaction products. The gaseous mixture of product was sequentially introduced into the Mass Spectrometer to identify the chemical formulas of desorbed products. The desorbed species detected by MS after photooxidation are summarized in Table 6.3. Additionally, the monitoring of the evolved species upon heating up to 623 K from the 2.5% Sb/2% Cr codoped AP-$SrTiO_3$ sample surface is presented in Figure 6.14.

For thermal oxidation, the acetate species were the main products, while during photochemical oxidation, ethanol, pentane, furan, and benzene species were also formed. Carbon oxide was formed only starting at 623 K during thermal oxidation, whereas it was observed during photooxidation at 273 K.

Table 6.3 Desorbed Species Identified by Mass Spectroscopy from the $SrTiO_3$ Surface after Photooxidation of Acetaldehyde

Fragments	Possible Compounds
44, 29, 43	Acetaldehyde
70, 69, 42, 41, 40, 39 38, 29, 27	Crotonaldehyde
70, 55, 54, 42, 41, 39, 29, 27	2-Pentane
79, 78, 77, 50, 51, 52	Benzene
68, 42, 40, 39, 38, 37, 29	Furan
46, 45, 31, 29, 27	Ethanol

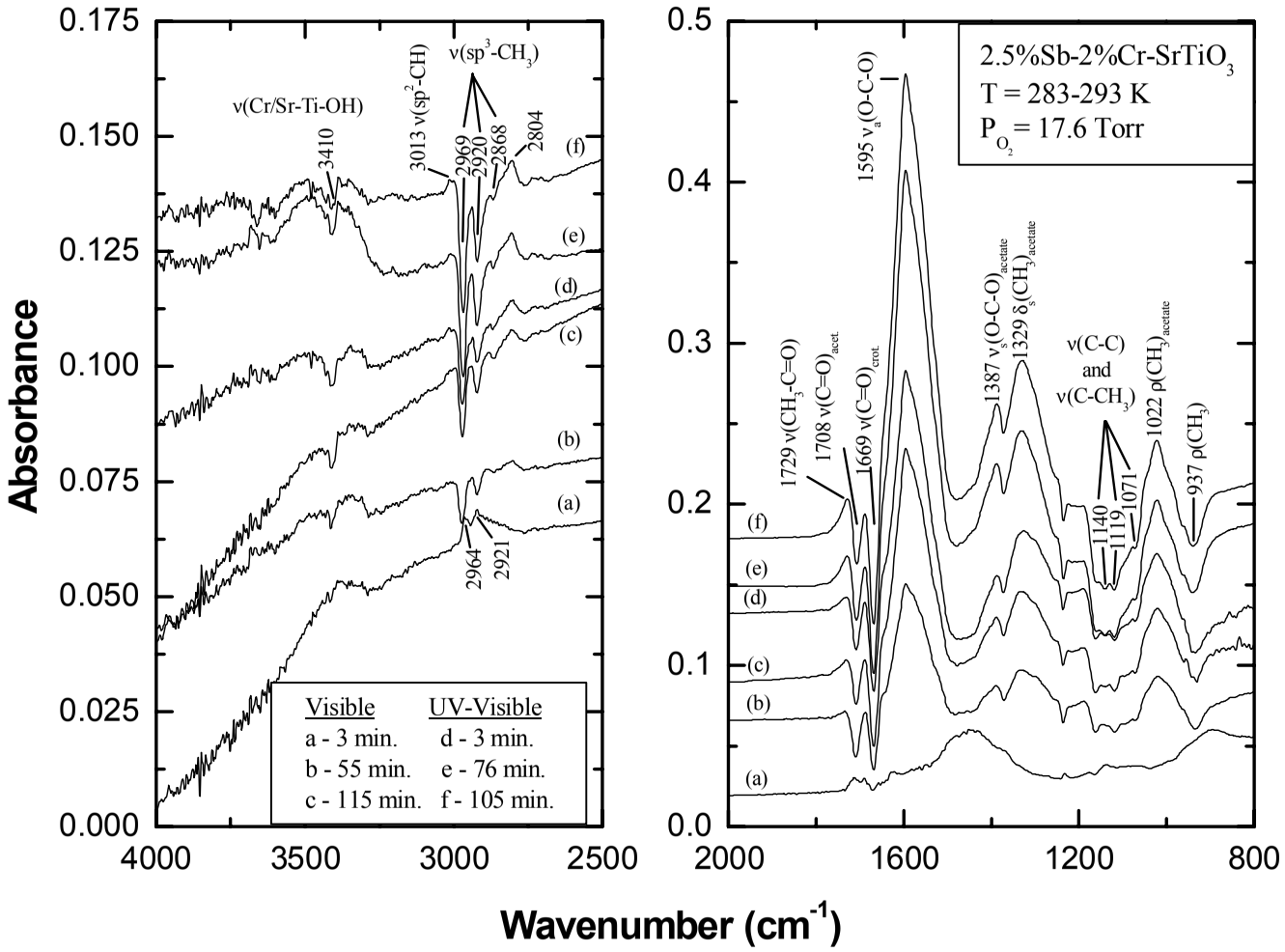

Figure 6.13 Visible and UV-Visible Photooxidation of Acetaldehyde as a Function of Time on 2.5%Sb/2%Cr-SrTiO$_3$

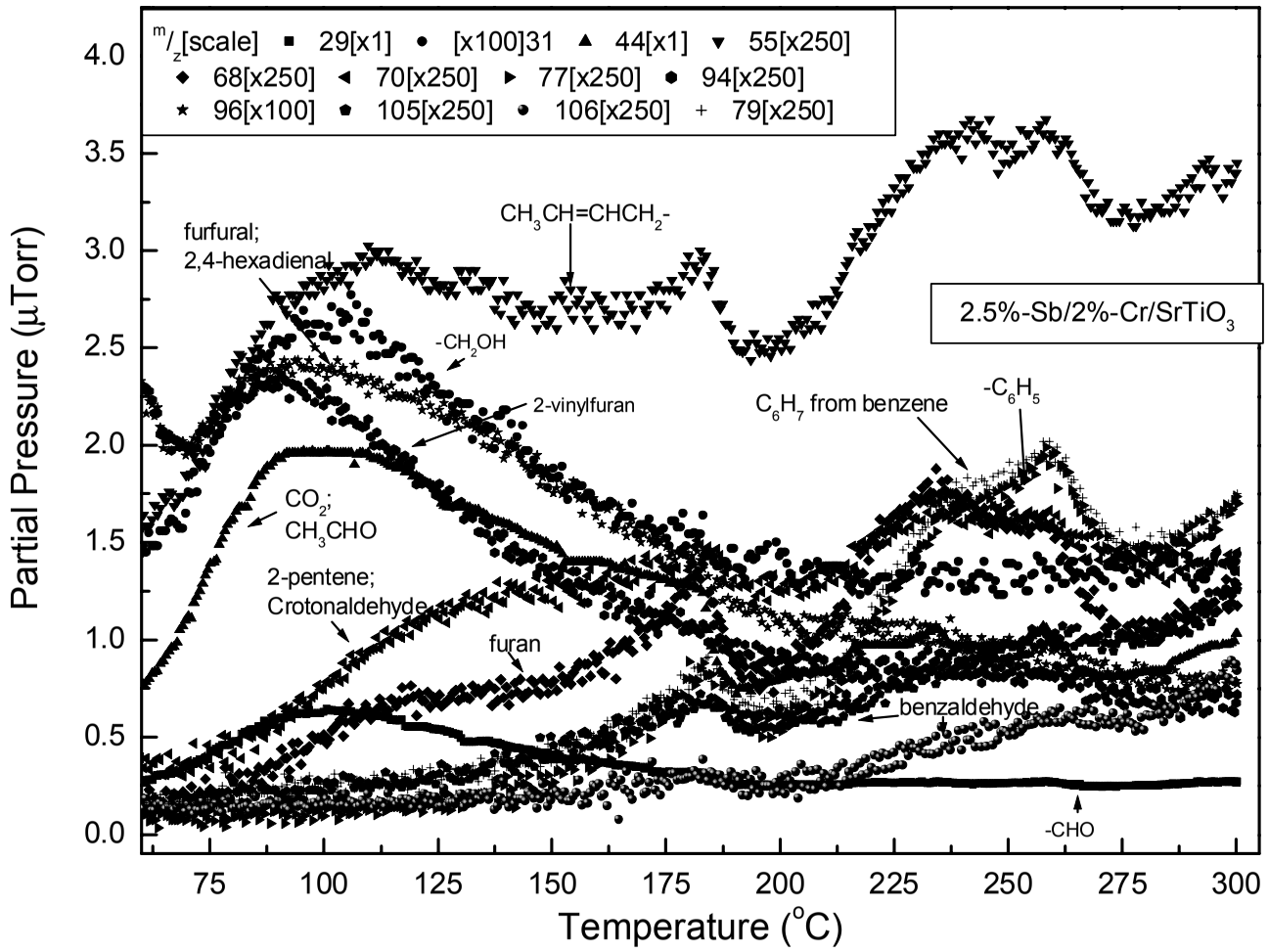

Figure 6.14 Temperature Programmed Desorption/ Mass Spectroscopy after Photooxidation of Acetaldehyde on 2.5%Sb/2%Cr-$SrTiO_3$

6.5 Conclusions

The unique properties of aerogels, such as high porosity, small crystallite size, and large surface area can be utilized to photocatalytically oxidize volatile organic compounds. IR vacuum is a useful technique to study the photooxidation of CH_3CHO on the $SrTiO_3$ surface in combination with Mass Spectrometry for the identification of reaction products. IR spectra gave a complex pattern of peaks, which show the production of crotonaldehyde (crotyl alcohol) during exposure to acetaldehyde for dark oxidation in the presence of oxygen.

Acetate species were produced by photooxidation in O_2 under UV irradiation while acetaldehyde and crotonaldehyde were consumed. Formation of ethanol, pentane, furan, and benzene were observed by MS after thermal programmed desorption. During thermal oxidation, CO_2 formation was observed at 623 K, whereas for photooxidation reaction it was observed at 273 K.

In Chapter 5 it was found that $SrTiO_3$ doped with chromium ions showed absorption in the visible light region and photoactivity for acetaldehyde decomposition. The photocatalytic activity for CO_2 evolution of the antimony/chromium incorporated $SrTiO_3$ aerogels was twice as high as that doped with only chromium under visible light irradiation. As predicted by the literature, the addition of antimony to the chromium doped strontium titanate nanoparticles did offer greater catalytic activity. The IR studies reported herein of the doped $SrTiO_3$ samples, and comparison with pure aerogel prepared $SrTiO_3$ samples, clarified the process of acetaldehyde adsorption, dark decomposition, and photooxidation under light irradiation on the $SrTiO_3$ surface.

From FTIR studies for pure aerogel and doped aerogel prepared $SrTiO_3$ samples, it was found that the products of the reactions appeared to be the same or at least within the same chemical group. Dark oxidation resulted in no significant catalysis indicating that the electron promotion via visible and/or UV light is necessary to activate the catalyst. While visible light alone was found to be sufficient to enable catalysis, the addition of ultraviolet wavelengths appears to increase the photocatalysis noticeably.

Upon exposure to ~15 Torr of oxygen in the absence of anything but minimal ambient light, no change in reaction was recorded. This indicates the necessity of light as an activating

factor for the catalytic properties of these nanoparticles. Upon exposure to the visible spectrum, reactions resulting in acetate species were observed on both samples with some differences. It was generally found that some additional reactivity was afforded by the incorporation of a charge balancing species such as antimony. Significant additional reactivity was observed when the spectrum of incoming light was widened to include wavelengths as low as 300 nm for samples containing Sb and Cr.

6.6 References

[1] S. Luo and J. Falconer, Catalysis Letters, 57 (1999) 89-93.

[2] H. Idriss and Madhavaram, Journal of Catalysis, 224 (2004) 358-369.

[3] H. Idriss, C. Diagne, J.P. Hindermann, A. Kiennemann, and M.A. Barteau, Journal of Catalysis, 155 (1995) 219-237.

[4] L. Wang and K.J. Ferris, J. Phys. Chem. B, 108 (2004) 1646-1652.

[5] C.-A. Chang, B. Ray, D.P. Paul, D. Demydov, and K.J. Klabunde, Photocatalytic Oxidation of Acetaldehyde over $SrTiO_3$ Nanoparticles: An *in situ* FTIR Study, in press.

[6] D.K. Paul, D.A. Panayotov, and J.T. Yates, Abstract, 39th Midvest Regional Meeting of the American Chemical Society in Manhattan, KS, United States, October 20-22, 2004.

[7] D. Demydov, K.J. Klabunde, C.-A. Chang, B. Ray, and D.P. Paul, in press.

Chapter 7 : Dielectric studies on titanates

7.1 Introduction

Barium titanate is widely used in electronic applications [1-3] as a material for

1) Multilayer ceramic capacitors,
2) Dielectric devices (flexible film capacitors, dielectric bolometers, IR focal plane arrays),
3) High-permittivity thin films (DRAMs, pyroelectric sensors, gas detection sensors)
4) Superconducting microwave tunable devices, tunable phase shifters, and ring resonators,
5) Acoustic imaging arrays (real-time acoustic cameras for underwater divers, medical imaging, and acoustic microscopy).

The application of $BaTiO_3$ for ceramic capacitors requires small diameter of particles, narrow size distribution and high purity of the $BaTiO_3$ phase. Nanosized $BaTiO_3$ samples prepared by wet chemical methods (sol-gel or aerogel) are highly pure powders of small monodispersed particles. The application of nanosized $BaTiO_3$ for ceramic capacitors can be beneficial, and it is important to determine if dielectric properties depend on the size of particles.

7.2 Dielectric properties of titanates

Barium titanate is the main titanate being used for capacitors. It is usually made by solid-state reaction of $BaCO_3$ with TiO_2 at temperature of 1100° C. Recently, the production of $BaTiO_3$ by wet chemical methods using alkoxide chemistry is becoming popular. Temperatures for calcination of $BaTiO_3$ prepared from alkoxides are significantly lower (500-700°C), and wet chemical methods allow better control of purity, Ba/Ti ratio, and particle sizes [4]. The textural properties of $BaTiO_3$ are important for consistent dielectric behaviors and reproducible structures in the sintered product.

The dielectric constant of a material can be calculated using the following equation

$$K = \frac{Ct}{\varepsilon_0 A} \qquad (7.1)$$

where - K is a dielectric constant of the dielectric material at specific frequency and specific temperature, C is capacitance (farads), *t* is distance between electrodes (thickness in cm), ε_o is permittivity of vacuum (8.854 x 10^{-14} F/cm), and $A = \pi r^2$ is an area of the electrode (cm^2).

$BaTiO_3$ is available in several phases including tetragonal, cubic, and hexagonal crystal structure (Equation 7.2). Cubic phase (Pm3m space group) has an ideal perovskite structure where a=b=c (Figure 7.1). At high temperature (>1432°C) it transforms into hexagonal structure ($P6_3mmc$ space group) where c>b=a and γ =120°C.

$$\text{Tetragonal} \xrightarrow[132°C]{} \text{Cubic} \xrightarrow[1432°C]{} \text{Hexagonal} \xrightarrow[1625°C]{} \text{Liquid} \qquad (7.2)$$

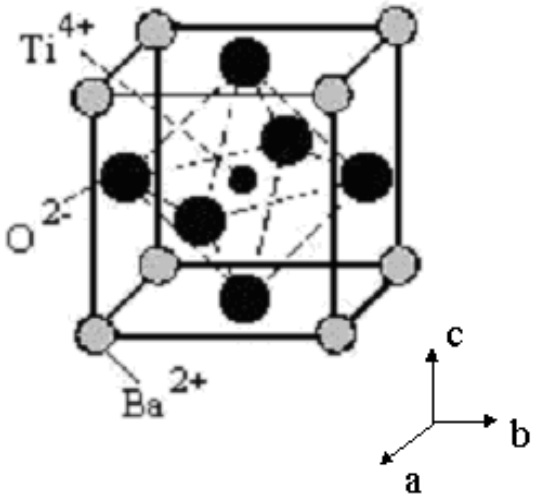

Figure 7.1 $BaTiO_3$ Structure

The tetragonal structure (P4mm space group and c>a=b) has atomic displacement for Ti and O atoms with respect to Ba atom and exhibits ferroelectricity. The transition from cubic to tetragonal occurs at 132°C (Curie temperature).

By cooling of $BaTiO_3$ through 132°C causes the cubic phase to undergo dipole charge changes on minor faces and transfers into the tetragonal phase. For grains larger than 3 μm, the

formation of domain walls relieves the stress from phase transformation and the material has a dielectric constant of 1500-1900 at room temperature. In materials with grains smaller than 1.5 μm, the 90° domain walls are not formed and the dielectric constant is significantly higher (2500-3500).

$SrTiO_3$ has a cubic perovskite structure and is paraelectric at room temperature. Its dielectric constant is smaller than $BaTiO_3$ and is about 300 at room temperature. The $SrTiO_3$ dielectric constant increases with cooling and is about 20000 near 0 K. Strontium titanate based materials are used for high-voltage capacitors with applied voltage up to 5 kV/mm [5].

Calcium titanate has similar dielectric properties to strontium titanate, but its dielectric constant is twice lower. Magnesium titanate has an ilmenite structure and a very low dielectric constant of 20. The advantage of $MgTiO_3$ is that its dielectric constant has a positive temperature coefficient. It can be added to $SrTiO_3$ or $CaTiO_3$ to adjust their negative temperature dependence. These materials give good high-frequency performance in multilayer capacitors [6].

Dielectric constant depends on the arrangement and bonding of atoms in the material, and the values for dielectric constant of different titanates are summarized in Table 7.1. The high value of dielectric constant and high thermal stability makes titanates good candidates for use in capacitors.

The dielectric constant of barium titanate is highly dependent on temperature, so cationic substitution is used to make the barium titanate suitable for capacitor applications and less dependent on temperature. The partial substitution of Ba^{2+} with Sr^{2+} allows decreasing the Curie temperature of the $BaTiO_3$ material. Strontium titanate and barium titanate can form a continuous series of solid solutions with different Sr/Ba ratios. These materials ($Ba_{1-x}Sr_xTiO_3$) have a very high dielectric constant (>5000) at room temperature. The linearity of the $SrTiO_3$ paraelectricity gives more stable capacitor performance in comparison with the pure $BaTiO_3$ material.

Table 7.1 Dielectric Constants of Titanates [7]

Material	Dielectric constant K, at 25°K
Titanium Oxide, TiO_2	100
Magnesium Titanate, $MgTiO_3$	20

Calcium Titanate, $CaTiO_3$	160
Strontium Titanate, $SrTiO_3$	320
Barium Titanate, $BaTiO_3$	1000-2000
Barium Strontium Titanate, $Ba_xSr_{1-x}TiO_3$	>5000

The dielectric constant in $BaTiO_3$ depends on the purity of the materials. The presence of impurities such as lattice hydroxyl (OH^-) and carbonate (CO_3^{2-}) groups decreased the dielectric constant [8]. The dielectric constant also decreased with decreasing particle sizes. The critical size for $BaTiO_3$ particles has been extensively studied by different research groups [9, 10]. It was found that tetragonality of barium titanate particles decreased at ~ 40 nm of particle diameter and changed to cubic phase at 20 nm [11, 12]. It was also found that the decrease of grain sizes from 50 μm to 0.8 μm causes increasing of dielectric constant [13]. With the decrease of grains smaller than 0.8 μm, the dielectric constant started to decrease too. This chapter aims to understand the size effect of $BaTiO_3$ nanoparticles on the dielectric properties.

7.3 Aerogels for electrical applications

Advances toward nanoscale electronics require application of nanosized materials for dielectric, piezoelectric, pyroelectric, and electro-optic ceramics. Due to their unique properties, including high surface areas and small particle sizes, aerogel oxide materials can be used for these electrical applications. The electrical applications of aerogel materials already include rechargeable batteries, capacitor electrodes, piezoelectric materials, and dielectric materials.

A larger amount of ions can reversibly intercalate into a porous structure of aerogel prepared material in comparison with conventionally prepared material. The pore size distribution of aerogels is more effective for enhancing ionic conductivity in comparison with xerogels [14]. Several oxide aerogels have already been studied for lithium ion intercalation, including vanadium oxide [15], manganese oxide [16], and molybdenum oxide [17] aerogels. Vanadium oxide aerogels with high surface area up to 450 m^2/g and a specific pore volume as much as 2.3 cm^3/g were able to intercalate up to 5.8 equivalents of lithium per mol of V_2O_5 aerogel [18]. This material can be used as a positive electrode in lithium batteries with high

capacity (500-600 mAh/g) [19]. Additionally, aerogels with high thermal insulation properties can be used for high-temperature electrical batteries [20, 21].

Aerogel materials can reversibly immobilize a large quantity of electrical charge carriers. Carbon aerogels which are good conductors of electricity were studied as double layer electrodes in supercapacitors, pseudocapacitors, capacitive deionization units, and fuel cells [22-24]. Due to the lower electric resistance and higher specific area of aerogels, they can store more electrical energy than that of conventional capacitors [25]. These materials are also good for ion storage and deionization applications and in particular can be used for metal removal from water (Cu, Zn, Ni, Cd, Cr, Pb, U) [26].

Highly porous piezoceramic materials can be prepared by the aerogel process and be used for the production of porous piezoelectric transducers with low acoustic impedance [27-29]. Aerogel prepared lead zirconium titanate (PZT) with composition $PbZr_{0.53}Ti_{0.47}O_3$ has porosity up to 90 % by volume, specific surface area above 300 m^2/g, high polarization and low coercive field strength. Thin films of silica aerogels have very low dielectric constants and can be applied for integrated circles to increase the computer speed [30].

7.4 Synthesis of $Ba_{0.5}Sr_{0.5}TiO_3$ aerogel

Barium strontium titanate aerogel was prepared in such a way that the molar ratio of $Ba_{0.5}Sr_{0.5}TiO_3$ would be preserved. Sr and Ba metals were separately dissolved in alcohol first and then mixed in 1:1 ratio and added to Ti alkoxide (Figure 7.2). The textural properties of this sample were characterized by XRD, TEM, and UV-visible spectrometry (More detailed information on sample characterization operation procedures can be found in Chapter 3.3).

A powder X-ray diffraction pattern was obtained on a Bruker D8 Adpvance spectrometer with a CuKα radiation source with an applied voltage of 40 kV and a current of 40mA. Scans were made in the 2θ range of 20-85º with a scanning rate of 2 º/min. The crystallite size was calculated from the XRD patterns using the Debye-Scherrer equation. The peaks from the diffractograms patterns were assigned to the pure barium strontium titanate phase, and no additional peaks were observed (Figure 7.3).

The surface area was measured on a Nova 1200 gas sorption analyzer (Quantachrome Corp.) from the amount o N_2 absorbed at 77K and calculated according to the Brunauer-Emmett-

Teller (BET) method. The samples were degassed at 423 K for 1 hour prior to the analysis. The surface area of AP- $Ba_{0.5}Sr_{0.5}TiO_3$ after calcination in oxygen for five hours was 59 m^2/g.

Light absorption spectra of the $Ba_{0.5}Sr_{0.5}TiO_3$ sample were obtained on a Cary 500 Scan UV-Visible Spectrometer with an integrating sphere attachment for diffuse reflectance in the range 200-800 nm. Similar to the $SrTiO_3$ and $BaTiO_3$ samples, $Ba_{0.5}Sr_{0.5}TiO_3$ absorbed only UV light and did not absorbed any visible light (Figure 7.4).

Transmission electron micrographs were obtained on a Philips CM 100. Samples were placed onto a carbon-coated copper grid by the physical interaction of the grid and powder in such a way that the particles remained adhered to the grids. The calcination of $Ba_{0.5}Sr_{0.5}TiO_3$ samples in oxygen at 500°C caused almost a double increase of crystallite sizes (Figure 7.5). The average crystallite sizes were 20 nm for a $Ba_{0.5}Sr_{0.5}TiO_3$ sample calcined in oxygen at 500°C for 5 hours.

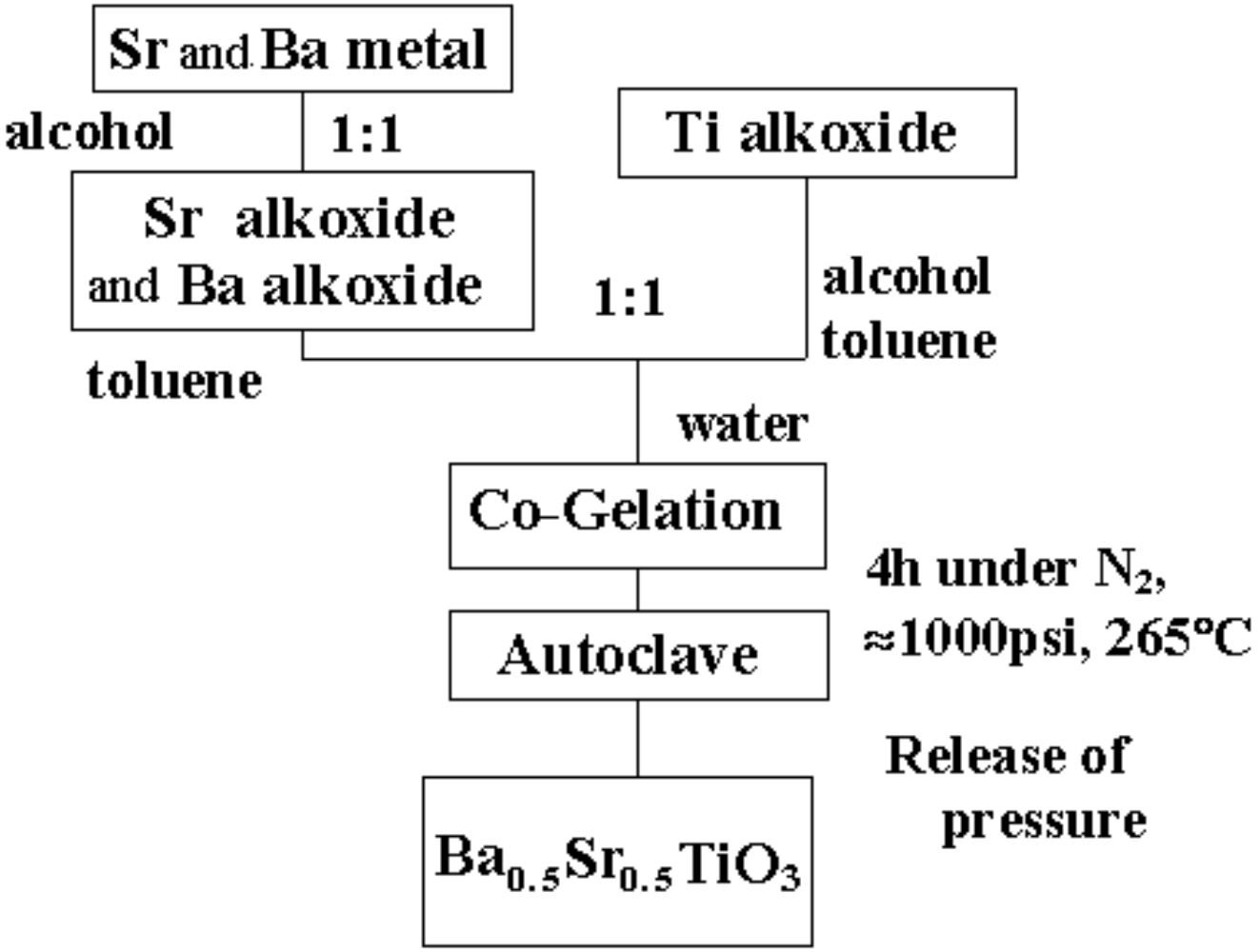

Figure 7.2 Modified Aerogel Procedure (MAP) from Alkoxides for $Ba_{0.5}Sr_{0.5}TiO_3$ Synthesis

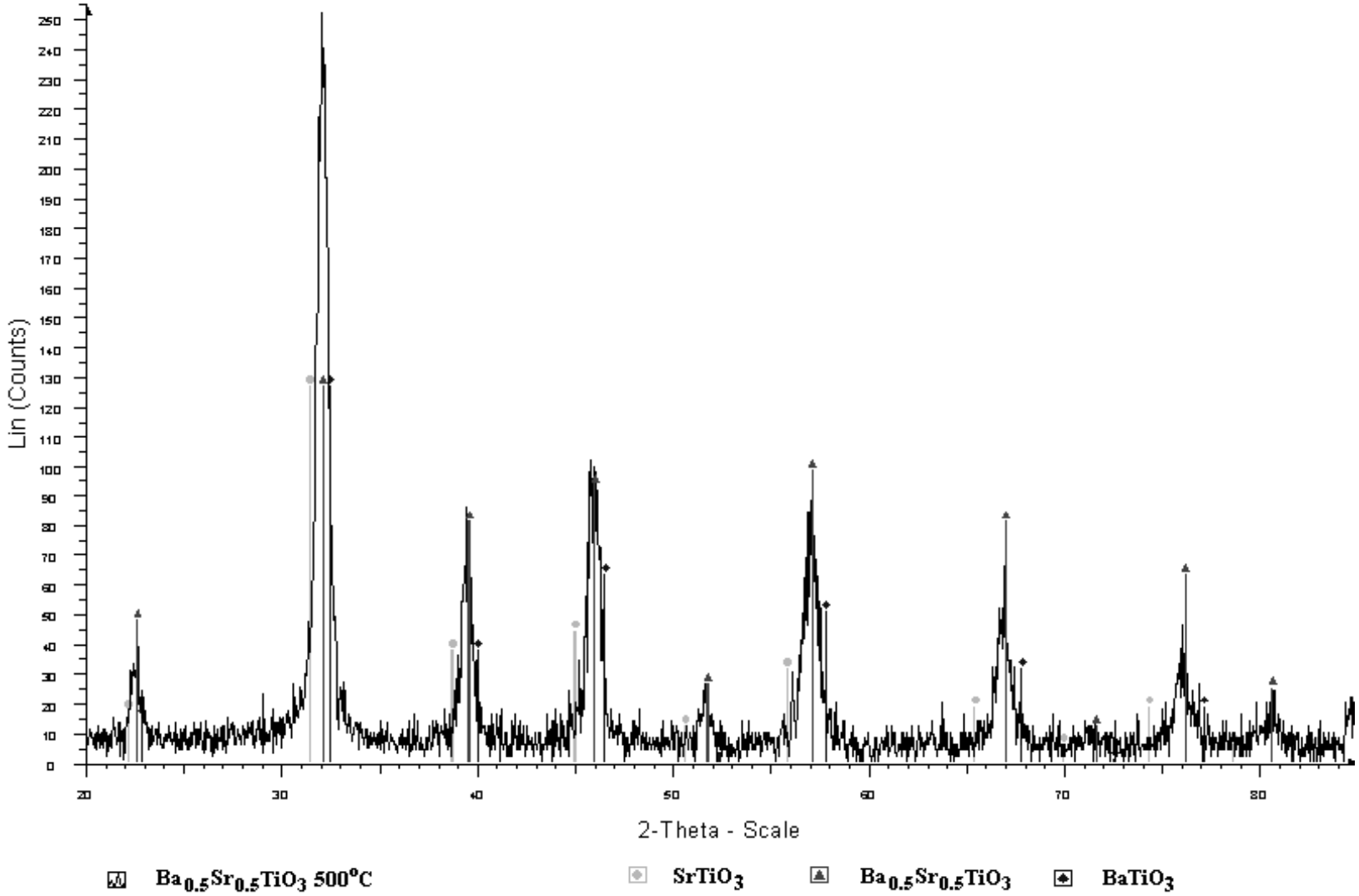

Figure 7.3 Modified Aerogel Procedure (MAP) from Alkoxides for $Ba_{0.5}Sr_{0.5}TiO_3$ Synthesis

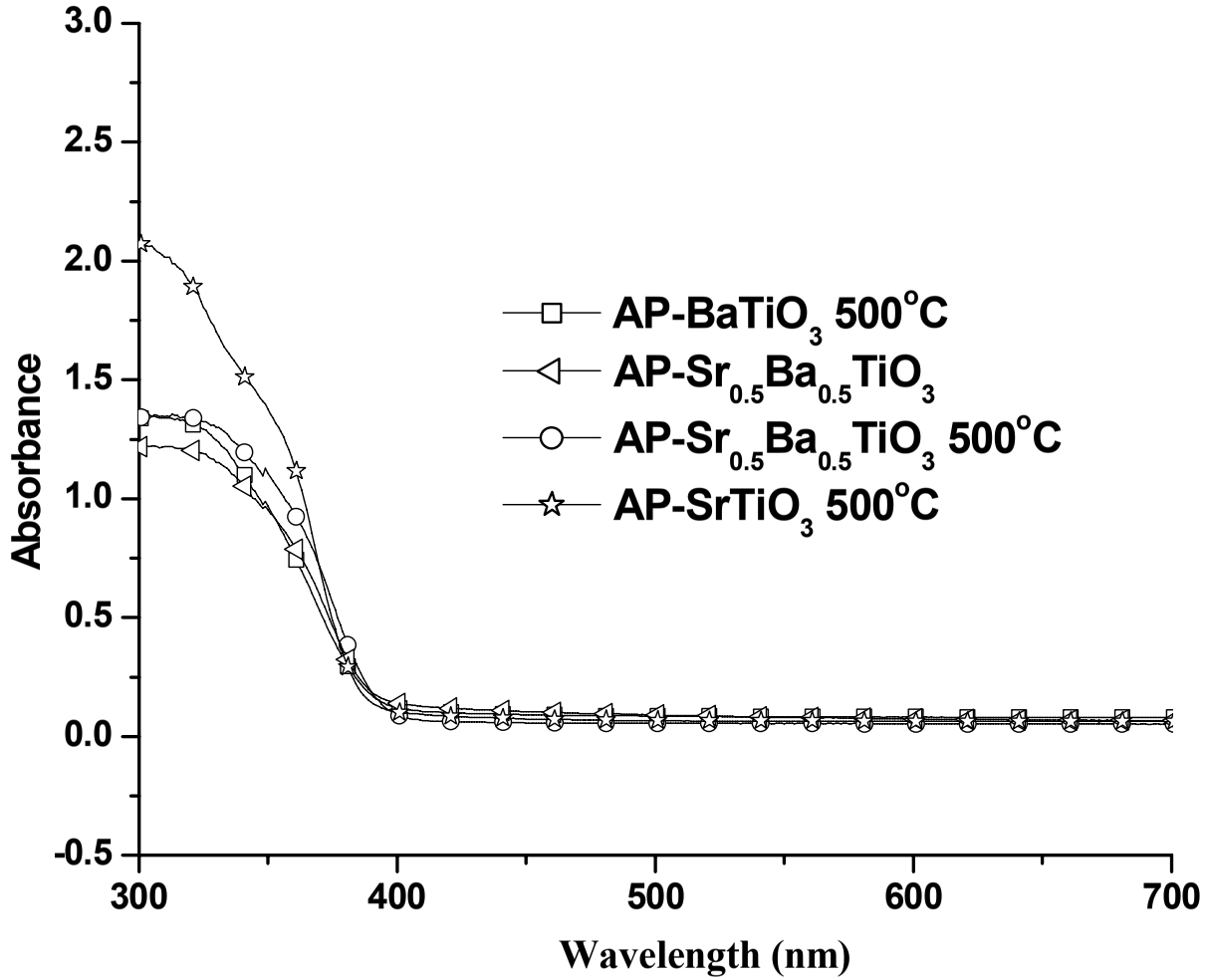

Figure 7.4 UV-visible Spectra of Different Aerogel Prepared Samples

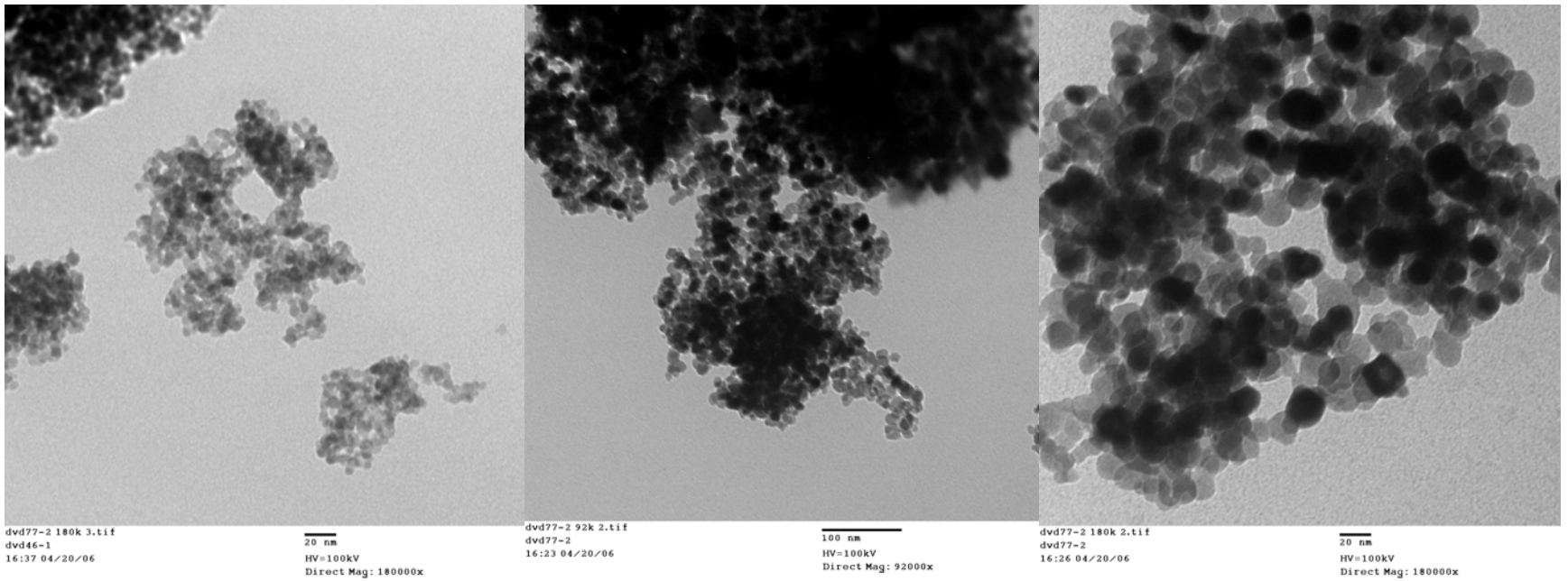

Figure 7.5 Transmission Electron Micrographs of AP-$Ba_{0.5}Sr_{0.5}TiO_3$ Freshly Prepared (left and middle) and Calcined in Oxygen at 500°C (right)

7.5 Dielectric measurements

Dielectric properties of barium titanate samples were studied by Impedance analysis and Raman spectroscopy.

7.5.1 Impedance analysis

For comparison, the dialectic response from aerogel prepared barium titanate, aerogel prepared barium strontium titanate, and commercial barium titanate samples were studied. The impedance behaviors of these samples in the form of pressed pellets were studied. Impedance measurements (Solatron SI-1260 Impedance/ Gain-phase Analyzer in combination with Solatron 1296 Dielectric Interface) from 10 mHz to 1 MHz were performed on barium titanium powders that were pressed into pellets (12 mm × 2 mm) using a IR pellet die and a press with pressure of 5000 lbs. The impedance analyzer was controlled by a personal computer with GPIB interface.

A special dielectric cell was built where the pellets were held in-between two alumina disks using platinum foil as the electrode contacts (See Appendix E). The sample cell was placed into furnace and heated in air. Dielectric measurements were made starting at room temperature and in 50°C steps between 50 and 500°C.

The disk-shaped pellets were calcined at 700°C for 7 hours for hardening. After calcination, the pellet surfaces were coated with silver metallic film for better contact with platinum electrodes. Coating was done by simply painting on the external flat faces with silver paste and following calcination at 400°C to get silver metallic coating (See Appendix E).

Before dielectric studies, the effect of pressing powder sample into pellets was studied. Surface area and pore volume measurements were made on the pellet of commercially available (CM-$BaTiO_3$) and nanosized commercially available (NCM-$BaTiO_3$) barium titanate samples and summarized in table 7.2. The surface area of pellets made from nanosized sample decreased significantly losing half of its total value, while the surface area of low surface area samples (pellets of commercial $BaTiO_3$) did not change. The powder X-ray diffraction (Figure 7.6) also shows the narrowing of the peaks which corresponds increasing in particle sizes for nanosized samples after pelletization.

Table 7.2 Textural properties of pelletized $BaTiO_3$

$BaTiO_3$ Sample	Surface area, m^2/g
CM-$BaTiO_3$	3
CM-$BaTiO_3$ pellet (700ºC)	1
CM-$BaTiO_3$ pellet (700ºC)	3
NCM-$BaTiO_3$	19
NCM-$BaTiO_3$ pellet (700ºC)	10
NCM-$BaTiO_3$ pellet (700ºC)	10

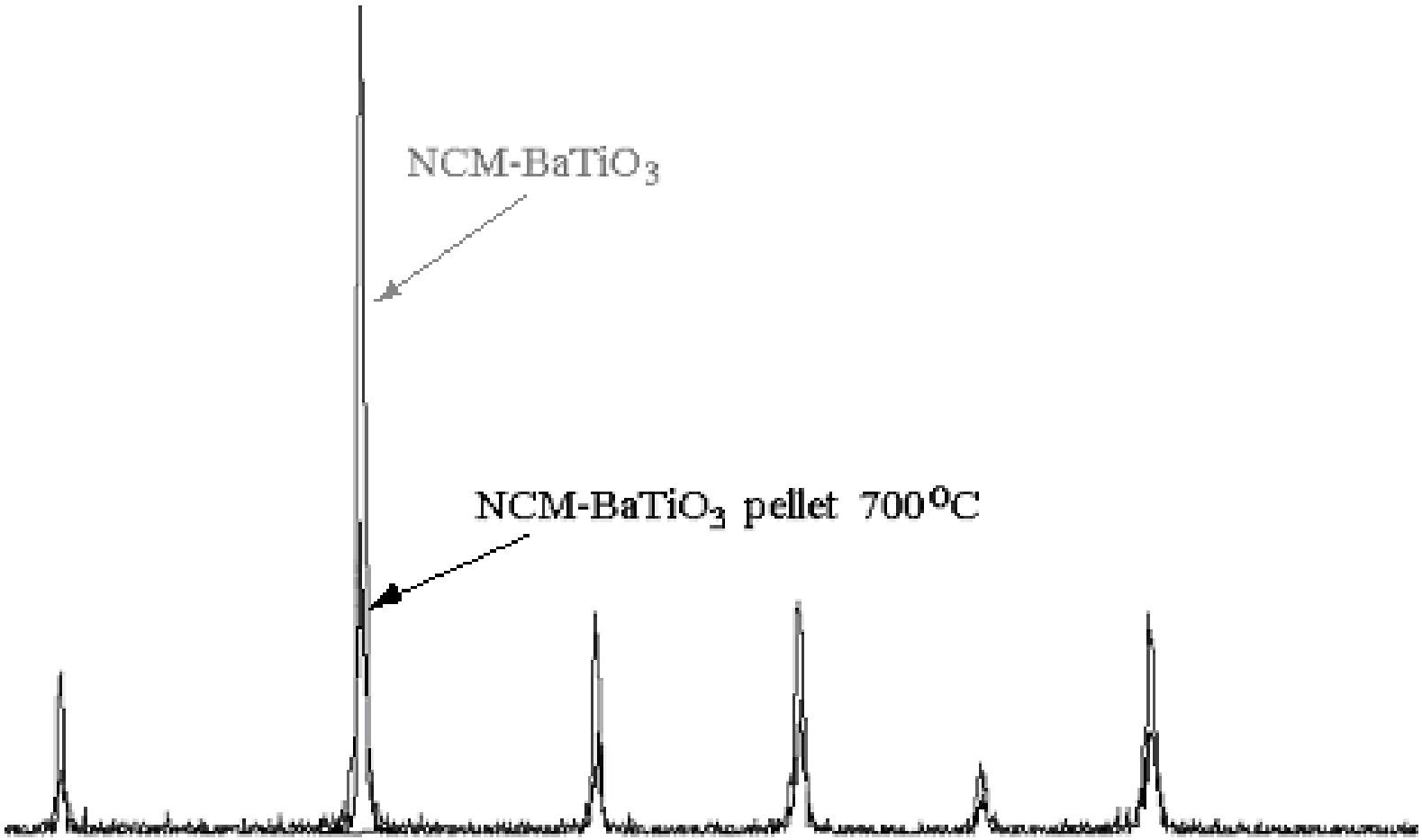

Figure 7.6 Powder XRD of NCM-$BaTiO_3$ Powder and Powder of Crashed NCM-$BaTiO_3$ Pellet

The impedance response was studied for commercial $BaTiO_3$, aerogel prepared $BaTiO_3$, and aerogel prepared $Ba_{0.5}Sr_{0.5}TiO_3$ pellets. The complex impedance spectrum for AP-$Ba_{0.5}Sr_{0.5}TiO_3$ pellet is presented in Figures 7.7. The imaginary impedance part (Z") is plotted against the real impedance part (Z'). The semicircle in the graph stands for the contribution from the bulk and grain boundaries. The contribution from the bulk and grain boundaries can not be separated in the high-frequency arc. The additional feature next to the semicircles is attributed to the interfacial effect at the contacting Ag electrodes.

The semicircles from resulting impedance spectra can be used for the calculation of the capacitance (C) and resistance (R) by the modulation of equivalent circuit (Equation 7.3) with two parallel RC elements where first element represents the conduction in the bulk and the second element represents the conduction of along grain boundaries:

$$\omega_{max}RC = 1 \qquad (7.3)$$

where $\omega_{max} = 2\pi f_{max}$, and f_{max} is the frequency at the arc maxima.

The resistance and relative permittivity of different $BaTiO_3$ samples were plotted and compared (Figures 7.8 and 7.9). The aerogel prepared $BaTiO_3$ bulk resistance values were significantly lower than that of commercial $BaTiO_3$, by several orders of magnitude. This can be explained by higher density of grain boundaries in aerogel samples.

The dielectric constants for $BaTiO_3$ samples at room temperature were calculated using Equation 7.1. The dielectric constant for AP-$Ba_{0.5}Sr_{0.5}TiO_3$ sample was 2250, for AP-$BaTiO_3$ sample - 2150, and CM-$BaTiO_3$ - 1890, respectively. There was no significant increase for aerogel prepared barium strontium titanium oxide in comparison with aerogel prepared barium titanate; however, the dielectric constant of the former sample was less dependent on the temperature. All aerogel samples had a higher dielectric constant, higher permittivity, and smaller resistance at room temperature in comparison with commercial barium titanate samples.

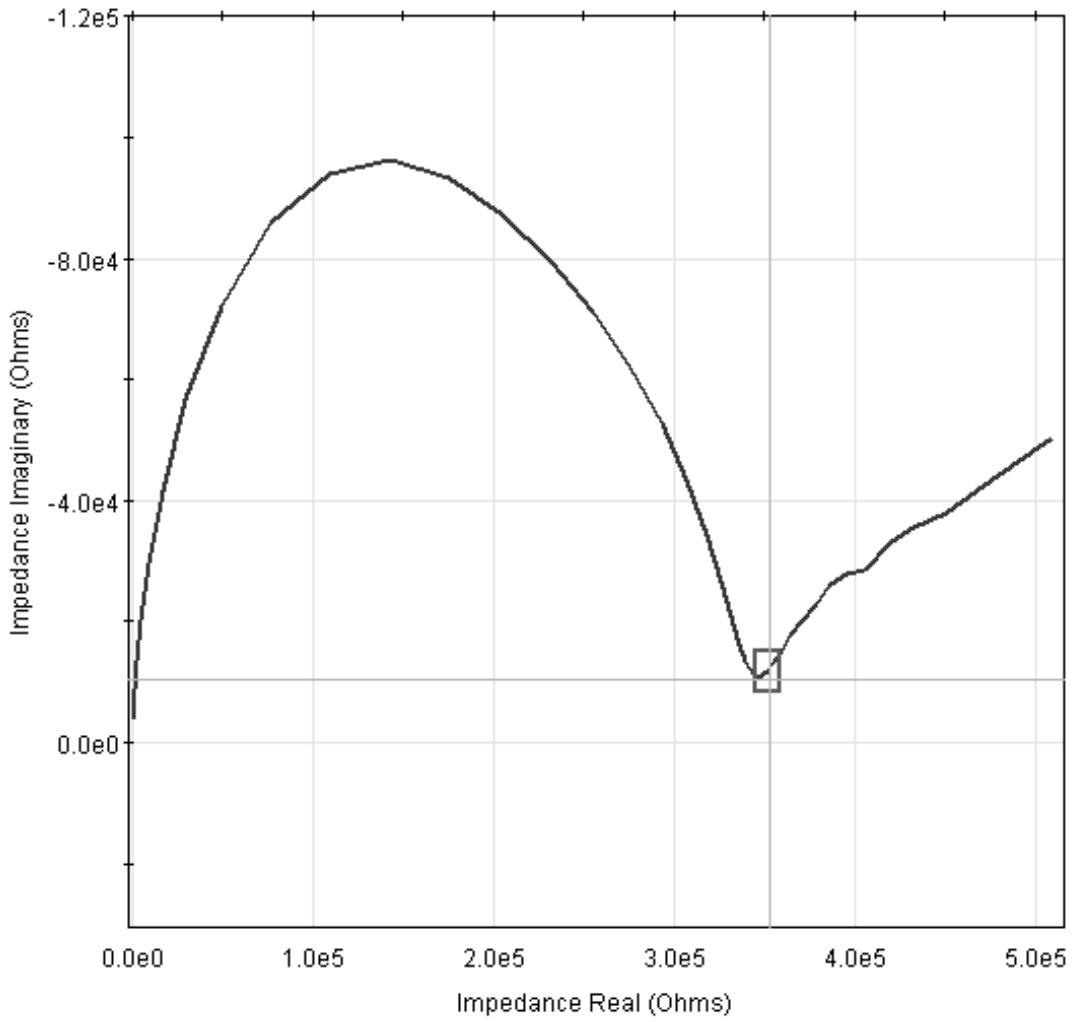

Figure 7.7 Complex Impedance Spectrum of Aerogel Prepared AP-$Ba_{0.5}Sr_{0.5}TiO_3$ at Room Temperature

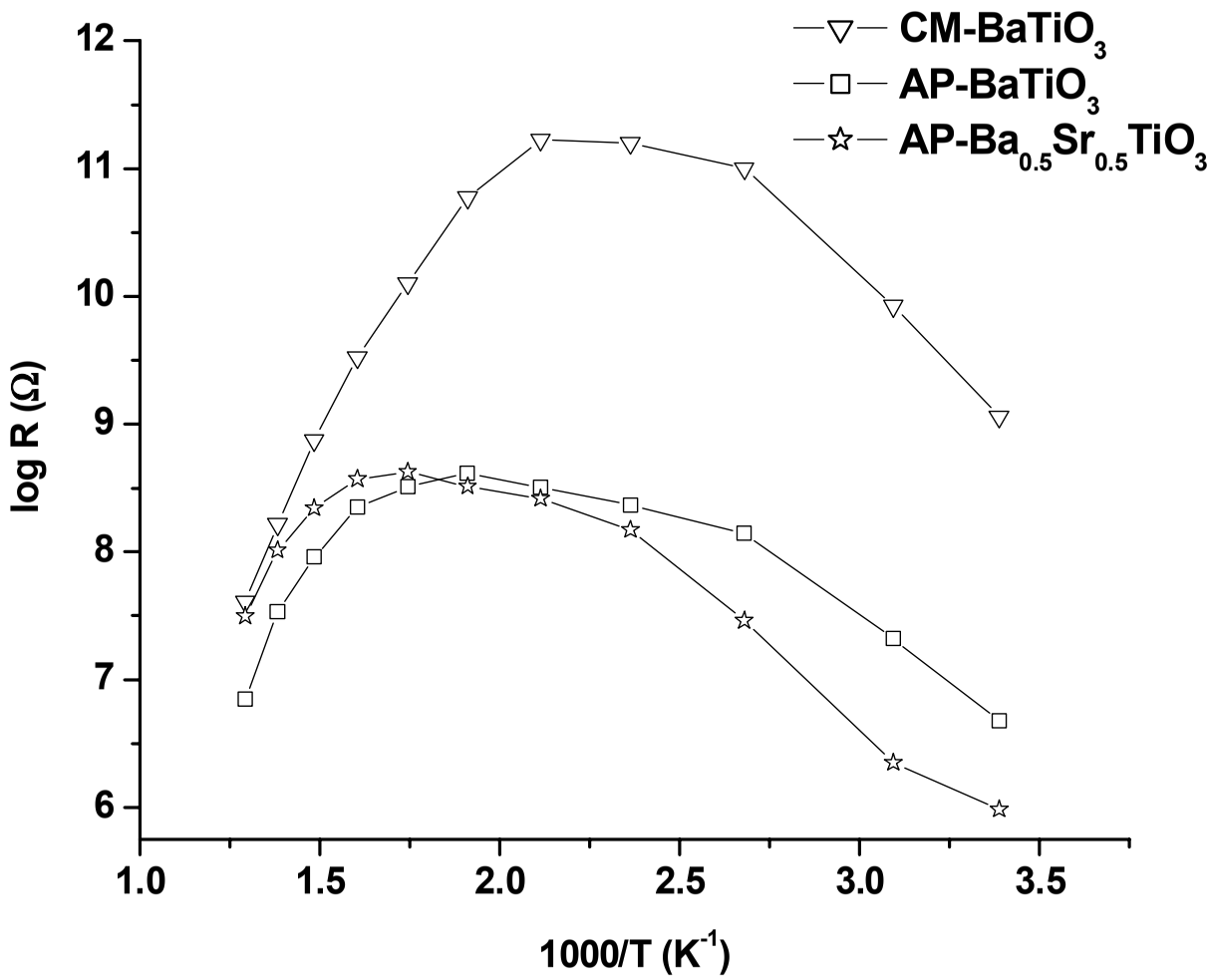

Figure 7.8 Resistance of Commercial $BaTiO_3$ and Aerogel Prepared $BaTiO_3$ and $Ba_{0.5}Sr_{0.5}TiO_3$

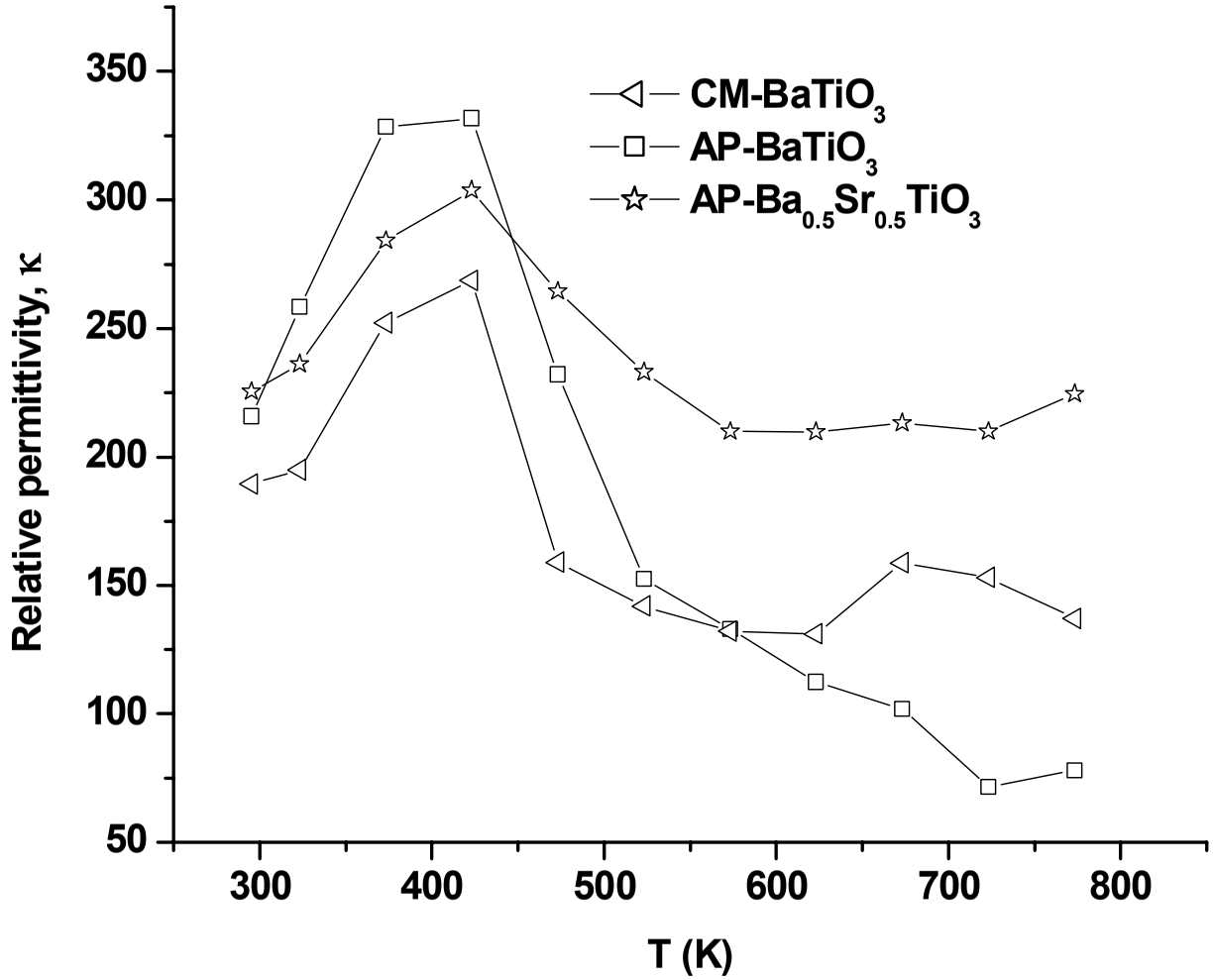

Figure 7.9 Relative Permittivity of Commercial $BaTiO_3$ and Aerogel Prepared $BaTiO_3$ and $Ba_{0.5}Sr_{0.5}TiO_3$

7.5.2 Raman spectroscopy

It is difficult to use XRD to analyze nanosized samples for phase structure in $BaTiO_3$ and almost impossible to distinguish between tetragonal and cubic phases when the peaks are broad. Raman spectroscopy is a significantly more sensitive as a method and can be used for detecting the presence of tetragonal or cubic phases in $BaTiO_3$. Some bands are active in the tetragonal and inactive in cubic phase. The intense band at 307 cm^{-1} indicates the presence of tetragonal phase in nanosized commercial $BaTiO_3$, while the aerogel prepared $BaTiO_3$ sample does not have a tetragonal phase and consists of only cubic phase (Figure 7.10).The average crystallite sizes of NCM-$BaTiO_3$ particles are 36 nm and the average crystallite sizes of AP-BaTiO3 are 11 nm. This confirms that the critical size for the cubic-tetrahedral transformation lays in-between 11-36 nm size range.

While Impedance analysis is used to calculate the extrinsic dielectric constant which includes the influence of $BaTiO_3$ compacting into a dense pellet, the effect of pores, space charge, and boundaries; Raman spectroscopy can be used for the calculation of intrinsic dielectric constant without the effect of pores, space charge, and boundaries. It can be calculated by Lyddane-Sachs-Teller (LST) equation from the Raman spectra [31]

$$\frac{\varepsilon}{\varepsilon_\infty} = \frac{\omega_1^{2}{}_{LO}}{\omega_1^{2}{}_{TO}} * \frac{\omega_2^{2}{}_{LO}}{\omega_2^{2}{}_{TO}} * \frac{\omega_3^{2}{}_{LO}}{\omega_3^{2}{}_{TO}} \qquad (7.4)$$

where ε is a dielectric constant at zero frequency, ω is a mode frequency for each phonon modes, ε_∞ is an optical dielectric constant for $BaTiO_3$ (a = 5.22, c = 5.07).The dielectric constant can be determined for c-axis using frequencies of the A1 modes, and for a-axis using frequencies of the E modes. To use these modes for calculation of dielectric constant, they need to be extrapolated from the Raman spectra (Figure 7.10).

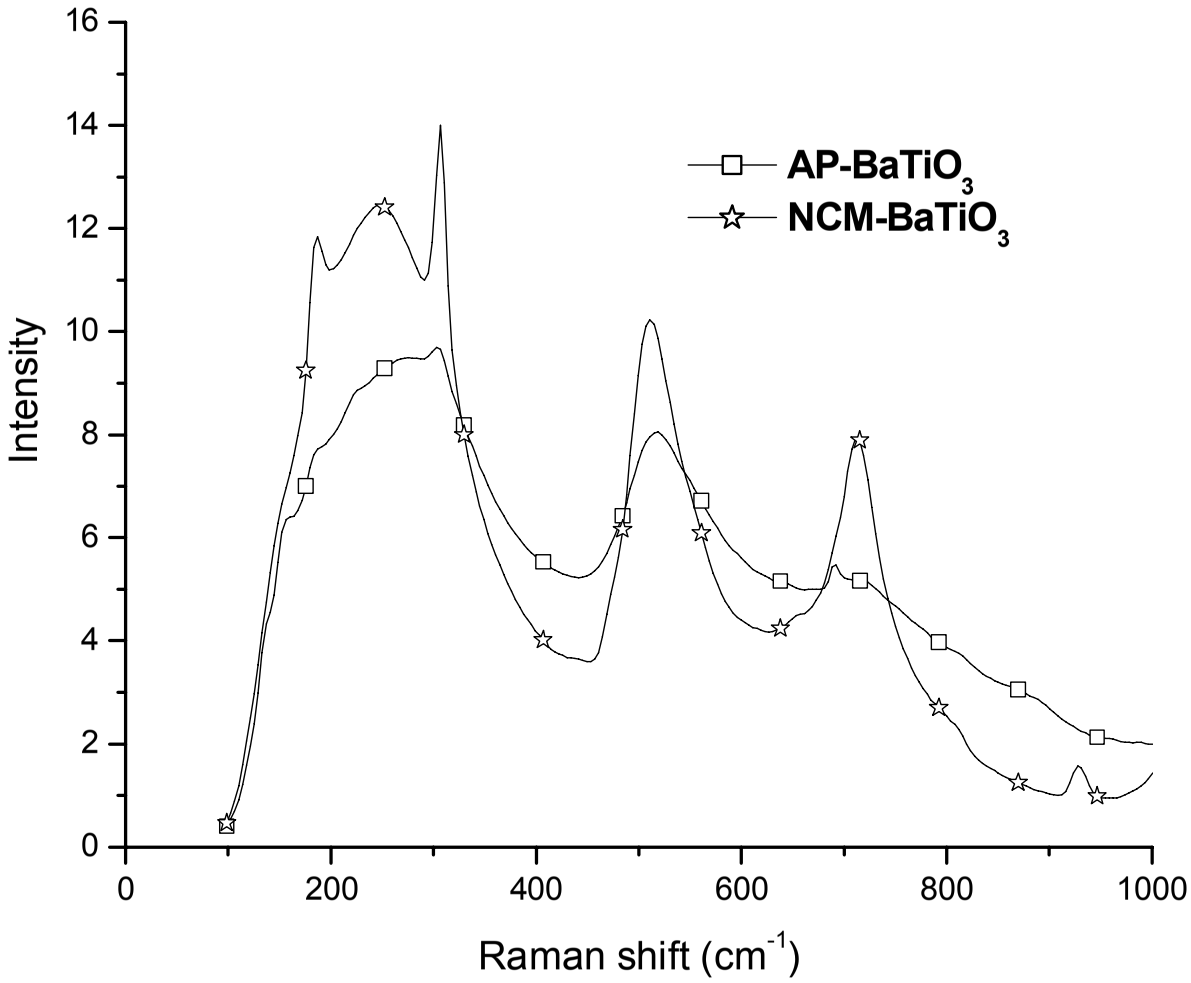

Figure 7.10 Raman Spectra of AP-$BaTiO_3$ and NCM-$BaTiO_3$

Unfortunately, the traditional mathematical software programs are not able to separate and extract the exact peak values of the modes. A special program that uses the sum of damped harmonic oscillators and a Debye relaxation mode may be useful for this purpose (Figure 7.12).

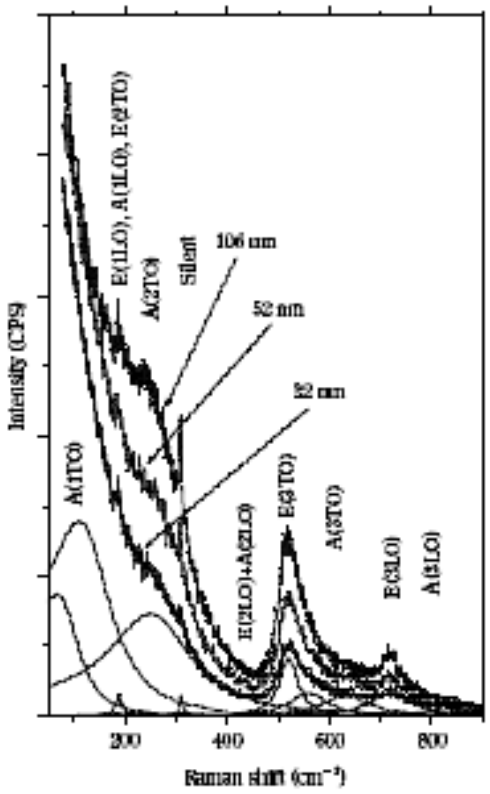

Figure 7.11 Raman Spectra of $BaTiO_3$ and Extraction of Soft Mode Frequencies [31]

7.6 Conclusions

Barium titanate is a well-known ferroelectric material with a high dielectric constant. The electrical properties of $BaTiO_3$ aerogels were evaluated from room temperature up to 500°C and compared to those of commercially available barium titanate samples. The pressed pellets of aerogel prepared barium titanate lost some of its surface area during pellet preparation.

The dielectric permittivity of $BaTiO_3$ samples was determined as a function of frequency up to 1MHz. The aerogel samples show higher permittivity than the commercial sample.

Permittivity in nanosized samples was higher due to higher density of grain boundaries. The aerogel prepared $BaTiO_3$ bulk resistance values were significantly lower than that of commercial $BaTiO_3$, by several orders of magnitude.

The dielectric constant for AP-$Ba_{0.5}Sr_{0.5}TiO_3$ sample was 2250, for AP-$BaTiO_3$ sample it was 2150, and for CM-$BaTiO_3$ sample it was 1890. There was no significant increase for aerogel prepared barium strontium titanium oxide in comparison with aerogel prepared barium titanate; however, the dielectric constant of AP-$Ba_{0.5}Sr_{0.5}TiO_3$ sample was less dependent on temperature. All aerogel samples had higher dielectric constant, higher permittivity, and smaller resistance at room temperature in comparison with the commercial barium titanate sample.

A further exploration of the aerogel prepared $BaTiO_3$ materials is necessary. The studies on $BaTiO_3$ samples with the high concentration of oxygen vacancy defects and doped with transition metals will bring more understanding in the dielectric behaviors of barium titanate and finding of advantages in possible application of these novel materials.

7.7 References

[1] A.D. Hilton and R. Frost, Key Engineering Materials, 66-67, Trans Tech Publications (1992) 142.

[2] D. Pandy, A.P. Singh, and V.S. Tiwari, Bull. Mater. Sci., 15 (1992) 391.

[3] L.E. Cross, Am. Ceram. Soc. Bull., 63 (1984) 586

[4] K.S. Mazdiyasni, R.T. Dolloff, and J.S. Smith, J. Amer. Ceram. Soc., 52 (1969) 523.

[5] S. Nishigaki, K. Murano, and A. Ohkoshi, J. Amer. Ceram. Soc., 65 (1982) 554.

[6] N. Kikuchi, T. Yoshioko, K. Furukawa, and, S. Fujimara, U.S. Patent 3951873, 1976.

[7] M. Kahn, D.P. Burks, I. Burn, and W.A. Schulze, in Electronic Ceramics, L.M. Levinson (ed.), Marcel Dekker, Inc., New York and Basel, 1988, p.533.

[8] S. Wada, H. Narahara, T. Hoshina, H. Kakemoto, and T. Tsurumi, J. Mater. Sci., 38 (2003) 2655.

[9] K. Uchino, E. Sadanaga, and T. Hirose, J. Am. Ceram. Soc., 72 (1989) 1555.

[10] F.-S. Yen, H.-I. Hsiang, and Y.-H. Chang, Jpn. J. Appl. Phys., 34 (1995) 6149.

[11] G. Arlt, D. Hennings, and G. de With, J. Appl. Phys., 58 (1985) 1619.

[12] M.H. Frey, Z.X.P. Han, and D.A. Payne, Ferroelectrics, 206-207 (1998) 337.

[13] M.C. Cheung, H.L.W. Chan, and C.L. Choy, J. Mater. Sci., 36 (2001) 381.

[14] K. Tadanaga, K. Imai, M. Tatsumisago, and T. Minami, J. Electrochem. Soc., 140 (2000) 4061.

[15] M. Giorgetti, S. Passerini, W.H. Smyrl, and M. Berrettoni, Chem. Mater., 11 (1999) 2257.

[16] S. Passerini, F. Coustier, M. Giorgetti, and W.H. Smyrl, Electrochem. Solid-State Lett., 2 (1999) 483.

[17] W. Dong and B. Dunn, Proceedings of the Fifth International Symposium on Aerogels (ISA 5), J. Non-Cryst. Solids, 225 (1998) 135.

[18] S. Passerini, D.B. Le, W.H. Smyrl, M. Berrettoni, R. Tossici, R. Marassi, and M. Giorgetti, Solid-State Ionics, 104 (1997) 195.

[19] B.B. Owens, S. Passerini, and W.H. Smyrl, Electrochim. Acta, 45 (1999) 215.

[20] U. Schubert and N. Husing, Angew. Chem., Int. Ed., 37 (1998) 23.

[21] J. Fricke, M.C. Arcduini-Schuster, D. Büttner, H.-P. Ebert, U. Heinemann, J. Hetfleisch, E. Hümmer, and J. Kuhn, J. Therm. Conduct., 21 (1990) 235.

[22] S.T. Mayer, R.W. Pekala, and J.L. Kaschmitter, J. Electrochem. Soc., 140 (1996) 446.

[23] R.W. Pekala, J.C. Farmer, C.T. Alviso, T.D. Tran, S.T. Mayer, J.M. Miller, and B. Dunn, Proceedings of the Fifth International Symposium on Aerogels (ISA 5), J. Non-Cryst. Solids, 225 (1998) 74.

[24] R. Saliger, U. Fischer, C. Herta, and J. Fricke, Proceedings of the Fifth International Symposium on Aerogels (ISA 5), J. Non-Cryst. Solids, 225 (1998) 81.

[25] R.W. Pekala and C.T. Alviso, Novel Forms of Carbon, Mater. Res. Soc. Symp. Proc. 270 (1992) 3.

[26] J. Fricke and A. Emmerling, J. Sol-Gel Sci. Technol., 13 (1998) 299.

[27] P. Lobmann, W. Glaubitt, S. Geis, and J. Fricke, J. Sol-Gel Sci. Technol., 16 (1999) 173.

[28] P. Lobmann, W. Glaubitt, and G. Muller, J. Mater. Sci., 33 (1998) 2371.

[29] P. Lobmann, W. Glaubitt, S. Geis, and J. Fricke, J. Proceedings of the Fifth International Symposium on Aerogels (ISA 5), J. Non-Cryst. Solids, 225 (1998) 130.

[30] A. Zunger, MRS Bull., 23 (1998) 8.

[31] T. Ohno, D. Suzuki, H. Suzuki, and T. Ida, KONA, 24 (2004) 195.

APPENDIX A: XRD analysis

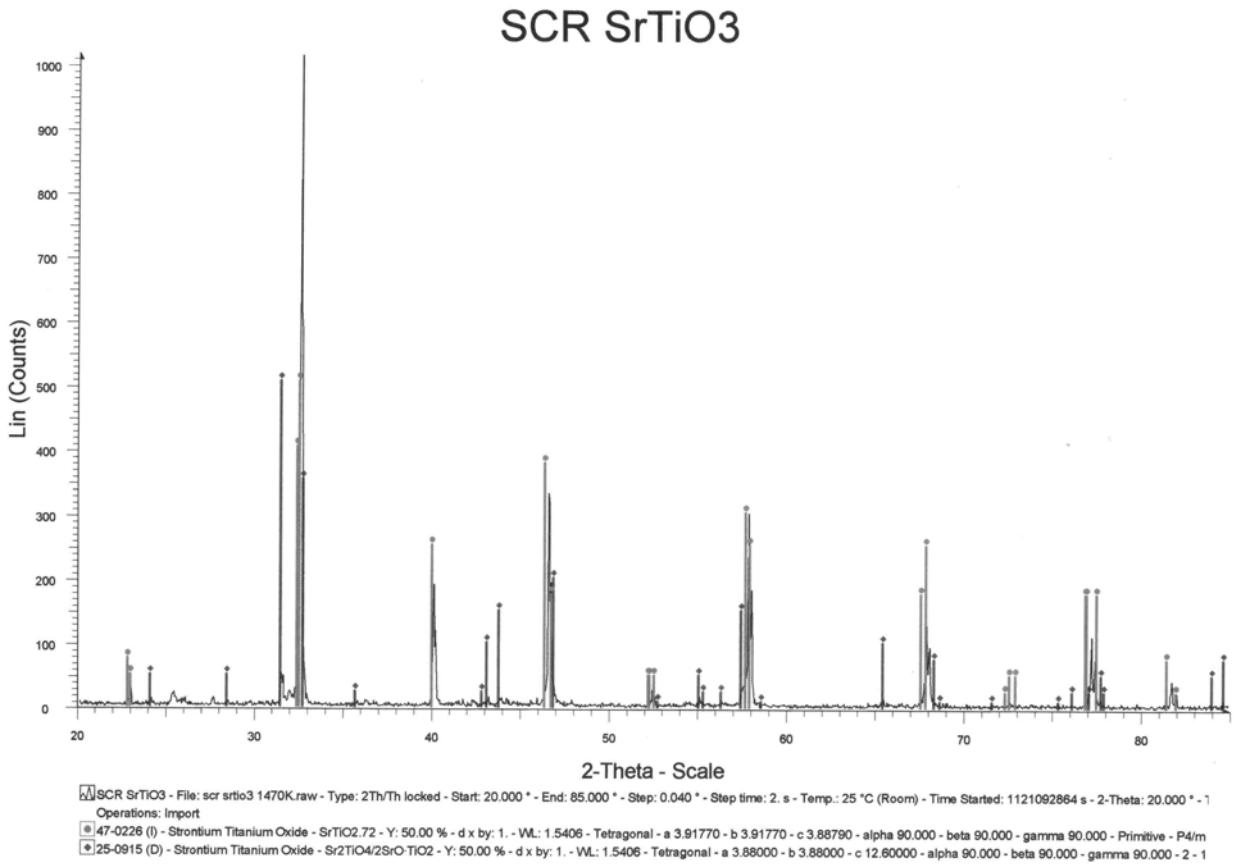

Figure A.1 Powder XRD Pattern of Solid-State Prepared Strontium Titanate

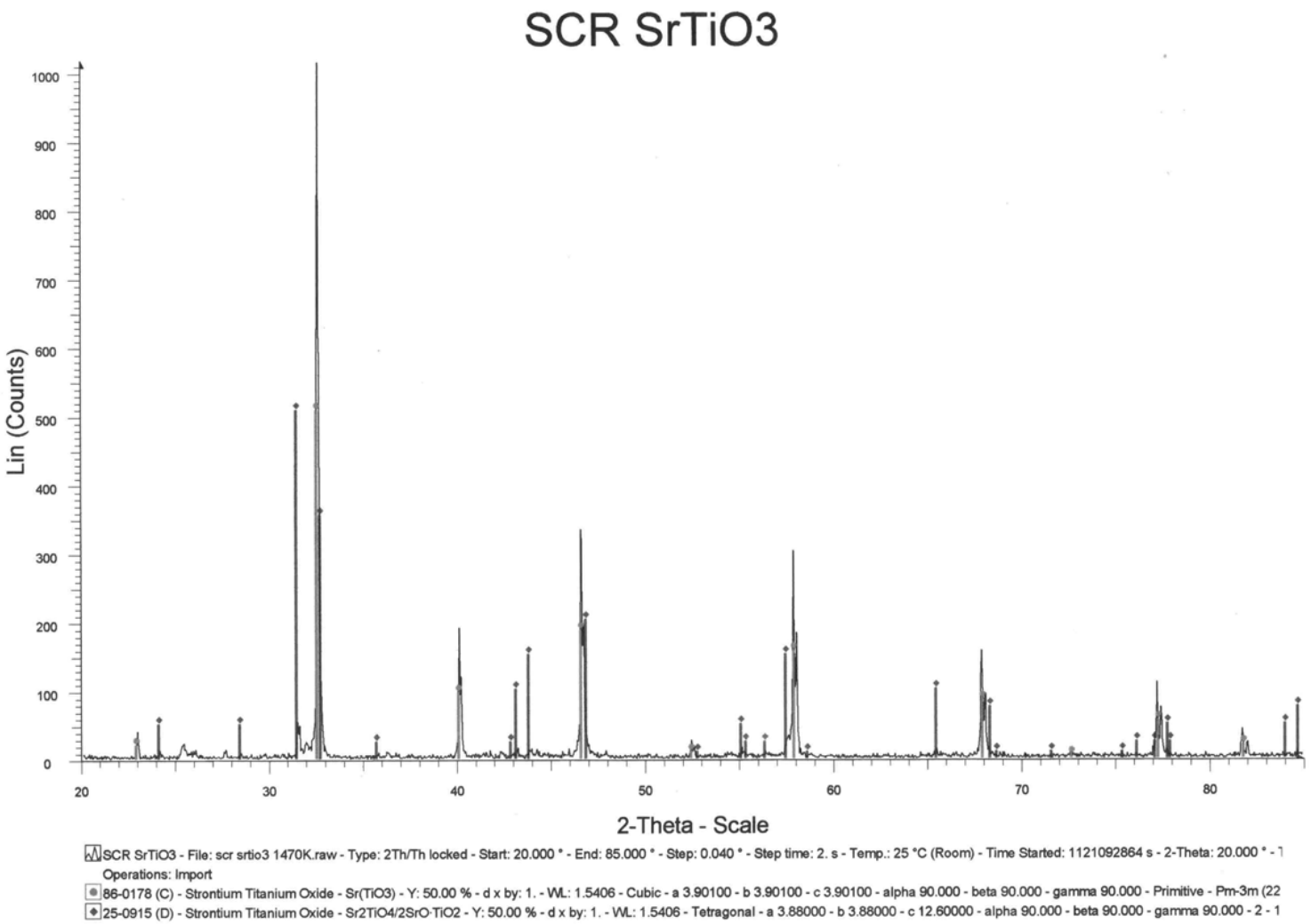

Figure A.2 Powder XRD Pattern of Solid-State Prepared Strontium Titanate

APPENDIX B: Elemental analysis

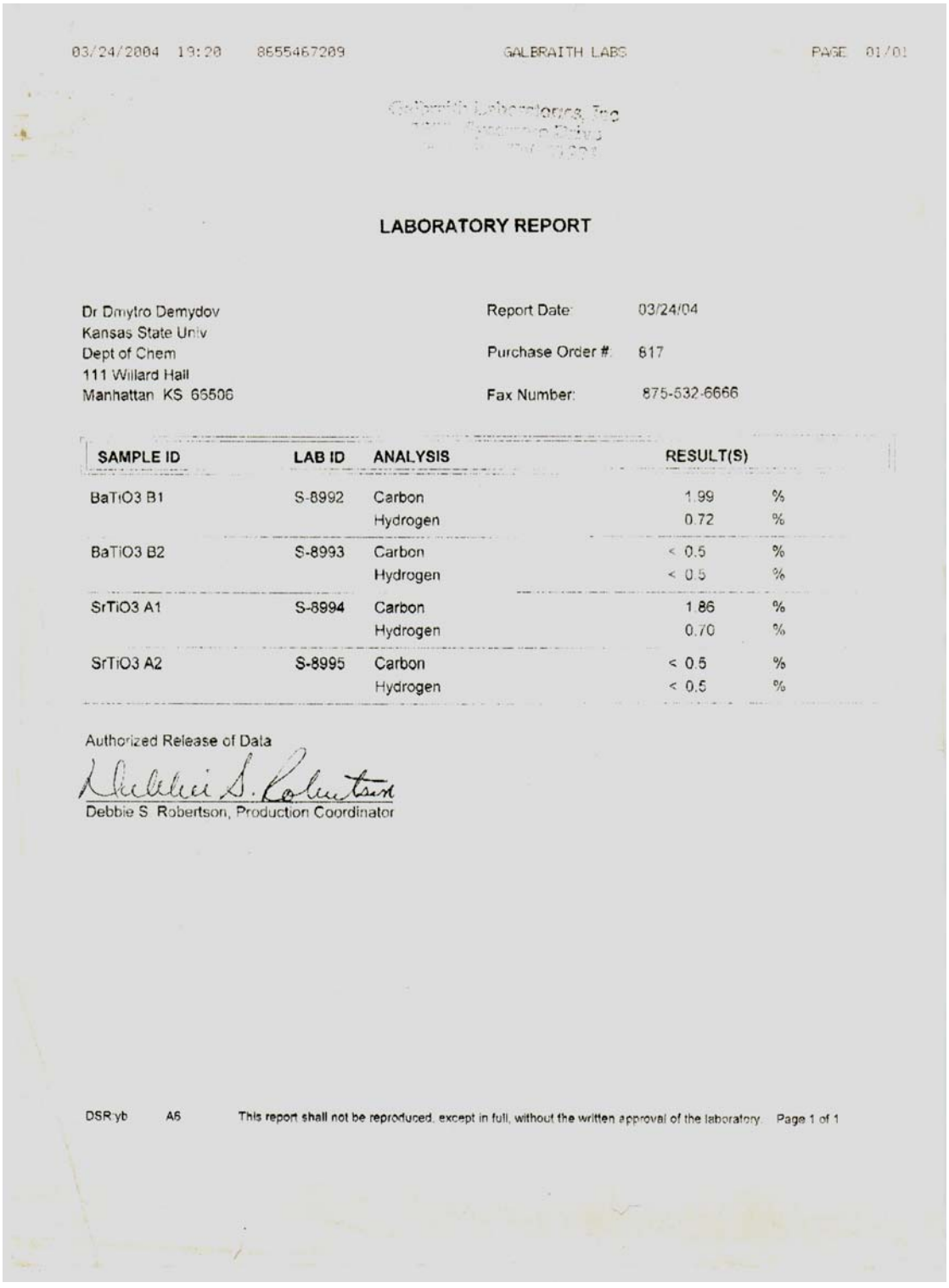

03/24/2004 19:20 8655467209 GALBRAITH LABS PAGE 01/01

Galbraith Laboratories, Inc.

LABORATORY REPORT

Dr Dmytro Demydov
Kansas State Univ
Dept of Chem
111 Willard Hall
Manhattan KS 66506

Report Date: 03/24/04
Purchase Order #: 617
Fax Number: 875-532-6666

SAMPLE ID	LAB ID	ANALYSIS	RESULT(S)	
BaTiO3 B1	S-8992	Carbon	1.99	%
		Hydrogen	0.72	%
BaTiO3 B2	S-8993	Carbon	< 0.5	%
		Hydrogen	< 0.5	%
SrTiO3 A1	S-8994	Carbon	1.86	%
		Hydrogen	0.70	%
SrTiO3 A2	S-8995	Carbon	< 0.5	%
		Hydrogen	< 0.5	%

Authorized Release of Data

Debbie S Robertson, Production Coordinator

DSR:yb A6 This report shall not be reproduced, except in full, without the written approval of the laboratory. Page 1 of 1

Figure B.1 CH Elemental Analysis for AP-$SrTiO_3$ and AP-$BaTiO_3$ (Galbraith Laboratories, Inc.)

APPENDIX C: TGA analysis

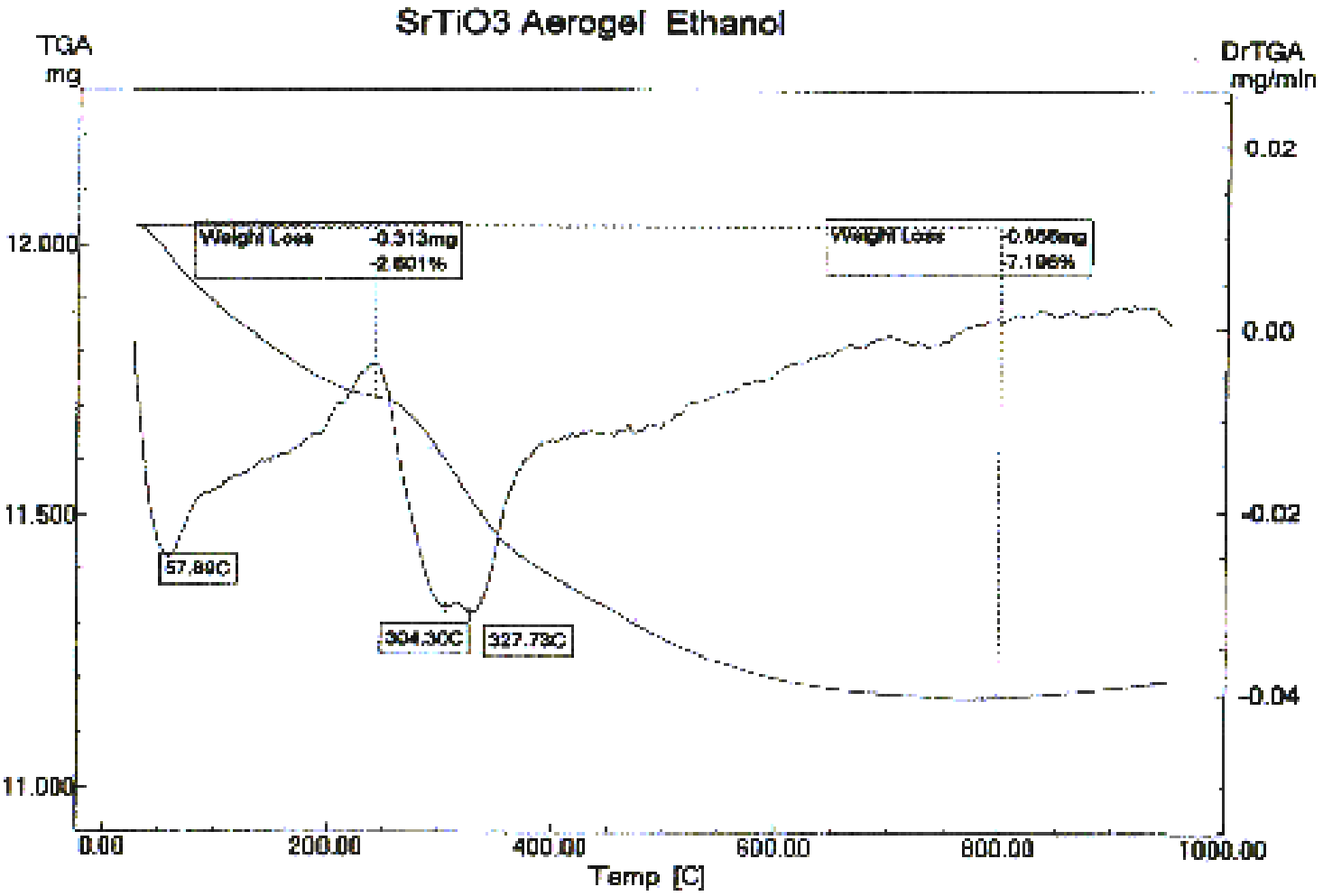

Figure C.1 Thermogravimetric Analysis of AP-$SrTiO_3$ (Ethanol)

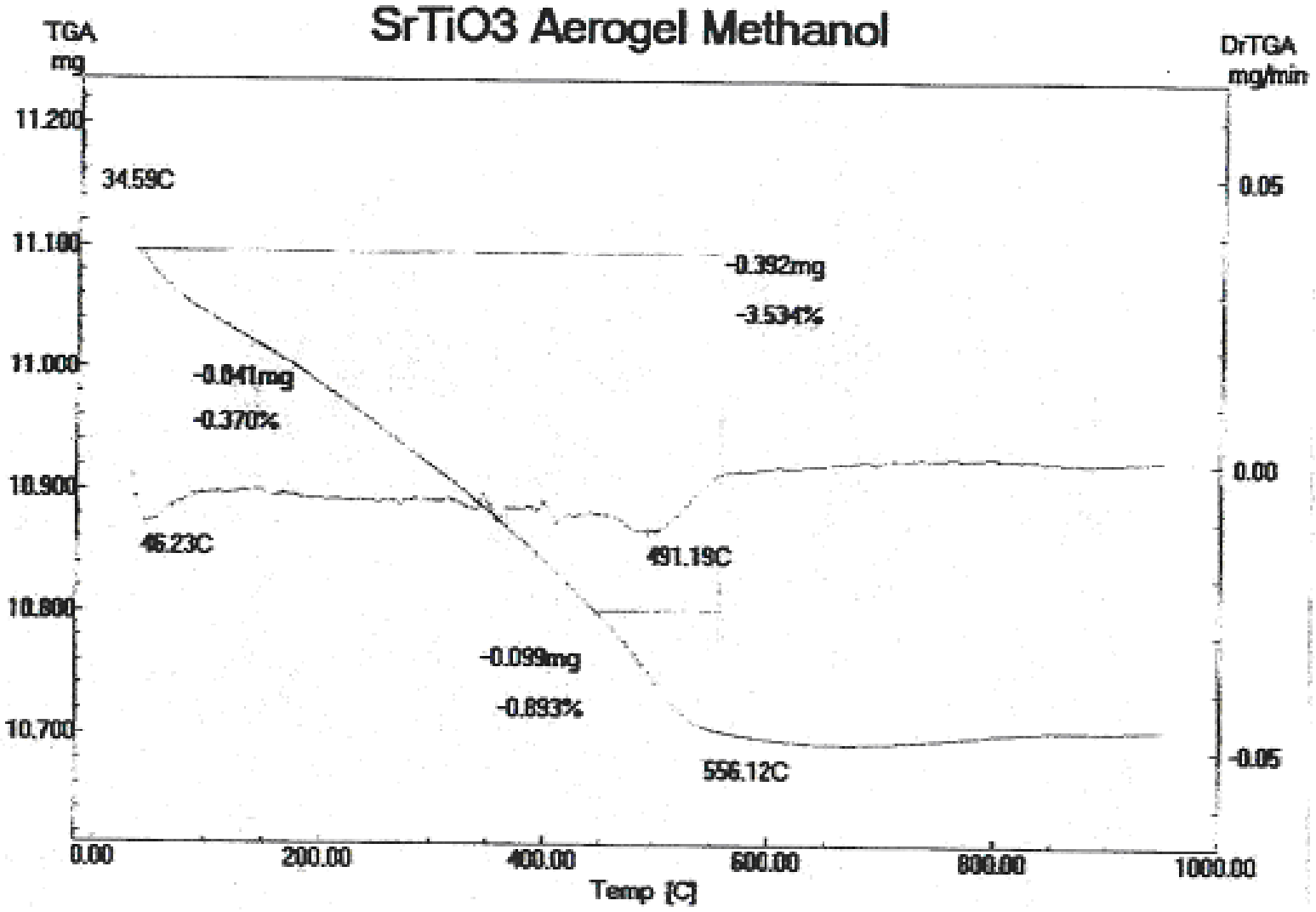

Figure C.2 Thermogravimetric Analysis of AP-$SrTiO_3$ (Methanol)

APPENDIX D: *in situ* FTIR

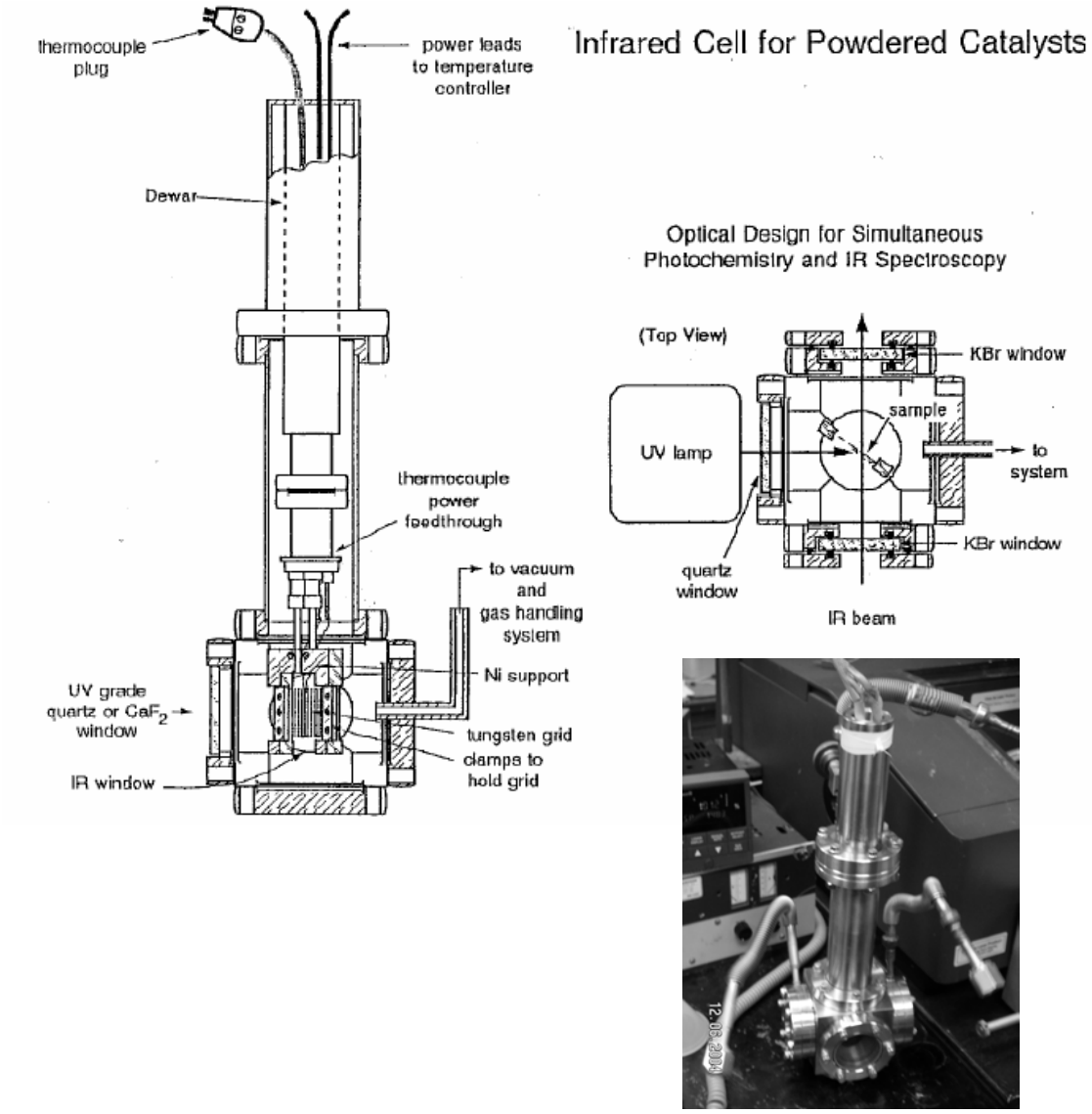

Figure D.1 Infrared Cell for Powdered Photocatalysis

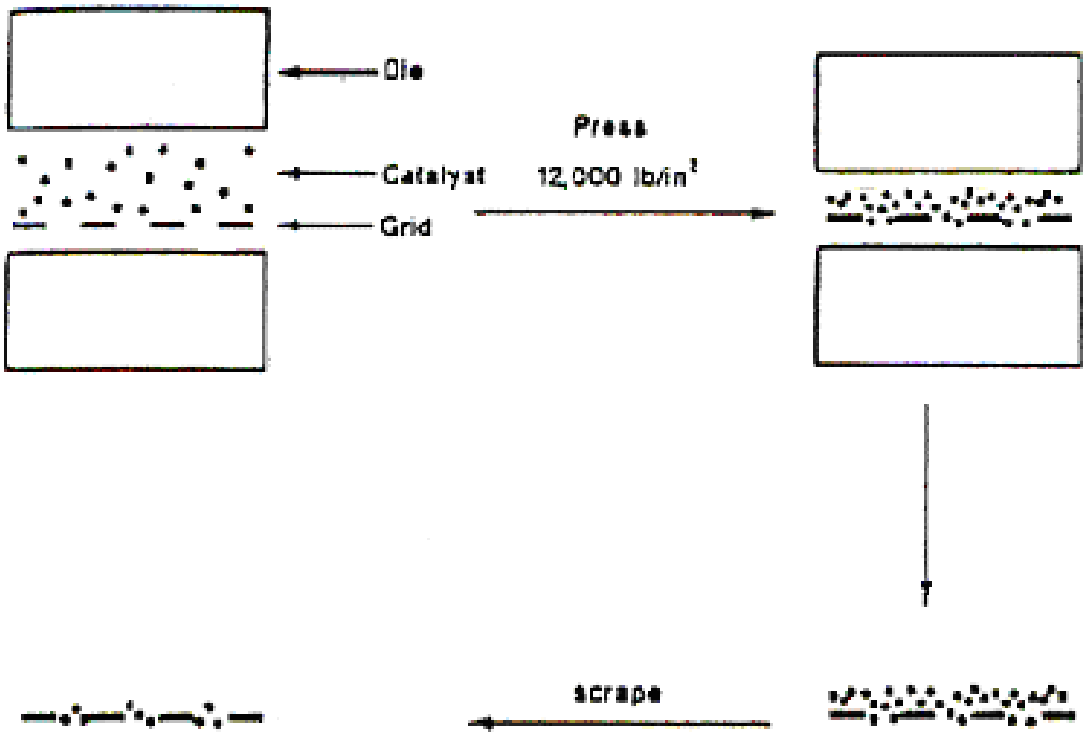

Figure D.2 Catalyst Sample Preparation on a Tungsten Grid

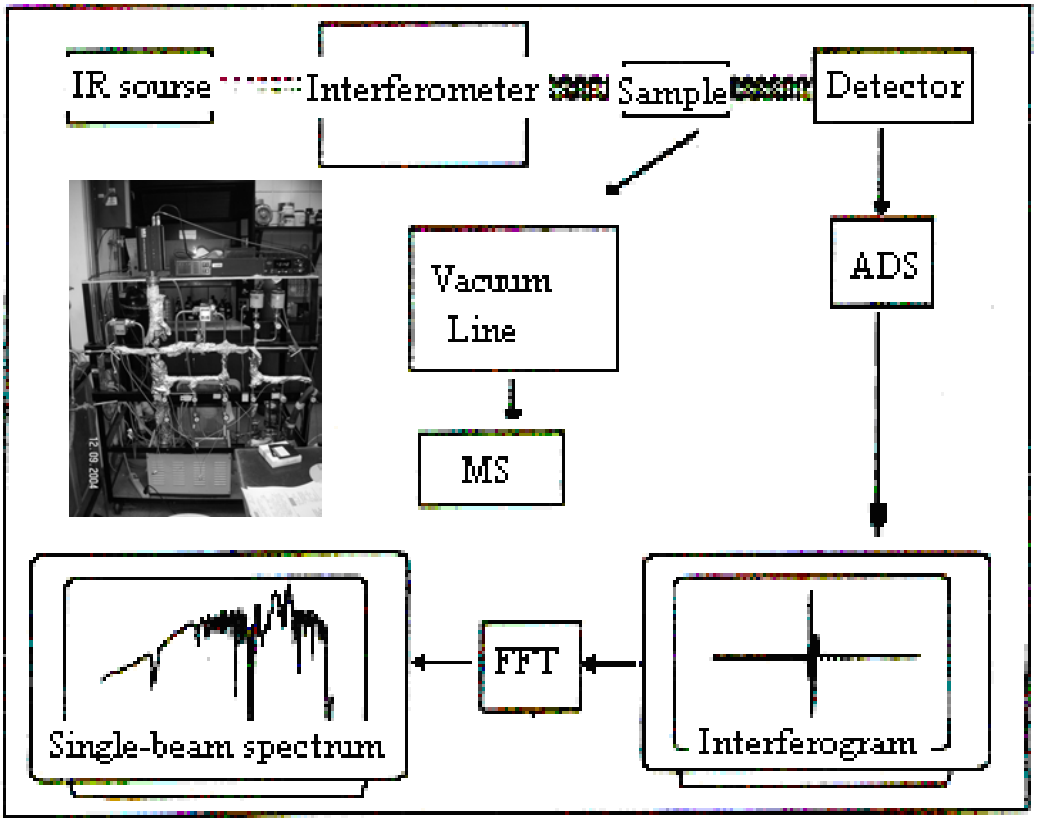

Figure D.3 Setup of Mattson Research Series RS-10000 FTIR, Vacuum Line, and MKS PPT Residual Gas Analyzer/Quadruple Mass Spectrometer

APPENDIX E: Dielectric measurements

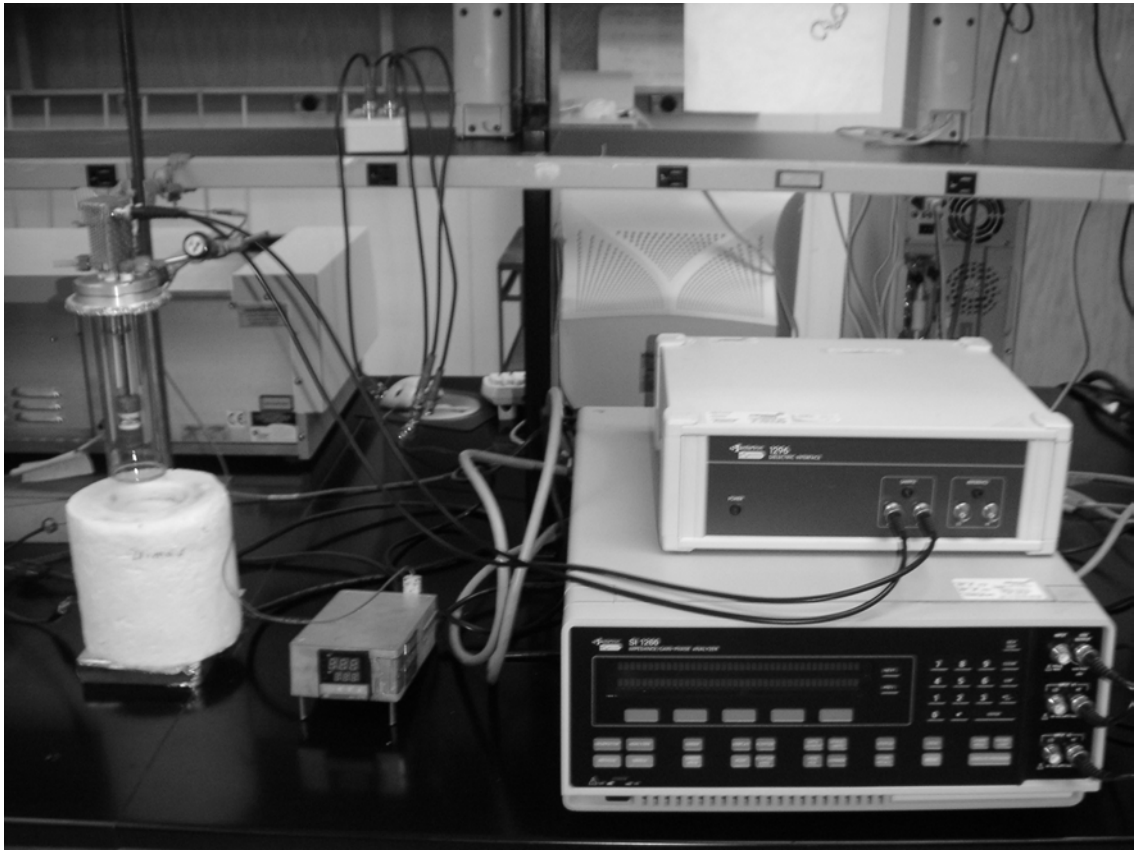

Figure E.1 Solatron SI-1260 Impedance/ Gain-phase Analyzer in Combination with Solatron 1296 Dielectric Interface and Dielectric Cell

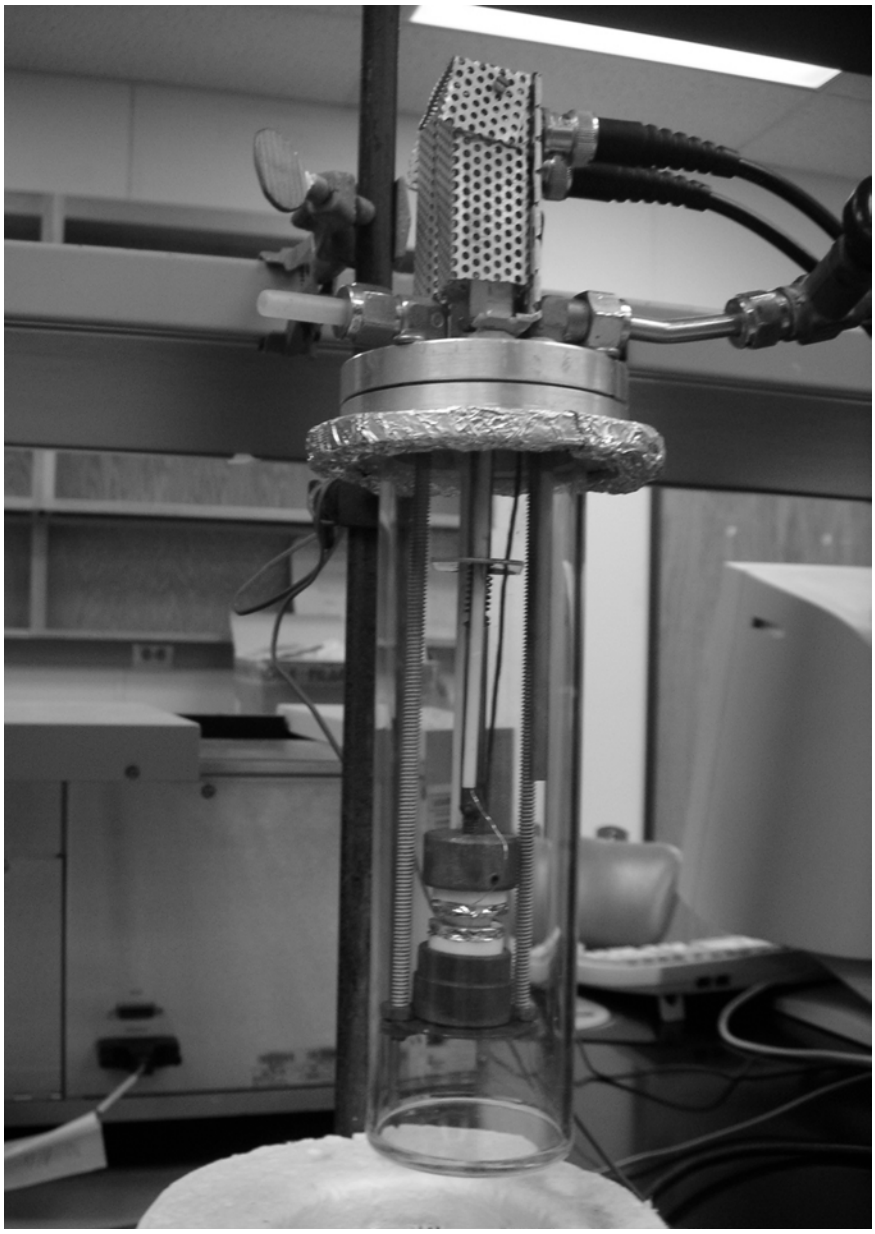

Figure E.2 Dielectric Cell with a Pellet between Platinum Electrodes

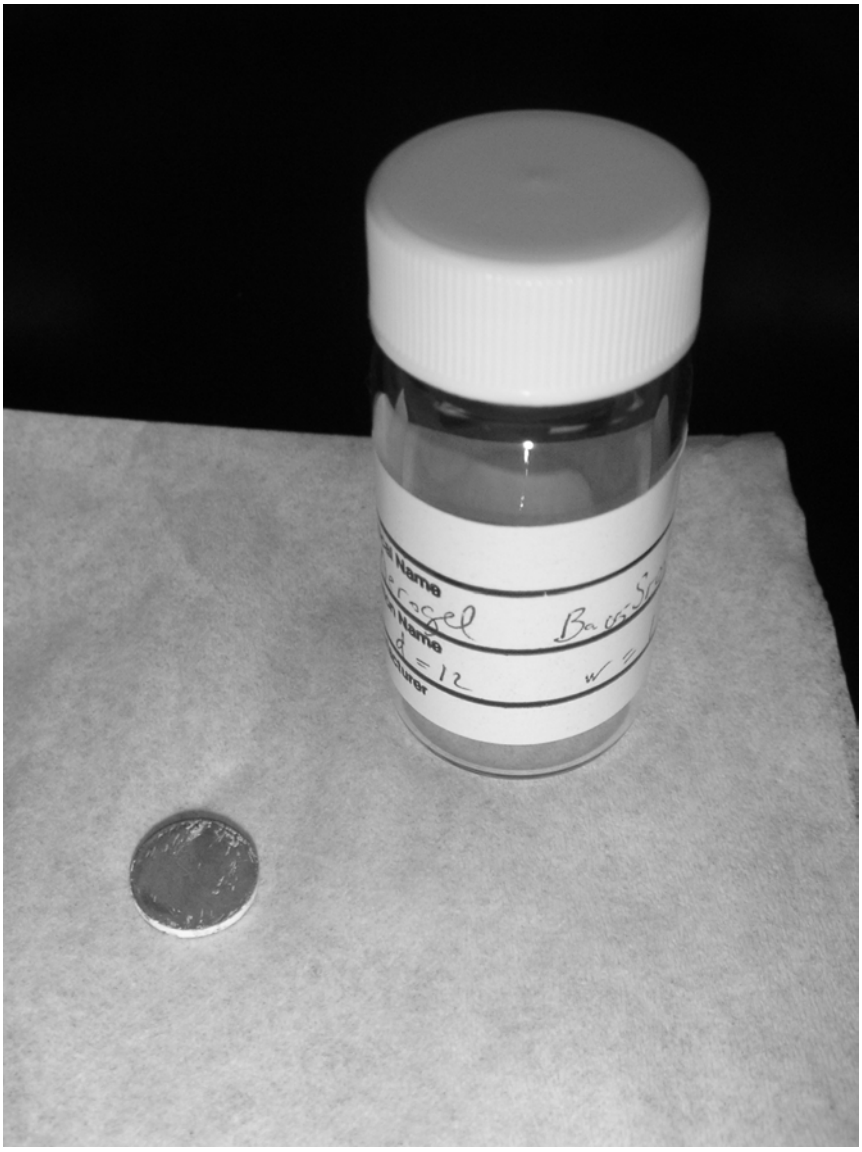

Figure E.3 AP-$Ba_{0.5}Sr_{0.5}TiO_3$ Pellet Coated with Silver

APPENDIX F: Permission to reproduce materials

1. Reprinted from **Journal of Non-Crystalline Solids** Dmytro Demydov and Kenneth J. Klabunde, "Characterization of mixed metal oxides ($SrTiO_3$ and $BaTiO_3$) synthesized by a modified aerogel procedure," 350, 165 -172, Copyright (2004), with permission from Elsevier.

2. Reprinted from **Nanostructured and Advanced Materials**, Vaseashta, A.; Dimova-Malinovska, D.; Marshall, J.M. (Eds.), Proceedings of the NATO Advanced Study Institute, held in Sozopol, Bulgaria, 6-17 September 2004, Series: NATO Science Series II: Mathematics, Physics and Chemistry, D.V. Demydov and K.J. Klabunde, "Synthesis, characterization, photocatalytic and dielectric properties of nanosized strontium and barium titanates," 204, 327-330, Copyright (2004), with kind permission of Springer Science and Business Media.